Thesis Submission

“Computational Investigation of Flow Dynamics in Acoustically Driven Cavitating Flow in Horn-type Reactors”

By

Basel Zaher (Mohamad Hesham) Al Bishtawi

Dr. Gianfranco Scribano (Principal Supervisor)
Dr. Khameel Bayo Mustapha (Co-supervisor)

Thesis Submitted to the University of Nottingham Malaysia in
fulfilment of the requirements for the degree of
Doctor of Philosophy
May 2025

Abstract

Acoustic cavitation remains, to this day, a peculiar acoustofluidic phenomenon that has recently attained highly concentrated research traction, as many seek new passive solutions to intensify a variety of chemical processes. However, the ever-increasing severity of water crisis serves as the primary driver to expand on this research. It has been previously established that ultrasonically induced cavitation retains the ability to induce high yields of volatile hydroxyl $OH^{\cdot}$ radicals within the working fluid domain through generating severe flow conditions upon their collapse. However, the underlying coupled behaviour of the acoustically induced flow behaviours and the acoustic cavitation remains prominently inconclusive. Therefore, the presented investigation revolves around numerically exploring multiphase flow behaviours observed in a horn-type reactor environment. This is performed by configuring a computational fluid dynamics (CFD) setup with a new cavitation model and a dynamic mesh model, generalizing the coupled flow behaviours observed under multiple horn tips of varying diameters, and establishing the relationship between the cavitating flow with the reactor performances observed.

In that manner, the CFD setup was coupled with a newly derived cavitation model based on a series of derivations of the Rayleigh-Plesset equation that define the bubble radial development in terms of water tension and inertial growth. Empirical values that surfaced from the model were statistically optimized through a Design of Experiments approach, coupled with Monte Carlo simulations, to assess the influence of empirical model constants on the model's performance by examining variations in amplitude and frequency responses. This was then coupled with a dynamic meshing model that defines the oscillating ultrasonic horn walls as uniformly and sinusoidally deforming. Upon comparatively assessing each model's performance, it was ultimately revealed that Kirchhoff-based model generally underpredicts the acoustic cavitation structure experimentally observed under the horn tip. Based on the Finite Time Lyapunov Exponent (FTLE) results, key differences lied within the vortex shape and position proximally generated; the Kirchhoff-based model predicted an eccentric vortex that induced an impinging jet that facilitates a two-step collapse of the cavitation, as opposed to the single-step collapse typically observed.

As the vortex was revealed to have a key role in the flow-cavitation coupling, a parametric analysis was conducted on a horn-type reactor domain considering multiple diameters, namely 3, 6, 13, 16, and 19 mm, to further explore the extent of this coupling. It was uncovered that the acoustic cavity structure falls between two geometrical structures, namely, mushroom-like structure (MBS) and cone-like bubble structure (CBS), based on the actuated ultrasonic horn tip diameter. The cavity structure is molded into MBS by the presence of a symmetric locomotive vortex structure that extends up to 1.5 times the horn tip diameter. Meanwhile, CBS takes shape in the presence of an eccentric locomotive vortex that attains a size within 0.2–0.6 times the horn tip diameter. Upon time-averaging the flow, the stream-linked vortex produced in all cases was found to consistently create a stagnation plane at a distance two times the horn tip diameter (2D) from the horn tip. A one-dimensional mathematical formulation was derived and solved based on the Stuart streaming conservation of momentum and its respective definition of the acoustic force ($\vec{F}_a$). This revealed that compound attenuation (α) of the acoustic force decreases exponentially at a maximum rate of ≈ 1.70 with the doubling of Reynolds number (Re). However, an inverse trend was demonstrated, upon considering the

influence of the diameter, by the dimensionless attenuation (Γ), as it gradually increased by a factor of ≈ 1.28.

Ultimately, the practical significance of this trend of acoustic attenuation induced by the presence of the cavitation structure was most pronounced after conducting yet another parametric investigation scrutinizing the reactor performance of horn-type reactors of the following sizes: 3 mm, 7 mm, 14 mm, 24 mm, 32 mm, and 40 mm. A numerical investigation of these cases highlighted that the vortex gradually becomes more viscous-dominant under larger horns, which, in turn, prevents it from creating the low-pressure nodes previously observed within the vicinity of smaller horns. As a result, this led to the shrinkage of the cavitation structure, and ultimately, creating a slowly oscillating thin flat attached cavitation structure. Due to the recurrence of this observation in cases of 24 mm, 32 mm, and 40 mm horns, it was concluded that such low frequency oscillations of such structures release more $OH^{\cdot}$ radicals and create more activity zones.

List of Publications

Journal Papers

Basel Al Bishtawi, Khameel Bayo Mustapha, Gianfranco Scribano; Modeling the mass transfer at acoustically generated bubble interface using Rayleigh–Plesset equation second-order derivatives. *Physics of Fluids* 1 November 2022; 34 (11): 113303. https://doi.org/10.1063/5.0124416

Basel Al Bishtawi, Khameel Bayo Mustapha, Gianfranco Scribano; Molding the acoustic cavity–analyzing the influence of toroidal vortex development on acoustic multi-bubble macrostructures under different ultrasonic horn tip diameters. *Physics of Fluids* 1 April 2024; 36 (4): 043336. https://doi.org/10.1063/5.0206290

B. Al Bishtawi, K. B. Mustapha, G. Scribano; On the early stagnation point during transient acoustic cavitation. *Physics of Fluids* 1 February 2025; 37 (2): 023312. https://doi.org/10.1063/5.0249003

B. Al Bishtawi, G. Viciconte, T. T. Truscott, W. L. Roberts, K. B. Mustapha, G. Scribano; The Two-way coupling between acoustically generated vortical flows and bubbly activity zone dispersion. *(In Preparation)*

Conference Papers

Basel Al Bishtawi, Khameel Bayo Mustapha, Gianfranco Scribano; Influence of toroidal vortex dynamics on acoustic cavitation development under different ultrasonic horn tip vibration modes. *Cavitation Symposium 2024 (CAV2024)*. July 2024

Acknowledgement

I would like to express my sincere gratitude to both of my esteemed main supervisor and co-supervisor, Dr. Gianfranco Scribano and Dr. Khameel Bayo Mustapha, for their invaluable guidance, encouragement, and patience during the course of my degree. Their thoughtful advice and constant support have been essential to both the academic and personal growth I experienced during this journey. My gratitude extends to the Faculty of Science and Engineering for granting me a full scholarship to undertake my studies at the Department of Mechanical, Materials, and Manufacturing Engineering.

I am also thankful to Gianmaria Viciconte from King Abdullah University of Science and Technology for facilitating our research collaboration and for his experimental and theoretical insights that added influential value to the interpretation and practical correlation to my numerical work and results.

I like to extend my thanks to Dr. Elena Vagnoni from Technology Platform for Hydraulic Machines, École Polytechnique Fédérale de Lausanne for warmly welcoming our research collaboration at her lab and for her treasured support throughout our collaborative project which significantly honed my experimental skills.

I also would like to sincerely thank my friends and colleagues, whose companionship, conversations, and kindness provided motivation and balance through the most challenging times. And I am deeply grateful to my family for their unwavering belief in me, especially during moments of doubt and fatigue. Their love and encouragement have been a steady foundation upon which I have built not just this thesis, but my entire academic path.

Lastly and most importantly, this thesis is dedicated to my grandfather, who always insisted on my perseverance to pursue a PhD long before I believed it was possible. His confidence in my potential and his deep respect for education were constant sources of motivation. May this stand as a small reflection of the love of learning he has instilled in me.

Table of Contents

List of Figures

List of Tables

Abbreviations

TSS	Total Suspended Solids	SS	Sum of Square
BOD	Biological Oxygen Demand	MS	Mean Square
COD	Chemical Oxygen Demand	FFT	Fast Fourier Transform
PFOS	Perfluorooctane Sulfonate	FTLE	Finite Time Lyapunov Exponent
PFOA	Perfluorooctanoic Acid	LCS	Lagrangian Coherent Structure
HAC	Hydrodynamic-acoustic Cavitation	CBS	Cone-like Bubble Structure
HC	Hydrodynamic Cavitation	MBS	Mushroom-like Bubble Structure
UDF	User-defined Function	MR	Momentum Ratio
UV	Ultraviolet	AR	Aspect Ratio
CFD	Computational Fluid Dynamics	RMS	Root Mean Square
EOS	Equation of State	LHS	Left-hand Side
PEG	Polyethylene Glycol		
HIFU	High Intensity Focused Ultrasound		
LBM	Lattice Boltzmann Method		
MRT	Multiple Relaxation Time		
BI	Boundary Integral		
RNW	Rayleigh-Nyborg-Westervelt		
RANS	Reynolds Averaged Navier-Stokes		
DES	Detached Eddy Simulation		
LES	Large Eddy Simulation		
SST	Shear Stress Transport		
ZGB	Zwart-Gerber-Belamri		
RSM	Response Surface Method		
SDS	Sodium Dodecyl Sulphate		
PRESTO!	Pressure Staggering Option		
RNG	Random Number Generator		
ANOVA	Analysis of Variance		
VIF	Variance Inflation Factor		

Nomenclature

Greek Letters

σ	Surface tension	Γ	Dimensionless attenuation
δ	Tolman length	Δ	Variable gradient
φ	Velocity of liquid induced by cavitation bubble	ϱ	Material derivative of time
r	Volume fraction	ϕ	Diameter
β	Compressibility	α	Acoustic attenuation
μ	Dynamic viscosity		

Latin Letters

P	Local pressure	U_∞	Freestream velocity
U	Bulk velocity	f	Frequency
R	Radius	T	Temperature
J	Nucleation rate	W	Net Energy
N	Bubble density	Q	Flow rate
S	Source term	M	Moment
D	Horn diameter	$\dot{m}^{+/-}$	Mass transfer rate

Subscripts

B	Bubble-related property	u	Upstream condition
v	Vapor-related property	d	Downstream condition
l	Liquid-related property	∞	Ambient/Free-stream condition
C	Critical-condition property	r	Radial coordinate
S	Surface-related property	z	Axial coordinate

Dimensionless Numbers and Constants

Gb	Gibbs number	St	Strouhal number
Re	Reynolds number	c_p	Pressure coefficient
k	Boltzmann constant	L_c	Loss coefficient
d_i	Desirability	R_g	Specific gas constant
r_{nuc}	Nucleation site volume fraction	F_{cond}	Condensation constant
F_{evap}	Evaporation constant	F_{evap}	Evaporation constant
β_{ij}	Regression model coefficients	σ_c	Cavitation number

1 Introduction

1.1 Background and Motivation

Water scarcity is a crucial issue that continues to exacerbate annually as prominent scarcity indicators, such as the Falkenmark matrix [1] and the Kummu et al. approach [2], successfully identified; there is clear evidence of diminishing freshwater sources. As a form of adaptation, a multitude of nation-sponsored research and projects were initiated in order to address and adopt new solutions that suggest utilizing non-drinkable water as a new source of freshwater by running it through multiple filtration processes. A major example of such is desalination plants where saline water from nearby seas are driven into them to remove the salt and regulate the total dissolved solids reasonably to meet the set standard for safe drinking water [3,4]. Leading technologies of such type are reverse osmosis [5], nano-filtration [6], and electrodialysis [7]. On the other hand, thermal-based techniques are phase-transition technologies that mimic the natural water cycle in a way where the saline solution is heated to initiate its evaporation and later condensed into freshwater leaving the dissolved salts behind [4,8]. However, this technology does not provide a solution to the problem of water contamination, instead, it has expanded on this problem by introducing brine as a refuse that is rejected into natural freshwater sources. Brine typically is composed of many toxic chemical residuals, such as polyphosphates and cationic polymers [9,10] used in pre-treatment and post-treatment stages.

Wastewater commonly refers to the polluted water discharged from communal sources, regardless of their domestic or industrial origins. Often, wastewater retain recognizable physical and chemical anomalies that critically harm the environment if disposed improperly. Evaluation of water quality rely on terms like pH, temperature, total suspended solids (TSS), biological oxygen demand (BOD), and chemical oxygen demand (COD) as key indicators to the degree of water pollution [11-13]. These quantities tend to fall within a significant range depending on the types of contaminants present in the aqueous solution; those can be grouped as organic, non-organic [14], and biological pollutants [15]. For example, industrial wastewater has an average of the following chemical attributes: pH – 9.2, COD – 1098 mg/L, BOD – 215.0 mg/L, TSS – 217.5 mg/L [13]. What these quantities indicate, in this case, is that the solution is basic and has large quantities of organic matter, both biologically reactive and non-biologically reactive. In other words, bacteria and other microorganisms hold a dominant presence in industrial wastewater which reduce the overall quality of water when rejected back to natural water bodies. In return, this acts as a potential threat to existing organisms in those water bodies. Therefore, many investigations have been allocated to finding novel solutions that could curb water pollution in an operationally efficient and cost-efficient way [16-18].

Conventional wastewater treatment approaches are many; however, the plant procedures are one and the same. As such, all wastewater treatment plants maintain pre-treatment, primary, secondary, and tertiary treatment stages [19]. Nonetheless, the point of difference typically lies in the specific mechanical and chemical methods used at these stages. Examples of such processes are presented in Figure 1.1 below.

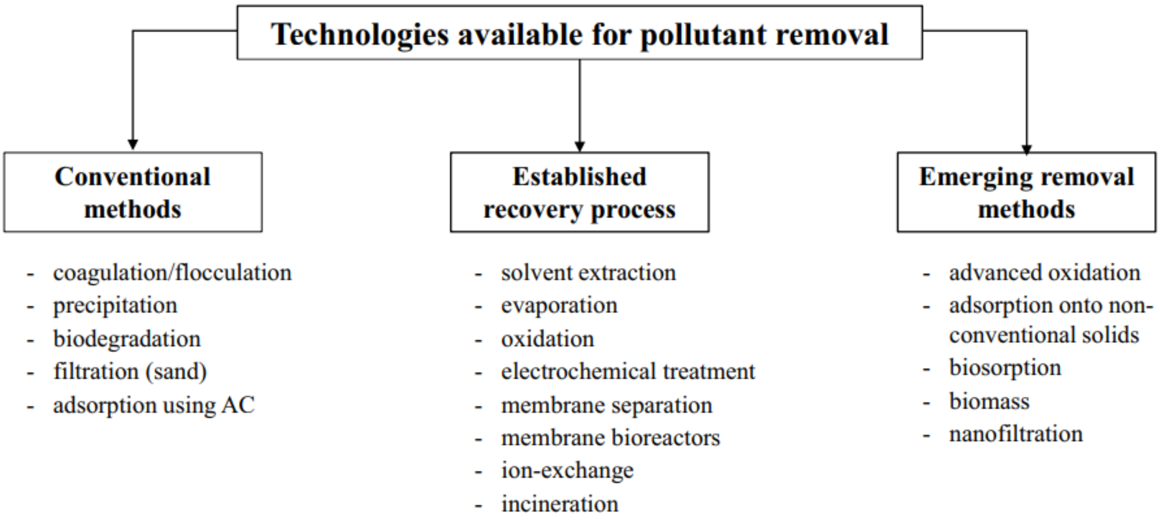

Figure 1.1: Groupings of existing mechanical, chemical, and biological treatment methods found commercially and in recent literature [20].

The selection of these methods is dependent on the nature of pollutants found in the wastewater effluent. Moreover, the selection process is constraint by its feasibility, efficiency, and operational costs [20-22]. In addition, the environmental impact and the generation of toxic by-products are also accounted for in the selection. Plants treating industrial wastewater encounter many stubborn industrial pollutants that are extremely difficult to remove, such as perfluorooctane sulfonate (PFOS) [23], ammonium nitrogen [24], perfluorooctanoic acid (PFOA) [25], and diethylhexyl phthalate [26]. However, these materials are considered grey-listed pollutants that pose as a potential risk to the environment but are not necessarily considered hazardous. On the other hand, black-listed pollutants are often referred to as bio-refractory pollutants that not only are toxic but lead to bioaccumulation. Particularly, these kinds of pollutants have a higher chance of escaping treatment and being disposed of into the environment in which it will, eventually, lead to a large growing population of these pollutants in the environment [27]. Generally, this is mainly due to its persistence and resistive nature towards conventional biological treatment. Moreover, microorganisms, specifically bacteria, fall within that category, as some are classified as Gram-positive bacteria that have thick peptidoglycan cell wall making them resistive to mechanical and chemical stresses [28]. As exotic as such bacteria may seem, they are, in fact, quite common; bacteria E. Coli, L. Pneumophila, B. Subtilis, and E. Faecalis all fall under the Gram-positive bacteria category. Reasonably so, this gave a platform for researchers to investigate novel, reliable techniques that would best solve the problem of environment intoxication.

One of the many techniques that have been, and remains consistently, investigated is cavitation. In simple terms, cavitation is a term first introduced by J. Thornycroft and S.W. Barnaby in 1895 [29] to describe the phenomenon of bubble formation and collapse in a liquid body rapidly passing through hydraulic machinery, such as ship propellers and pumps. This phenomenon is typically initiated by a gradient in fluid pressure reducing the tensile strength holding the liquid molecules together and allowing a formation of an unstable ‘cavity’ between the molecules [30]. Cavitation is considered an unfavorable phenomenon in hydraulics because of the mechanical complications that can occur in the machine due to the bubble implosions. However, and ironically enough, this very phenomenon has attracted the attention of researchers in the environmental engineering field to, perhaps, employ this in a such a way that would tackle the water pollution problem generated by the bio-refractory pollutants. This is justified by the extreme mechanical and chemical conditions that the bubble implosions induce in the liquid body, such as high local temperatures reaching 6000 K, and strong shockwaves producing a pressure of approximately 5500 bar at a jet velocity of 2000 m/s [31].

These bubbles can be generated both hydrodynamically and acoustically. Hydrodynamic cavitation, in other words, is the passive change in liquid pressure, such as a cross-sectional area change, in order to induce a drop below the vaporization pressure line [32]. On the other hand, acoustic cavitation is the production of an ultrasonic field, in the range of 20kHz and above, to create a pressure gradient. Under such circumstance, the cavitation bubbles will oscillate in and out of multiple expansion and compression acoustic cycles in which bubbles will grow and collapse based on the rate of dissolved gas mass transfer occurring at the interface between the bubbles and the liquid medium [33].

1.2 Wastewater Treatment Cavitation-based Methodologies

Wastewater treatment has undergone multiple stages of technological evolution, however, that eventually settled at the use of adsorption, ultraviolet (UV) degradation, and membrane filtration [32]. Such techniques are now recognized as conventional treatments that not only prove to be energy inefficient but ineffective against persistent organic components. Currently, a typical wastewater treatment plant consists of multiple stages, namely the primary, secondary, and tertiary stages. As mentioned in the background, each commercialized method used at any of these stages have their limitations. For example, aeration units commercially make up the secondary stage of wastewater treatment plants and are composed of a large basin with multiple air diffuser units fixed at the bottom to provide oxygen to the mechanically filtered influent to induce a reaction between released oxygen molecules and any volatile contaminant compounds. The unit then vents out these contaminants from the water. A simplified sketch of the operation is shown in Figure 1.2.

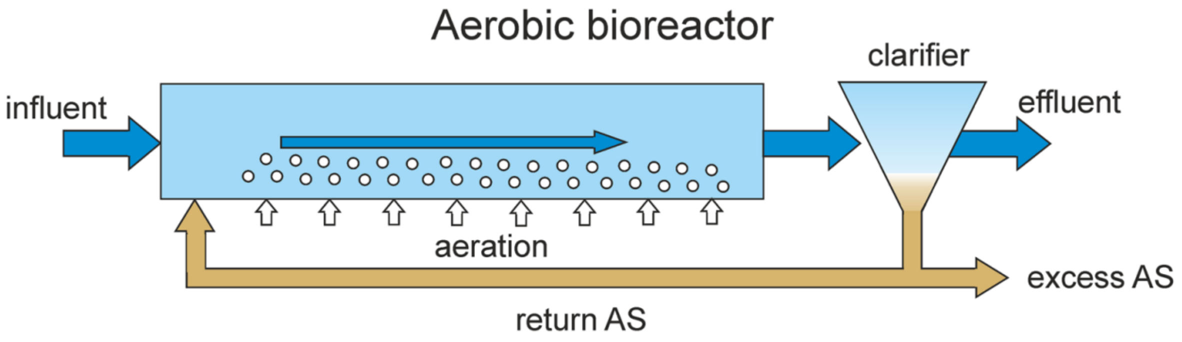

Figure 1.2: Schematic of a typical aerobic bioreactor utilizing aeration units at the bottom of the basin [34].

Despite that, with these units, bacteria and fungi still tend to escape with the filtered influent. In fact, around 80 - 6,900 CFU/m^3 and 510 – 3,900 CFU/m^3 worth of bacteria and fungi concentrations, respectively, are found in treated effluent [35]. Thus, recent explorations on alternative methods for wastewater treatments began gaining traction. Mainly, the usage of cavitation has been the primary field of investigation in alternative treatment plants. This could be owed to its volatile hydrodynamic nature as highlighted in previous sections. So, such cavitation units are referred to as hydrodynamic cavitation (HC) reactors. The literature divides these HC reactors into multiple categories depending on their geometries and types of flow. However, the five main forms of HC reactors are the venturi, orifice, vortex based, and rotating types.

1.2.1 Conventional Hydrodynamic Cavitation Reactors

Cavitation reactors typically come in many different geometries; however, they all share the same core mechanism, i.e. initialize bulk cavitation nucleation and facilitate their collapse. These reactors, ranging from the common venturi-type reactors to vortex-based reactors, operate by manipulating the pressure field along the flow path whereby a series of low-pressure zones are established at one end, and a high-pressure zone is maintained at the other end [36]. However, the most recent type of cavitation reactors is rotational type reactors. As this type of reactor is considerably new and emerging, they mostly exist on lab scales in the literature. Generally, the reactor consists of a rotor and a stator that rotate against one another generating shear forces that then result in shear cavitation of the liquid flowing between the rotor and stator. One positive reported on such reactors is that they are usually capable of generating a suction force, through a pressure differential, into the reactor without the use of an external pump. This way the power consumption witnesses a relative decrease compared to other reactor types [31].

In the literature, there exists multiple geometrical variations of this basic operational concept. Such geometrical variations typically revolve around the distributions and shapes of indentations on the rotor and/or the stator. Table 1.1 summarizes recent novel developments of rotational cavitation reactors in terms of their geometries and operational capabilities.

Table 1.1: Tabulation of developments in hydrodynamic cavitation reactors.

Reactor schematic	***Reference***	***Geometric parameters***	***Cavitation regime***	***Pollutant***	***Operating conditions***	***Conclusions***
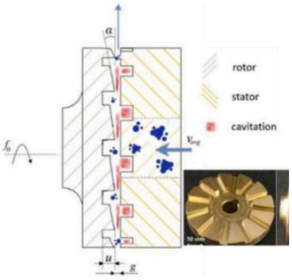	Sezun et al. [37]	Rotor-stator dia. = 50 mm. No. of CGUs = 12. CGU depth = 3 mm. α = 8°.	Periodic cavitation formation in rotor-stator gap, rotor teeth, and rotor-stator grooves.	Paper mill sludge and pulp.	V = 1L, t = 30 mins, T < 30°, P = 400 W.	Decrease in CODt by 53%. CODs increased by 36%.
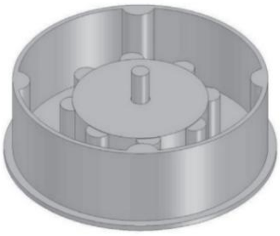	Cerecedo et al. [38]	No. of outer vanes = 4, No. of inner vanes = 8. Vane radius = 5 mm.	Attached, unsteady, cloud cavitation is formed by water flowing across vanes.	E. coli, E. faecalis of concentrations = 102 – 106 CFU/ml.	P = 650 W	High bubble collapse intensity and frequency. Significant reduction in concentration
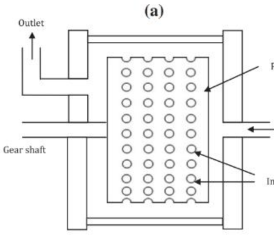	Badve et al. [39]	No. of CGUs = 204, CGU dia. = 12 mm, CGU depth = 20 mm.	Vortex cavitation due to high surface velocity of fluid creates low pressure fields	Wastewater sludge with COD = 38,000 mg/l	V = 4L, T = 20-25 °C, P = 1.1 kW, 2200 rpm.	COD decreased by 56%.
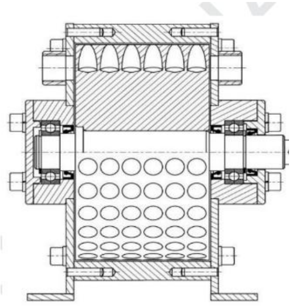	Marsalek et al. [40]	Rotor dia. = 160 mm, No. of CGUs = 162. CGU dia. = 12 mm, CGU depth = 20 mm.	Cloud cavitation and vortex cavitation in CGUs and gap between rotor and stator.	Cyanobacteria	V = 20-250 L, P = 105-265 kPa, 4000-5000 rpm	99% of cyanobacteria colonies were removed from wastewater with a single cycle lasting 6 s.
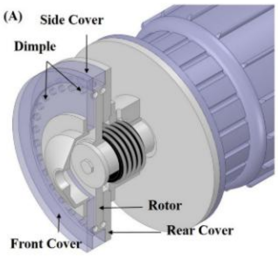	Kim et al. [41]	Rotor and stator consisting of 32 CGUs.	Vortex, sheet, and shear cavitation took place at CGU, perimeter of CGU, and gap between rotor and stator.	Waste activated sludge	Flow rate = 6.3 L/min, P = 15 kW.	CODs increased by 500%, 77.3% of contaminant particles were removed.

1.2.2 Unconventional Wastewater Treatment Cavitation Methods

While there are many variations in the utilization of hydrodynamic cavitation in treatment, recent research trends have been emerging on the development of reactors that utilize both acoustic and hydrodynamic cavitation. This coupling was essentially seen to tackle prominent controllability issues that rose in hydrodynamic cavitation. Additionally, a rather favorable byproduct of the said cavitation coupling was substantially enhancing the overall treatment performance of the reactor, otherwise known as process intensification. Currently, such coupling is typically implemented on base reactor designs that resemble a typical Venturi tube due to its simplicity and modularity. Meanwhile, the additional component to the Venturi base reactor is an ultrasonic source, that is more commonly an ultrasonic sonotrode. Prime examples of this, for instance, are the reactor models designed by Wu et al. [42] and Johansson et al. [43] that generally consist of a converging-diverging tube configuration, aimed to induce hydrodynamic cavitation, and an ultrasonic transducer along the sides of the tube to facilitate the production of acoustic cavitation within the same region. The two reactor designs are summarized in Figure 1.3 below.

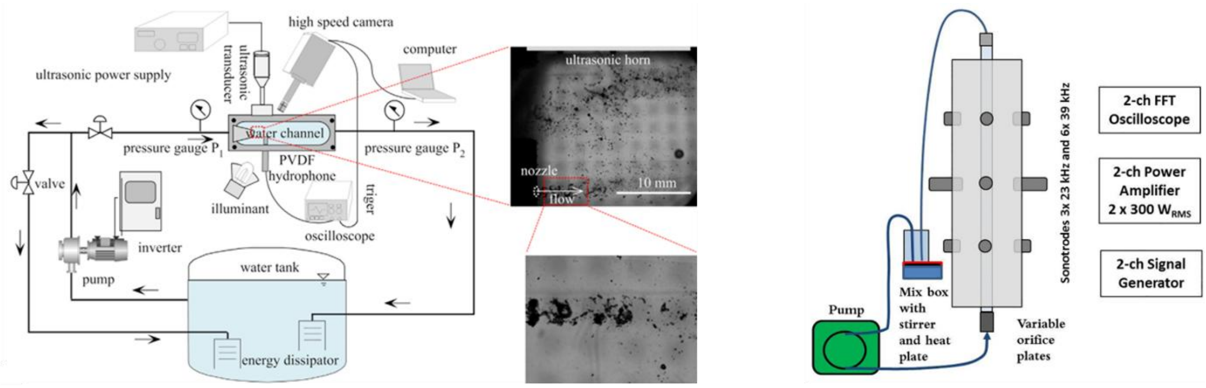

(a) *(b)*

Figure 1.3: Experimental setups of HAC reactors designed by (a) Wu et al. [42] and (b) Johansson et al. [43]

1.3 Problem Statement

Aeration is generally defined as a major segment of the secondary treatment process responsible for circulating air through the activated sludge to encourage microbial growth and degradation of organic matter. With conventional wastewater treatment plants consuming around 1% of the national electricity produced in European countries [44], in which Aeration is responsible for an approximate of 50-90% of the plant's total energy consumption [45] as illustrated in Figure 1.4, implementation of hydrodynamic cavitation techniques in prototypes of wastewater treatment alternatives gained notable momentum in recent works of literature. However, as such techniques introduce more mechanical parts, it can be confidently speculated that the usage of such technology may increase maintenance costs deeming it an inefficient solution. Moreover, hydrodynamic cavitation, by nature, is typically governed by the reactor geometry that influences the pressure distribution along the water flow trajectory. As a result, this adds another barrier to performance optimization and tuning of such reactors. However, with further investigations seeking development of novel HAC reactors, this issue can be mitigated, as the usage of static geometries and, in turn, a more passive generation of cavitation, acoustic cavitation can be introduced to potentially intensify this process while sustaining a reduced operational and maintenance costs.

The implementation of ultrasound has become rather common in the past several decades in cases of hydrometallurgy leaching and fibre refining, however, challenges arise in upscaling, robustness, and energy efficiency of ultrasonic reactors [43]. As such, there seems to be a noticeable gap in the theoretical understanding in implementing acoustic cavitation as a form of wastewater treatment. Thus, further investigation is required to explore its potential as a catalyst of hydrodynamic cavitation in hydrodynamic-acoustic hybrid cavitation (HAC) generation techniques. Ultimately, the lack of knowledge on the nonlinear bubble dynamics of acoustically nucleated cavitation bubbles, such as their structural formations, their dissipation, and their region of influence, act as barriers to the optimization of the acoustic part of HAC.

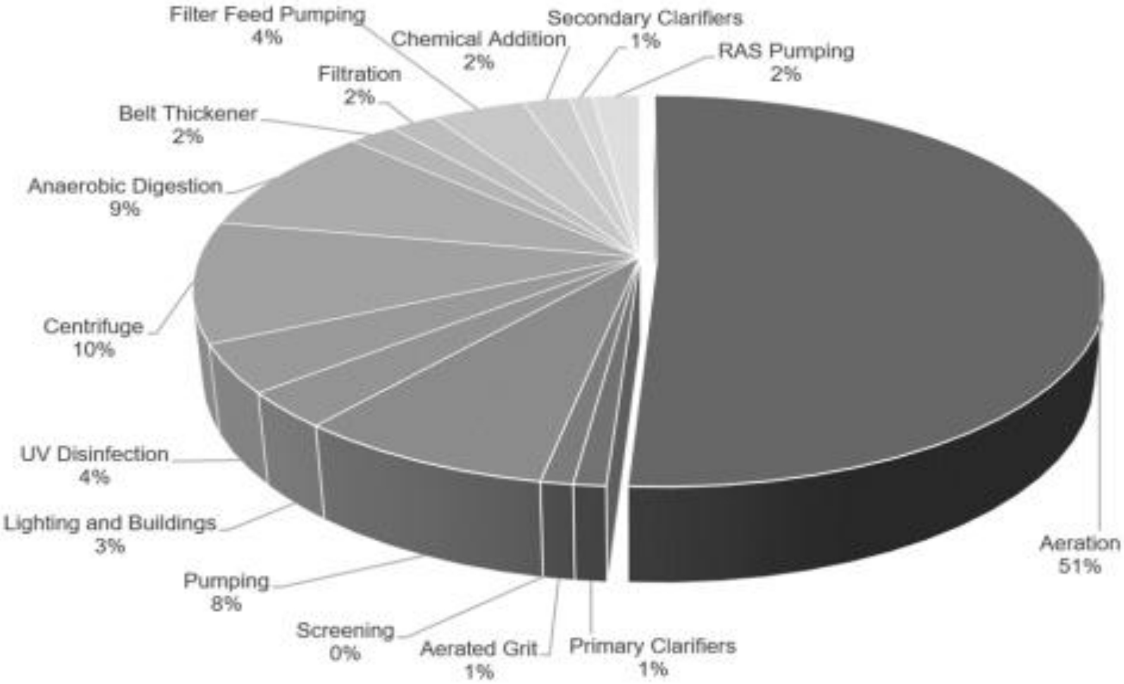

Figure 1.4: Power usage approximations for Polish wastewater treatment plants, 20-mgd nitrifying activated sludge [45].

1.4 Research Aims and Objectives

The main aim of this thesis is to numerically explore the different cavitation flows and structures produced under an ultrasonic transducer, or horn, submerged in an aqueous solution. It aims to initially, and more essentially, demonstrate a series of prerequisite numerical modelling of such horn-type reactors in order to ensure the accurate capturing of the phenomenon. Afterwards, the presented thesis would then scrutinize the underexplored flow-structure interactions between the bubbly structures and different acoustically streamed flow regimes formed under differently sized horn tip diameters. The presented thesis seeks to extrapolate and employ these observations in aims to justify aforementioned process intensifications and performance enhancers in HAC wastewater treatment methodologies. In that way, a well-rounded study that facilitates a strong platform for further development and optimization of HAC is presented.

As for the key objectives the thesis aims to address are as follows:

- Construct and statistically optimize a Rayleigh-Plesset-based multiphase model that accurately predicts macroscale acoustic cavitation nucleation and behavioral dynamics in ultrasonic reactors operating within 20 – 40 kHz operational frequency range.
- Explore the produced bubbly macrostructures under different ultrasonic horn tip sizes and evaluate any underlying bubble-flow interactions and couplings between the different cavitation macrostructure shapes and the accompanied proximal flow regimes.
- Derive a generalized mathematical model that describes the proximal cavitating flow behavior to facilitate horn-type reactor optimization.
- Correlate the shape and dynamic behavior of the bubbly macrostructures with the treatment performance in an aqueous solution.

1.5 Thesis Overview

The thesis comprises 9 chapters with the current chapter summarizing the motivation of the study, providing a general overview of conventional and unconventional wastewater treatment methods that implement cavitation as their primary mechanism, and stating the project's aims, objectives, and novelty.

Chapter 2 then follows with an elaborate discussion of the previous literature on the nucleation mechanism of cavitation-type bubbles, especially focusing on acoustically induced nucleation. Moreover, the chapter discusses previously implemented ultrasonic horn geometries, commonly explored operating conditions, and their impacts on resulting flow regimes and cavitation structures. Lastly, a detailed review of commonly practiced acoustic cavitation numerical modelling techniques is presented with a strong focus on defining key strengths and weaknesses found in such modelling habits.

Chapter 3 then carries on with a detailed explanation of the numerical governance of the chosen mathematical models and an elaborate justification of the choice of models used to model and predict the cavitating flow produced within the considered horn-type reactor.

Furthermore, Chapter 4 describes the mathematical derivation and statistical optimization of an additional model, based on the generalized Rayleigh-Plesset equation [46], that governs the multiphase flow by specifically predicting the lifecycle of each cavitation instance in ultrasonic reactors that operate within 20 – 24 kHz operational frequency range. The coupling of this model with other governing models, such as the turbulence and compressibility models, is demonstrated in this chapter as well to ultimately define and validate the multiphysics configuration for implementation in the explorations that follow afterwards.

Moreover, Chapter 5 presents a comparative study that assesses the different flow fields generated with different dynamic motion modelling of the ultrasonic horn tip. This chapter highlights the underlying role of the horn's periodic motion on the proximal flow behavior.

Chapter 6 then follows to discuss the two-way coupling between the vortical flows generated and the attached acoustic cavitation about different sized horn tips in aims to reveal the underlying nonlinearity induced by the horn tip geometry, specifically its diameter, on the flow and cavitation development.

Afterwards, Chapter 7 demonstrates the derivation of a one-dimensional mathematical formulation that generalizes the proximal vortical flow typically observed under the horn tip. Ultimately, Chapter 8 ventures towards a more practical study that explores the influence of the dynamic behavior of the attached cavitation structure on the performance of wastewater treatment. As such, Chapter 9 summarizes the key findings of the works and suggests potential future work.

2 Literature Review

2.1 Fundamentals of Cavitation

Cavitation is nothing more than an occurrence of a phase change where a simple kinetic theory [30] understanding of the gaseous state is a sufficient head start to delve into a discussion on cavitation nucleation. However, such discussions must be preceded with an elaborate explanation of the behaviour of the liquid state. The pure liquid enters a metastable state when the local pressure decreases past the saturation pressure threshold. Within this regime, the liquid can continue in a 'stretched state' without vaporizing, however, the metastable state ultimately becomes thermodynamically unstable upon a further pressure drop. This results in the spontaneous vapor bubble nucleation in the bulk liquid. This transition is characterized by the following criterion:

$$\left(\frac{\partial p}{\partial V}\right)_T = 0 \tag{2.1}$$

which defines the spinodal limit where isothermal compressibility diverges. This provides valuable information on fluid metastability, especially for Equation of State (EoS) developments [47]. Specifically, this substantially defines different paths of nucleation a fluid can take. Moreover, in more practical flows, this pressure drop is often captured by the cavitation number:

$$\sigma_c = \frac{p_\infty - p_v}{\frac{1}{2}\rho_l U^2} \tag{2.2}$$

where p_∞ is the reference pressure, p_v is the vapor pressure, ρ_l is the liquid density, and U is the flow velocity. Typically, as σ_c goes to zero, the flow approaches the cavitation threshold. Once nucleation taken place, the subsequent bubble development dynamics is described by the Rayleigh-Plesset equation:

$$R\frac{d^2R}{dt^2} + \frac{3}{2}\left(\frac{dR}{dt}\right)^2 = \frac{p_v - p_\infty}{\rho_l} - \frac{2\sigma_0}{\rho_l R} - 4\frac{\mu_l}{\rho_l R}\frac{dR}{dt} \tag{2.3}$$

where R is the instantaneous bubble radius, σ_0 is the surface tension, μ_l is the liquid's dynamic viscosity, and t is time. This equation expresses the balance between the inertial, pressure, viscous, and surface tension forces acting on the bubble's interface. However, the governance of bubble growth and collapse dynamics is further discussed in Section 2.3.

2.1.1 Cavitation Inception and Nucleation

Generally, nucleation occurrences in a fluid are catalysed by many external parameters (discussed further in later sections) involving the liquid medium's properties, such as its purity, dissolved gases, temperature, viscosity, and most importantly, the presence of nucleation sites. In such cases, any liquid imperfections can cause spontaneous nucleation and instability. Therefore, the liquid at such point is typically said to be in tension and the magnitude of said tension is the pressure gradient.

This analogy of tensile strength representing a liquid's molecular forces has been first made by Harvey et al. [48], as the investigation uncovered the effect of pre-existing nano-sized gaseous nuclei on the development of cavitation. Moreover, Frenkel et al. [49] elaborates on this attribution and illustrates tensile strength of a pure liquid through a series of simple, yet informative calculations. The calculations consider two molecules at some distance r from each other. The intermolecular forces that exist between the two molecules are represented in Figure 2.1 in terms of intermolecular potential energy plotted against their separation distance. The equilibrium state of the molecules at which it is still able to sustain some attractive force is at the energy minimum at r ≈ 2.64 Å; meanwhile, the water surface tension ruptures past that point as the liquid is no longer able to counteract the translational tensile force. Frenkel et al. [49] goes about quantifying the tensile strength through considerations of the liquid's compressibility moduli, κ, and a pressure p expressed as follows:

$$p = -\kappa \left({}^{\Delta V}/_{V_0} \right) \tag{2.4}$$

where $\frac{\Delta V}{V_0}$ is the fractional volumetric expansion. In return, Frenkel et al. estimates pure water's tensile strength ranges from -3×10^9 to -3×10^{10} kg/m s^2. Experimentally, these numbers defy all practical measurements and thus deemed inaccurate. Although the simplistic model highlights its failure in predicting the tensile strength, many researchers have adopted the attribution and addressed the dilemma to describe the process of liquid rupture from a decrease in pressure below the vaporization pressure at constant liquid temperature [50, 51]. The process of liquid rupture is referred to as cavitation and is governed by the difference in pressure.

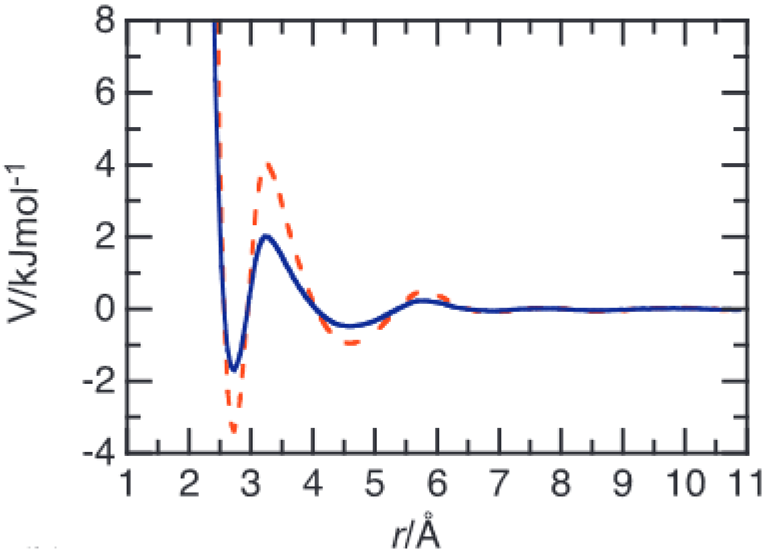

Figure 2.1: A typical intermolecular potential graph of water dimer molecules where potential energy (kJ/mol) is plotted against the separation distance r (Å) [49].

The tensile strength of the liquid refers to its ability to resist formations of discontinuities, or nucleation, within its medium. 'Weaknesses' in the liquid medium typically refers to the presence of impurities. Therefore, these weaknesses are what describe nucleation sites, since they could be any of which: suspended rough particulates, contaminant gases, or crevices in the fluid container and act as initiation points [52]. However, depending on the form of weakness cavitation nucleation occurs at, nucleation is classified into two types: homogeneous nucleation and heterogeneous nucleation. Their differences can be summarized as visualized in Figure 2.2. In essence, the key differences the figure highlights are the mode of nucleation and its progression. Homogeneous nucleation occurs in a pure liquid body under nucleation-encouraging conditions, where both pressure and liquid density sharply fall. In that sense, new bubbles may appear. On the contrary, heterogenous nucleation occurs within a liquid body containing impurities, such as dissolved gases, that act as seeds for nucleation. Under such conditions, existing microbubbles grow out of these pockets and become larger with time.

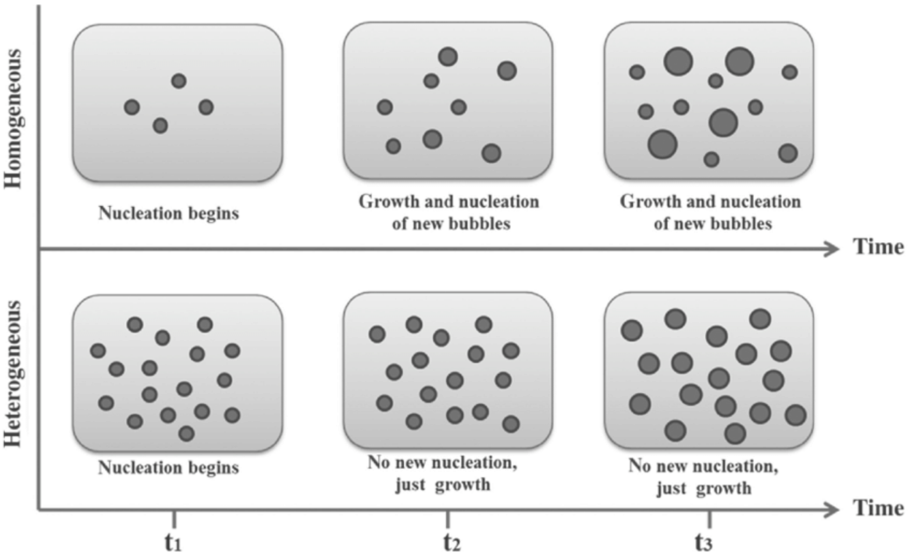

Figure 2.2: A visualization of the nature of development of homogeneous and heterogeneous nucleation in a body of pure liquid [50].

2.1.2 Homogeneous Nucleation

Homogeneous nucleation is induced by the pre-existing impurities in the liquid body, possibly due to thermal motions within the medium, that are sufficient in size and considerably metastable to rupture and develop into macroscopic cavities [53]. According to many researchers [54, 55], most of the current developments in the homogeneous nucleation theory are based on Gibbs' pioneering work in the field [56]. Gibbs' work was aimed to lay the foundation of homogeneous nucleation by deriving an expression for the net energy required to form a bubble from pre-existing cavities W_{CR}. This was done by assuming a pure liquid where the surface tension of the presumed bubble, otherwise termed as surface energy, is used to approximate the tensile strength of the liquid. Therefore, given that the bubble only contains vapor, the interior bubble pressure P_B is safely assumed to be equivalent to the saturated vapor pressure P_V. This is expressed by Eq. 2.5.

$$P_B - P = P_V - P = \Delta P_C = \frac{2\sigma_0}{R_C} \tag{2.5}$$

Where P is the local ambient pressure, $\sigma_0(x)$ is the planar surface tension of the bubble wall, and R_C is the bubble radius. ΔP_C is termed the tensile strength required to rupture the liquid and create a cavity. Accordingly, W_{CR} was then formulated by taking into account the energy stored in the surface of the bubble and the energy applied to displace the liquid outward from the cavity. Thus, the net energy is equated as follows in Eq. 2.6.

$$W_{CR} = 4\pi R_C^2 \sigma_0 - \frac{4}{3}\pi R_C^3 \Delta P_C = \frac{4}{3}\pi R_C^2 \sigma_0 \tag{2.6}$$

Since R_C is practically difficult to approximate, Eq. 2.6 can then be re-written as follows:

$$W_{CR} = \frac{16\pi {\sigma_0}^3}{3\Delta {P_C}^2} \tag{2.7}$$

Following this, Gibbs then adopts a correlation between a given Gibbs number to W_{CR} and the molecules' kinetic energy kT_C, where k is the Boltzmann's constant and T_C is the critical temperature at which nucleation occurs, to express the probability of nucleation occurrence given a specific volume and time.

$$Gb = \frac{W_{CR}}{kT_C} \tag{2.8}$$

2.1.3 Heterogeneous Nucleation

This type of nucleation typically refers to nucleation emerging from surfaces in contact with the liquid medium. More specifically, it is when weaknesses in the bulk liquid occur at the boundary between the liquid and a solid surface in which a rupture in the liquid occurs. Such surfaces are not limited to container walls but also include rough contaminant particles. By definition, this type of nucleation is much more commonly present in practice compared to homogeneous nucleation. Examples of different modes of heterogeneous nucleation, based on the contact angle θ at the liquid/vapor/solid intersection, can exist in practice as shown in Fig. 2.3.

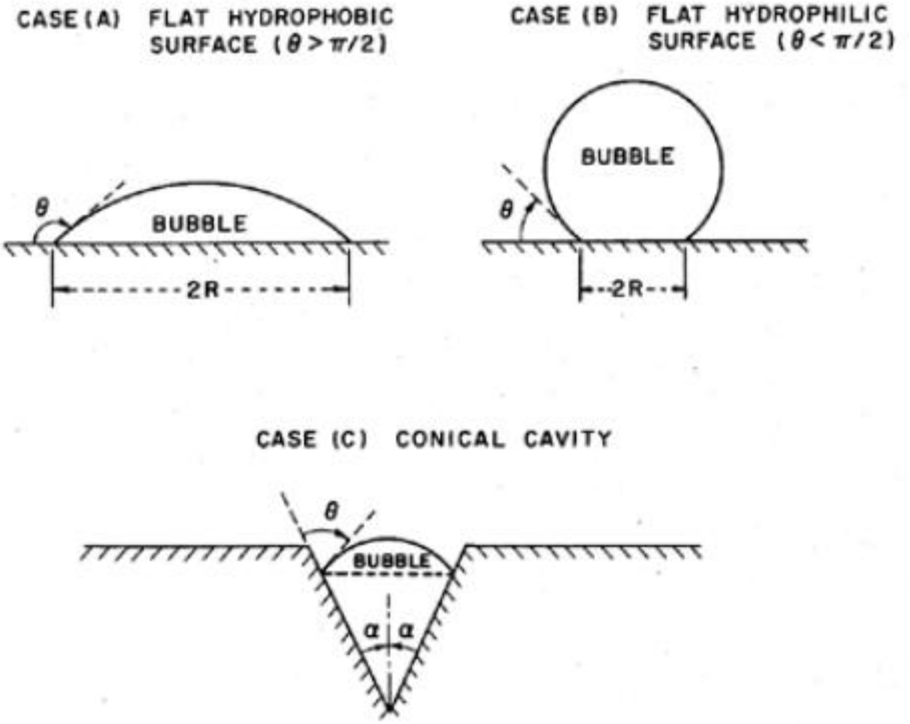

Figure 2.3: Cases of heterogeneous nucleation (A) nucleation at a plane hydrophobic surface (B) nucleation at a plane hydrophilic surface (C) nucleation at a conical cavity [30].

By recalling the expression of tensile strength, stated in Eq. 2.6, heterogeneous nucleation is generally defined with some minute variations. Considering Case A in Figure 2.3, the tensile strength is given as such:

$$\Delta P_C = \frac{2\sigma_0 \sin\theta}{R_C} \tag{2.9}$$

Ideally, a tensile strength of zero could be achieved when applying the limit as $\theta \to \pi$. Practically, this scenario is deemed impossible, however, many recent studies have shown that hydrophobic surfaces do in fact encourage heterogeneous nucleation due to the hefty reduction in tensile strength. For instance, Zhou et al. [57] investigated the heterogeneous development of nanobubbles on the surface of colloidal mineral particles. These mineral particles assume hydrophobic surfaces, and thus, nanobubbles are able to actively form and enhance general floatation performance of the particles, such as the attraction between the particles and increased particle aggregation. Similarly, Huang et al. [58] observed changes in the behaviour of heterogeneous nucleation as the surface hydrophobicity of gypsum was varied. The study concluded that higher surface hydrophobicity was a direct influence on enhanced surface-induced nucleation where this phenomenon was attributed to low tensile strength and energy barrier. This conclusion has been supported by Lu et al. [59] by which the investigation revolved around visualizing this phenomenon. On the other hand, hydrophilic surfaces tend to do the exact opposite. Such surfaces induce an increased tensile strength and thus a larger energy barrier for heterogeneous nucleation to occur. As a matter of fact, the tensile strengths of such cases are comparable to that of homogeneous nucleation, since they share the same bubble maximum dimensions. However, this property has been studied and utilized in many investigations that attempt to explore nucleation inhibiting techniques. Guo et al. [60] witnesses the great extent of using a hydrophilic substance, known as PVA, as an anti-icing coating due to its nucleation inhibiting properties.

All studies discussed, regardless of whether it was on hydrophobic or hydrophilic surfaces, infer that such nucleation scenarios occur on suspended particles. Thus, for heterogeneous nucleation occurring at a container wall, for example, it is typically initiated from an exemplified conical cavity found in said wall due to its irregular, rough nature. Figure 2.4 visualizes the bubble development in the conical cavity. The bubble growth begins at the cavity vertex O and develops upwards. As the void proceeds to grow, θ is actively compared with the conical angle α as an indicator for the bubble's new geometrical configurations [59,60].

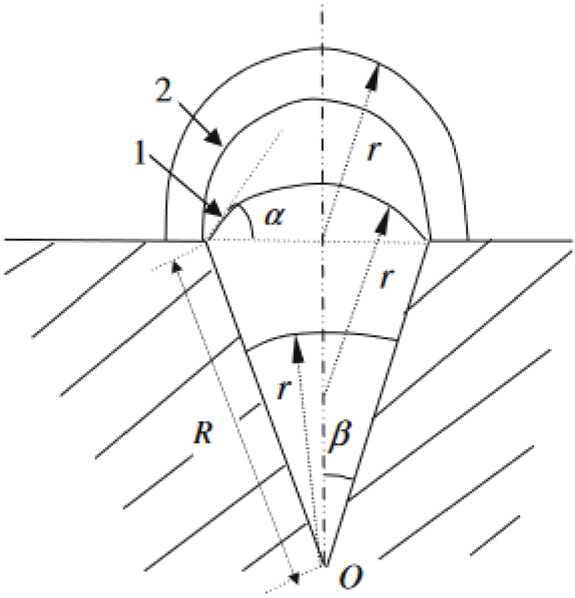

Figure 2.4: Evolution of a bubble in a conical cavity [59].

2.2 Cavitation Bubble Dynamics

Most investigative works on cavitation carry a recurring theme that typically infers the negative impacts of cavitation in a variety of hydraulic machinery, such as pumps and turbines [62]. In that sense, with the understanding of early bubble nucleation, it is crucial to further scrutinize the bubble's development in the downstream medium to broaden the understanding of cavitation's fluid dynamic behaviour in critical hydraulic systems. Moreover, similarly to the studies on nucleation, previous studies on bubble dynamics, and generally cavitation, classify vaporous cavitation on the basis of the mode of inducing a pressure change. These classifications are namely hydrodynamic cavitation and acoustic cavitation.

2.2.1 Acoustic Cavitation

However, despite all advancements in hydrodynamic cavitation passive control systems, a different mode of cavitation generation stands out owing to its active controllability. This type of cavitation is commonly known in literature as acoustic cavitation. Acoustic cavitation is a reproducible, complex phenomenon generated where the liquid's surface tension is broken apart due to exposure to an ultrasonic field oscillating at a frequency that typically falls within the range of 20 kHz and above [30]. Under such circumstance, the cavitation bubbles generated oscillate within a series of cyclic expansions and compressions in which the bubbles grow and collapse based on the rate and direction of dissolved gas, or vapor, mass transfer occurring at the bubble interface with the liquid medium [63].

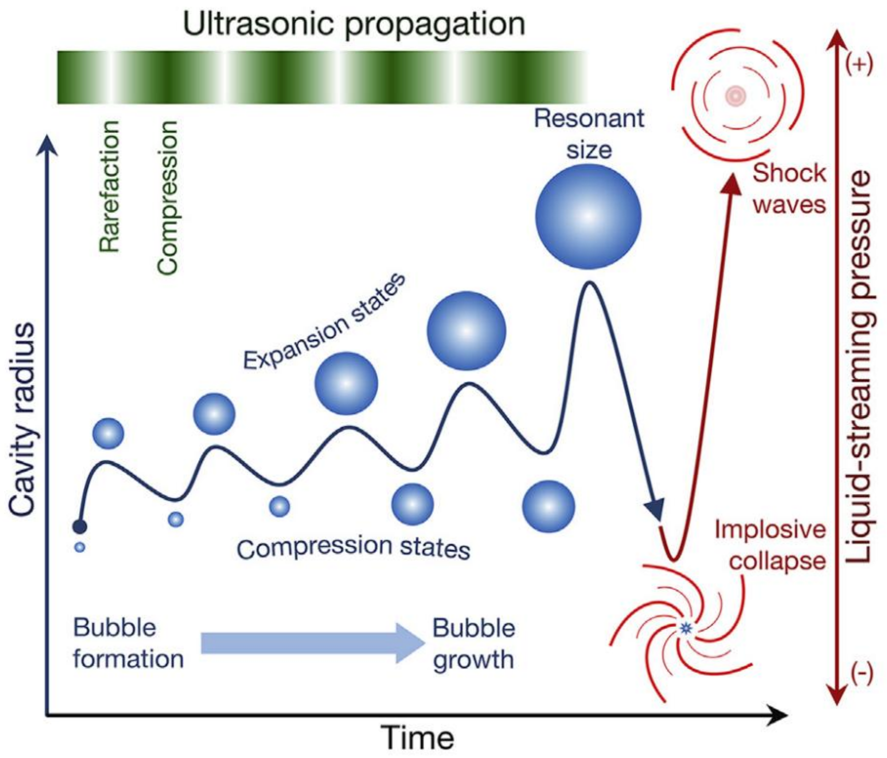

Figure 2.5: Acoustically generated bubble evolution at rarefaction and compression pressure wave phases [61].

This is illustrated in Figure 2.5 where a bubble embryo begins to oscillate and expand with each rarefaction peak until it reaches a critical resonant size. At this size, the bubble energy absorption is synchronized with the ultrasonic waves leading to its rapid growth. However, this fast growth rate induces major instabilities within the bubble leaving it unable to support itself. As a result, the bubble implodes during a compression trough followed by a series of shockwaves and hotspots capable of generating, local temperatures that reach 6000 K and localized pressures and velocities that reach 5500 bar and 2000 m/s, respectively [64]. Therefore, unlike the practical occurrences of hydrodynamic cavitation, where it is considered an unfavourable phenomenon due to the mechanical complications that follows it, acoustic cavitation is in fact employed as a controllable phenomenon that catalyses a variety of processes in a multitude of industries. Examples of such processes are viscosity reduction of crude oil [65], hydrogen production [66], tungsten extraction [43], and synthesis of polyethylene glycol (PEG) [67]. Hence, this creates a solid platform for many novel process intensification methodologies. However, the main obstacle faced is the parametric dependency of acoustic cavitation; and thus, developing a strong understanding of their sonochemical and physical activities would allow better control over the phenomenon.

2.2.1.1 Acoustic Cavitation Structures

In that regard, many studies have been conducted experimentally and numerically in an attempt to scrutinize the bubble dynamics witnessed during cavitation development. For instance, Tzanakis et al. [68] has investigated acoustic cavitation behaviour by varying multiple parameters: medium viscosity by changing the liquid medium and the oscillation amplitude by alternating the transducer power. Ultimately, the study's key findings were on a macroscopic level in which the morphing of cavitation zone structures from one medium to another was examined; a conical cavitation zone occurs in water, a thick round layer occurs in glycerine, while ethanol observes ultrasonic degassing where bubbles are dispersed and actively oscillate towards the free surface of the cuvette. These observations are universal as multiple studies have reported the same macrostructures.

Similarly, studies have taken a deeper look into the liquid medium properties and its influence on the acoustic cavitation evolution. In a study conducted by Žnidarčič et al. [69], an experimental investigation takes place on the potential transfigurations of acoustic cavitation regions due to changes in the ultrasonic horn diameter and variations in liquid properties to analyse their degree of influence.

The experimental setup used consisted of an ultrasonic horn emitter, with a small diameter of 3 mm, submerged in a 50x50x50 mm cuvette filled with water with varying properties. Meanwhile, the emitter's operating frequency is kept at 20 kHz. The control case consisted of a water medium with a temperature at $23°C$, dynamic viscosity of $0.000932\ Pa\ s$, a liquid density of $998\ kg/m^3$, and a vaporization pressure of $2808\ Pa$. The qualitative, and quantitative, results of the investigation first deduced that changes in liquid properties seem to have no significant effect on the cavitation life cycle corresponding to 1/4th of the horn driving frequency (5 kHz subharmonic frequency from the 20 kHz driving frequency). On another note, it was concluded that the instant in which attached cavities partly cover the full horn tip is comparable to the hydrodynamic 'super-cavitation'. This hints at a possible shift in understanding of acoustic cavitation nucleation away from considering negative acoustic pressure fields being the direct cause of nucleation and towards accounting for the direct influence of the fast-moving horn surface on nucleation.

On the other hand, studies, such as Altay et al. [70], investigate the influence of geometrical setups. More specifically, the study scrutinizes the effect of ultrasonic horn roughness on the acoustic cavitation bubble behaviour by varying the roughness between 100 nm to 1 μm. The investigation concluded that the overall bubble radius of the cavitation stream shrunk in size, as the roughness increased. Those bubbles with a diameter of 50 μm were targeted while those sized 10 μm showed no change. In turn, recorded temperatures dropped by 10 K with the increase in roughness, and this was attributed to the lower intensity generated by smaller bubbles.

However, a parameter that has been recently considered for further studies is the dual/multi-frequency ultrasound and its effect on ultrasonic cavitation. Multi-frequency ultrasound, referred to as high intensity focused ultrasound (HIFU), is generally known in the biomedical field for its employment potential as a non-invasive surgery modality. This can be attributed to the key observation witnessed by many biomedical explorations and that is its ability to exaggerate cavitation intensity. A study conducted by Suo et al. [71] have explored this phenomenon by observing the change in the inertial cavitation threshold due to the exposure to multi-frequency ultrasound. It has been concluded that multi-frequency ultrasound reduces this threshold and reduces the required power for cavitation production. This observation was mirrored by the changes in pressure and bubble radius induced when comparing single band of 500 kHz and multi-band of 500 kHz + 1.5 MHz.

Therefore, the increased cavitation intensity is due to the increase in bubble radius that is not facilitated in single-frequency ultrasound. In addition, the pressure fluctuation shows that bubble collapse occurs much more frequently, further supporting the intensity claim. Another study by Ye et al. [72] delves deeper into optimizing the frequency ratio and the phase difference of dual-frequency ultrasound. It has been found that with the increase of the frequency ratio, the maximum bubble radius, pressure, and bubble gas content decreases, and thus the intensity decreases, due to an increase in the frequency ratio. Meanwhile, these cavitation parameters show no change towards a change in the phase difference.

2.2.1.2 Single-Bubble Dynamics

While studies performed on macroscale ultrasonic cavitation structures provide practical insight on acoustic cavitation performance under varying conditions, however, a noticeable gap in understanding the behaviour of acoustic bubbles at a microscale level remains. Thus, many studies attempt filling this knowledge gap by investigating single bubble and bubble-bubble dynamic behaviour at different positions and conditions.

For instance, Liang et al. [73] investigated the influence of the ultrasonic horn's distance from the bottom of the cuvette on the bubble-bubble interaction in the cavitation region under the ultrasonic horn. It has been observed that a nonlinear effect on bubble oscillation is caused by increased bubble density, and bubble radii induced by the decreasing distance. Generally, the increase in bubble radii is owned to the decrease in distance between smaller bubbles, thus, forcing them to merge. Moreover, Wu et al. [74] has decided to isolate the effect of near-wall positioning on a single bubble as shown in Figure 2.6 below.

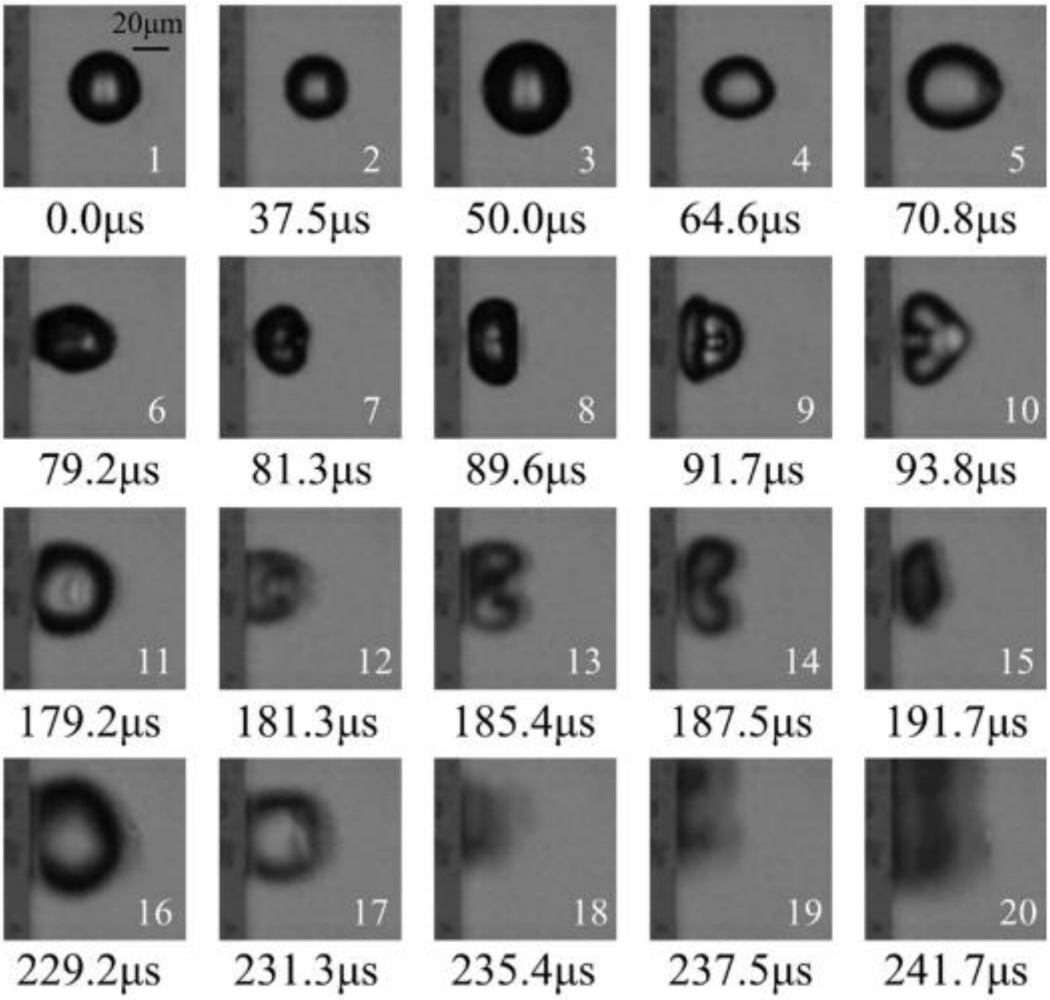

Figure 2.6: Microbubble evolution near a rigid wall in a medium of deionized water (initial radius = 20 μm, surface tension = 72.59 mM/m) [72].

Fig. 2.6 shows a bubble of radius R = 20 μm near a rigid wall in a deionized water. It has been said that the bubble experiences two kinds of movements: (i) oscillation in place and that is due to the sound field's primary Bjerknes force and (ii) small transverse movements towards the rigid wall due to the secondary Bjerknes force induced by the rigid wall. As the bubble inches towards the wall, its firstly assumed spherical shape turns elliptical. However, as the bubble achieves direct contact with the wall, the far bubble side away from the wall transforms into a high jet that strikes the rigid wall by penetrating the bubble. Afterwards, a rebound formation of the bubble can be seen marking the end of a single collapse cycle. Wu et al. [74] further investigates the influence of a decreased liquid surface tension on this bubble-wall dynamic. It has been found that with the decrease of surface tension, the bubble generally follows the same initial collapse cycle; however, it has been shown that the bubble experiences exaggerated surface depression and noticeable asymmetries, as it moves towards the wall. Moreover, the bubble bursts into smaller bubbles and later merge together instead during the second collapse cycle. This trend is clearly illustrated in Figure 2.7.

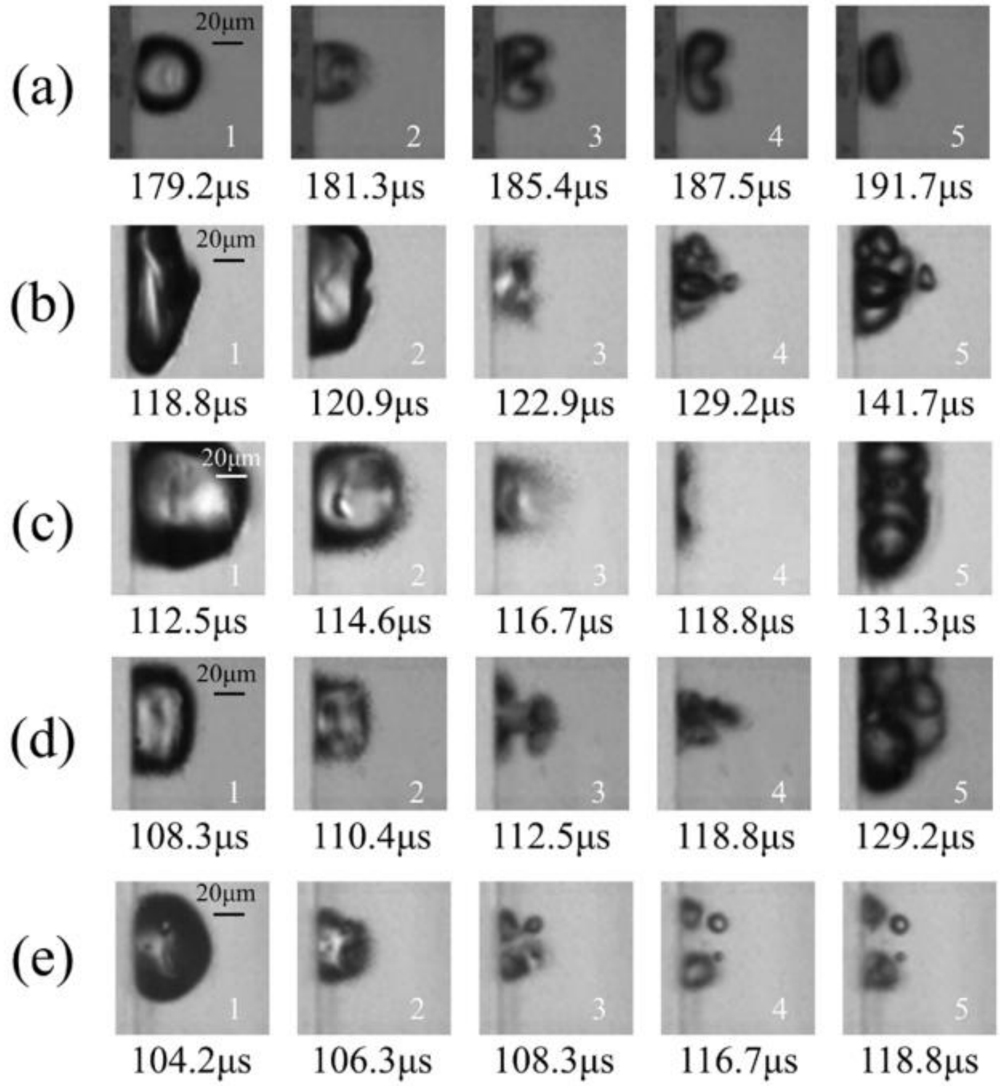

Figure 2.7: Comparison of microbubble evolution in mediums of different surface tensions (a) 72.59 mN/m (b) 58.75 mN/m (c) 49.34 mN/m (d) 38.47 mN/m (e) 27.13 mN/m [72].

Furthermore, attempted justification of the small bubble cluster has been shown in the works of Crum [75] in which it has been revealed that the splitting of small bubbles from the main cavity growth is due to the inertia induced by the rapid radial motion of the bubble that generates an air jet. Inertia and its major role in bubble evolution is further pronounced in Suslick et al.'s investigation [76] at which bubble radial oscillation becomes highly nonlinear. Essentially, the bubble experiences rapid cyclical growths and collapses with compression and rarefaction stages respectively. Particularly, this occurs due to strong compressions of gas and vapor present in the bubble that allows the bubble to rebound nonlinearly during rarefaction, which eventually leads to its runaway collapse.

Generally, a reduced surface tension reduces the bubble's ability to maintain its typical spherical shape. Another observation made in the study reiterates the direct relationship surface tension shares with the nucleation pressure threshold; therefore, the time interval between the first collapse cycle and the second collapse cycle of the bubble is shortened compared to the bubble collapse cycle in deionized water.

As acoustic bubble near-wall dynamics show intriguing collapsing cycle behaviours, Yamamoto et al.'s numerical investigation [77] emphasizes the role walls have on acoustic bubbles' growth behaviour as well. Specifically, the study simulates bubble growth dynamical changes due to a variation in the crevice geometry. The exploration suggests the bubble oscillation amplitude increases with the increase in the crevice depth. This, in turn, results in a new non-linear oscillation and a vigorous bubble growth. A similar effect is observed at larger contact angles, or larger crevice diameters. Typically, such phenomenon is seen as potential improvement in the sonochemical reaction induced by the ultrasonic field.

Moving away from the wall, free surface acoustic bubble dynamics is yet another important field of exploration. An exclusive dynamic behaviour found in ultrasonically induced acoustic bubbles is a phenomenon known as the shielding effect. This was scrutinized by Ezzatneshan et al. [78] in which he introduces a computational methodology that employs the Lattice Bolztmann Method (LBM) coupled with the Multiple Relaxation Time (MRT) to visualize acoustic bubble cluster dynamics. A crucial observation made was one the collapse behaviour of the bubble cluster shown in Figure 2.8, where the collapse sequence of the cluster due to the ultrasonic horn's pressure pulse begins at the top bubble.

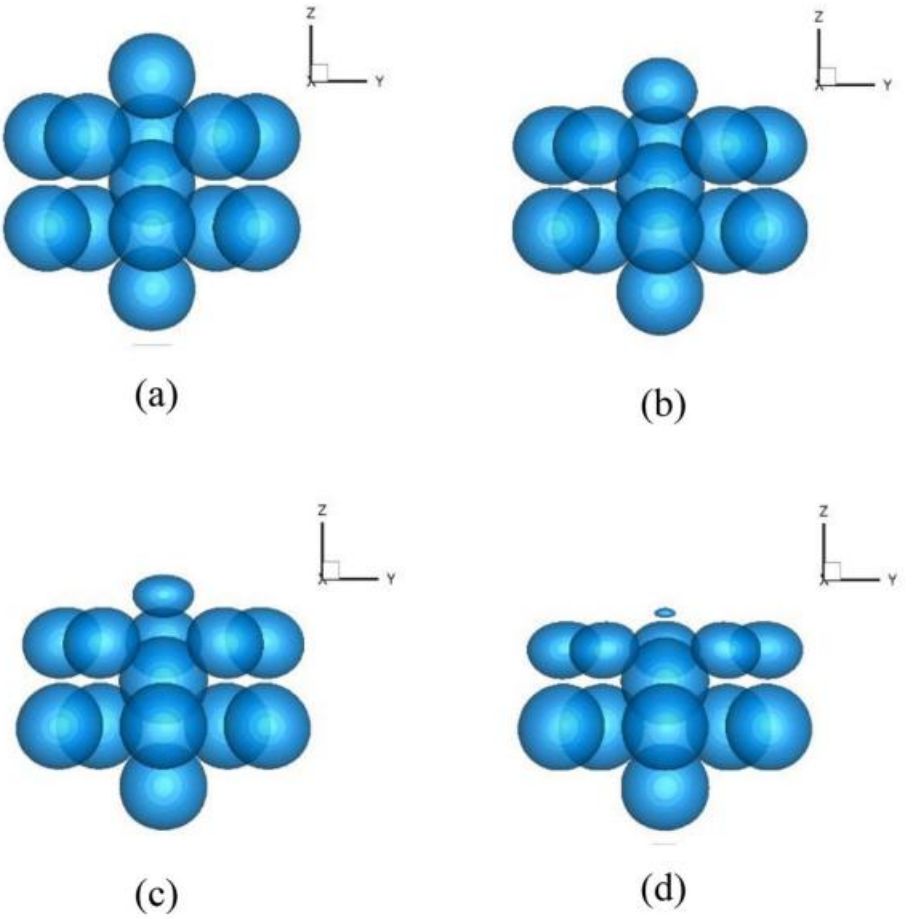

(a) (b) (c) (d)

Figure 2.8: Acoustically drive bubble cluster collapse at timesteps (a) ts = 10 (b) ts = 70 (c) ts = 110 (d) ts = 120 [76].

Interestingly, parallels can be drawn from both the top bubble's symmetrical changes and a typical bubble's near-wall collapse. The bubble's imbalance in energy induces an initiation of collapse near the bubble cluster at the bottom layer of the top bubble. The kinetic energy is concentrated at the collapsing bubble top side which, in turn, flattens the top surface. This is known to result in a liquid jet that penetrates the bubble from the top and into the bubble core. This occurrence was justified by concluding that the lower bubble behaves as a wall and prevents the top bubble's symmetrical collapse. It seems that the acoustically induced energy imbalances predominantly effect the top layer of bubbles compared to the lower bubbles in the cluster. This is explained by suggesting a "shielding effect" induced by the top bubble layer collapse that prevents the pressure impulse from travelling to the lower bubble layers.

Bubble-bubble interactions like are known to occur in deionized, clear water. This suggests the question on whether such interactions hold the same behaviour when the liquid medium is changed. This question is explored by Qin et al. [79] by investigating the effect of lipid deposits on the bubble surface on the commonly observed bubble-bubble interactions. It has been confirmed that the encapsulating shell applies restraining effects of radial bubble oscillations. This coating forces the bubbles into two modes of dynamic behaviour, namely compression and expansion dominated oscillations. It has been observed that changes in bubble radius during the compression cycle is larger than the compression phase of uncoated bubbles. This could be due to the rupture of the lipid shell that induces a radius-dependent shell elasticity. However, during the expansion phase, the shell elasticity and viscosity play a major role in controlling the bubble oscillation and bubble expansion ratios. For instance, a negative relationship between the increase of the two properties and the oscillation is concluded; as the elasticity and viscosity increases, the bubble oscillation and expansion ratio decrease drastically. This phenomenon could be used as an active controller for acoustic bubble dynamics, in turn, making it useful for therapeutic and pharmaceutical applications.

Cavitation and its hydrodynamic behaviours make it an intriguing phenomenon to investigate and to implement in many industrial processes. As its violent expansion and collapse dynamics are shown to be flexible and controllable throughout the previous sections, multiple studies took the initiative to find novel ways of utilizing cavitation as a catalyst for many processes.

2.3 Numerical Cavitation Models

Cavitation models have become a primary integration of many commercial CFD programs. It is for their ease of implementation and their ability to facilitate cavitation flow predictions. Typically, cavitation models are classified as either single-bubble or multi-bubble models. From their names, the categories describe the bubble density extent at which the models are able to simulate.

2.3.1 Single-bubble Models

For single bubble models, they generally follow a direct numerical simulation of bubbles. In other words, they directly solve the changes in the bubble interface in such a way that takes accounts for sources of asymmetry in the interface. Examples of such are high speed jets due to the presence of a gravitational force or a solid wall [80], high bubble viscous stresses during a near-wall collapse [74], and high energy dissipation due to the development of vortex rings [81].

The Front Tracking method [82] is one of the few models that previous works adopted to model the bubble interface. It simply places a set of discrete points at a bubble's surface and updates them according to a kinematic condition expressed as:

$$\frac{dx^I}{dt} = u^I \tag{2.10}$$

where x is the position of the particle, t is the flow time, and u is the velocity vector in x, y, and z direction. The key advantage of this method is its simplicity to implement and solve numerically. On the basis of this method, the Boundary Integral (BI) method and the free surface method merge to numerically model bubble interfaces based on a set of assumptions. The BI method assumes that the liquid flow is potential to directly solve the velocity of a Lagrangian set of points without discretizing the Navier-Stokes equation [83]. This model has been shown to successfully capture the bubble dynamics at near-wall conditions. One work that has considered a particle tracking model to assume spherical particles for cavitation bubbles was Altay et al. [70]. The investigation focused on deriving the effect of both the acoustic generator surface roughness and the acoustic field frequency on bubble cluster behavior, through single bubble numerical observations.

Another method of modelling the bubble surface boundary condition is through a coupling between a modified Bernoulli equation and the wave equation. The wave equation is typically expressed as:

$$c^2\nabla^2\varphi = \varphi_{tt} \tag{2.11}$$

Where c is the speed of sound in the medium, and φ is the velocity of the fluid induced by the cavitation bubble. This way the compressibility of the fluid is modelled, however, with the assumptions that the speed of sound is constant and that the fluid is irrotational and inviscid. The Bernoulli equation is then modified to become inclusive of the pressure induced by bubbles P,the acoustic field pressure P_{st}, and the far-field pressure P_∞. In addition, to include the incompressibility, the equation is then re-written as:

$$P = P_{st} + P_\infty - \rho_\infty \varrho \varphi + \frac{\rho_\infty}{2}|\nabla\varphi|^2 \tag{2.12}$$

Where ρ_∞ is the density of the fluid and ϱ is the material derivative of time t. In a study conducted by Xi et al. [84], this was used to define the bubbles' interface and their motion when examining dynamics of multiple cavitation bubbles near a rigid wall.

Lastly, some studies have been seen implementing a modified Keller-Miksis equation [85] describing the radial dynamics of the cavitation bubble; the bubble's expansion and collapse based on its exposure to specific pressure gradients. The equation was employed in a study conducted by Kerboua et al. [86]. The study reported an energy analysis of an acoustic cavitation bubble as a form of identification of energy gain and loss sources. The literary work used the modified Keller-Miksis equation to express the bubble formation and deformation. It appears that compressive work is a predominant source of energy gain while diffusive heat is the main form of energy loss, with the exception of acoustic oscillation at 35kHz where water condensation is the dominant source of energy loss.

Based on the aforementioned modeling techniques, it can be safely concluded that most of the numerical studies of acoustic cavitation are mainly limited to the single acoustic cavitation bubble model. This tends to be the case due to the complexity of the models used for single bubble modelling that makes it computationally difficult to implement it for a multi-bubble analysis.

2.3.2 Multi-bubble Models

Consequently, in order to investigate multi-bubble parameters, such as bubble density, bubble-bubble interaction, and bubble size distributions, researchers began adopting cavitation models developed on the basis of the Rayleigh-Plesset equation [46, 87]. This equation is formulated while assuming a constant spherical geometry for cavitation bubbles in an infinite body of incompressible liquid; bubble deformation is neglected.

$$R\frac{d^2R}{dt^2} + \frac{3}{2}\left(\frac{dR}{dt}\right)^2 = \frac{P_{sat} - P_\infty}{\rho_l} - \frac{2\sigma}{\rho_l R} - 4\frac{\mu_l}{\rho_l R}\frac{dR}{dt} \tag{2.13}$$

While the Rayleigh-Plesset equation attempts to describe the bubble dynamics and evolution of a single spherical bubble, many pioneering works on developing multi-bubble models have sourced from this very equation. Typically, a set of governing equations is solved for each phase of the multiphase fluid. However, to account for the change in the vapor volume fraction, an additional transport equation is introduced based on the mathematical model presented in Frikha et al. [88]. Its general volume fraction expression is:

$$\frac{\partial \alpha_{lv}}{\partial t} + div(\alpha_{lv}\boldsymbol{u}) = \alpha \tag{2.14}$$

where l and v are subscripts representing the liquid and the vapor phase, respectively. α is the volume fraction, t is the time, and $\boldsymbol{u}$ is the velocity vector. Moreover, the equation can be morphed into representing the mass fraction of each phase as follows:

$$\frac{\partial \rho_{lv}\alpha_{lv}}{\partial t} + div(\rho_{lv}\alpha_{lv}\boldsymbol{u}) = \dot{m}^{+} + \dot{m}^{-} \tag{2.15}$$

where ρ is the density of the phase. The transport equation in Eq. 2.15 is expressed in terms of a new variable known as the mass transfer rate, or the mass transfer source term. It is written as $\dot{m}$ where $\dot{m}^{+}$ represents the condensation process, or the bubble collapse, in which the liquid mass increases. Meanwhile, $\dot{m}^{-}$ represents the evaporation process in which the liquid mass decreases when bubbles begin to grow.

The first study to propose a homogeneous model based on Eqns. 2.13 and 2.15 was Kubota [89] in which the investigation presents a local homogeneous model derived from the nonlinear Rayleigh-Plesset equation. However, one of the proposed model's weaknesses is its numerical instability. Therefore, many proceeding studies presented their own solutions to address the weakness. This was done through a series of simplifications and manipulations of the Rayleigh-Plesset equation. For instance, Merkle et al. [90] presented a set of source terms independent of the bubble radius, instead, it tracks the change in the liquid density. Kunz et al. [91], on the other hand, present another set of source terms based on the Ginzburg-Landau potential. However, an issue that has been highlighted in the mentioned models is that they heavily depend on empirical constants. Hence, Schnerr and Sauer [92] suggested a transport-based cavitation model independent of many empirical constants, while keeping the bubble density as the only model constant. Moreover, the source terms of the model describe the dynamics of bubble growth and collapse through tracking changes in the bubble radius. Similarly, Zwart et al. [93] presented model source terms derived based on the manipulations of turbulence governing equations of the eddy viscosity and the mixture density. However, four model constants emerge in its source terms, namely the bubble radius, nucleation site volume fraction, evaporation constant, and condensation constant. The constants are intended to control the rate of growth and collapse of the bubbles in a validated and simple way. Following the same derivation logic of both Schnerr-Sauer and Zwart et al., Singhal et al. [94] implemented a 'full cavitation model' in which the model goes beyond tracking changes in the bubble radius and considers changes in the turbulent kinetic energy, the surface tension, and the non-condensable gas presence in the medium.

The usage of a single-bubble model like the Rayleigh-Plesset equation is based on its physically grounded and computationally tractable means to describe bubble dynamics in practical flows (i.e. hydraulic machines and ultrasonic horn reactors). From such governing equation, the macroscopic vapor-liquid mass transfer source terms can be systematically derived and incorporated into a phase continuity equation. While multi-bubble population balance or Lattice Boltzmann Method (LBM) approaches do in fact grant higher fidelity and can resolve bubble size distributions and interactions, they are computationally more demanding. As such, a Rayleigh-Plesset-based model can facilitate a formulation that sufficiently governs the coupling of cavitation dynamics to macroscopic flow behaviour. Meanwhile, it can also implicitly capture multi-bubble effects through averaged, empirical parameters, such as the aforementioned model constants, ultimately providing a robust compromise between physical fidelity and computational efficiency. Table 2.1 below summarizes the aforementioned models, alongside other similar models, and their source terms.

Table 2.1 Common multi-bubble cavitation models and their mass transfer rate source terms.

Model Name	***Source Terms***
Merkle et al. [90]	$S_{evap.} = \frac{2C_{evap.}\rho_l \, min\{0, P_\infty - P_v\}\alpha_l}{\rho_l \rho_v u_\infty^2 t_\infty}$ $S_{cond.} = -\frac{2C_{cond.} \, max\{0, P_\infty - P_v\}(1-\alpha_l)}{\rho_l u_\infty^2 t_\infty}$
Kunz et al. [91]	$S_{evap.} = \frac{2C_{evap.}\rho_l \, min\{0, P_\infty - P_v\}}{\rho_l u_\infty^2 t_\infty}$ $S_{cond.} = -\frac{2C_{cond.}\rho_v \alpha_l^2 (1-\alpha_l)}{t_\infty}$
Schnerr and Sauer [92]	$S_{evap.} = \frac{\rho_l \rho_v}{\rho_m}\frac{3\alpha(1-\alpha)}{R}\sqrt{\frac{2}{3}\frac{\lvert P_\infty - P_v\rvert}{\rho_l}}$ $S_{cond.} = -\frac{\rho_l \rho_v}{\rho_m}\frac{3\alpha(1-\alpha)}{R}\sqrt{\frac{2}{3}\frac{\lvert P_\infty - P_v\rvert}{\rho_l}}$
Zwart et al. [93]	$S_{evap.} = C_{evap.}\frac{3\alpha_{nuc}(1-\alpha_v)\rho_v}{R}\sqrt{\frac{2}{3}\frac{\lvert P_\infty - P_v\rvert}{\rho_l}}$ $S_{cond.} = -C_{cond.}\frac{3\alpha_{nuc}\alpha_v \rho_v}{R}\sqrt{\frac{2}{3}\frac{\lvert P_\infty - P_v\rvert}{\rho_l}}$
Singhal et al. [94]	$S_{evap.} = C_{evap.}\frac{\sqrt{k}}{\sigma}\rho_v \rho_l \sqrt{\frac{2}{3}\frac{\lvert P_\infty - P_v\rvert}{\rho_l}}(1 - f_v - f_g)$ $S_{cond.} = -C_{cond.}\frac{\sqrt{k}}{\sigma}\rho_v \rho_l \sqrt{\frac{2}{3}\frac{\lvert P_\infty - P_v\rvert}{\rho_l}} f_v$
Frobenious et al. [95]	$S_{evap.} = C_{evap.}\frac{n_0}{1 + 4/3 n_0 \pi R^3} 4\pi R^2 \sqrt{\frac{2}{3}\frac{\lvert P_\infty - P_v\rvert}{\rho_l}}$ $S_{cond.} = -C_{cond.}\frac{n_0}{1 + 4/3 n_0 \pi R^3} 4\pi R^2 \sqrt{\frac{2}{3}\frac{\lvert P_\infty - P_v\rvert}{\rho_l}}$

2.4 Ultrasonic Horn Tip Modelling

2.4.1 Stuart Streaming Theory

The Stuart streaming theory is an extension of the Rayleigh [96], Nyborg [97] and Westervelt [98] (RNW) streaming theory that establishes the quantification of acoustic streaming using the continuity equation and the Navier-Stokes equation as shown in Eq. 2.16 and Eq. 2.17, respectively:

$$\frac{\partial \rho}{\partial t} = -\nabla \cdot (\rho \vec{v}) \tag{2.16}$$

$$\rho\left(\frac{\partial \vec{v}}{\partial t} + \vec{v} \cdot \nabla \vec{v}\right) = -\nabla p + \mu \nabla^2 \vec{v} + \vec{F} \tag{2.17}$$

Where ρ is the density, $\vec{v}$ is the velocity, t, is the time, p is the pressure, μ is the viscosity, and F is the force per unit volume induced by streaming. This force term is expressed by Rayleigh as the Reynolds stress spatial variation [96] and can be written as:

$$F = -\frac{\partial\left(\rho\overline{v_i v_j}\right)}{\partial x_i} \tag{2.18}$$

Moreover, this force is typically calculated from the sound field attenuation with respect to the plane waves [99]:

$$F = -\frac{1}{c}\nabla\vec{I} \tag{2.19}$$

In Eq. 2.23, c is the speed of sound and $\vec{I}$ is the acoustic intensity. In an attempt to solve the continuity and the Navier-Stokes equations, Nyborg [97] implemented the successive approximations method to represent each of the excess pressure, excess density, and excess velocity at any point by expanding them into a series of terms, as such:

$$p^1 = p_1 + p_2 + p_3 + \cdots \tag{2.20}$$

$$\rho^1 = \rho_1 + \rho_2 + \rho_3 + \cdots \tag{2.21}$$

$$\vec{v}^1 = \vec{v}_1 + \vec{v}_2 + \vec{v}_3 + \cdots \tag{2.22}$$

Where the excess pressure is essentially $p^1 = (p - p_0)$, the excess density is $\rho^1 = (\rho - \rho_0)$, and the excess velocity is $\vec{v}^1 = (\vec{v} - \vec{v}_0)$. Here, the excess value of each term is subtracted by its unperturbed value of the fluid property. The subscript 1 for each fluid property in Eqns. 2.20-2.22 represent first order approximation of the property and are typically considered as the solutions of the wave equation. This is because they vary sinusoidally in time at a given frequency ω, which in turn, represents the sound field produced. Moreover, the second order approximations are time-averaged property terms acting as correction terms added to their respective first order approximations. While this provides a reasonable approximation of the streaming properties, the RNW theory is only true for creeping motions or extremely slow fluid flow at Reynolds numbers $Re < 1$. The reason behind this is because the inertial terms presented in Eq. 2.17 were neglected in the approximation calculations. Since, this is inapplicable for generic streaming motions generated by ultrasonic horns, Stuart [100] has led a mathematical investigation to reintroduce the neglected inertia terms back into the equation of motion, as follows:

$$\rho(\bar{v} \cdot \nabla\bar{v}) = -\nabla\bar{p} + \mu\nabla^2\bar{v} + \vec{F} \tag{2.23}$$

However, key differences in the Stuart's Navier-Stokes equation is the omitting of the transient term and replacing the vector terms with time-averaged terms (i.e. $\bar{v}$ and $\bar{p}$). As discussed earlier, the time-averaged terms simply are simply represented by the second-order approximations in the RNW theory. Thus, this equation of motion is made applicable for the estimation of acoustic streaming formed by concentrated high power acoustic beam in the form of inertially dominated turbulent jets.

The imagery drawn about this high-power acoustic streaming is a narrow beam of sound with an acoustic power of $W_0 = I_0 A_0$ at its inlet. This is graphically illustrated in Figure 2.9. In an ideal model, it is said that the energy entering this beam is equal to the energy exiting it.

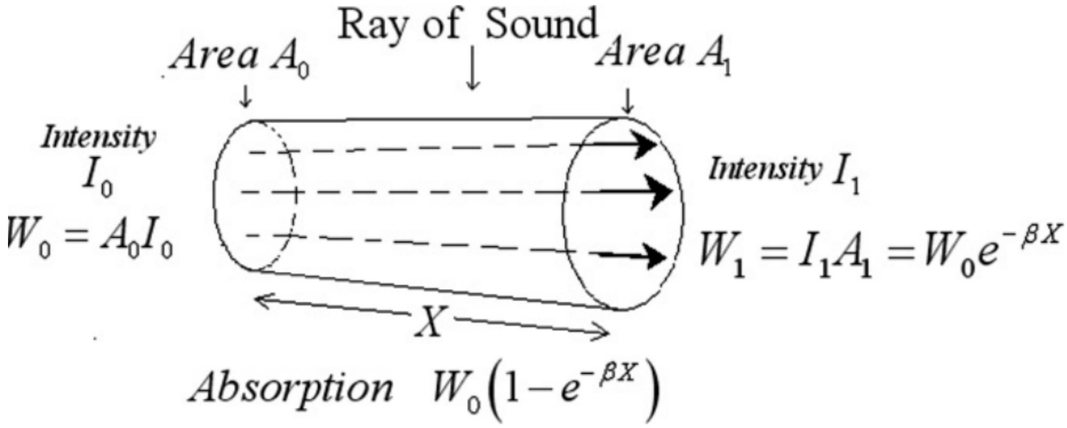

Figure 2.9: Lighthill's assumption of the attenuated acoustic beam [101].

And since the intensity I is defined as the rate of transport of energy per unit area A, this then is idealized as $IA = constant$. However, upon attenuating the acoustic beam, the acoustic power will then be expressed as:

$$W = W_0 e^{-\beta X} \tag{2.24}$$

Here, X is the distance from the sound source and the exponential value $e^{-\beta X}$ is the damping term with respect to the beam's spatial attenuation with β as the attenuation coefficient. An acoustic momentum flow rate F_a is defined, alongside the acoustic energy flow in Eq. 2.24, as:

$$F_a = \frac{W}{c} = \frac{W_0}{c} e^{-\beta X} \tag{2.25}$$

Where the acoustic momentum flow rate is similarly attenuated with respect to the distance from the source X. Furthermore, the law of conservation of momentum can be applied to obtain:

$$F_{h/a} = \frac{W_0}{c} - \frac{W_0}{c} e^{-\beta X} = \frac{W_0}{c}\left(1 - e^{-\beta X}\right) \tag{2.26}$$

In which acoustic streaming momentum appears as the hydrodynamic momentum which is represented by F_h. The momentum's spatial rate of decay is then expressed as:

$$F_L = \frac{dF_a}{dX} = \frac{\beta}{c} W_0 e^{-\beta X} = \frac{\beta}{c} W \tag{2.27}$$

Here, F_L is considered to be the net force per unit length that induces this streaming. The kinematic momentum of this acoustic beam is then represented in the equation below:

$$K = \rho_0 F_h = \rho_0 \frac{W_0}{c}\left(1 - e^{-\beta X}\right) \tag{2.28}$$

In the case of turbulent jetting, the attenuation coefficient is extremely high leading to the exponential term $e^{-\beta X}$ approach zero at a short distance X. This makes the hydrodynamic momentum delivered equal to $\frac{W_0}{c}$. Regardless of that, it has been concluded by Schlichting [101] that the turbulent jet mean flow retains strong similarity to the laminar jet when taking a constant eddy viscosity that equates to:

$$\mu_t = 0.016(K)^{1/2} \tag{2.29}$$

With Eqs. 2.28 and 2.29, one can now describe the change in turbulent viscosity along the sound beam. Finally, to define the velocity profile of the turbulent jet presumably generated by the acoustic streaming, a Gaussian distribution is assumed as follows:

$$v = \left(\frac{2K}{\rho^2 \pi S^2}\right)^{1/2} e^{[-(r/S)]} \tag{2.30}$$

In Eq. 2.30, r is the radius of the beam's axis and S represents the width of the jet. Now, with this boundary defining model, it circumvents the numerically complex problem of modelling streaming and heat generation caused by the oscillation of a high-power ultrasonic horn. However, if the aim of a given study is to numerically explore the Multiphysics problem of acoustic cavitation formation and motion, then the model would be deemed inapplicable due to the highly nonlinear nature of the problem induced by the bubbles' reduction of the acoustic field's speed of sound and the attenuation from their scattering. Moreover, the model fails to consider the Bjerken forces applied by the acoustic field on the bubbles due to sound absorption. Thus, for a multiphase problem as such, alternative boundary conditions have been considered instead.

2.4.2 Pressure Determination Modelling

Instead of defining the ultrasonic horn tip as a velocity-inlet boundary condition, some studies have considered implementing a pressure-based boundary condition instead. This was done with the consideration of the pressure expansion-compression waves propagating within the medium and governing the wave equation [102, 103]. So, the thought process of deriving the pressure boundary condition is through solving for the wave equation stated in Eq. 2.31 and applying a thermal boundary condition to solve the equation.

$$\nabla\left(\frac{1}{\rho}\nabla P(X,t)\right) - \frac{1}{\rho c^2}\frac{\partial^2 P(X,t)}{\partial t^2} = 0 \tag{2.31}$$

With the harmonic pulsation induced by the horn and the domain boundaries generally being set at a pressure equating to zero, the pressure field is then defined as harmonically fluctuating, respectively. As such, the general solution to the Helmholtz equation (Eq. 2.31) is:

$$P(X,t) = p(X)e^{i\omega t} \tag{2.32}$$

And substituting Eq. 2.32 into Eq. 2.31 will result in:

$$\nabla\left(\frac{1}{\rho}\nabla P(X,t)\right) - \frac{\omega^2}{\rho c^2}P(X) = 0 \tag{2.33}$$

With the above equation, many things can be inferred, such as the pressure distribution is dependent on the transducer frequency, fluid density, and speed of sound. In addition, the reliance on the density and the sound speed indirectly correlates to being dependent on temperature, as both fluid parameters are influenced by it. Therefore, potential thermal effects must be taken into consideration. The pressure magnitude of the horn tip face pressure is computed from the ultrasonic horn's acoustic intensity expression:

$$I_{US} = \frac{P_{US}}{A_H} = \frac{{P_{total}}^2}{2\rho c} \tag{2.34}$$

In which P_{US} is the power input of the ultrasonic horn, A is the horn area, and P_{total} is the pressure wave amplitude. By computing P_{total}, one can calculate the required pressure value set at the horn tip face by capturing its sinusoidal temporal variation:

$$P = P_{total} \sin(\omega t) \tag{2.35}$$

This boundary condition surely defines the horn tip more accurately than the boundary definition the velocity-inlet presents. This is because acoustic pressures from high-power ultrasonic transducers are easily adapted into the numerical boundary condition. However, another limitation appears with this kind of boundary condition and that is its inability to capture influence of wall movement on the formation and development of cavitation in the proximal region. Therefore, more recent studies have begun scrutinizing dynamic mesh models instead.

2.5 Horn Tip Vibration Modelling

When it comes to adopting moving wall boundary condition, some studies went with a simpler solution to assign a sinusoidal motion to the horn tip, while others have gone the extra mile to adopt a sinusoidal model inspired by the achievable mode shapes of the piezoelectric element, and thus the horn tip, during its oscillation at 20 kHz. For the simple model, the equation defined is simply based on a sine function multiplied by the maximum amplitude achieved by the horn at a specific power input. Eq. 2.36 demonstrates its general expression.

$$v_u(t) = \xi_{max} 2\pi f \cos(2\pi f t) \tag{2.36}$$

Where $v_u(t)$ is the displacement of the nodes from its neutral position, ξ_{max} is the maximum displacement of the node, and f is the oscillation frequency. However, some studies, like Rahimi et al. [104], suggest that the mode shapes experienced by the piezoelectric ceramic integrated in the transducer is completely transmitted to the ultrasonic horn tip. It has been inferred that the symmetrical, longitudinal vibrational modes of a circular piezoelectric disk are the most prominent [105]. Specifically, the mode shape indicating a maximum displacement at the horn tip centre is what has been commonly observed at approximately 20 kHz and thus has been considered as the base of the following vibration model derivation.

Before beginning with the derivation, a few assumptions were made prior to reduce the complexity of the mathematical model. These assumptions were made based on Kirchhoff's bending theory for circular thin plates [106]. The assumptions made are the following, and are illustrated in Figures 2.10a and 2.10b:

- The plate material is linearly elastic and obeys Hooke's law.

- Elastic deformation of plate is characterized by Modulus of Elasticity and Poisson's ratio.
- Horn tip vibrates due to a load applied on top of radiating surface perpendicular to circular cross-section.
- Straight lines normal to middle plane before bending remain straight and normal to said plane during deformation based on the hypothesis of straight normals [107].

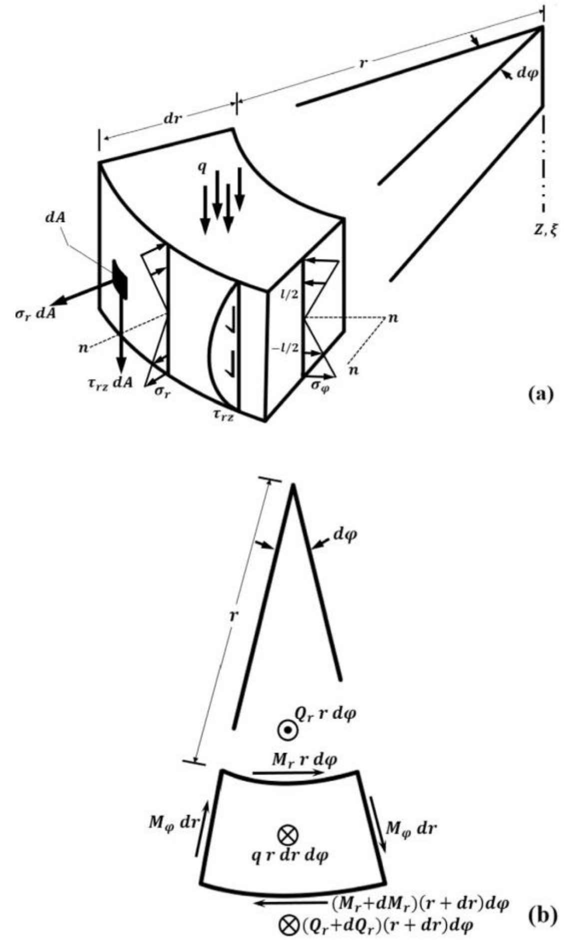

Figure 2.10: (a) A schematic of a segment of a circular piezoelectric disk displaying the stresses and shear forces acting on the segment in the cylindrical coordinates, (b) A top-view schematic of the segment illustrating a balance in the moments acting on the segment illustrating a balance in the moments acting on the segment [104].

Kirchoff's bending theory allows the assumption of normality of lateral sides of circular plate by simply rotating about neutral axes, thus:

$$u^z = -z\frac{d\xi}{r}, \qquad u^z = u^z(r) \tag{2.37}$$

Where u^z is the displacement of some point at a distance z from the middle surface, ε is a small displacement of circular plate in z direction. Normal strains (elongation) of edges in the direction of coordinate axes can then be:

$$\varepsilon_r = \frac{du^z}{dr} = -z\frac{d^2\xi}{dr^2} \tag{2.38}$$

$$\varepsilon_{\varphi} = \frac{(r + u^{z})d\varphi - rd\varphi}{rd\varphi} = -\frac{z}{r}\frac{d\xi}{dr} \tag{2.39}$$

where ξ is the specific displacement component. Moreover, assuming that the shear strain in rφ plane is negligible, we can move to finding the normal stresses in that plane using Hooke's law.

$$\sigma_{r} = \frac{E}{1 - v^{2}}\left(\varepsilon_{r} + v\varepsilon_{\varphi}\right) = \frac{Ez}{1 - v^{2}}\left(\frac{d^{2}\xi}{dr^{2}} + \frac{v}{r}\frac{d\xi}{dr}\right) \tag{2.40}$$

$$\sigma_{\varphi} = \frac{E}{1 - v^{2}}\left(\varepsilon_{\varphi} + v\varepsilon_{r}\right) = \frac{Ez}{1 - v^{2}}\left(\frac{1}{r}\frac{d\xi}{dr} + v\frac{d^{2}\xi}{dr^{2}}\right) \tag{2.41}$$

Where v is the poisson's ratio, σ_{r} and σ_{φ} are the normal stresses in r and φ directions, E is the Young's modulus. Now, deriving the moment equations acting along the circumferential section:

$$M_{r} = \int_{-l/2}^{l/2} \sigma_{r} z dz = \frac{El^{2}}{12(1 - v^{2})}\left(\frac{d^{2}\xi}{dr^{2}} + \frac{v}{r}\frac{d\xi}{dr}\right) \tag{2.42}$$

$$M_{\varphi} = \int_{-l/2}^{l/2} \sigma_{\varphi} z dz = -\frac{El^{2}}{12(1 - v)}\left(\frac{1}{r}\frac{d\xi}{dr} + v\frac{d^{2}\xi}{dr^{2}}\right) \tag{2.43}$$

Where $\frac{El^{2}}{12(1-v)}$ is flexural rigidity, and l is thickness of circular plate. The shearing force per unit length of the cylindrical section is defined as:

$$Q_{r} = \frac{1}{2\pi r}\int_{0}^{2\pi}\int_{0}^{r} qrdrd\varphi \tag{2.44}$$

where q is intensity of load as a function of r. Summing up the moments of the element:

$$\left(M_{r} + \frac{dM_{r}}{dr}dr\right)(r + dr)d\varphi - M_{r}rd\varphi - M_{\varphi}drd\varphi + Q_{r}rdrd\varphi = 0 \tag{2.45}$$

Neglecting small quantities of higher order differential terms:

$$M_{r} + \frac{dM_{r}}{dr}dr - M_{\varphi} + Q_{r} = 0 \tag{2.46}$$

where M_{r} and M_{φ} are the radial and hoop moment per unit length, respectively. Finally, substituting previous definitions of moments and shear strain:

$$\frac{d^{3}\xi}{dr^{3}} + \frac{1}{r}\frac{d^{2}\xi}{dr^{2}} - \frac{1}{r^{2}}\frac{d\xi}{dr} = \frac{Q_{r}}{D} \tag{2.47}$$

In the case of acoustic radiation, Q_{r} represents the equivalent radiating forces per unit length for peak-to-peak displacements:

$$Q_r = \frac{F_{vib}}{2\pi r} \tag{2.48}$$

Integrating three times to get the displacement equation:

$$\xi = \frac{F_{vib}}{8\pi D}(r^2 \, ln \, r^2 - r^2) + C_1 \frac{r^2}{4} + C_2 \, ln \, r + C_3 \tag{2.49}$$

To get the three constants, apply three boundary conditions:

$$\xi(r = 0) = limited \; (horizontal \; asymptote) \tag{2.50}$$

$$C_2 = 0 \tag{2.51}$$

$$\frac{d\xi(r = R)}{dr} = 0 \tag{2.52}$$

$$C_1 = \frac{F_{vib}}{4\pi D}(1 - 2\ln R) \tag{2.53}$$

$$\xi(r = R) = 0 \tag{2.54}$$

$$C_3 = \frac{F_{vib} R^2}{16\pi D} \tag{2.55}$$

By direct replacement of the three constants into Eq. 2.49, the simplified equation then becomes:

$$\xi = \frac{F_{vib} R^2}{16\pi D}\left(1 - \left(\frac{r}{R}\right)^2 - 2\left(\frac{r}{R}\right)^2 ln\left(\frac{r}{R}\right)\right) \tag{2.56}$$

Given that the motion is sinusoidal, Eq. 2.56 can then be written as:

$$\xi = \xi_{max}\left(1 - \left(\frac{r}{R}\right)^2 - 2\left(\frac{r}{R}\right)^2 ln\left(\frac{r}{R}\right)\right) sin(2\pi f t) \tag{2.57}$$

Such model represents a rather realistic micro-scale boundary condition that attempts to account for the potential variation in the proximal flow field under the horn tip with the change of shape of the horn tip surface. A basic schematic of what the displacement boundary condition translates to in the physical domain can be observed in Figure 2.11.

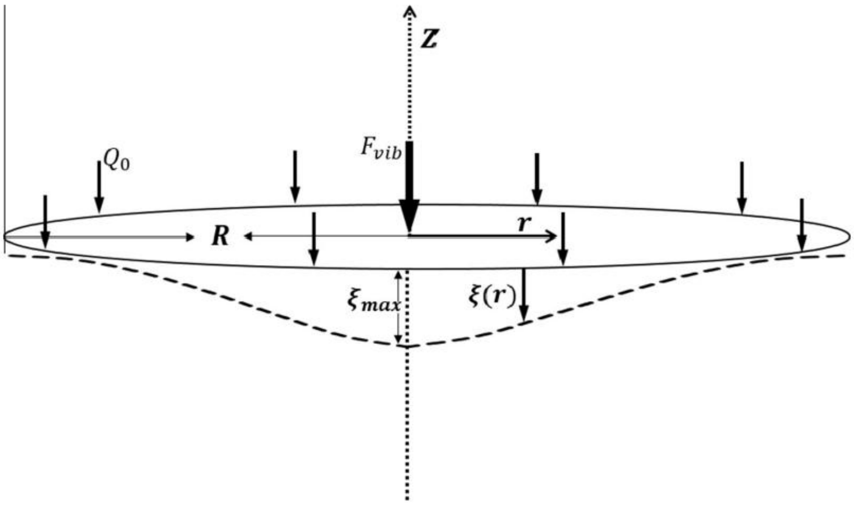

Figure 2.11: Schematic of the deformation of the horn tip surface with respect to mode shape 1 of the piezoelectric ceramic [104].

While the derivation has been validated and holds true in multiple studies, numerical setups with that apply the simple sinusoidal model have also witnessed a strong agreement between their numerical results and their respective experimental results [108-110].

3 Establishment of the Base Numerical Model

3.1 Introduction

The following chapter delves into the theory and implementation of different numerical models considered for the foundational numerical configuration carried throughout different segments of the investigation. Detailed descriptions of different governing equations and their working principles are elaborated on throughout this chapter. Ultimately, this chapter provides reason for the selection of each model involved in the CFD Multiphysics system that is developed in ANSYS FLUENT 23R2. Essentially, the governing equations solved within the simulation compute turbulence, the compressibility of the two phases of water liquid and vapor, and the mass transfers between them. However, as a primary part of the investigation objectives of the presented project is to further the development of the numerical modelling of cavitation, it is important to note that models discussed here are implementations of pre-existing governing equations in ANSYS FLUENT that were utilized to configure the base numerical setup. As such, the methodology discussed in this chapter lays out the foundation of the CFD model used to describe, build on the models, and ultimately capture key attributes of the multiphase flow in an ultrasonically irradiated domain. The newly derived physics model, specifically, the cavitation model is discussed later in-depth in Chapter 4.

3.2 Turbulence Modelling

Generally, the essence of implementing a turbulence model sources from the existence of the acoustofluidic byproduct known as acoustic streaming, as discussed previously in Chapter 2. Such phenomenon instigates a time-averaged turbulent flow within the radiation column under the ultrasonic horn. This, in turn, both initializes and governs many other physical phenomena, primarily acoustic cavitation. Therefore, modeling turbulence becomes a necessity to accurately capture the flow field, both proximal and far, from the radiating source.

Typically, there exist many turbulence models previously derived and commonly used in a multitude of modeling applications. Simply put, they are more commonly categorized as Reynolds Averaged Navier-Stokes (RANS) [111]. It is true that there are other complex and computationally intensive models, such as the Detached Eddy Simulation (DES) and Large Eddy Simulations (LES) [111]. However, such models provide marginal benefit of modelling key time-averaged flow phenomena observed in a typical horn-type reactor. Therefore, these models were not considered.

Instead, with the shear stress transport (SST) $\mathrm{k}-\omega$ model [112], turbulence was approximated. This RANS turbulence model was set based on its ability to accurately capture proximal flow near the horn wall [109]. Such flow is crucial, as the horn tip acts as the source of flow agitation in the domain and the hub of cavitation nucleation. As such, the model was deemed fit to capture the expected turbulent flow within the proximity of the horn. The two additional equations introduced by the turbulence model solve for the turbulent kinetic energy k and the specific rate of turbulence energy dissipation ω as follows:

$$\frac{d(\rho k)}{dt} = \tau_{ij}\frac{\partial u_i}{\partial x_j} - \beta^{*}\rho\omega k + \frac{\partial}{\partial x_j}\left[(\mu + \sigma_k\mu_t)\frac{\partial k}{\partial x_j}\right] \tag{3.1}$$

$$\frac{d(\rho w)}{dt} = \frac{\gamma}{\nu_t}\tau_{ij}\frac{\partial u_i}{\partial x_j} - \beta\rho\omega^2 + \frac{\partial}{\partial x_j}\left[(\mu + \sigma_\omega\mu_t)\frac{\partial \omega}{\partial x_j}\right] + 2(1 - F_1)\rho\sigma_{\omega 2}\frac{1}{\omega}\frac{\partial k}{\partial x_j}\frac{\partial \omega}{\partial x_j} \tag{3.2}$$

The ρ term represents the density, t represents time, τ_{ij} is the shear stress between cells i and j, μ is the molecular viscosity, μ_t is the turbulent viscosity, ν_t is the eddy viscosity, ω is the specific dissipation rate, k is the specific turbulent energy. model constants are given as: $\beta^* = 0.09$, $\beta = 0.075$, $\sigma_k = 0.85$, $\sigma_\omega = 0.5$, $k = 0.41$, $\gamma = \frac{\beta}{\beta^*} - \sigma_w \frac{k^2}{\sqrt{\beta^*}}$,. Meanwhile, the F term represents a rational function designed to produce binary values (0,1). This function is expressed as follows:

$$F = \tanh\left(\arg_1^4\right) \tag{3.3}$$

in which,

$$\arg_1 = \min\left[\max\left(\frac{\sqrt{k}}{0.09\omega y}; \frac{500\nu_t}{y^2\omega}\right); \frac{4\rho\sigma_{\omega 2}k}{CD_{k\omega}y^2}\right] \tag{3.4}$$

where y is the distance to the closest wall and $CD_{k\omega}$ is the postive part of the cross-diffusion term in Eq. 3.2. This is expressed as:

$$CD_{k\omega} = \max\left(2\rho\sigma_{\omega 2}\frac{1}{\omega}\frac{\partial k}{\partial x_j}\frac{\partial \omega}{\partial x_j}, 10^{-20}\right) \tag{3.5}$$

With such function integration, the governing equations of both k and ω transfigure between Wilcox's standard $k - \omega$ model [113] and the standard $k - \epsilon$ model [114] based on the proximity of flow to the wall, or in the current case, the horn surface and container walls. As such, the model implements the prediction effectiveness of $k - \omega$ for near-wall flows and the $k - \epsilon$ for far-field flows.

3.3 Compressibility Modelling

Regarding the liquid phase compressibility, the Tait equation of state [115] was used to define a nonlinear isotropic relationship between water density and pressure, considering that cavitation is generally an isothermal, thus barotropic, process. The nonlinear density-pressure relationship is defined as follows:

$$p(\rho) = a + b^n \tag{3.6}$$

$$p(\rho) = (p_\infty + B)\left(\frac{\rho}{\rho_\infty}\right)^n - B_M \tag{3.7}$$

In Eq. 3.6, p is the absolute pressure, a and b are coefficients derived from an assumption stating linear proportionality of the bulk modulus B_M and the pressure. In Eq. 3.7, p_∞ is the atmospheric pressure, ρ and ρ_∞ are the liquid density and the atmospheric density respectively, and n is the density exponent. Moreover, a rearranged expression is implemented in the form of Eq. 3.8.

$$\left(\frac{\rho}{\rho_\infty}\right)^n = \frac{B_M + n(p(\rho) - p_0)}{B_M} \tag{3.8}$$

Here, the bulk modulus relates to the effect a pressure gradient has in inducing a relative change in density. In fact, the bulk modulus is defined as the inverse of the compressibility β expression shown in Eq. 3.9.

$$\beta = -\frac{1}{V}\left(\frac{\partial V}{\partial p}\right) \tag{3.9}$$

Hence, the speed of sound is in the compressible liquid phase is then defined as:

$$c = \sqrt{B_M/\rho} \tag{3.10}$$

Meanwhile, as vapor phase compressibility sources from the bubble's spherically symmetrical collapses, the ideal gas law was set to govern the compressibility of vapor structures during cavitation. This was implemented by assigning the following density-pressure relationship to the vapor phase:

$$\rho = \frac{p}{RT} \tag{3.11}$$

In which R is the specific gas constant and T being the liquid temperature. Furthermore, the speed of sound of an ideal gas is then expressed as:

$$c = \sqrt{\gamma RT} = \sqrt{\frac{c_p RT}{c_v}} = \sqrt{\frac{c_p RT}{c_p - R}} = \sqrt{\frac{c_p}{c_p - R} \times \frac{p}{\rho}} \tag{3.12}$$

In Eq. 3.12, c_p and c_v are specific heat capacities at constant pressure and volume respectively.

4 Modelling the mass transfer at acoustically generated bubble interface using Rayleigh–Plesset equation second-order derivatives

4.1 Introduction

As it was previously discussed in Chapter 3, modeling acoustic cavitation in a typical horn-type reactor requires a strong coupling between multiple physical models to tackle this Multiphysics flow problem. In this chapter, cavitation modelling, along with its mathematical and theoretical backgrounds, is thoroughly explained, in Sections 4.2 and 4.3, in aims to identify the shortcomings of popular cavitation models. Moreover, the derivation of a new cavitation model is demonstrated and later validated against previously published experimental work. The following investigation is dissected as follows: (i) In Sections 4.4 and 4.5, a thorough explanation of the methodology is presented including a complete mathematical derivation of the modified ZGB model. (ii) Section 4.6 demonstrates the procedure of the four statistical analysis techniques utilized in the study. (iii) Section 4.7 illustrates the numerical comparative analysis results and validates them against experimental findings. (iv) Lastly, Section 4.8 summarizes conclusions drawn out from the respective results.

4.2 Conventional Cavitation Numerical Methods

Many studies have been conducted on acoustic bubble dynamics to experimentally scrutinize the bubble dynamics witnessed during acoustic cavitation development [116-118]. For instance, Tzanakis et al.[68] has investigated acoustic cavitation behavior by varying multiple parameters: viscosity by changing the liquid medium and the oscillation amplitude by alternating the transducer power. Ultimately, the study's key findings were on a macroscopic level in which morphing of cavitation zone structures from one medium to another was examined; a conical cavitation zone occurs in water, a thick round layer occurs in glycerin, while ethanol observes ultrasonic degassing where bubbles disperse and actively oscillate towards the free surface of the cuvette. Similarly, Jiang et al.[73] investigated the influence of the ultrasonic horn's distance from the bottom of the cuvette on the acoustic cavitation structure produced and their interaction with one another. It has been observed that the nonlinearity of bubble oscillation is caused by increased bubble density and bubble radii induced by the decreasing distance. Despite its insightfulness, experimental work can be costly, and thus limiting; therefore, recent studies developed an interest in numerical cavitation modelling techniques.

Generally, numerical explorations on the dynamics of acoustic cavitation essentially rely on a single assumption that states that the cavitation bubble retains its spherical form throughout its lifecycle. However, some studies utilized a different approach in an attempt to achieve a substantially realistic model. Hence, single-bubble cavitation models were employed to capture the dynamics and geometrical transformations of a single cavitation bubble. Common models as such applied in the literature were the particle tracking model [119], the coupled modified Bernoulli-Wave equation [84], and the Keller-Miksis model [120]. Many numerical investigations were successful in observing multiple acoustic bubble dynamic features at a microscopic scale, such as Altay et al. [121] and Ye et al. [84] where both scrutinized the bubble-surface interactions and the effect of surface features, such as wall roughness, on bubble evolution. Moreover, Kerboua et al. [86] reported an energy analysis of an acoustic cavitation bubble to identify energy gain and loss sources using the aforementioned approach. While this approach successfully demonstrates non-spherical bubble oscillations, it is computationally expensive to scale these models for multi-bubble cavitation modelling. Therefore, multi-bubble modelling typically refers to the spherical bubble assumption for easier computational adaptations.

Multi-bubble oscillations have been modelled by the Rayleigh-Plesset equation [46, 87], the Gilmore equation[122], and the Keller-Miksis equation [123]. Despite their assumption, the models consider the effects of pressure and temperature enabling them to predict hydrodynamic phenomena witnessed in experiments, such as non-linear bubble oscillations, stability of bubble oscillations, and the bifurcation of bubble oscillation modes [124-126]. Furthermore, the Rayleigh-Plesset model appears to be relatively the most favorable model, as it considers the influence of liquid surface tension, viscosity, and nucleation inertia on bubble evolution. In fact, most commercially available models, namely the Kunz et al. [91], Schnerr-Sauer [92], and Zwart-Gerber-Belamri (ZGB) [93] models, are derived and implemented based on a simplified Rayleigh-Plesset model. Generally, these models define a pair of source terms resembling mass transfer rate per unit volume occurring at the bubble interface during both condensing and evaporating conditions. Moreover, these models have undergone thorough validations against hydrodynamic experiments in which rapid changes to driving pressure are unlikely to occur; thus, implementing these models may not qualify as accurate representations of acoustic cavitation.

Previous experimental studies have explored the effect of liquid properties and geometrical variations on acoustic cavitation evolution to pinpoint any underlying dependencies that acoustic cavitation may have with other parameters [126, 127]. A prime example was a study conducted by Žnidarčič et al. [128] that investigates potential transfigurations of acoustic cavitation regions due to changes in the ultrasonic horn diameter and variations in air saturation, viscosity, surface tension, and temperature of the medium. Qualitative and quantitative results conclude that the liquid properties have no significant effects on acoustic bubble oscillation; however, they suggest rapid horn surface vibrations play a major role in nucleation leading to an “acoustic supercavitation”. Typically, this reiterates the distinct features acoustic cavitation compared to traditional hydrodynamic cavitation: fast propagation of pressure within microseconds timeframe, bubbles may attain an extended lifetime before collapse, and bubble oscillation acoustic impendence’s influence on driving pressure.

4.3 Previous Modifications of Cavitation Models

Typically, modifications of cavitation equations to fit case-specific models are common in literature [129, 130], whether it was through changing model constants or introducing new terms. For the case of acoustic cavitation, Znidarcic et al. [109] adopts this approach by modifying the Schnerr-Sauer model by reintroducing Rayleigh-Plesset’s inertia term into the derived source terms to improve acoustic cavitation prediction accuracy. Afterwards, a series of validations was conducted with the new source terms. Moreover, the choice of using the original Schnerr-Sauer model as a base model was justified by stating that the model was the most competent in predicting micro-scale vapor structures that follow the driving frequency of the horn, 20 kHz. Furthermore, Znidaricic et al. further elaborate that their model constants showed marginal influence on calculation results based on a performed sensitivity analysis and hence kept as is. However, their comparative analysis illustrated a noticeable discrepancy between numerical and experimental results; acoustic pressure peaks are overestimated by an average of 1.08 bar, in addition to the overprediction of cavitation volume. Furthermore, it is also arguable that the assumption of constant bubble density may lead to some modelling inaccuracies, since it varies with acoustic intensity and ultrasonic frequency [131].

The current investigation attempts to contribute to improving existing cavitation models' accuracy in predicting acoustic cavitation by adopting Znidaricic et al.'s approach of introducing the inertial term from the Rayleigh-Plesset equation to the Schnerr-Sauer model, but instead, using the ZGB model as the base model. This is because the ZGB model is numerically stable and easier to implement, since its continuity equation is casted in volumetric form while retaining its conservativeness without the need for an additional transport equation[93]. In addition, during any cavitation model modifications, empirical constants often pose as a major challenge for researchers due to their ambiguous physical nature. For instance, in the case of using the ZGB model as a base model, constants emerging like bubble density, bubble radius, and nucleation site volume fraction can potentially affect acoustic cavitation prediction. Despite the important roles of these constants in characterization of acoustic cavitations, most past studies have not considered the sensitivity of these constants to the pressure fluctuation amplitude and frequency associated with acoustic cavitation. Thus, this study aims to obtain an optimal combination of these model constants to achieve the desired acoustic pressure and frequency oscillation objectives. The study employs a Design of Experiments methodology consisting of a full factorial design matrix and response surface methodology (RSM) coupled with the desirability method and Monte Carlo simulations to establish a complete statistical understanding of model constants' significance and underlying interactions. To the best of the authors' knowledge, the methodological framework adopted in this study is unique and the framework provides new perspectives into the numerical characterizations of acoustic cavitation.

4.4 Cavitation Model Derivations

4.4.1 ZGB Cavitation Model

4.4.1.1 Governing Conservation Equations

Here, the ZGB model is taken as the base model, as mentioned earlier. Initially, the multiphase model is governed by a set of conservation equations; the conservation of mass for each phase α, shown in Eq. 4.1, and the conservation of momentum for the homogeneous mixture where no interphase slip is assumed, shown in Eq. 4.2.

$$\frac{\partial(r_\alpha \rho_\alpha)}{\partial t} + \frac{\partial(r_\alpha \rho_\alpha u_i)}{\partial x_i} = \dot{S}_\alpha \qquad (4.1)$$

$$\frac{\partial(\rho_m u_i)}{\partial t} + \frac{\partial(\rho_m u_i u_j)}{\partial x_j} = -\frac{\partial P}{\partial x_i} + \rho_m r_\alpha g_i + \frac{\partial(\tau_{ij})}{\partial x_j} \qquad (4.2)$$

P stands for the pressure, and r_α, ρ_α, and S_α represent the volume fraction, density, and mass generation rate of phase α respectively. Subscript m simply indicates the mixture phase observed. Meanwhile, u_i, g_i, and τ_{ij} are the Cartesian velocity components, gravitational acceleration, and the shear stress exerted on the bubble-liquid spherical interface in the i and j directions, otherwise known as the Stokes' law stress tensor [132].

One of the model's assumptions when solving for conservation equations is that mass transfer only occurs at the interphase. In other words, the mass transfers of dissolved gases into and out of the bubble are vector quantities that are equal but opposite in direction. Another assumption states that the homogeneous mixture is composed of N number of phases in which the addition of their volume fractions equates to unity representing the mixture. Working on the basis of the two assumptions, Eq. 4.1 and 4.2 form a system of N+4 equations with N+4 unknowns. The system of equations is presented as a summation of continuity equations simplified as follows:

$$\sum_{\alpha=1}^{N} \frac{1}{\rho_\alpha}\left(\frac{\partial(r_\alpha \rho_\alpha)}{\partial t} + \frac{\partial(r_\alpha \rho_\alpha u_i)}{\partial x_i} - \dot{S}_\alpha\right) = 0 \tag{4.3}$$

If the said multiphase model was to be implemented in a system of incompressible phases, Eq. 4.3 is then further rearranged reduced, while assuming incompressibility, to an equation as such:

$$\frac{\partial u_i}{\partial x_i} = \dot{S}_{lv}\left(\frac{1}{\rho_v} - \frac{1}{\rho_l}\right) \tag{4.4}$$

Of course, as cavitation typically revolves around alternating phase changes between liquid and vapor, their source terms, referring to the mass transfer rates, adopt the following relationship:

$$\dot{S}_{lv} = \dot{S}_v = -\dot{S}_l \tag{4.5}$$

However, in the case of observing turbulent flow, Eq. 4.4 then denotes mean velocities from the Reynolds decomposition. Moreover, the Reynolds Stress term makes an appearance in the momentum conservation equations. In such case, a viscous model must be chosen and coupled with the multiphase model which will be later discussed in Section 4.5.2.

4.4.1.2 The derivation of the original source terms

With the continuity equation defined, the source terms are then derived from the six-term Rayleigh-Plesset equation.

$$R\frac{d^2R}{dt^2} + \frac{3}{2}\left(\frac{dR}{dt}\right)^2 + \frac{2\sigma}{\rho_l R} - \frac{4\mu}{\rho_l R}\frac{dR}{dt} = \frac{p_v(T_\infty) - p_\infty}{\rho_l} + \frac{p_{g0}}{\rho_l}\left(\frac{R_0}{R}\right)^{3\gamma} \tag{4.6}$$

Starting from the left-hand side, the first two terms represent the second and first order derivatives for the rate of change of the bubble radius R. The third term refers to the partial contribution of surface tension σ at the bubble interface where it acts radially inwards against bubble growth. Afterwards, the fourth term considers the contribution of the medium's dynamic viscosity µ on the rate bubble growth and collapse alike. However, one may notice the inverse relationship between both surface tension and dynamic viscosity have with bubble radius R; the importance of this relationship is its suggestion that the terms do not carry much significance for fully developed bubbles with large radii. As for the term containing the pressure difference between the temperature-dependent vaporization pressure and the liquid ambient pressure, it presents the foundational understanding of bubble evolution. This is because it quantifies the pressure threshold required for cavitation bubble nucleation. Lastly, the final term describes the effect of non-condensable gas partial pressure p_{g0} in the bubble as it grows from its initial radius R_0 to R.

In the original ZGB model, Eq. 4.6 is reduced by a series of assumptions including neglecting the effects of the second-order inertia term, surface tension, dynamic viscosity, and non-condensable gas, where a simplified expression is then yielded as shown in Eq. 4.7.

$$\frac{3}{2}\left(\frac{dR}{dt}\right)^2 = \frac{p_v(T_\infty) - p_\infty}{\rho_l} \tag{4.7}$$

Such assumptions are generally found appropriate by Sauer [133] for hydrodynamic cavitation operating in a water medium at room temperature. Moreover, the acceleration term is typically insignificant in cases of macroscopic hydrodynamic cavitation, as bubble evolution acceleration occurs within the window of 10^{-4} s and becomes further insignificant with the increase of the pressure gradient between the bubble and the medium. Thus, with a bit of rearranging, the first-order derivative becomes the equation's subject directly relating it to the bubble evolution driving term.

$$\frac{dR}{dt} = \sqrt{\frac{2}{3}\frac{p_v(T_\infty) - p_\infty}{\rho_l}} \tag{4.8}$$

Before deducing the general form of the source terms, the rate of change of mass and the vapor volume fraction expressions of an assumed single spherical bubble are defined in Eq. 4.9 and 4.10 respectively.

$$\frac{dm}{dt} = A_{sphere}\rho_v\frac{dR}{dt} = 4\pi R^2\rho_v\sqrt{\frac{2}{3}\frac{p_v(T_\infty) - p_\infty}{\rho_l}} \tag{4.9}$$

$$r_v = V_{sphere}N_{bubble} = \frac{4}{3}\pi R^3 N_{bubble} \tag{4.10}$$

Where N_{bubble} in Eq. 4.10 represents the number of bubbles per unit volume. Finally, a general form for the total interphase mass transfer rate per unit volume is:

$$\dot{S_{lv}} = FN_{bubble}\frac{dm}{dt} = F\frac{3r_v\rho_v}{R}\sqrt{\frac{2}{3}\frac{\pm\left|p_v(T_\infty) - p_\infty\right|}{\rho_l}} \tag{4.11}$$

F is an added empirical multiplier [136]. Moreover, the pressure gradient alternates in sign depending on the type of mass transfer process, i.e., evaporation or condensation. In the expression's current form, it assumes no interaction between cavitation bubbles and thus it is only accurate and numerically stable during the bubble's condensation process due to its small size; it is inaccurate to adopt for the evaporation process. Therefore, an inversely proportional relationship is introduced between the vapor volume fraction and the nucleation site density; as the vapor volume fraction increases, the nucleation site density decreases respectively. For this reason, a variable r is introduced in which $r = r_{nuc}(1 - r_v)$ during evaporation and $r = r_v$ during condensation. Thus, Eq. 4.11 then transforms to:

$$\dot{S_{lv}} = F\frac{3r\rho_v}{R}\sqrt{\frac{2}{3}\frac{\pm|p_v(T_\infty) - p_\infty|}{\rho_l}} \tag{4.12}$$

4.4.1.3 The Derivation of the Modified Source Terms

Similar to the derivation logic carried out in deducing the source terms of the original ZGB model, the derivation starts off by reducing Eq. 4.6 to three terms instead of two: the driving term, the velocity term, and the additional acceleration term, otherwise known as the inertial term. This simplification has been discussed by Znidarcic et al.[109] in which it has been found that most of the fluid parameters, hypothesized to have an effect on the attached cavity oscillation frequency and the cavitation maximum volume, do not have any notable impact on the two cavitation properties. For instance, the mean frequency and the maximum volume negligibly shift from 5058 Hz and 8.97 mm^3 to 5085 Hz and 8.58 mm^3 respectively when 50% saturation of dissolved gas is added into the water medium. Moreover, a frequency and volume of 5095 Hz and 8.95 mm^3 when water's surface tension is increased with the addition of Sodium Dodecyl Sulphate (SDS). Finally, when changing the medium from water to Ethylene Glycol ($C_2H_6O_2$) to decrease viscosity, the frequency increases to 5074 Hz and the volume drops to 8.63 mm^3. It can easily be noted that the surface tension has the greatest impact on the mean cavitation oscillation frequency, while the presence of dissolved gases has the most influence over the maximum cavitation volume. Despite that, those changes remain considerably small and thus negligible.

In this regard, the time step of the numerical simulation will have to fall below $t_s < 10^{-4}$ s (a time step $t_s = 5 \times 10^{-6}$ s is selected, more on that can be found in Section 4.5.2) to capture the inertial effect on acoustic cavitation development [109]. Thus, the simplified Rayleigh-Plesset equation then becomes:

$$R\frac{d^2R}{dt^2} + \frac{3}{2}\left(\frac{dR}{dt}\right)^2 = \frac{p_v - p_\infty}{\rho_l} \tag{4.13}$$

Given that there are two derivative terms of bubble radius, the source term derivations require an additional step before proceeding with the traditional derivation procedure witnessed in the original model. It is worth noting that, with this model derivation, the interpretation of R changes; R_B here is interpreted as a constant reference radius characterizing the interfacial area density, and not the instantaneous physical bubble size. This way, its derivatives represent the growth and acceleration rates of the representative interface obtained from local pressure gradients and vapor volume fraction and evaluated at the constant scale R_B. This makes d^2R/dt^2 an "effective inertia" of the phase interface only. Hence, the additional step is rearranging Eq. 4.13 to create a general solution for this acceleration term:

$$\frac{d^2R_B}{dt^2} = \frac{p_v - p_\infty}{\rho_l R_B} - \frac{3}{2R}\left(\frac{dR_B}{dt}\right)^2 \tag{4.14}$$

Given the two unknowns of Eq. 4.14, a differential equation is expressed to define the velocity term based on its previous value and its acceleration term as shown below:

$$\frac{dR_B}{dt}(t) = \frac{dR_B}{dt}(t-1) + \frac{d^2R_B}{dt^2}(t) \times t_s \tag{4.15}$$

The Cauchy boundary conditions for $\frac{dR_B}{dt}(t)$ and $\frac{d^2R_B}{dt^2}(t)$ are set in a way where both equate to 0 at t = 0. As flow time progresses and becomes t = t_1, Eq. 4.15 then expresses the new velocity in terms of the previous velocity and the acceleration. Lastly, in similarity with the original source term derivations, the bubble evolution velocity equation in Eq. 4.15 can then be replaced in the general source term expression suggested in Eq. 4.11.

$$\dot{S_{lv}} = F\frac{3r\rho_v}{R_B}\frac{dR_B}{dt}(t) \tag{4.16}$$

Where the evaporation and condensation source terms can be defined as:

$$\dot{S_{lv}} = \begin{cases} F_{vap}\dfrac{3r_{nuc}(1-r_v)\rho_v}{R} \times \dfrac{dR_B}{dt}(t)\,, if\ P < P_v \\ F_{cond}\dfrac{3r_v\rho_v}{R_B} \times \dfrac{dR_B}{dt}(t)\,, if\ P > P_v \end{cases} \tag{4.17}$$

Following the same procedure, Eq. 4.14 and Eq. 4.15 shall be looped and reiterated after each time step $t_n = t_{n-1} + t_s$ to calculate the new acceleration term, velocity term, and then the source terms, in that order.

4.5 Numerical simulation setup and modelling

4.5.1 Cuvette and ultrasonic horn geometry

The numerical setup used in this study is an imitation of the simple experimental setup shown in the investigation conducted by Znidarcic et al. [109]. The setup consists of an ultrasonic horn, a tapered metal rod containing a piezo-ceramic element to excite longitudinal waves, that is 175 mm long with its 3 mm diameter tip submerged 1 cm deep into a 50x50x50 mm rectangular cuvette. The sonotrode is operated at its maximum power of 70 W where the tip oscillates with an amplitude of 164 µm. Its output signal fed into the horn by the power generator has a nominal frequency of 20 kHz and an uncertainty of ± 500 Hz. The significance of this setup is in its simplicity, and thus the setup translation into a numerical model is made much easier. Therefore, the numerical setup follows a two-dimensional fluid domain with a rectangular model of the ultrasonic horn tip submerged 20 mm down the cuvette for considered planar calculations. As for the hydrophone, a numerical monitor point 7 mm away from the horn is coded into the fluid domain for pressure data collection. The 2D axisymmetric geometry is illustrated in Figure 4.1a with the red dot representing the monitor point placement.

4.5.2 Setting of boundary conditions

The cuvette boundaries are categorized into two groups: rigid static wall and free surface. As the name suggests, the static wall boundary condition simply defines a non-moving wall with the addition of the no-slip condition where the velocity boundary layer is described by a zero-velocity at the boundary wall. As for the free surface boundary condition, it instates the top surface of the fluid domain as a surface experiencing zero parallel shear stress that defines the homogeneous interface between water and atmospheric air. Numerically, this is interpreted as a pressure outlet boundary condition with a gauge pressure of 0 Pa and an operating pressure of 1 atm. Moreover, as a setup assumption, boundary conditions related to modelling a gravitational field were not considered for the simulation.

As for the ultrasonic horn, its rigid walls are designed to oscillate at a frequency of 20 kHz, thus making it a “moving wall” to present a moving boundary problem Essentially, the nodes that lie along the horn walls and tip are temporally oscillated to accommodate for the boundaries’ motion. In this study, dynamic meshing is chosen as the preferred modelling method for this, since the validity of the method has been verified in previous works of literature [134]. Therefore, using dynamic meshing, a User-Defined Function (UDF) is written in C language to define the sinusoidal motion of all three horn boundaries to set an oscillating motion corresponding to 20 kHz and an amplitude of 164 μm reached by the horn. The UDF assigns the transient velocity function stated in Eq. 4.18 to the horn boundaries.

$$v = A\omega \cos \omega t \tag{4.18}$$

Where v is the axial velocity, A is the amplitude, ω is the angular velocity, and t refers to the flow time of the simulation. The general working principle of dynamic meshing here is to move the discretized boundary’s nodes sinusoidally stated in Eq. 4.18. However, the technique considered in this study to simulate the mesh motion is a joint method of spring-based smoothing [135] and local remeshing. The working principle behind the spring-based method is assuming that each edge between any two nodes is a series of interconnected springs. Accordingly, Hooke’s law [136] is used to calculate the force transmitted due to a displacement found at a neighboring boundary node using Eq. 4.19 [135].

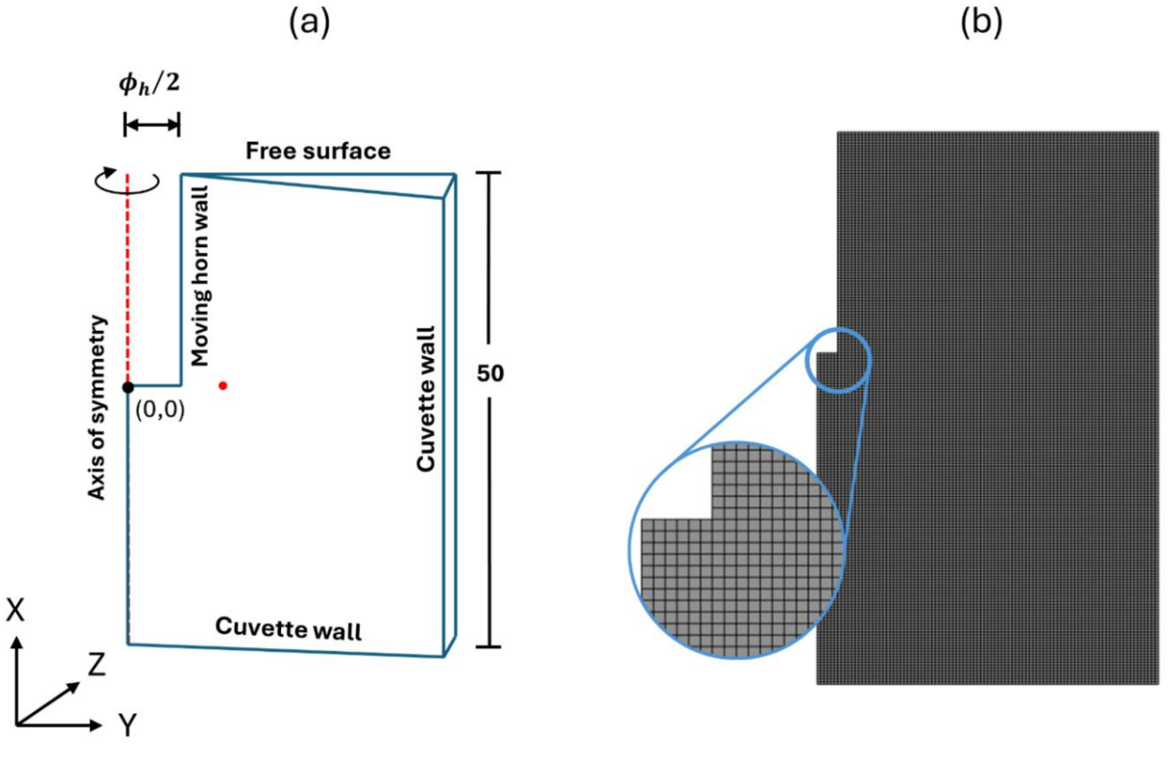

Figure 4.1: (a) A dimensioned schematic (in mm) of the axisymmetric calculation domain representing the 50 x 50 mm cuvette where the rectangular cut from the top surface represents the vibrating ultrasonic horn of $\phi_h = 3$, and the red dot represents the pressure monitor point 7 mm away from the horn tip. (b) A representation of the structured mesh used for domain discretization.

$$F_i = \sum_{j}^{n_i} k_{ij}\left(\Delta x_j - \Delta x_i\right) \tag{4.19}$$

In which i and j subscripts represent two neighboring nodes, and thus F_i is the net force, n_i is the number of nodes connecting to node i, k_{ij} is the spring constant of the springs at the edge between nodes i and j. Moreover, the k_{ij} is presented as:

$$k_{ij} = \frac{F_i}{\sqrt{\left|x_i - x_j\right|}} \tag{4.20}$$

Using Eq. 4.19 and the assumption of force equilibrium at the observed node, an iterative equation is deduced, as shown in Eq. 4.21, that is then solved using the Jacobi iterative method until convergence to obtain the final position using Eq. 4.22.

$$\Delta x_j{}^{n+1} = \frac{\sum_j^{n_i} k_{ij} \Delta x_j{}^{n}}{\sum_j^{n_i} k_{ij}} \tag{4.21}$$

$$x_i{}^{n+1} = x_i{}^{n} + \Delta x_i{}^{n,converged} \tag{4.22}$$

Where n and n+1 represent the positions at the current and the next timestep, respectively. This method is then coupled with the smoothing remeshing method to account for potentially large displacements in the dynamic mesh that can lead to numerical instability and convergence problems. The method sets a criterion that it follows to classify the aspect ratio and skewness of each cell during the mesh evaluation that takes place before finalizing the mesh motion [135].

Meanwhile, a full coupling between the pressure and velocity solvers was selected based on convergence optimization considerations. As for the selection of spatial discretization schemes, a second-order upwind scheme was used to discretize density, momentum, turbulent kinetic energy, and energy transport equations. Meanwhile, a first-order upwind scheme was chosen for volume fraction and the specific dissipation rate equations. The pressure interpolation scheme used in the current setup is the Pressure Staggering Option (PRESTO!). Lastly, the transient formulation adopted in the setup was a first order implicit scheme. Moreover, in accordance with the inertial term added to the cavitation model to account for its influence on acoustic cavitation evolution, the time step size chosen for the transient calculation is 5 µs with 600 timesteps and a maximum of 40 iterations per time step. This way, the simulation captures approximately 1.5 times the period of the expected acoustic cavitation life cycle. Furthermore, the convergence criteria set for the governing equations were 10^{-4}, with the exception of the energy equation where 10^{-8} was used instead.

4.5.3 Geometry grid independence test

With the aforementioned setup settings in the previous sections, an iterative calculation was performed with six grids. Illustrated in Figure 4.2 is a graph showing the gradual mesh refinement and its effect on the maximum pressure detected by the assigned monitor point. It can be clearly seen that the maximum acoustic pressure attained drops drastically as the mesh is refined up to 40,000 elements in which the effect of the grid is no longer significant after that point. The percentage change in the maximum pressure is highlighted in Table 4.1. Therefore, the mesh pertaining to 40,000 cells, with a 0.25 x 0.25 mm cell size is then chosen for the study with a cell size, as shown in Figure 4.1b.

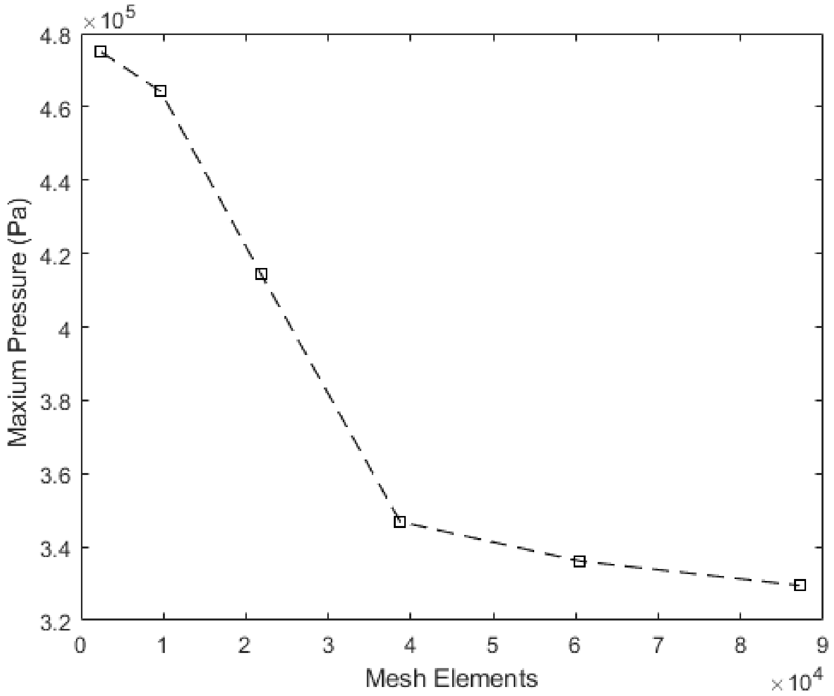

Figure 4.2: Grid independence test comparing the number of mesh elements with the maximum pressure recorded by the monitor point shown in Figure 4.1a.

Table 4.1: Grid independence test percentage change in pressure readings per increase in number of elements.

Meshing Elements (-)	*Maximum Pressure (Pa)*	*Percentage Change (%)*
2,053	474,736.84	-
9,459	463,976.61	2.27
21,793	414,152.05	10.74
38,623	347,017.54	16.21
60,299	336,257.31	3.10
86,971	329,941.52	1.88

4.6 Statistical design of experiments

4.6.1 Full factorial design

Observing the new bubble growth and collapse mass transfer equations shown in Eq.4.17, one can notice that it contains a set of four constants that are yet to be defined. Specifically, the constants are the evaporation, condensation, bubble radius, and nucleation site volume fraction constants. Given that these constants are originally empirically derived, as noted in Section 4.4.1, there is no analytical justification for setting their values. Therefore, in this study, a statistical approach, known as Design of Experiments, is adopted to establish an understanding of each constant's statistical significance on the cavitation model's performance in predicting acoustic cavitation. Particularly, the full factorial approach is employed to identify the effects of multiple parameters on the maximum acoustic pressure and oscillation frequency responses [137]. In this investigation, a four-factor, two-level (2^4) full factorial design is implemented, as shown in Table 4.2.

Table 4.2: 2^4 Full Factorial Design Setup.

Numeric Factors	*Factor Label*	*Lower Level* *-1*	*Higher Level* *+1*
Evaporation Constant, F_v	A	10	50
Condensation Constant, F_c	B	0.01	0.1
Bubble Radius, R (m)	C	15×10^{-6}	25×10^{-6}
Nucleation Site Volume Fraction, r_{nuc}	D	5×10^{-4}	15×10^{-4}

The lower and higher levels of factors F_v, F_c, and r_{nuc} were chosen on the basis of values that previous studies in literature have investigated when scrutinizing the effect of the ZGB model constants on their simulation results in which they go about selecting their set values by incrementing each model constant value about its original value [138-140]. As for factor R, the levels were chosen based on the qualitative observation made in Znidarcic et al.'s experiment [109] and quantitative observation in the bubble radius probability distribution in Reuter et al.'s investigation [141]. In retrospect, the aforementioned studies have revealed that the variations in any of the coefficients in the ZGB model tend to have a linear effect on the cavitation predictive performance. This could be due to the coefficients representing 'gain' parameters, as shown in Eq. 4.7. As such, it could be assumed that a 2^4 factorial design is sufficient to scrutinize crucial parametric interactions, such as two-way and three-way interactions, that influence the predictive performance of the cavitation model. Moreover, the range of values presented in Table 4.2 is selected in such a way that it provides a reasonable, but sufficient, 'distance' between them to capture the factors' 'true effects' on the response values.

Table 4.3: 24 Full Factorial Design Matrix.

	Basic Design				
Run	*A*	*B*	*C*	*D*	*Treatment Combination*
1	-1	-1	-1	-1	1
2	1	-1	-1	-1	a
3	-1	1	-1	-1	b
4	1	1	-1	-1	ab
5	-1	-1	1	-1	c
6	1	-1	1	-1	ac
7	-1	1	1	-1	bc
8	1	1	1	-1	abc
9	-1	-1	-1	1	d
10	1	-1	-1	1	ad
11	-1	1	-1	1	bd
12	1	1	-1	1	abd
13	-1	-1	1	1	cd
14	1	-1	1	1	acd
15	-1	1	1	1	bcd
16	1	1	1	1	abcd

Table 4.3 above tabulates a design matrix of all 16 possible combinations of the four factors that are then replaced in the new cavitation model equations and used in the numerical simulation to obtain their response values for a comparative analysis.

4.6.2 Response surface methodology

The response surface methodology, generally, is the proceeding step after developing a full-factorial design matrix and obtaining each treatment's response. The said methodology provides a platform for a comparative analysis of the responses collected and attempts to draw hidden statistical trends. One way of doing so is by developing a regression model; a general expression, derived from response data collected, that attempts to generalize the degree of effect each factor has on the response model. In this study, this was done by employing Minitab 21 [142] in which it generated main effect, interaction effect, and response surface plots as a qualitative demonstration of conclusive trends drawn out of the dataset.

To take into account both main effects, two-way interaction effects, and three-way interaction effects, a second order polynomial model multiple regression model is generated for each response term, i.e. maximum pressure and oscillation frequency, using the following equation:

$$Y = \beta_o + \sum_{i=1}^{2} \beta_i X_i + \sum_{i=1}^{2} \beta_{ii} {X_i}^2 + \sum_{i=1}^{n} \beta_{ij} X_i X_j + \varepsilon \tag{4.23}$$

where Y is the response, I and j are factor indexes, and thus Xi and Xj are coded values of the factors. Meanwhile, β_o, β_i, β_{ii}, and β_{ij} are the intercept, linear, quadratic and interaction coefficients respectively. Lastly, ε represents the experimental error. Moreover, to optimize the obtained regression model, a stepwise regression analysis was conducted. Particularly, a backward-elimination method was chosen to examine the statistical significance of each variable in the regression model. This is performed by observing the change in variance by removing each predictor to the model one step at a time. As a result, unnecessary terms and interactions are eliminated from the model accordingly.

4.6.3 Response optimization and desirability

After finalizing the regression model, an optimal combination of evaporation constant, condensation constant, bubble radius, and nucleation site volume fraction values can be found through the desirability optimization approach [143]. This approach, among many other methods, stands out due to its simplicity and flexibility in designating different weightings and importance level to each factor. Furthermore, this approach takes an input of optimization objectives that can be either to maximize, minimize, or obtain a specific target value for the response. Thus, depending on the given objective, the approach utilizes different desirability functions. Moreover, the selected function then transforms the estimated response, Y_i into a dimensionless value known as desirability, $d_i(Y_i)$. With that in mind, the desirability of each response is calculated by the following objective-specific equations accordingly.

$$d_i(Y_i) = \begin{cases} 0, & Y_i < l_i \\ \left(\dfrac{Y_i - l_i}{t_i - l_i}\right)^s, & l_i < Y_i < t_i \\ \left(\dfrac{Y_i - u_i}{t_i - u_i}\right)^t, & t_i < Y_i < u_i \\ 0, & Y_i > u_i \end{cases} \tag{4.24}$$

In Eq. 4.24, the subscript i indicates the response iteration, and thus l_i and u_i represent the lower limit and the upper limit of the response. Moreover, t_i is the target response value. Meanwhile, s and t are the weightings of the response that dictate the shape of the desirability function. Generally, the weights vary from 0.1 to 10 in which weights less than 1 indicate low emphasis on the response, while weights greater than 1 indicate otherwise. The desirability value $d_i(Y_i)$ obtained is then fed into another dimensionless function known as the overall desirability function, D, where $0 \leq D \leq 1$.

$$D = \left(\prod_{i=1}^{n} d_i(Y_i)^n\right)^{1/n} \tag{4.25}$$

The variable n in Eq. 4.25 represents the number of responses. As for the interpretation of Eq. 4.25, a high value of D simply indicates a more desirable function, hence, revealing the optimal solution. Ultimately, the main goal of the desirability approach is to maximize D; therefore, the optimum factor values of the four model constants are indicated by the value of the desired function $d_i(Y_i)$ they achieve, that then maximizes D accordingly.

4.6.4 Monte Carlo simulation

With the regression and optimization procedure completed, the analysis is taken further to provide a complete statistical overview of the influence of the model constants on the acoustic cavitation modelling performance. In other words, insight on the influence of randomness present in the model constants' values on the response values is limited. Therefore, a sensitivity analysis was used to fill this knowledge gap and validate the optimized model constants chosen. More specifically, the Monte Carlo method was employed to quantify the degree of influence random errors have on the input-dependent outcome of a regression model resembling the physical process of acoustic cavitation. This method follows an iterative process that simulates a real experiment being run several times to observe any changes in the distribution of the outcome. In the case of acoustic cavitation modelling, the investigative interest emphasizes the impact of variability in the already optimized governing factors, i.e., evaporation and condensation constants, bubble radius, and nucleation site volume fraction, on the maximum acoustic pressure and its oscillation frequency. In this study, MATLAB code was created to conduct the Monte Carlo simulation by using MATLAB's random number generator (RNG) to create random variations in each factor within the range of ± 10%. Furthermore, as a mode of controlling the variation due to MATLAB RNG, seeding is used to lead the RNG towards producing a predictable sequence of random numbers affiliated to the random errors being investigated. Shown in Figures 4.3a and 4.3b are two plots illustrating variations in the standard deviation of the maximum acoustic pressure and oscillation frequency respectively, as the sample size is increased.

As both graphs show that the standard deviation of both samples fluctuate minimally and converge at approximately 7,000 iterations, this sample size is then reasonably chosen to be used for this study.

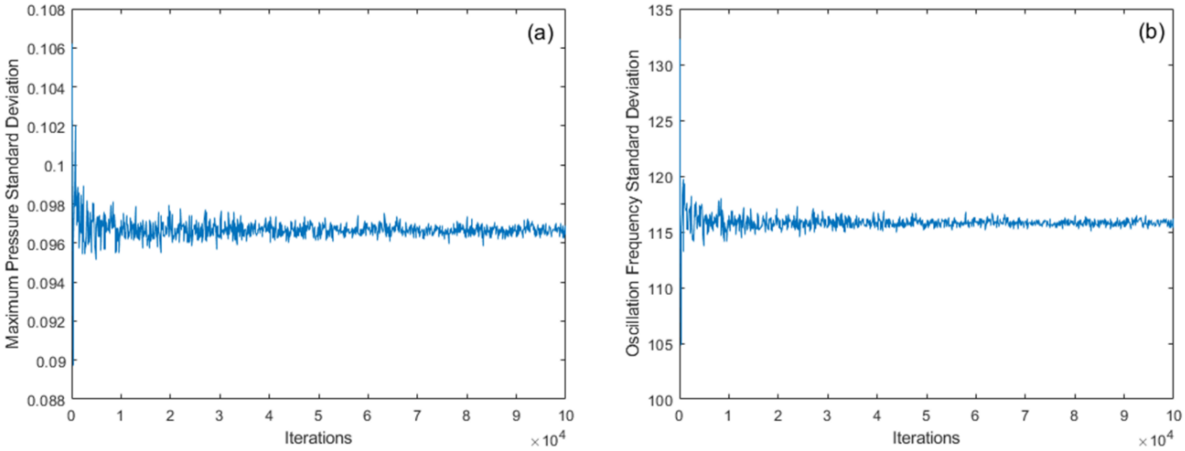

Figure 4.3: The standard deviation of (a) maximum acoustic pressure (b) oscillation frequency plotted against the number of iterations executed by the Monte Carlo simulation.

4.7 Simulation Results and Statistical Analysis

4.7.1 Original model acoustic cavitation prediction

Initially, as means to assess the true acoustic cavitation performance of the original ZGB model, the numerical calculations were performed with the original model and qualitatively and quantitatively compared to Znidarcic et al.'s experimental results [109]. Figure 4.4 below presents a comparative illustration between the numerically generated contour plots and the high-speed camera pictures taken of cyclic cavity structures formed. As Znidarcic et al. [109] explains, the experimental results generally display a single large 'mushroom-shaped' cavity covering the ultrasonic horn tip and is undergoing periodic expansion-collapse cycles. This observation is reiterated by Tzanakis et al. [68] and justified by the usage of water as the cavitation medium. However, the mushroom structure is only retained during the expansion phase and later transforms into a conical shape during the structure's shrinkage. Moreover, a stream of micro bubbles emerges during the large cavity development. In addition, these clouds of micro bubbles are then released downstream into the medium and oscillate at their own sub-harmonic frequency.

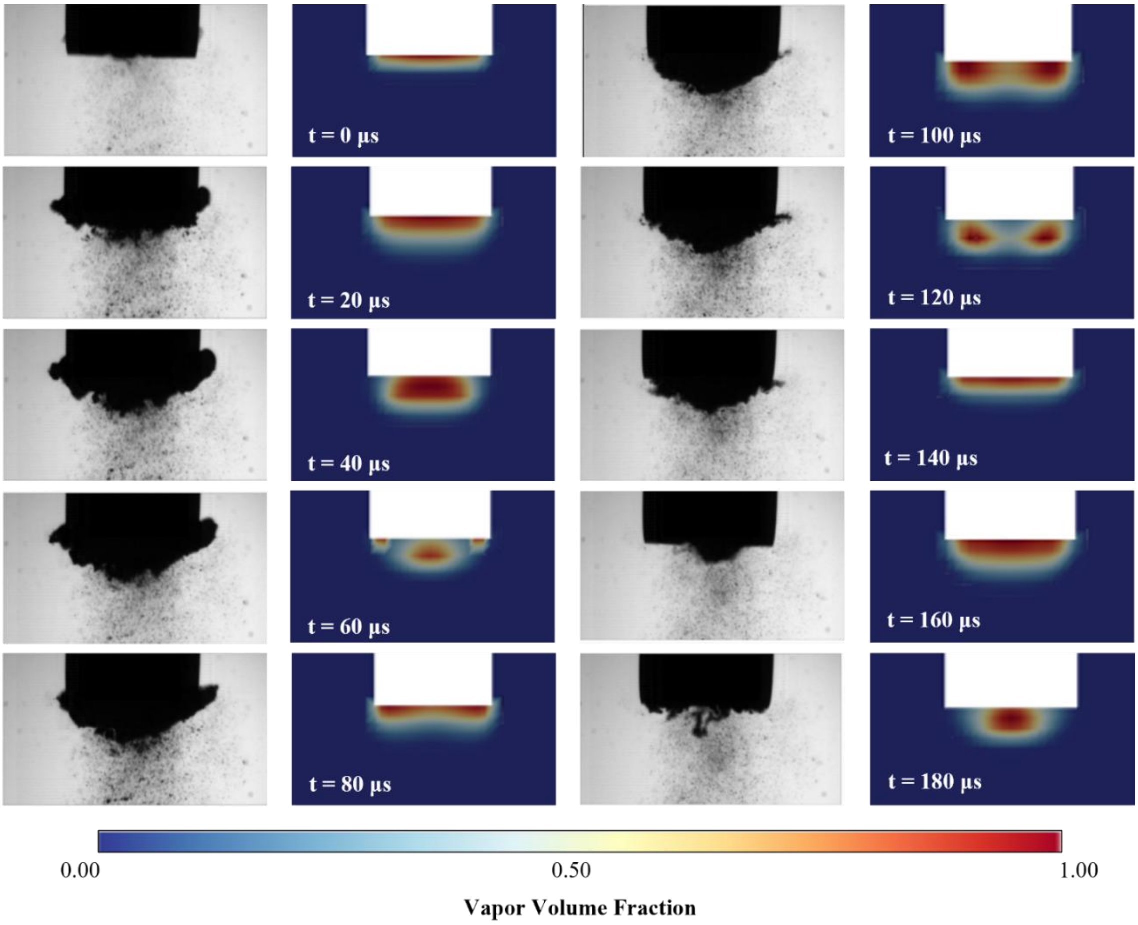

Figure 4.4: Comparative illustration of instantaneous cavitation structures observed experimentally [109] and predicted by the original ZGB model numerical setup at coinciding time steps.

Meanwhile, numerical results obtained highlight multiple structural and periodic differences in the cavity. Firstly, a parallel can be drawn during the first stages of development where large cavity structure begins to engulf the horn tip; the mushroom-like shape is visible during t = 0

– 20 µs. However, at t = 40 µs, the cavity structure diverges from the experimental observation, as it adopts a conical phase instead. As mentioned earlier, this typically suggests that the cavity structure is entering its shrinking phase; however, it begins to expand again from t = 80 – 100 µs before it shrinks again at t = 120 µs. At later time steps, a repeated structural pattern can be seen when compared to the structure found at t = 0 – 40 µs. This simply marks the end of a single expansion-collapse cycle and the beginning of a new cycle at t = 140 µs. On the other hand, a single cycle is experimentally shown to take place at t =180 µs and generally illustrating a longer cycle period. Figure 4.5 plots the static pressure at the monitor against flowtime, where it shows the variations in pressure due to acoustic cavitation evolution.

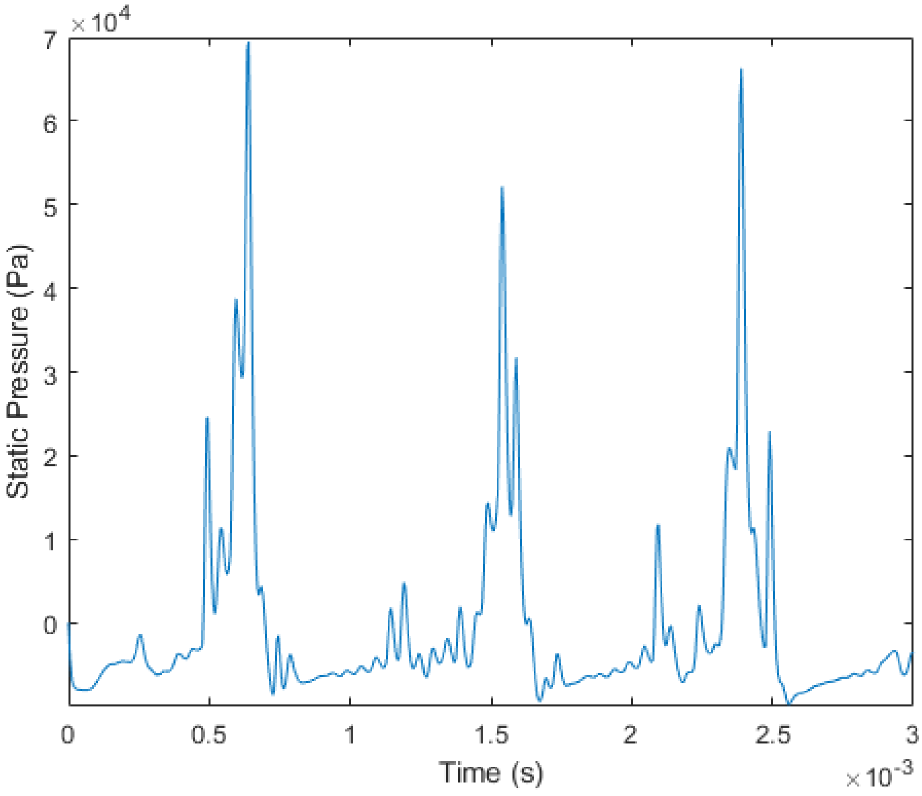

Figure 4.5: Static pressure fluctuation predicted by the Original ZGB model plotted against flowtime at the monitor point.

Given that the pressure peaks do not occur the end of each cycle indicates that the cavitation structure does not entirely collapse at the end of the cycle, instead, it shrinks while retaining its shape. Therefore, this indicates that the large cavity structure is oscillating at its own subharmonic frequency. In other words, the complete collapse of the structure takes place every 4.54 periodic cycles or within approximately 1176 kHz. Another major difference Figure 4.5 highlights is the inability of the original ZGB model to capture micro-scale bubble collapse. This is noted by the minimal oscillations that occur between each pressure peak. Thus, cavitation model modifications are justified to tune the pressure oscillation and its frequency to that of the experimental acoustic cavitation.

4.7.2 Response surface optimization results

In this section, the model constants of the modified ZGB model, namely the evaporation and condensation constants, bubble radius, and nucleation site volume fraction, undergo a series of statistical analysis with the analysis of variance (ANOVA) being the principal model analysis.

The statistical significance of the four factors considered including two-way and three-way interactions were assessed on the basis of their resultant F-statistic and p-values for each response, i.e., maximum pressure and oscillating frequency, as shown in Table 4.4. In this case, a backward elimination stepwise regression analysis was applied to sieve the model from unnecessary predictors, in return, to improve out-of-sample accuracy by yielding a sample size larger than the number of variables. Mainly, the statistical criterion adopted to rule a factor's significance is the 95% confidence level in which the p-values shall be less than <0.05 for a factor, or an interaction, to qualify as significant [137]. In addition, the larger the F-statistic for a source, the safer the assumption of significance.

Table 4.4: ANOVA of Maximum Pressure and Oscillation Frequency Responses for Backward-Stepwise Regression.

		Maximum Pressure, P_{max}					*Oscillation Frequency, F*				
Source	*DF*	*Adj SS*	*Adj MS*	*F-Value*	*P-Value*	*VIF*	*Adj SS*	*Adj MS*	*F-Value*	*P-Value*	*VIF*
Model	*10*	*28.9907*	*2.8991*	*9.87*	*0.010*		*12199231*	*1524904*	*6.88*	*0.010*	
Linear	*4*	*17.7244*	*4.4311*	*15.09*	*0.005*		*8260133*	*2065033*	*9.32*	*0.006*	
A	1	8.9559	8.9559	30.50	0.003	*1.00*	1604795	1604795	7.24	0.031	*1.00*
B	1	0.4114	0.4114	1.40	0.290	*1.00*	1578202	1578202	7.12	0.032	*1.00*
C	1	4.3356	4.3356	14.77	0.012	*1.00*	2454988	2454988	11.07	0.013	*1.00*
D	1	4.0214	4.0214	13.70	0.014	*1.00*	2622149	2622149	11.83	0.011	*1.00*
2-Way Interactions	*5*	*7.8155*	*1.5631*	*5.32*	*0.045*		*3003661*	*1001220*	*4.52*	*0.046*	*1.00*
A x B											
A x C	1	0.1590	0.1590	0.54	0.495	*1.00*					
A x D	1	1.3090	1.3090	4.46	0.088	*1.00*					
B x C	1	2.5385	2.5385	8.65	0.032	*1.00*	901997	901997	4.07	0.083	*1.00*
B x D	1	2.2963	2.2963	7.82	0.038	*1.00*	1312170	1312170	5.92	0.045	*1.00*
C x D	1	1.5127	1.5127	5.15	0.072	*1.00*	789494	789494	3.56	0.101	*1.00*
3-Way Interactions	*1*	*3.4508*	*3.4508*	*11.75*	*0.019*		*935437*	*935437*	*4.22*	*0.079*	
A x B x C											
A x C x D	1	3.4508	3.4508	11.75	0.019	*1.00*					
B x C x D	1					*1.00*	935437	935437	4.22	0.079	*1.00*
Error	5	1.4682	0.2936				1551754	221679			
Total	15	30.4589					13750985				

Table 4.4 tabulates values of sum of square (SS), mean square (MS), F-statistic, and p-statistic for the reduced models of maximum pressure and oscillation frequency. Both SS and MS represent a measure of variation from the mean indicating variation attribution to a specific factor. Thus, this reiterates the degree of significance a factor has over the response. As a result, a cubic multivariant regression model is fitted for the maximum pressure response while a quadratic multivariant regression model has been found appropriate to model the oscillation frequency response where both are statistically significant at a 95% confidence level.

Furthermore, to evaluate the goodness of fit of experimental data into the resultant models, the coefficient of determination, R^2, is used as a statistical indicator for the evaluation. Typically, a value of 0 means that experimental data do not fit the regression line, while a value of 1 indicates otherwise. In the current case, an inference of a strong correlation between experimental and predicted can be safely assumed given that R^2 values were 0.9518 and 0.8872 for the maximum pressure and oscillation frequency respectively. Moreover, the adjusted R^2 values for pressure and frequency show a high value, yet lower than the non-adjusted R^2, of

0.8554 and 0.7582 respectively. This is justified as the adjusted R^2 is corrected to identify the degree of variance in the response explained by the input variables. As such, the indicator provides a more realistic evaluation of goodness-of-fit rather than an optimistic one. However, this noticeable difference may be an indicator that introducing additional terms to the model does not necessarily improve its reliability, let alone its accuracy, by a significant value.

Despite that, one may question the reliability of the regression models due to the usage of a stepwise regression method which typically results in errors, mainly overfitting led by multicollinearity. However, the Variance Inflation Factor (VIF) for all factors appear to be equal to = 1. A value of 1 suggests that there is no correlation between the predictor variables. Meanwhile, a value between $1 < \text{VIF} < 5$ shows moderate correlation but can often be neglected. However, in the case of a value great than > 5, this infers severe correlation between the predictor variables making the p-values generated unreliable.

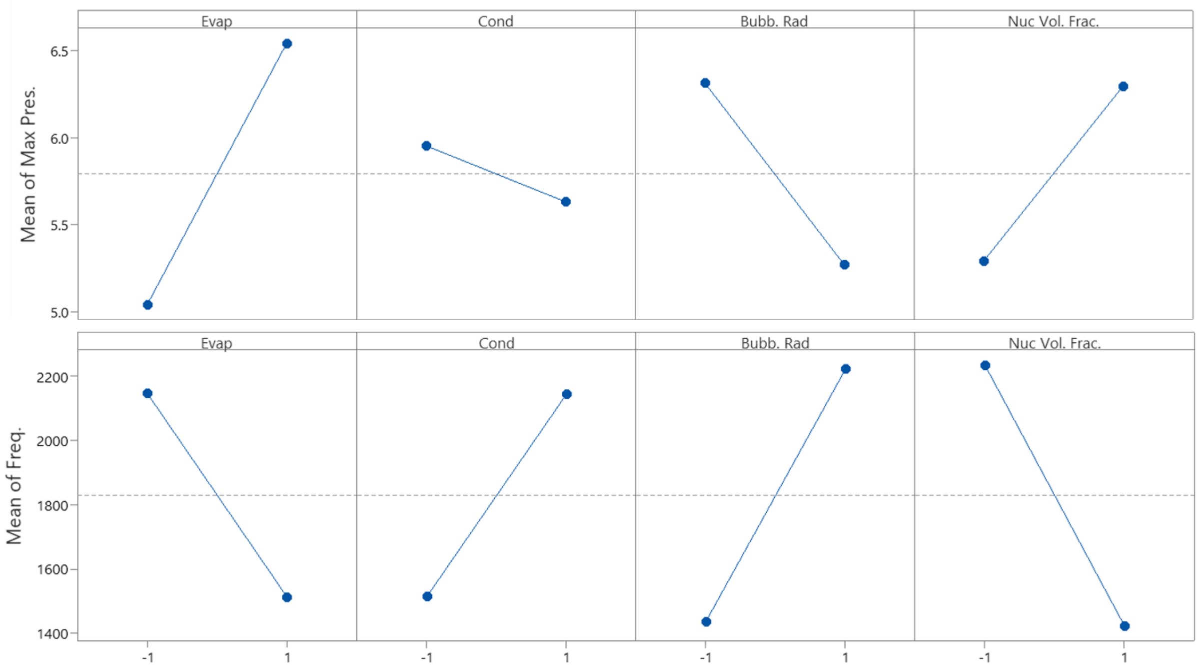

Figure 4.6: Main effect of the four model constants on the response values of pressure peak (Pa) and pressure oscillation frequency (Hz).

4.7.2.1 Analysis of regression predictors' effects on maximum pressure

As per the ANOVA presented in Table 4.4, most of the factors, main effects and interaction effects, are included in the maximum pressure regression model, with the exception of the evaporation-condensation constant (AB) two-way interactions and the evaporation-condensation-bubble (ABC) radius three-way interaction effects. However, while the mentioned interactions were removed due to their complete failure to meets the F-test and P-test, B main effect, evaporation-nucleation site volume fraction (AD), evaporation-bubble radius (AC), and bubble radius-nucleation site volume fraction (CD) two-way interaction effects were included regardless of their inability to meet the same criterion. These exceptions were made on the basis of examining both main effect plots and their respective interaction plots to avoid making any immature interpretations.

Initially, the condensation constant (B) main effect, as per the p-value, appears to be insignificant; meanwhile, its interactions with bubble radius (C) and nucleation sit volume fraction (D) are significant. This is graphically demonstrated in both Figures 4.6 and 4.8 respectively. By observing the main effects alone, Figure 4.6 highlights the change in the maximum pressure peak by changing each variable one at a time while keeping the remaining variables at their lower values as default. The figure reiterates that the evaporation constant (A) has the highest influence relative to the other constants given that the pressure value changes from 5.1 bar to 6.5 bar as the constant is increased from 10 to 50. Meanwhile, B shows its insignificance by demonstrating a small change in pressure from 5.9 to 5.6 bar when decreased from 0.1 to 0.01. Here, this statistical anomaly is further examined by deducing the type of interaction that exists at BC and BD. In this case, there exists a significant antagonistic effect shown in Figure 4.7 for both interactions where any change along either of the factors leads to an interaction in the opposite direction. Graphically, this is highlighted by assigning a light green color to represent the highest achievable value for the maximum pressure peak while dark green represents the lowest value achieved. Moreover, a with twisted surface plots due to its edges' opposing directions. Furthermore, an inference that B is a main effect in the current case is misleading, as it does not show an independent effect, instead of a conditional effect. In other words, the coefficient of B is interpreted as the effect of B when A = 0 where in this case, it is insignificant. Thus, it can be inferred that B may carry larger significance for other values of A, as decomposed by Figure 4.7.

Therefore, to interpret the influence of the condensation constant on the maximum peak, BC and BD are observed. Pressure peak generally intensifies as bubble radius is reduced; however, this effect is more pronounced with the increase of the condensation constant. From a mathematical perspective, the decrease in bubble radius reduces the emphasis of both bubble growth and collapse mass transfers. However, when coupled with an increase in the condensation gain coefficient, this effect is compensated for at the collapse mass transfer. In physical terms, bubbles are limited to grow to a smaller size and pushed to collapse at a higher rate.

On the other hand, the remaining factors A, C, and D retain their main effect status in the model, according to the p-test. This is due to the statistical insignificance of AC, AD, and CD carry. However, as Table 4.4 shows, a three-way interaction ABC is statistically significant inferring that the two-way interactions do exist physically; however, they vary across a third continuous factor, i.e., AC vary significantly along factor D.

In Figure 4.6, main effects A and D are shown to have positive independent effects on the pressure peak while C shares a negative relationship with the pressure peak. Moreover, A shows the most influence on the pressure. The interaction effects of AC, AD, and CD are shown in Figure 4.7. Surprisingly, interaction AC does not show that the bubble radius C shares the same effect it had on the condensation constant B. Instead, it appears to only highlight the main effects of both A and C. Meanwhile, interaction AD emphasizes its significance where maximum pressure is achieved with the increase of both nucleation site volume fraction and the evaporation constant. Physically, this translates to intense cumulative collapses in regions of high bubble density. Lastly, the CD interaction demonstrates its negative interaction in which an increase in nucleation site volume fraction and a decrease in bubble radius leads to a maximum pressure peak. In this case, both mass transfer directions experience an inflated effect, hence, leading to a more intense collapse.

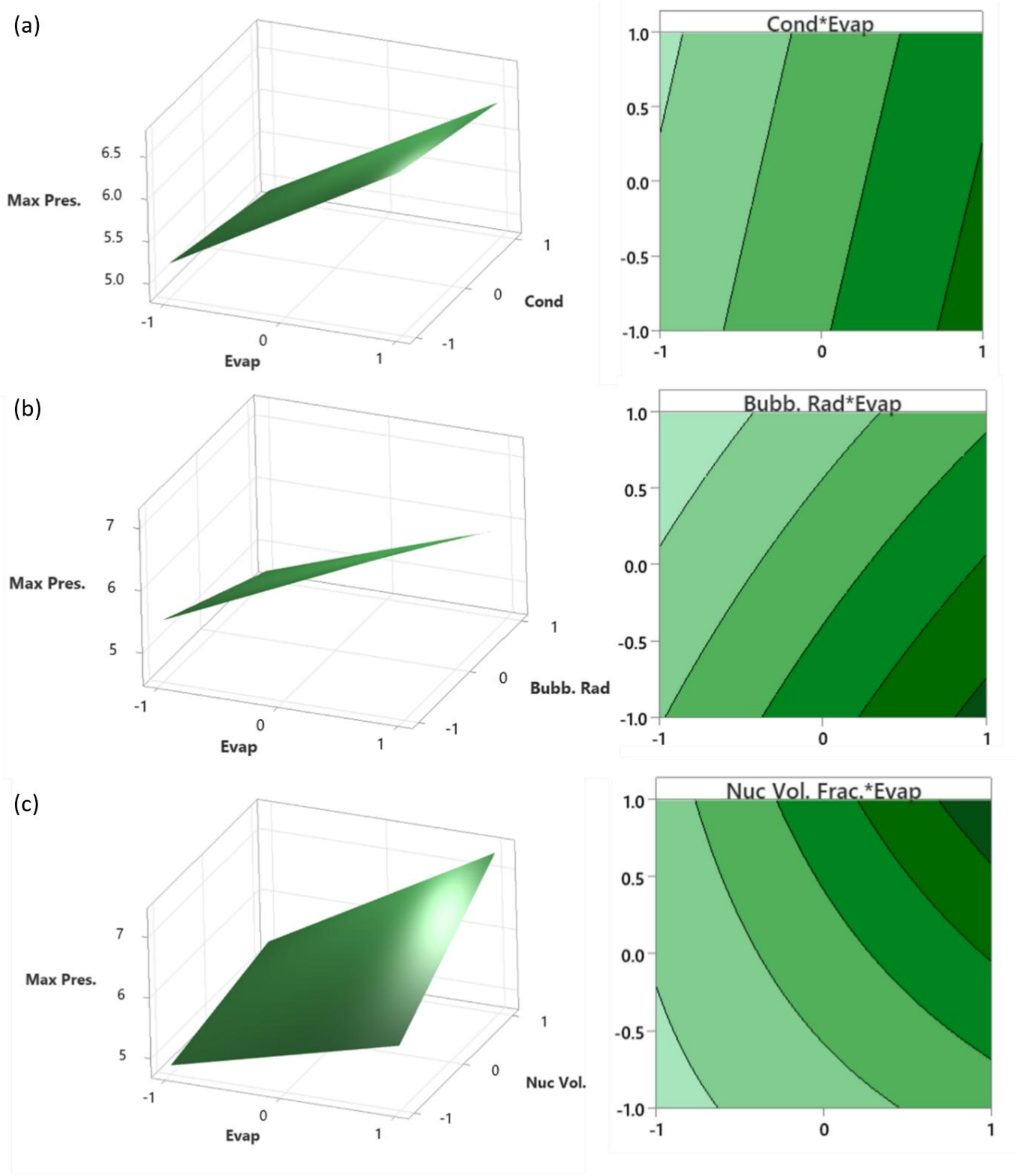
(a)
Max Pres.
6.5
6.0
5.5
5.0
-1
0
1
Evap
Cond
Cond*Evap
1.0
0.5
0.0
-0.5
-1.0
(b)
Max Pres.
7
6
5
Evap
Bubb. Rad
Bubb. Rad*Evap
(c)
Max Pres.
7
6
5
Evap
Nuc Vol.
Nuc Vol. Frac.*Evap

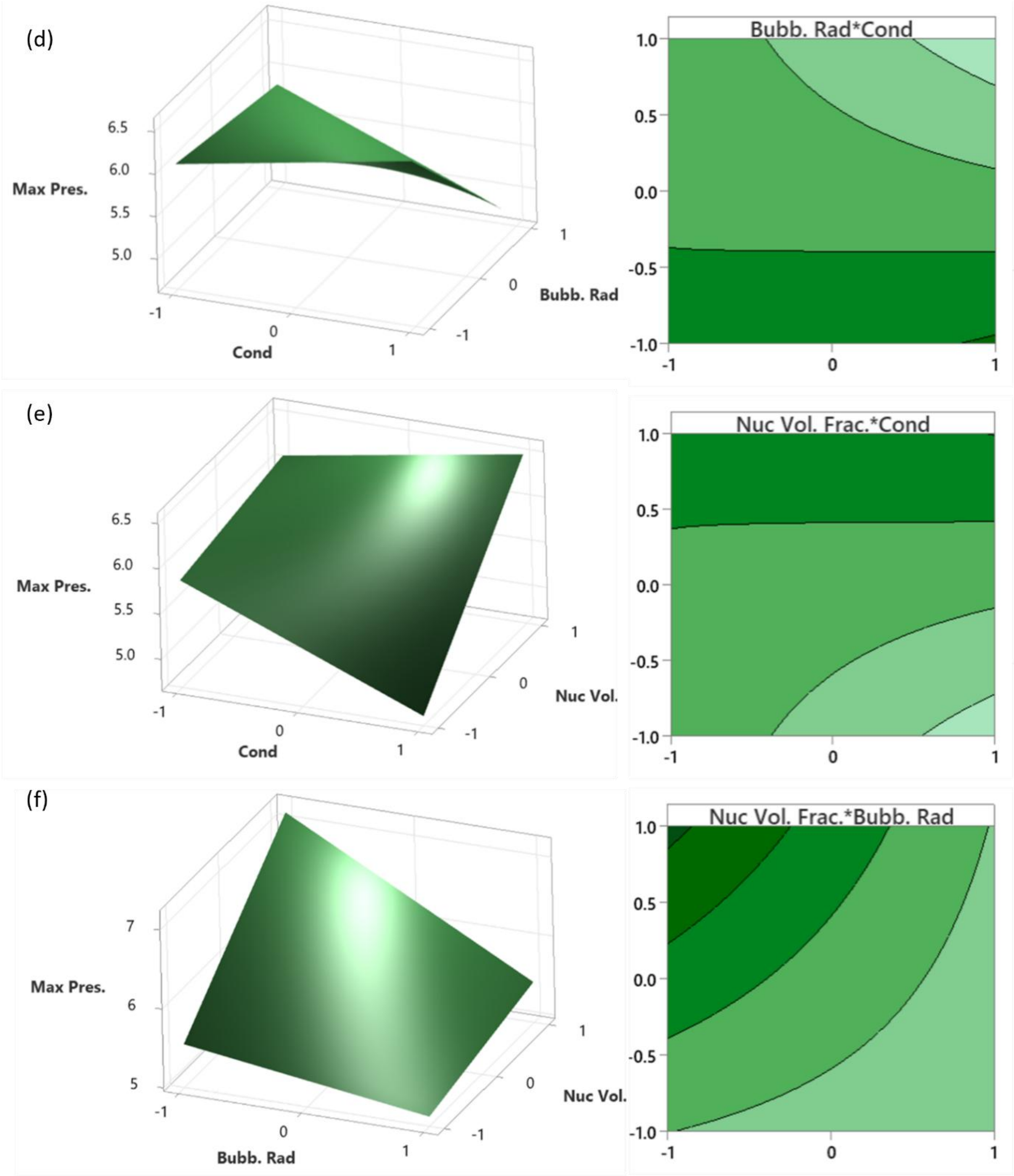

Figure 4.7: Surface and contour plots showing two-way interaction effects between the four model constants on the response values of pressure peak (Pa). The constants' interactions are (a) Condensation - Evaporation (b) Bubble Radius – Evaporation (c) Nucleation Volume Fraction – Evaporation (d)Bubble Radius – Condensation (e) Nucleation Volume Fraction – Condensation (f) Nucleation Volume Fraction – Bubble Radius.

4.7.2.2 Analysis of regression predictors' effect on oscillation frequency

Unlike the maximum pressure regression model, all factors A, B, C, and D can be interpreted as main effects on the frequency response. The evaporation constant A appears to have a negative relationship where any increase leads to a decrease in the oscillation frequency. On the other hand, an increase in the condensation constant, bubble radius, and nucleation site volume fraction lead to an increase in frequency. Figure 4.8 further points out that both main effects C and D share the status of being the most impactful effects on the frequency response.

An analysis of the interaction terms in both Table 4.4 and Figure 4.8 shows that BD shows most significance compared to BC and CD. As Table 4.3 suggested and Figure 4.8 supports, interactions AB, AC, and AD are completely neglected in the regression model. Specifically, this emphasizes that the evaporation constant (A) has no noticeable effect on the frequency responses when any of B, C, or D are changed, and it is indicated by the parallel edges of surface plots.

An additional dissimilarity in the interactions' behavior from pressure peak responses is that there are no significant three-way interaction effects; interaction BCD is shown to be insignificant in Table 4.3. This way, BD is the only interaction that qualifies to remain in the model, while BC and CD are not required, as they are unable to justify the significance of any three-way interaction. The frequency regression model is then a quadratic model with one second-order term, as opposed to the cubic regression model obtained for the maximum pressure response.

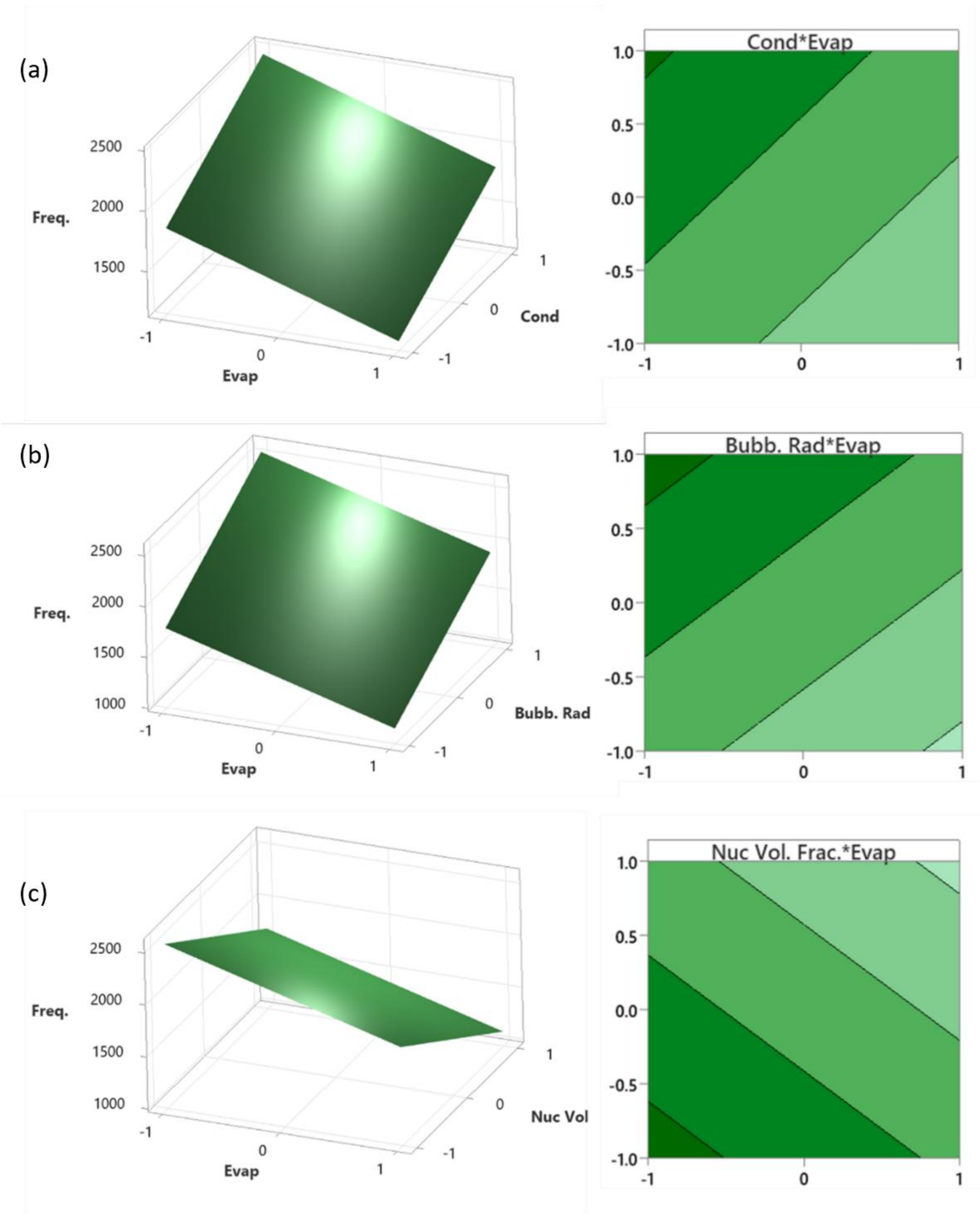

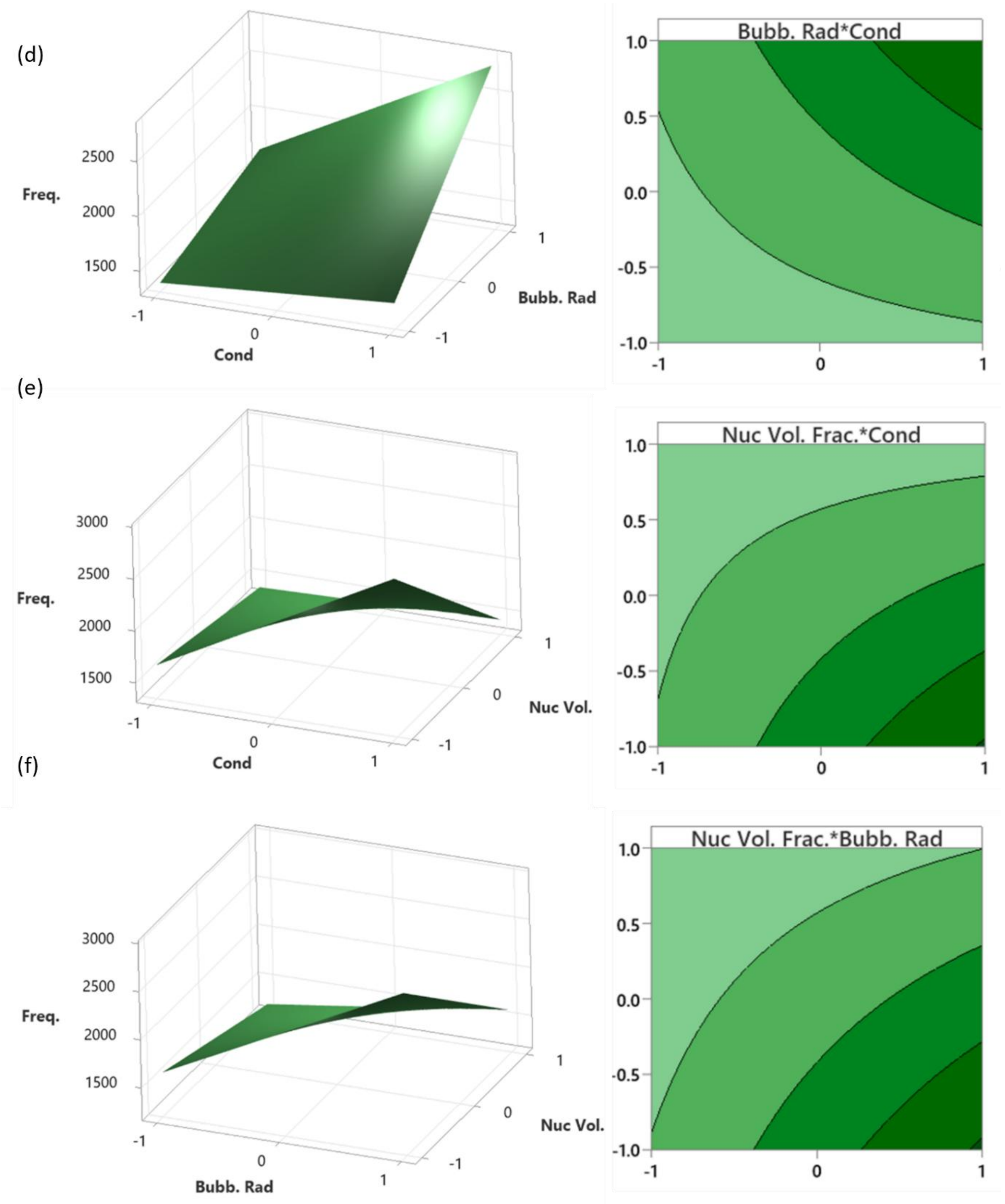

Figure 4.8: Surface and contour plots showing two-way interaction effects between the four model constants on the response values of oscillation frequency (Hz). (a) Condensation - Evaporation (b) Bubble Radius – Evaporation (c) Nucleation Volume Fraction – Evaporation (d)Bubble Radius – Condensation (e) Nucleation Volume Fraction – Condensation (f) Nucleation Volume Fraction – Bubble Radius.

4.7.2.3 Regression model optimization

The regression models obtained only show a cubic and a quadratic relationship that the model constants statistically maintain with the pressure fluctuation peak and its oscillation frequency, respectively. However, in this study, the main objective is to tune the modified cavitation model to enhance its acoustic cavitation predictions. Thus, the optimization criteria set, as presented in Table 4.5, is dissected to acceptable ranges of model constants' lower and upper limits, their weightages, and their importance. The selected targets for both pressure and frequency responses are 3.62 bar and 5058 Hz, respectively`, as they represent the values obtained experimentally by Znidarcic et al. [109]. Moreover, both targets are given the same weight and high importance, indicated by the set value of 1, to the multiple response optimization method.

Table 4.5: Optimization Criteria for Pressure and Frequency Responses

		Limits				
Response	*Goal*	*Lower*	*Target*	*Upper*	*Weight*	*Importance*
Freq. / Hz	Target	4109.090	5058.00	5563.80	1	1
Max Pres. / Bar	Target	3.482	3.62	4.07	1	1

Figure 4.9 and Table 4.6 summarize the selection process of model's optimal values by utilizing the desirability approach. The solutions obtained for each of the evaporation constant, condensation constant, bubble radius, and nucleation site volume fraction were through an input set in Minitab. The interpretation process of the optimal results was simply off their desirability values; those solutions with highest desirability are often chosen as the optimal solution. Thus, Table 4.5 shows the uncoded optimal settings as follows: Factor A = 17.35988, Factor B = 0.1, Factor C = 25 x 10^{-6} m, and Factor D = 5 x 10^{-4}. This setting has achieved responses of 3.62 bar and 4928.73 Hz for pressure and frequency respectively. The maximum desirability achieved by the solution was 88.092%.

Table 4.6: Optimal Solution Achieved by Multiple Response Optimization

						95% CI		*95% PI*	
Factors	*Coded Setting*	*Uncoded Setting*	*Freq. Fit*	*Max Pres. Fit*	*Composite Desirability*	*Press.*	*Freq.*	*Press.*	*Freq.*
A	-0.632006	17.35988	4128.73	3.62	0.880920	(2.599, 4.641)	(3322, 4935)	(2.893, 5.347)	(3754, 5504)
B	1	0.1							
C	1	25 x 10^{-6}							
D	-1	5 x 10^{-4}							

Figure 4.9 below illustrates the consideration of optimized values for each factor by comparing their desirability values and adjusting their settings accordingly. The vertical red lines running through each column represent the optimal level at which the factor is set in to achieve maximum desirability. Perhaps, the factor with the most volatile effect in both the responses is

the evaporation constant. This is highlighted by the visible kink in the desirability graph of the factor; any increase in the evaporation factor will skew both pressure and frequency responses away from 3.62 bar and 5058 Hz target values respectively. Meanwhile, the remaining factors were comfortably set at either low or high value ends signified by their linear desirability relationship.

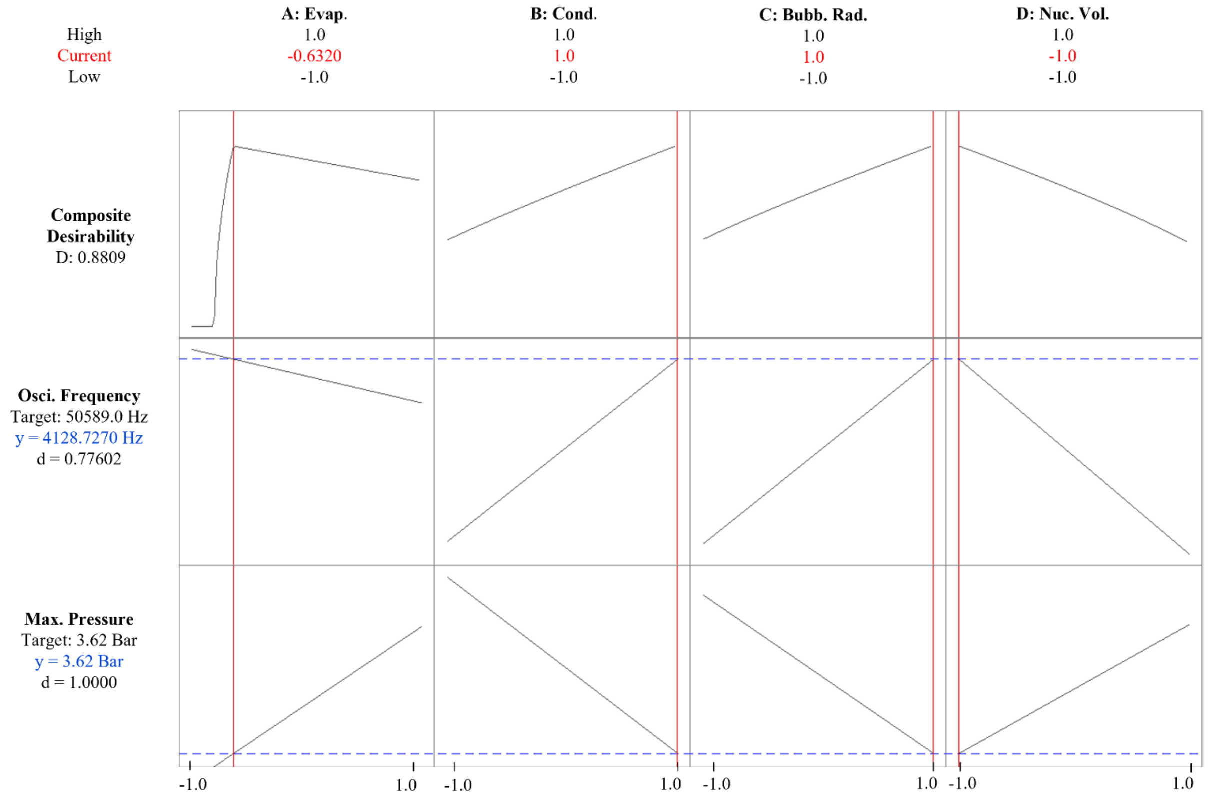

Figure 4.9: Desirability and main factor effect plots for pressure and frequency responses highlighting the optimal settings for highest desirability.

4.7.2.4 Monte Carlo sensitivity analysis

While it is true that the desirability approach resulted in two optimized regression models, insight on the induced scatter on the response values due to uncertainty in the governing model constants is lacking. With the ANOVA study revealing the extent of control the empirical constants have over the model's predictive performance of acoustic cavitation properties, exploring the sensitivity of results to any variation in the empirical constants become crucial. Therefore, a series of Monte Carlo simulations is implemented to identify the random input of model constants that contribute the most to the random scatter of pressure and frequency response values. This approach was setup and performed in a MATLAB environment. The number of iterations used for the simulations is 7000 iterations, as suggested by Figures 4.3a and 4.3b. The simulations were setup by setting the two regression models as the simulation objectives and assuming a ± 10% randomness in each model constant to study the response sensitivity to input uncertainty. The uncertainty value is assumed based on the range of values commonly used in literature [138-140]. This way, a uniform distribution was deliberately chosen for the model constants' values, as the true probabilistic distribution of their values is not available. The aim of the analysis is to perform a non-informative sensitivity assessment that would identify dominant parameters affecting the collapse pressure and cavitation lifecycle frequency.

Table 4.7 summarizes important statistical properties the response variables showed during the Monte Carlo simulations. One of the parameters highlighted is the mean for both responses. Interestingly, the mean values demonstrate a strong agreement with the deterministic values achieved during optimization. The maximum pressure is of particular interest, as its standard deviation indicate that response values are retain low variance and are closely distributed around about the mean. Meanwhile, this cannot be said about the oscillation frequency response, since its standard deviation shows relatively larger variance. Nevertheless, the near-zero skewness values highlight that the random response variables are not skewed to either side of the mean. Moreover, kurtosis values of less than < 3 show that the response values examine a platykurtic distribution, which typically describes a distribution with a lower likelihood of achieving response mean values compared to a normal distribution. While this is statistically true, kurtosis values are also considerably close to 3, and hence, ultimately, it is more reasonable to consider the response values well-modelled with a normal distribution. This is reiterated in the corresponding histograms shown in Figure 4.10.

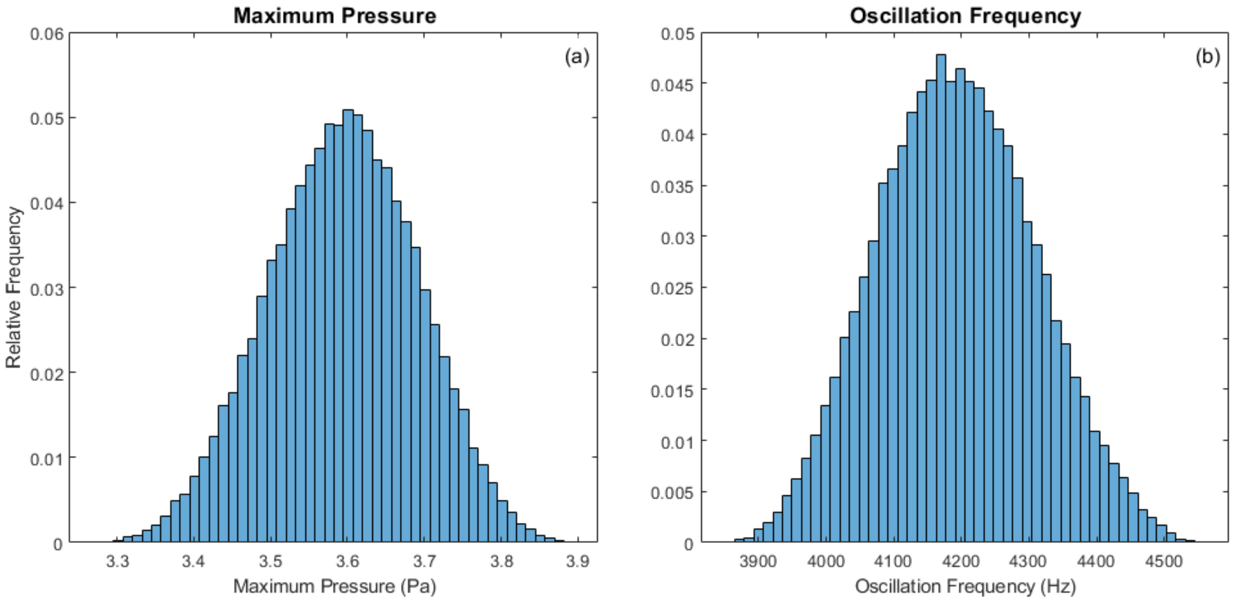

Figure 4.10: Histograms of output random responses of (a) Maximum pressure (b) Oscillation frequency considering a ± 10% uncertainty in all four model constants.

Table 4.7: Statistical Properties of Random Response Variables

Response Name	*Unit*	*Mean*	*St. Deviation*	*Skewness*	*Kurtosis*	*Min.*	*Max.*
Maximum Pressure	Bar	3.5941	0.096111	-0.069492	2.693	3.295	3.883
Oscillation Frequency	Hz	4193.0288	115.285	0.084987	2.631	3864.2	4545.8

A sensitivity analysis is then performed to find reason for the obscure trends presented in the Monte Carlo simulation and to identify the factor with the greatest influence on the response output. Figure 4.11 draws a sensitivity plot that shows percent contributions of each random input factor to the uncertainty of random output responses. For instance, Figure 4.11a considers the maximum pressure response in which it uncovers that randomness in all four factors generally share equal responsibility for the scatter in the pressure response. The condensation constant seems to have the most influence. This can reasonably be attributed to the fact that cavitation collapse intensity equally depends on the cavitation region and bubble size, and the rate of their collapse that generates the spike in pressure. On the other hand, this trend is not reiterated in the Oscillation Frequency sensitivity plot. Figure 4.11b highlights that the main contributors to output randomness are the nucleation site volume fraction, bubble radius, and condensation constant. Meanwhile, the evaporation constant contributes only 8% of frequency response randomness. Interestingly, this occurrence can be attributed to the dependence of the oscillation frequency primarily to the rate of cavitation collapse.

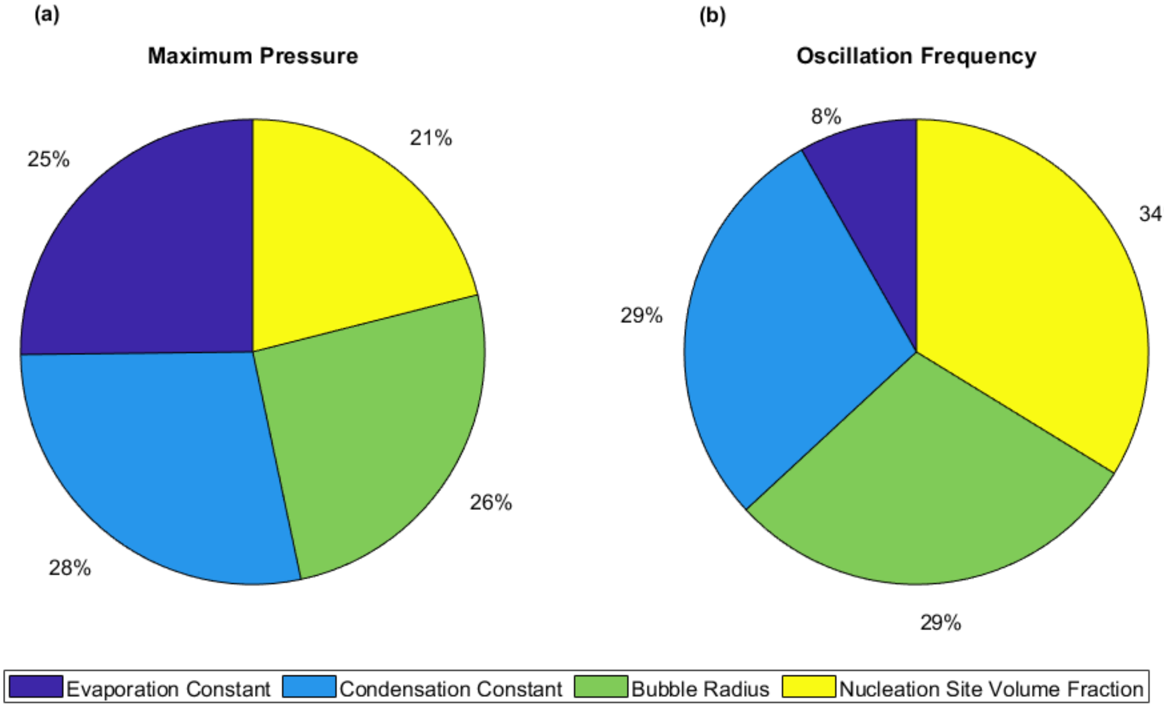

Figure 4.11: Desirability and main factor effect plots for pressure and frequency responses highlighting the optimal settings for highest desirability.

Table 4.8: Correlation Coefficient Matrix between Input Factors and Response Values.

Response Name	*Evap.*	*Cond.*	*Bubb. Rad.*	*Nuc. Site Vol. Frac.*
Maximum Pressure	0.4980	0.5568	0.5065	0.4162
Oscillation Frequency	0.1525	0.5302	0.5439	0.6248

Moreover, Table 4.8 provides the correlation matrix between input factors and output responses. Generally, a correlation coefficient equal to one defines a perfectly correlated relationship between the input and output; however, a zero represents the lack of a statistical correlation. In that sense, the matrix reiterates the information shown in Figure 4.11 by showing that correlation coefficients for nucleation site volume fraction are lowest for maximum pressure response and lowest for the oscillation frequency.

4.7.2.5 Numerical validation of the modified ZGB model with the response surface optimized parameters

With the completion and optimization of the modified ZGB cavitation model, the model has to undergo validation against physical experiments to ensure that the statistically obtained model, with its optimized model constants, does in fact achieve the predicted acoustic cavitation performance. The reader is referred to Appendix A for the source code of the optimized cavitation model. In this section, the new model was implemented into the ANSYS FLUENT numerical setup described in Section 4.4 and prepared for validation against Znidarcic et al. [109] Case A experiment setup. The new model's performance in acoustic cavitation modelling is assessed based on its ability to predict acoustic cavitation structures and pressure oscillations of amplitude and frequency agreeable to that measured during the experiment.

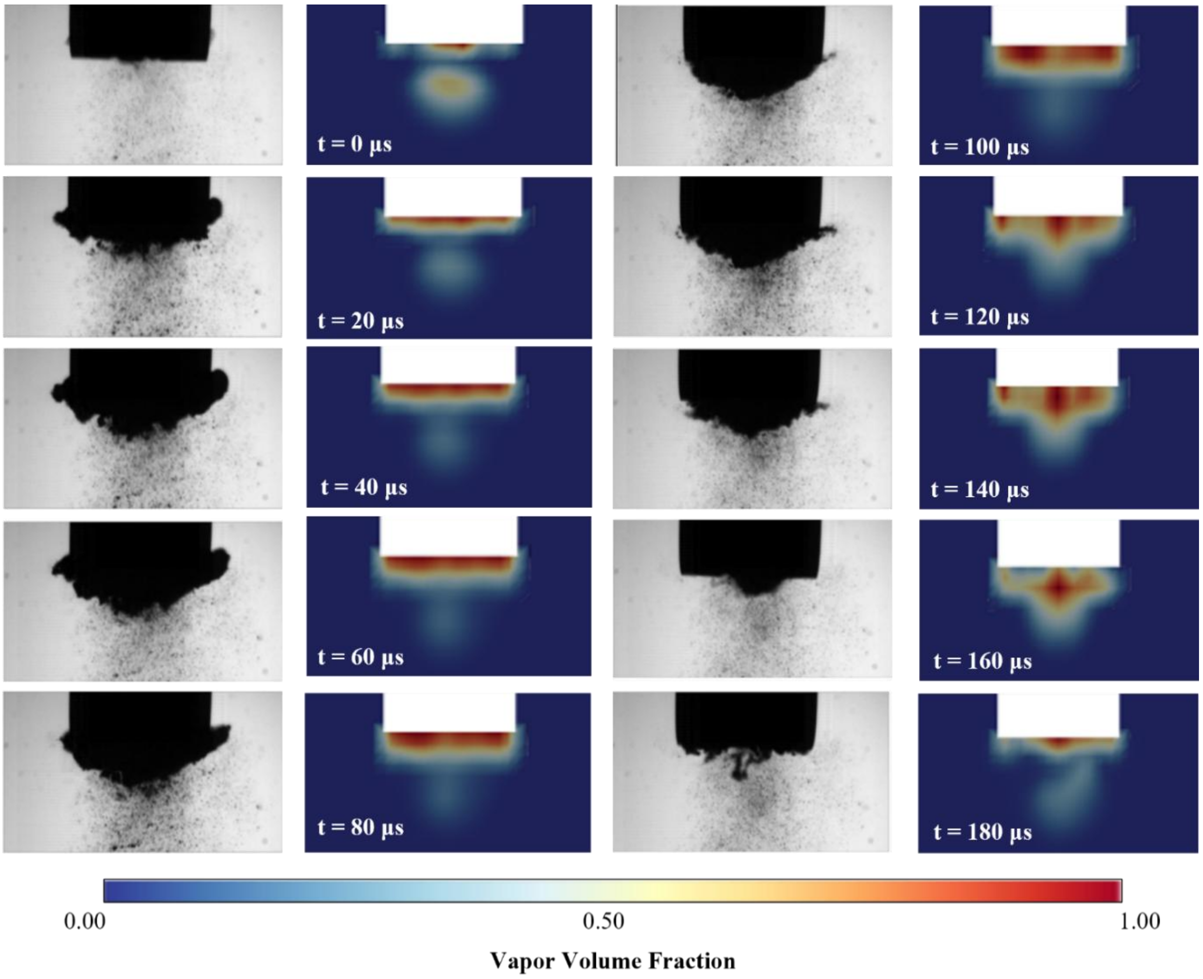

Figure 4.12: Comparative illustration of instantaneous cavitation structures observed experimentally [109] and predicted by the modified ZGB model numerical setup at coinciding time steps.

Figure 4.12 shows snapped grey-scaled pictures of acoustic cavitations structures observed experimentally with vapor volume fraction contour plots. When comparing Figure 4.12 to Figure 4.4, a clear contrast in the cavitation structure and its evolution becomes noticeable. Firstly, the contour plots, in Figure 4.12, show an underprediction in the early mushroom-shaped cavitation region, and instead, it predicts a thick flat sheet of cavitation engulfing the horn tip at t = 0 – 80 µs. However, it predicts the late conical shaped attached cavitation transformation shown at t = 100 – 140 µs followed by its collapse at t = 160 – 180 µs. In addition, the model no longer assumes complete symmetry of cavitation region and is able to predict the existing asymmetries of attached cavitation. Perhaps, this can be linked to the decrease in the model's evaporation constant which in turn limited the rate of cavitation growth. Interestingly, with the new model, the simulation could predict the presence of downstream cloud cavitation micro-structures under the horn tip throughout the entire expansion-collapse cycle. As illustrated, cloud cavitation shows an inverse relationship with attached cavitation. As the attached cavitation enters its expansion phase, cloud cavitation slowly begins to collapse. Meanwhile, it begins to regrow during the attached cavitation collapse phase eventually leading to complete detachment. Ultimately, the new model qualitatively shows excellent performance in modelling acoustic cavitation.

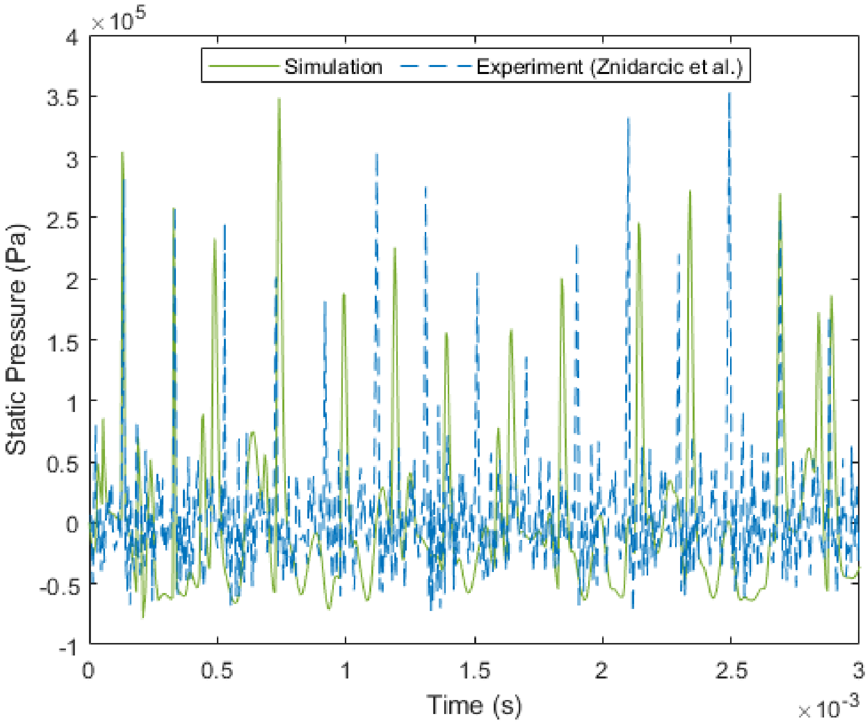

Figure 4.13: Comparative illustration of instantaneous cavitation structures observed experimentally [109] and predicted by the modified ZGB model numerical setup at coinciding time steps.

However, to assess the new model quantitively, Figure 4.13 plots the pressure fluctuation captured in both the experiment and the simulation. As illustrated, there is a strong agreement between the simulation and the experiment, as the new model is now capable of capturing microscale acoustic bubbles, frequent, small oscillations can be seen between one peak and the other. Furthermore, the pressure peaks resemble attached cavitation collapse marking the end of each expansion-collapse cycle. These peaks appear to be overlapping pressure peaks observed in the experiment at times, while mostly appearing slightly delayed. Moreover, another model prediction inaccuracy can be seen at time t = 2.49 s where the pressure peak is underpredicted. By looking at the proceeding peaks, it is clearly shown that they are overpredicted instead. This phenomenon can be attributed to a mode of cavitation described by Qin et al. [79] as inertial cavitation where the cavitation in a single cycle does not collapse at its critical size, instead, it grows to a new critical size before it violently collapses. A comparative summary of pressure fluctuation predictions is provided in Figure 4.14 where both the maximum pressure attained, and the mean oscillation frequency of both the simulations and the experiment are plotted.

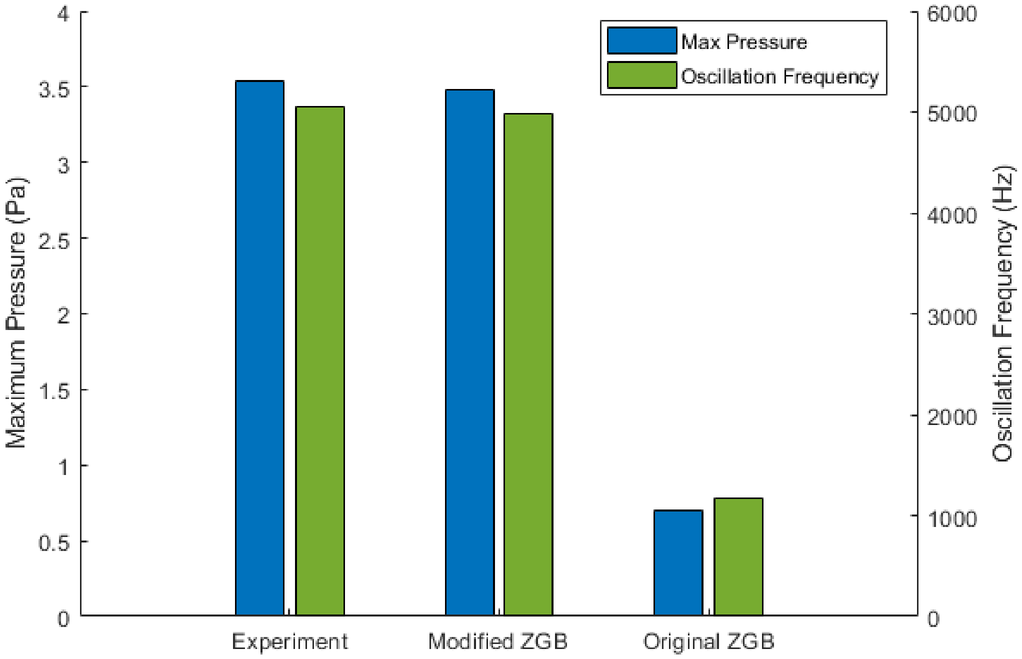

Figure 4.14: Bar diagrams of experimentally measured and numerically predicted, using both the original and modified ZGB cavitation model, maximum pressure amplitude and mean oscillation frequency.

The figure further emphasizes the strong agreement between the modified ZGB model's results and the experimental results. While the experiment attains a maximum pressure of 3.54 bar and a mean subharmonic frequency of 5058 Hz, the modified ZGB model achieves a maximum pressure and a mean frequency of 3.48 bar and 4894.56 Hz respectively. As for the original model, the figure quantifies its inaccurate predictions of acoustic cavitation where it assumes 0.70 bar and 1176.47 Hz for the pressure peak and the mean oscillation frequency respectively. Lastly, the values generated by the modified ZGB model validates the predicted values provided by the response optimization of the pressure and frequency regression models. The response optimization concluded that with the suggested model constants, the modified ZGB model will output 3.62 bar and 4128.72 Hz. As predicted, the modified ZGB model generated values considerably close to the statistically predicted values with the pressure response being closer than the frequency response. Perhaps, this could be attributed to the omitting of many two-way and three-way interaction terms which, in turn, resulted in the neglection of important terms and in an oversimplified model. However, the values remain satisfactory and show a similar correct trend.

4.8 Conclusion

In the presented investigation, inaccuracies of current cavitation models, specifically the ZGB model, in predicting acoustically induced attached cavitation. Results from Znidarcic et al.'s experimental investigation [109] were used to evaluate the numerical results achieved by the original ZGB cavitation model implemented in a numerical setup that captured the experimental setup used. The model was incapable of accurately capturing primary features that included attached cavity structural formations, downstream cloud cavitation regions, pressure pulse amplitudes and cavity oscillation frequency. To resolve these problems, mathematical manipulations suggested by Znidarcic et al. [109] were applied on the original ZGB model. Furthermore, a statistical Design of Experiment approach, coupled with the Monte Carlo method, was adopted to scrutinize and optimize the model constants to improve the model's acoustic cavitation prediction performance. The optimized model constants were later validated against the experimental results. The following conclusions were drawn from the study:

- The stepwise regression uncovered that all four model constants are in fact significant to both maximum pressure and oscillation frequency responses. However, the condensation constant did not appear statistically significant for the pressure response, but it later showed hierarchal importance due to its two-way interaction significance.
- Response optimization, using the desirability approach, of the two regression models suggested that model constants of 17.35988, 0.1, 25 x 10^{-6} m, and 5 x 10^{-4} for the evaporation constant, condensation constant, bubble radius, and nucleation sit volume fraction, respectively, will achieve a maximum pressure value of 3.62 bar and an oscillation frequency of 4128.73 Hz. The optimization desirability $d = 0.88$ attained is considered satisfactory.
- Investigative Monte Carlo simulations on the optimized regression models summarized the sensitivity of each model from a 10% random variation in the four model constants. It illustrated that the pressure response was approximately equally influenced by any randomness present in all four model constants. Meanwhile, the frequency response scatter was mainly affected by uncertainty in the nucleation site volume fraction constant showing 34% correlation. The condensation constant and the bubble radius equally contributed 29% to the frequency response randomness, while the evaporation constant had a minimal contribution of 8%.
- Validation of the modified ZGB model showed that with the statistically optimized model constants, the cavitation model predicted 3.48 bar and 4894.56 Hz for the pressure peak and mean oscillation frequency, respectively. These values showed strong agreement with the experimental values and further emphasized the accuracy of the statistical model optimization. Nevertheless, it is crucial to acknowledge that the model was only developed and optimized for reactor configurations operating within the 20 kHz range, therefore, additional validation is required to assess its performance in higher operation frequency ranges.

The next stage of the project consists of developing a numerical model of the hydrodynamic reactor for a series of setup validations. This is then followed by a modified numerical model of the reactor where an ultrasonic horn is introduced, and the acoustic cavitation model is implemented.

5 Influence of Toroidal Vortex Dynamics on Acoustic Cavitation Development under Different Ultrasonic Horn Tip Vibration Modes

5.1 Introduction

With the validation of the complete numerical configuration and model of the horn-type reactor, this chapter delves into what was extensively discussed in Chapter 2, as many investigators have attempted to strategize improving the horn's sonochemical efficiency through a series of parametric analyses that explore underlying relationships between cavitation development, sonication media, operational conditions, and transducer geometries [144-146]. With further reading of literature, however, it has been notably interesting that each investigation conducted has implemented its own transducer operating conditions, such as input power, horn tip diameter, and tip amplitude. Moreover, it has been revealed that there is noticeable inconsistency in the numerical modelling of ultrasonic horn's vibration, where some studies consider the entire horn structure to oscillate at a frequency of 20 kHz and above, while others assume an isolated oscillation performed by the horn tip surface submerged in the fluid. It has been noted that the choice of vibration model varies vastly with the ultrasonic horn geometry, specifically, the horn tip diameter. A sample of recent studies has been tabulated and categorized in Table 5.1 to summarize this trend.

Table 5.1: Ultrasonic transducer operating conditions previously used in experimental studies to explore developed cavitation behaviors.

Authors	*Size Category*	*Input Power, W*	*Horn Tip Amplitude, μm*	*Horn Tip Diameter, mm*
Žnidarčič et al. [128]	Small Horns	7 – 70	68 – 212	3
Kozmus et al. [144]		-	135 – 270	3 – 4.8
Petkovsek et al. [147]		150 – 300	130 – 270	4.8
Patil et al. [148]	Mid-ranged Horns	100	-	13
Fattahi et al. [149]		24.7 – 87.15	-	13
Tzanakis et al [68]	Large Horns	78 – 230	8.5 – 17	40

Typically, this myriad of horn properties is primarily driven by the cavitation performance required for a specific ultrasonic-assisted task, such as process intensifications and rheological manipulations [150, 151]. In terms of acoustic cavitation, its performance is both qualified and quantified by assessing the cavity structures produced at the horn's proximity and the pressure/volume fluctuations generated, respectively. Many studies have adopted the route of numerical methodologies, as they can facilitate the instantaneous capturing of such data. A thought-provoking trend noticeable in previous studies is that those considering a small tip diameter tend to assume a uniform sinusoidal vibration model for the oscillating tip 'wall' [128, 152]. Meanwhile, studies considering notably larger diameters lean towards adopting a classical thin-plate vibration theory to model the sinusoidal motion [104, 148]. The simple uniform sinusoidal motion is typically modelled as a smoothly cyclical variance based on the sine function. On the other hand, those that adopt the classical elasticity equations generally attempt to simplify their boundary value problem by essentially implementing the Gurtin-Murdoch theory [153]. Moreover, this has been extrapolated to simplify the boundary problem using Kirchhoff's plate theory [154].

This begs the question, what is the reason behind this modelling habit, why has it been subliminally deemed that the uniform vibration model is unfit for larger tip diameters, and why has the thin-plate vibration models not been adopted in smaller diameters?

Therefore, a numerical investigation has been commenced to compare the performances of two recurring mathematical vibration modelling methods in the literature, namely the 'uniform sinusoidal vibration model' and the 'Kirchhoff-based vibration model'. With the use of a validated numerical setup of acoustic cavitation, the two vibration models were implemented as horn wall boundary conditions in that setup through the use of user-defined functions (UDFs) that define the special cases of dynamic meshing. Moreover, as a way to further examine the potentially underlying relationship between the vibration model performance and the horn tip diameter, the study takes into consideration two horn diameters, a 3 mm and a 12 mm horn tip diameter. The methodology implemented for this investigation carried forward from the previously discussed numerical configuration in Chapters 3 and 4.

5.2 Horn Tip Vibration Models

In this study, the two horn tip vibration models described in Chapter 2.5 were implemented for a comparative numerical analysis on the same validated domain created in Chapter 4.5. The general mode of implementation of the two models was simply through drafting and compiling a user defined function (UDF) source code and importing it into ANSYS Fluent 23R2 [54] as a moving wall boundary condition assigned to the horn tip boundary. However, the type of boundary condition slightly differs between the two vibration models.

To reiterate, the simple sinusoidal motion simply defines the sinusoidal movement of the entire boundary wall by moving its nodes, as defined in Eq. 2.36, which translates to a uniform motion of all the nodes along the horn tip boundary in both of negative and positive displacements. Therefore, the UDF enforces an automated dynamic meshing of the proximal grid elements to ensure that no extreme defeaturing, such as drastic increase and drop in skewness and aspect ratio of the elements respectively, occurs during the movement of the horn tip.

On the other hand, the Kirchhoff-based vibration model is slightly different. As stated in Eq. 2.57, each segment of the horn tip boundary experiences a different magnitude of force, and thus displacement. Therefore, the programming logic adopted here is to assign a unique displacement value for each of the nodes lying about the horn tip, where the maximum displacement is assigned to the node at the horn's axis and zero displacement at the horn's maximum radius. Nevertheless, the displacement direction of all nodes remains unified.

With that said, both vibration models adopted consider the same displacement amplitude of 164 μm. The full source codes can be found in Appendix B and Appendix C for the simple sinusoidal vibration model and the Kirchhoff-based vibration model, respectively.

5.3 Analysis Methodology and Results Discussion

5.3.1 Front Fourier Transform Analysis of the 3 mm Horn Tip

We began the investigation by closely monitoring the pressure and vapor volume signals recorded by the monitor point and within the fluid domain, respectively. This way, a quantitative distinction between key quasiperiodic features of both signals is drawn out.

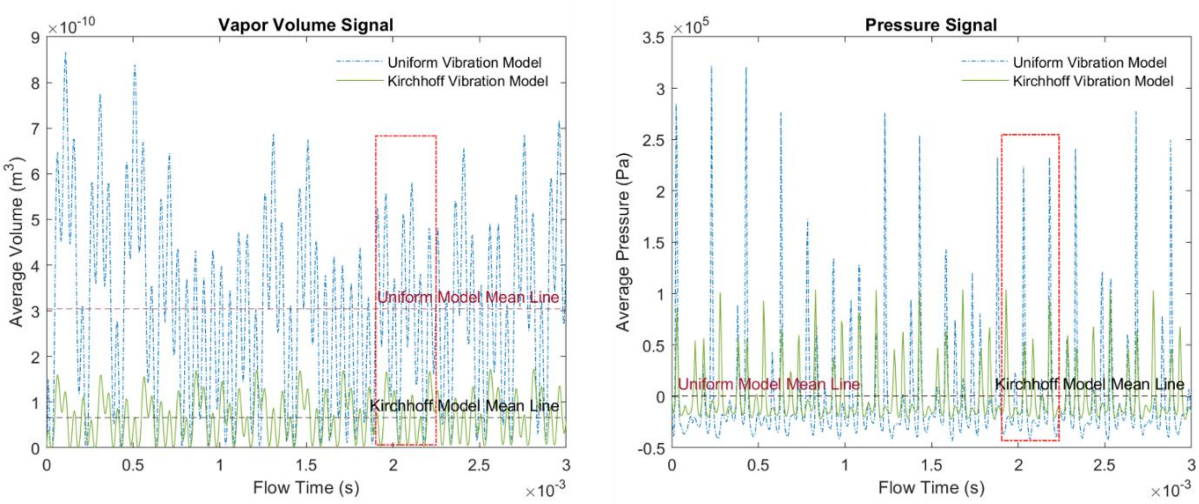

Figure 5.1: Vapor volume signals (left) and pressure signals (right) resulting from uniform and Kirchhoff model-coupled 3mm horn tip boundaries. Red boxes highlight a signal segment showing the frequency offset between the two predicted signals.

Figure 5.1 illustrates pressure and vapor volume signals obtained from numerical models of the 3 mm tip implementing both uniform and Kirchhoff-based models. Here, the numerical model coupled with the uniform model has been validated in a previous study [110] and taken as the correct solution, and the reader is referred to Section 4 for the validation encompassing this model. There exists a significant difference in the predicting powers of the uniform and the Kirchhoff-coupled numerical models. The implementation of the Kirchhoff model has led to a severe underprediction of both the pressure and vapor volume amplitudes. Mean lines were drawn to emphasize this difference in which the differences in the vapor volume and the pressure signal means are $2.38457 \times 10^{-10}\ m^3$ and 445.32 Pa, respectively. However, to give meaning to these values, it is crucial to acknowledge the meaning of the amplitudes. A pressure peak suggests a major collapse in the cavity's structure, while a vapor volume peak suggests maximum growth in this cavity structure, which generally occurs before its sudden collapse [155,156]. Cavitation does not appear to expand with the Kirchhoff model in comparison with the cavitation produced under the uniform model. Therefore, this justifies why the pressure spike produced by the collapse is not equivalent to the uniform model.

To derive further insight, a Front Fourier Transform (FFT) was performed on the two signals produced by each of the vibration models to accurately isolate and quantify the low characteristic frequencies of the signals, which is illustrated in Figure 5.2. Initially, the figure highlights the frequencies of the decomposed pressure and volume signals, where multiple spikes can be observed. Each spike refers to a frequency found in the signal that are categorically either low or high frequencies. In the present analysis, the high frequencies are considered as sub-oscillation frequencies that represent the frequent minor collapses of cavitation during its growth stage. Thus, only the low frequencies are sought out to extract the main oscillation frequency. Figures 5.2a and 5.2b highlight the lowest frequencies of the respective vapor volume signals where the signal obtained from the uniform vibration model is 4991.68 Hz. However, the Kirchhoff model presents a rather unorthodox trend where there exist two distinct low oscillation frequencies, 3660.57 Hz and 7986.69 Hz. To sieve the frequencies into a single characteristic frequency, FFT has been performed on the pressure signals to identify the shared low frequency. As Figs. 4c and 4d demonstrate, the same low frequency of 4991.68 Hz has been obtained in the uniform model's pressure signal; moreover, the frequency of 7986.92 Hz has been captured which validates the same frequency obtained in the model's vapor volume signal.

Building on the established fact that the Kirchhoff model underpredicts the amplitudes of both pressure and vapor volume, it seems that there is an inverse trend regarding the frequency of their oscillation. As such, the Kirchhoff model overpredicts the cavitation cycle frequency hinting at a series of short-lived cavities under the horn. It can only be suspected that the plate mode shape-inspired vibration model, represented by Eq. 2.57, has an underlying influence on the flow structures around the tip that may cause this fast-paced disintegration of the cavities under the horn. Therefore, a qualitative analysis may provide supplementary insight on the said flow structures. Going back to Figure 5.1, one can notice a few recurring trends between the uniform and Kirchhoff model signals, such as offset peaks and, surprisingly, occasional overlapping peaks. These trends can be found in the sample highlighted in the red box.

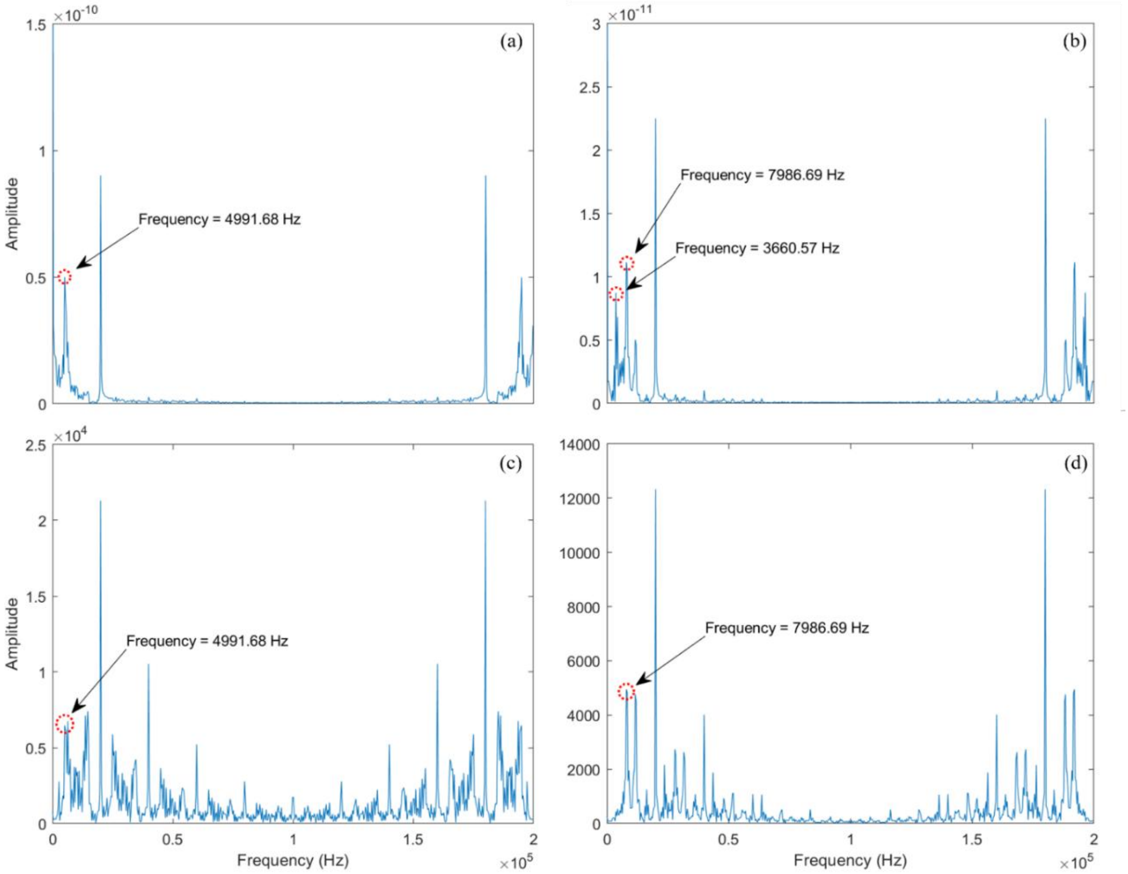

Figure 5.2: FFT plots of pressure and vapor volume signals obtained from the two numerical simulations where (a) represents the vapor volume signal (uniform model) (b) vapor volume (Kirchhoff model) (c) pressure signal (uniform model) and (d) pressure signal (Kirchhoff model).

5.3.2 Finite Time Lyapunov Exponent Lagrangian Analysis

The finite time Lyapunov exponent fields were calculated on MATLAB, which can be found in Appendix D, to materialize hyperbolic manifolds of particle trajectories $\boldsymbol{x}(t)$ to define the resulting proximal Lagrangian coherent structures (LCS) induced by the oscillatory motion of the ultrasonic horn in the fluid domain [157]. This was performed by importing velocity fields $\boldsymbol{u}$ calculated in ANSYS Fluent into MATLAB for a sequence of integrations that result in the creation of the particle flow map Φ_0^T, and the eventual mapping of the FTLE contours. The computational steps involved in calculating FTLE typically start with the creation of a grid of particles, $X_0 \subset \mathbb{R}^n$, is initialized over a selected subdomain from the primary fluid domain created in section 2.1. The particles are then integrated along the flow from an initial time 0 s to a final time T, in which Φ_0^T is then defined as:

$$\Phi_0^T: \mathbb{R}^n \to \mathbb{R}^n, \qquad x(0) \longmapsto x(0) + \int_0^T \boldsymbol{u}(x(\tau), \tau) d\tau \tag{5.1}$$

Here, τ is the instantaneous integration time. The next step is to differentiate the Jacobian flow map to compute the Cauchy-Green deformation tensor defined as follows:

$$\Delta = (D\Phi_0^T)^{Tr} D\Phi_0^T \tag{5.2}$$

In this equation, the transpose operation is denoted with Tr to not confuse with the final time T. Lastly, the eigenvalue λ is calculated and filtered to obtain its largest value λ_{max}. The maximum eigenvalue is then used as input to obtain the respective FTLE field as such:

$$\sigma(\Phi_0^T; x_0) = \frac{1}{|T|} \log \sqrt{\lambda_{max}\big(\Delta(x_0)\big)} \tag{5.3}$$

In the given exploration, the subdomain selected for the Lagrangian analysis is a 5×5 mm region under the horn where a grid of particles with a grid spacing of $\Delta x = 25\ \mu m$ is initialized into the subdomain, as shown in Figure 5.3. The particle advections were computed using a fixed timestep equivalent to 5 μs and the fourth order Runge-Kutta scheme.

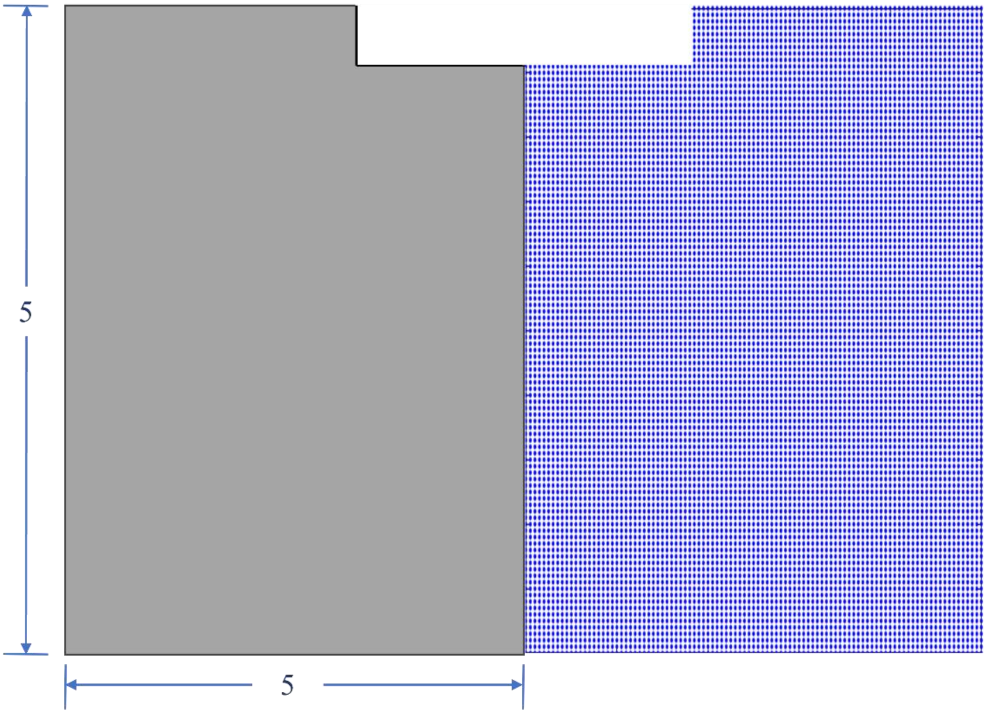

Figure 5.3: A dimensioned sketch of the chosen subdomain (left) and particle grid (right) showing that the size of the selected subdomain and its respective particle grid is 5 x 5 mm.

To analyse vectors and contours of the flow velocity, Finite-Time Lyapunov Exponent (FTLE) has been used to compute the backward integration of these flows at their instantaneous flow times to examine Lagrangian Coherent Structures (LCS) and resolve the spatial locations of temporal vortex boundaries. The grid resolution implemented for the FTLE was 25 µm. By matching the diagrams, in Figures 5.4 and 5.5, corresponding to the pressure peaks and troughs observed in Figure 5.1, the difference between the two models in the cavity structural development becomes obvious.

Essentially, this difference is highlighted in the cavity growth and collapse cycles predicted by both models. In Figures 5.4b and Fig 5.5a, the difference in the collapse cycles is introduced as a single-stage collapse predicted by the uniform-based model against a two-staged collapse in the Kirchhoff-based model at t = 0.00193 s. In each of Figures 5.4b, 5.4c, and 5.4e, a complete collapse of the attached cavity and a departure of a smaller cavity downstream of the tip is shown as the collapse mechanism of a uniformly vibrating tip, as opposed to the Kirchhoff-based vibration, where a small cavity remains situated on the side of the tip during the collapse phase of the center cavity. However, this collapse mechanism is only observed in Figures 5.4a, 5.4c and 5.4f. Meanwhile, in Figures 10d and 10e, while they also demonstrate a collapse phase, a different collapse mechanism appears at t = 0.002085 s and t = 0.002135 s. Here, the collapse is shown as the collapse of the side cavity with the support of the attached center cavity instead. As a preliminary observation, this collapse phase was interpreted as a two-stage collapse mechanism, where in the first stage, the side cavity could plausibly be inhibiting the pressure pulse generated by the center cavity collapse, in turn, inducing an underpredicted pressure peak at the monitor point. Meanwhile, the smaller side cavity collapses correspond to the smaller pressure pulses that remain within the range of 53.1484 kPa and 56.1832 kPa. The second stage collapse could just be the underlying reason behind the increased pressure and vapor signal frequency predicted by the Kirchhoff model.

Moreover, the vector plots highlight the dynamic flow behaviours corresponding to cavitation development. Generally, it can be drawn out that the vortices, whether produced by the uniform or the Kirchhoff sinusoidal horn oscillation, react the same way to cavitation growth and collapse. During cavity growth, Karman vortex structures are maintained within the horn's proximity due to low pressures within the region; however, with the cavity's collapse, vortex breakdown is seen to occur by the shockwaves induced by the said collapse [158]. While this behaviour is shared between the two models, many differences exist in their vortices' positioning and length. Firstly, the uniform vibration of the horn appears to be inducing a circular vortex that shifts from the tip downstream to the tip side; on the other hand, the Kirchhoff model consistently predicts an elliptical vortex in the same position downstream of the tip.

With the FTLE contours, the boundaries of those vortices are highlighted as continuous ridges that gradually extend downstream of the tip. The ridges appear primarily parallel with the horn's centerline. Moreover, thin stretching examined at the tip of the ridges can be interpreted as an inertia-dominant turbulent jet that sources from the tip, as described by Lighthill [159] and Trujillo et al. [160]. With this definition, it can extend the observation and relate it to the thin ridges at the tip, coincident with the cavitation zones, and as such, it is interpreted as a secondary jet impinging the cavitating zone. Its temporal development can be seen with each collapse phase, where its presence becomes more prominent. Since the jet is present in both vibration models, it can be associated with the primary collapse mechanism of their respective cavitation zones. However, the primary difference is outlined as the angle at which the impinging jet penetrates the cavity. In the case of uniform vibration, the jet enters almost parallel to the tip, while the jet cuts through the zone diagonally with the Kirchhoff-based model. Interestingly, this could be linked back to the collapse mechanisms discussed earlier. As the uniform model induces a secondary jet in the horizontal direction, the jet penetrates through the attached cavities and detaches a smaller cavity downstream. Meanwhile, with the diagonal entry of the jet in the Kirchhoff model, the center cavity is attacked first, splitting it into two smaller side cavities. This jet's angle of attack appears to pulsate within a tight range between $28° - 31°$ with the cavitation's development cycle. Based on that, it could be ultimately said that spatial non-uniformity of displacement, such as the suggested by Kirchoff's model, has a negligible effect in this regime due to the dominance of axial motion and low radial gradients. This is due to the high acoustic energy concentration in smaller tip diameters that facilitate this dominant axial flow, which is captured by the uniform model's near-rigid behaviour.

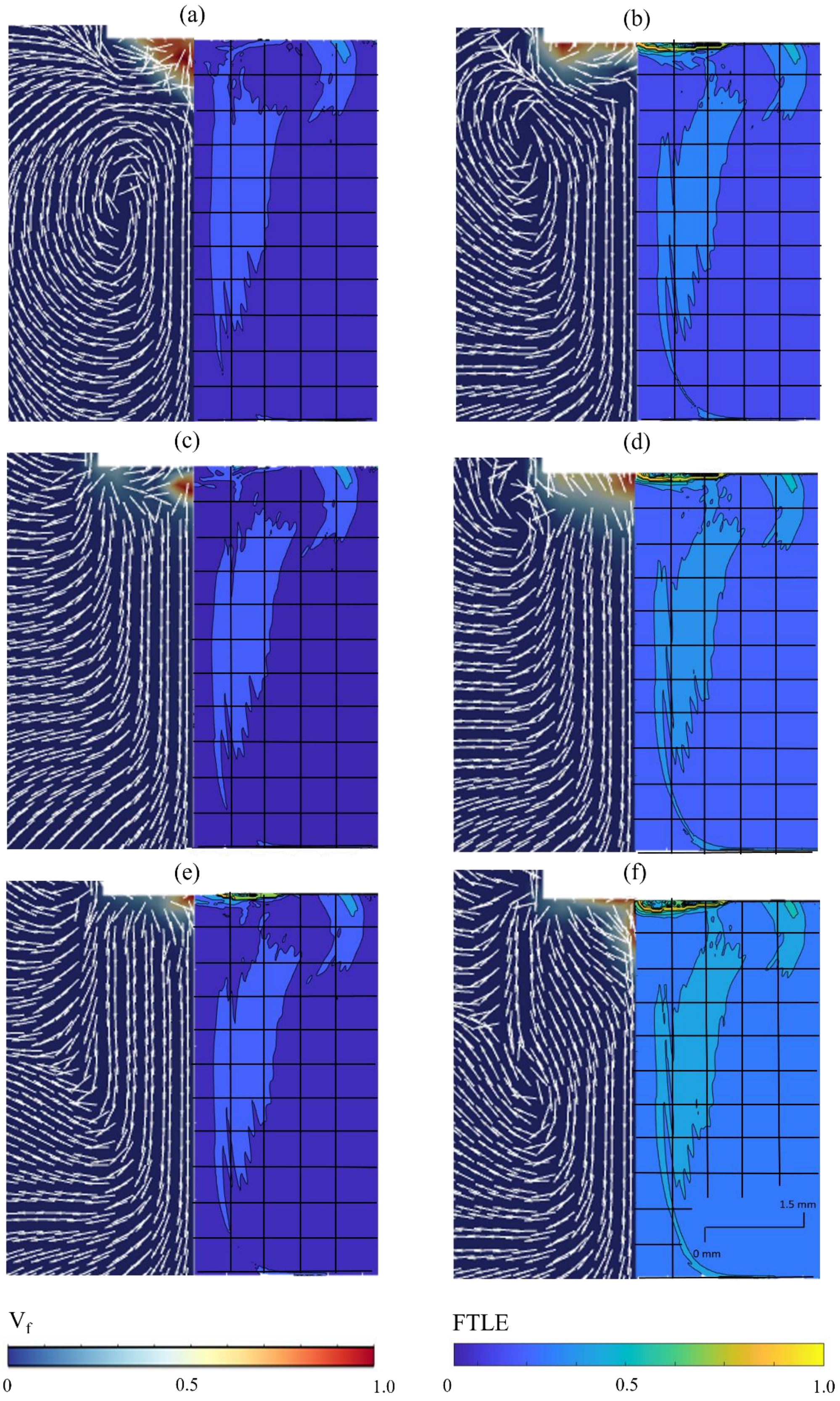

Figure 5.4: Diagram of a 5 x 5 mm region in proximity of the horn (Uniform Model) illustrating the vector and contour plots of flow direction and vapor volume fraction on the left and FTLE on the right where (a-f) represent flow times at t = 0.00193, 0.00198, 0.00203, 0.002085, 0.00218, and 0.002135 s, respectively.

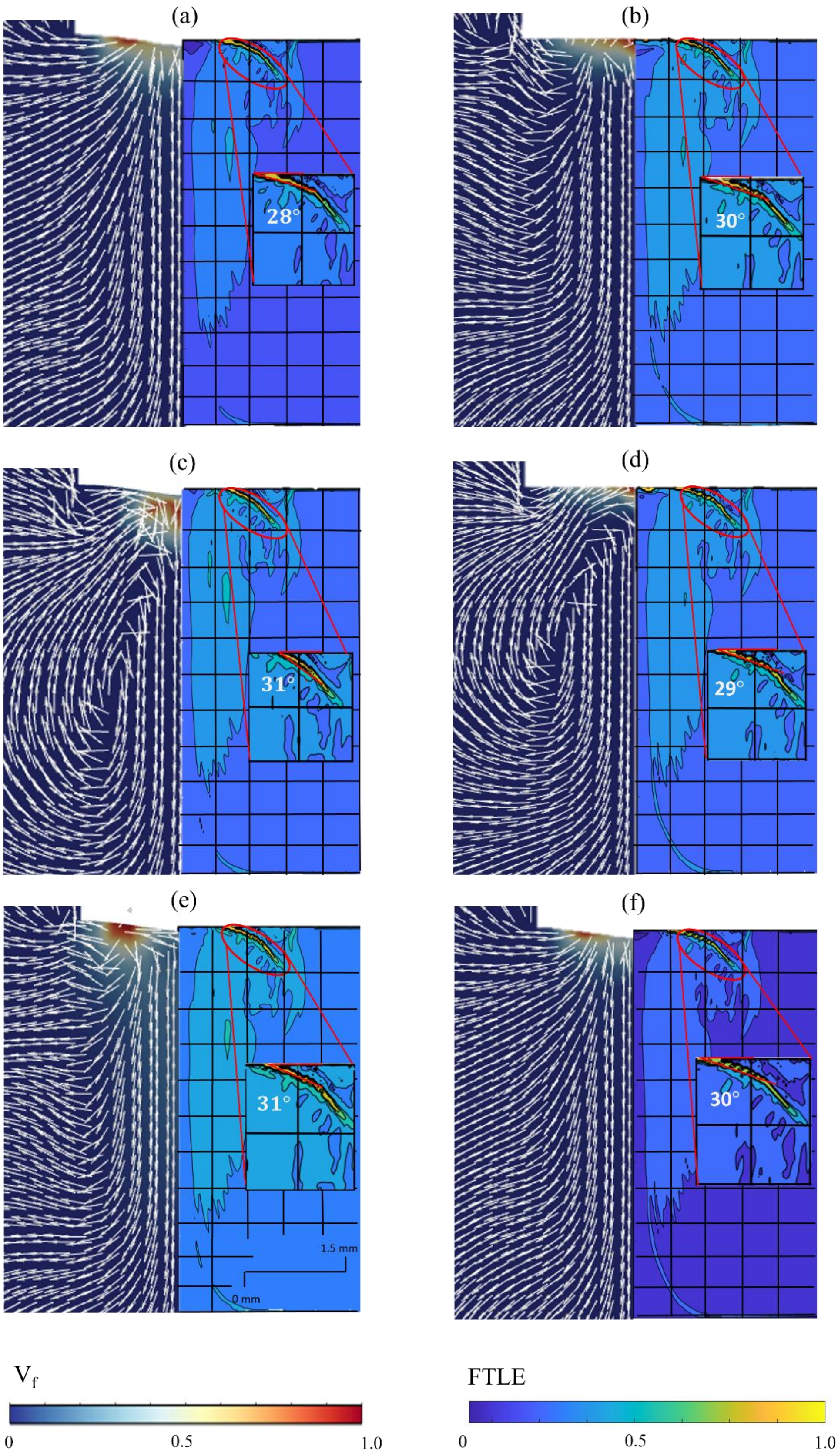

Figure 5.5: Diagram of a 5 x 10 mm region in proximity of the horn (Kirchhoff Model) illustrating the vector and contour plots of flow direction and vapor volume fraction on the left and FTLE on the right where (a-f) represent flow times at t = 0.00193, 0.00198, 0. 00203, 0.002085, 0.00218, and 0.002135 s, respectively.

5.3.3 Front Fourier Transform Analysis of the 12 mm Horn Tip

Evidently, the Kirchhoff vibration model significantly diverges from experimental observations when applied to a small horn tip of 3 mm. However, this contradicts the observations made in previous studies that utilize this vibration model and obtain comparable results to those obtained experimentally. Therefore, the same numerical setups were used, with a 12 mm horn tip, to observe the degree of skewness of results obtained by either model. The choice of a 12 mm horn tip diameter was inspired by the dimensions of many horn models used in the literature, such as the horn investigated by Rahimi et al. [104]. Like Figures 5.1, Fig. 5.6 below compares the raw pressure and vapor volume signals obtained when implementing both models.

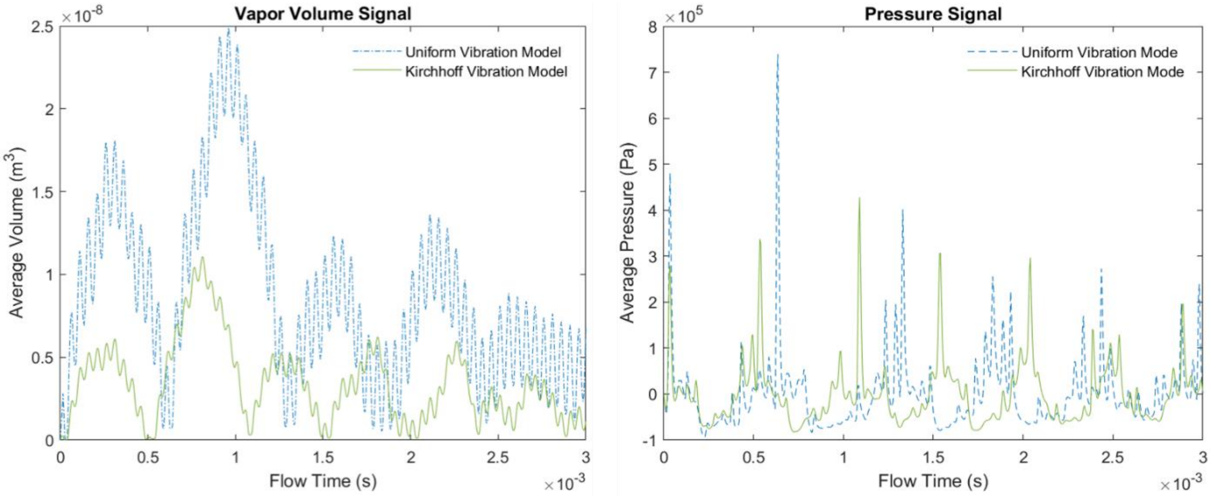

Figure 5.6: Vapor volume signals (left) and pressure signals (right) resulting from uniform and Kirchhoff model-coupled 3mm horn tip boundaries.

The Kirchhoff model displays drastic improvement in its performance and illustrates relatively comparable results with the Uniform model's output. While it is true that the amplitudes are still underpredicted in the Kirchhoff model, its signal frequency almost matches the uniform model's signal frequency. Here, the Kirchhoff model and uniform model output signals oscillate at a frequency of 1996.67 Hz and 1663.89 Hz, respectively. This slight phase shift suggests that the cavitation produced by the Kirchhoff-based vibration induces early onset collapse. This could be due to the fixation of the side edges of the horn tip where minimal cavitation is formed. In addition, the shape adopted by the vibrating wall may be agitating the center cavity inducing its early collapse.

To further visualize the mismatch between the amplitudes and frequencies, a set of consecutive timesteps was selected about the red box highlighted in Figures 5.6. The flowtimes chosen are 0.00043, 0.00049, 0.000535, 0.000585, 0.000635, and 0.000695 s highlighting instances of peak differences and overlap achieved by the two vibration models. Therefore, vector plots drawing flow structures and contour plots outlining the generated vapor volume fraction and FTLE were generated for the respective flowtimes and presented in Figures 5.7 and 5.8. For the uniform model, it is shown that the peak mushroom-shaped cavity growth alongside its following collapse has been captured within this 0.265 ms timeframe. Generally, the main cavity structure's shape retains its mushroom shape, as it shrinks symmetrically during the early stages of its collapse phase. However, what is interesting is that soon after, the main cavity is punctured in its center by an impinging jet inducing the same phenomenon observed in the 3 mm horn tip condition, where two side cavities are created. This instant can be observed at t = 0.000695 s. Looking at the corresponding FTLE plots of each timestep, it can be drawn out that the location and the entrance angle of the impinging jet remain the same compared to the 3 mm horn tip condition. Thus, this could justify the similarity in the collapse structure of the cavity. Furthermore, judging by the direction of the vectors and their particle stretching drawn by the FTLE, the main player for the formation of this jet in this manner could be the vertical motion of the horn tip vertices on both sides. The small vortical structures generated at those sides could be the reason behind this flow formation in those respective tip regions. However, a primary difference between the 3 mm and the 12 mm horn tip is the contraction of the recirculation zone in the region under the horn tip, as it became more localized near the cavity structure. This could be due to the large size of the main cavity zone inducing a more localized recirculation due to the pressure gradient resulting from it. Additionally, based on the vortex tracking method conducted by Rahimi et al. [104], it seems that the Kirchhoff-based model underestimates the size of the secondary counter-rotating vortices on the side of the horn tip.

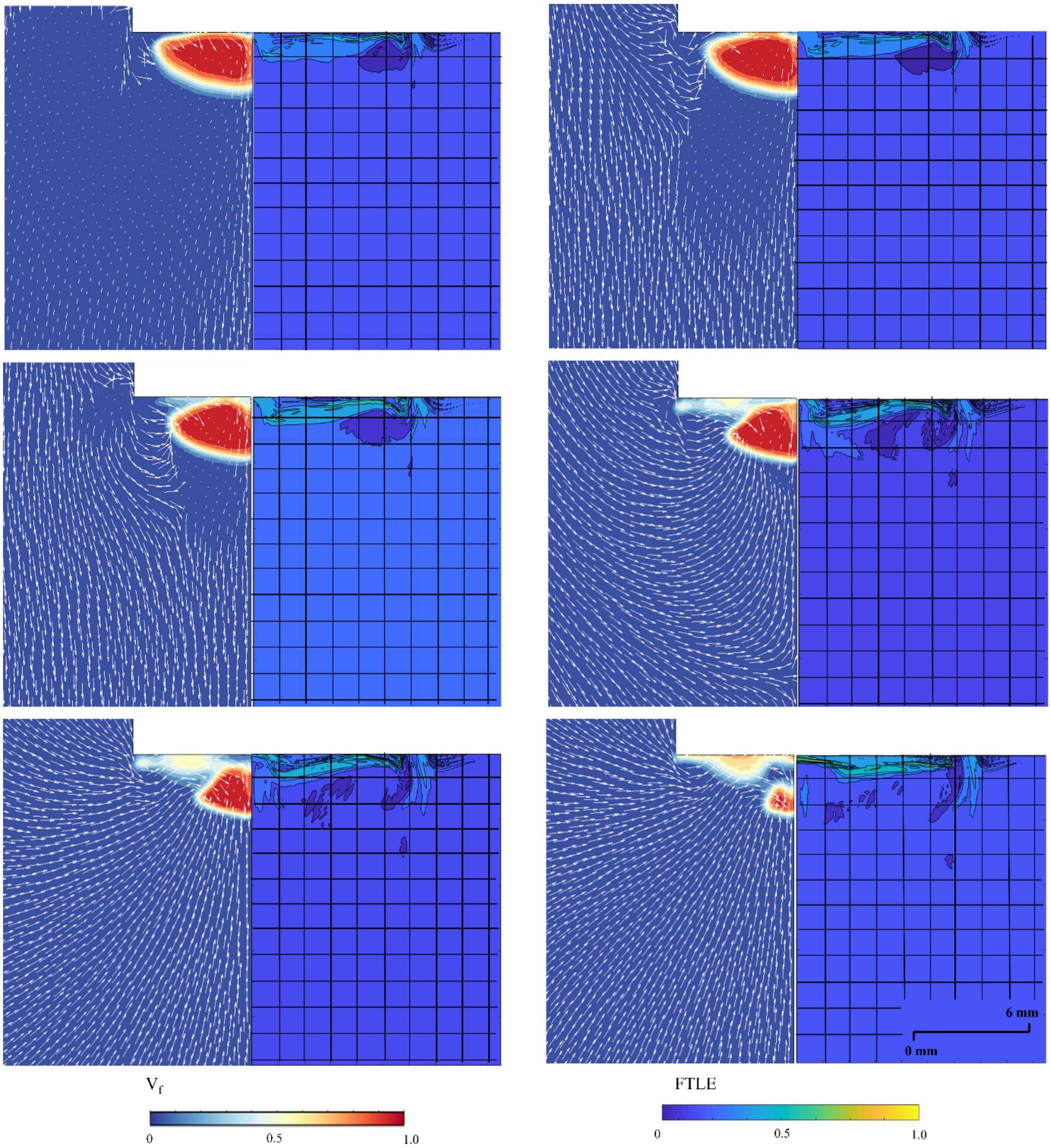

Figure 5.7: Diagram of a 9.5 x 19 mm region in proximity of the horn (Uniform Model) illustrating the vector and contour plots of flow direction and vapor volume fraction on the left and FTLE on the right where (a-e) represent flow times at t = 0.00043, 0.00049, 0.000535, 0.000585, 0.000635, and 0.000695 s, respectively.

As for the Kirchhoff model, there are clear differences between the 3 mm and the 12 mm horn tip conditions. Firstly, the phase cycle of the cavity structure seems to overlap with the phase cycle of the cavity present in the uniform model. In other words, both cavity structures appear to have peaked in growth at t = 0.00043 s and are experiencing shrinkage, and eventual collapse, during the chosen timeframe. This indicates that the two models' predictions are relatively in-phase. Moreover, the cavity structures generated share the same mushroom-like shape as observed in the uniform model. This generation of this structure is confirmed by the experimental observations made by Rahimi et al. [104]. However, parallels can still be seen in the mid and late sections of the collapse cycle. It still appears that the Kirchhoff model predicts a two-step collapse cycle where a complete collapse of the cavity structure occurs at t = 0.000535 s to 0.000585 s and is later followed by a brief growth and eventually followed by shedding of the main cavity. Judging by the vector and FTLE plots, the impinging jet here does not appear to attack at an inclined angle, but instead, is shown to be horizontal along the surface of the tip. Perhaps, this could be the justification for the disappearance of the prominent collapse phase where two smaller cavities appear on the side. Moreover, this change in jet angle is accompanied by the appearance of a small vortical structure at the horn tip vertices as well confirming its major association with the impinging jet direction. The large vortex that used to appear about the horn axis downstream of the horn tip in the 3 mm case has shrunk. A similar observation was made by Rahimi et al. [104] and Tzanakis et al. [68]. Perhaps, its absence plays yet another role in the direction of the impinging jet. Moreover, it can be strongly suggested that the acoustic field generated in larger tip diameters are relatively insensitive to the radial displacement distribution, as reflected by the vector and FTLE profiles.

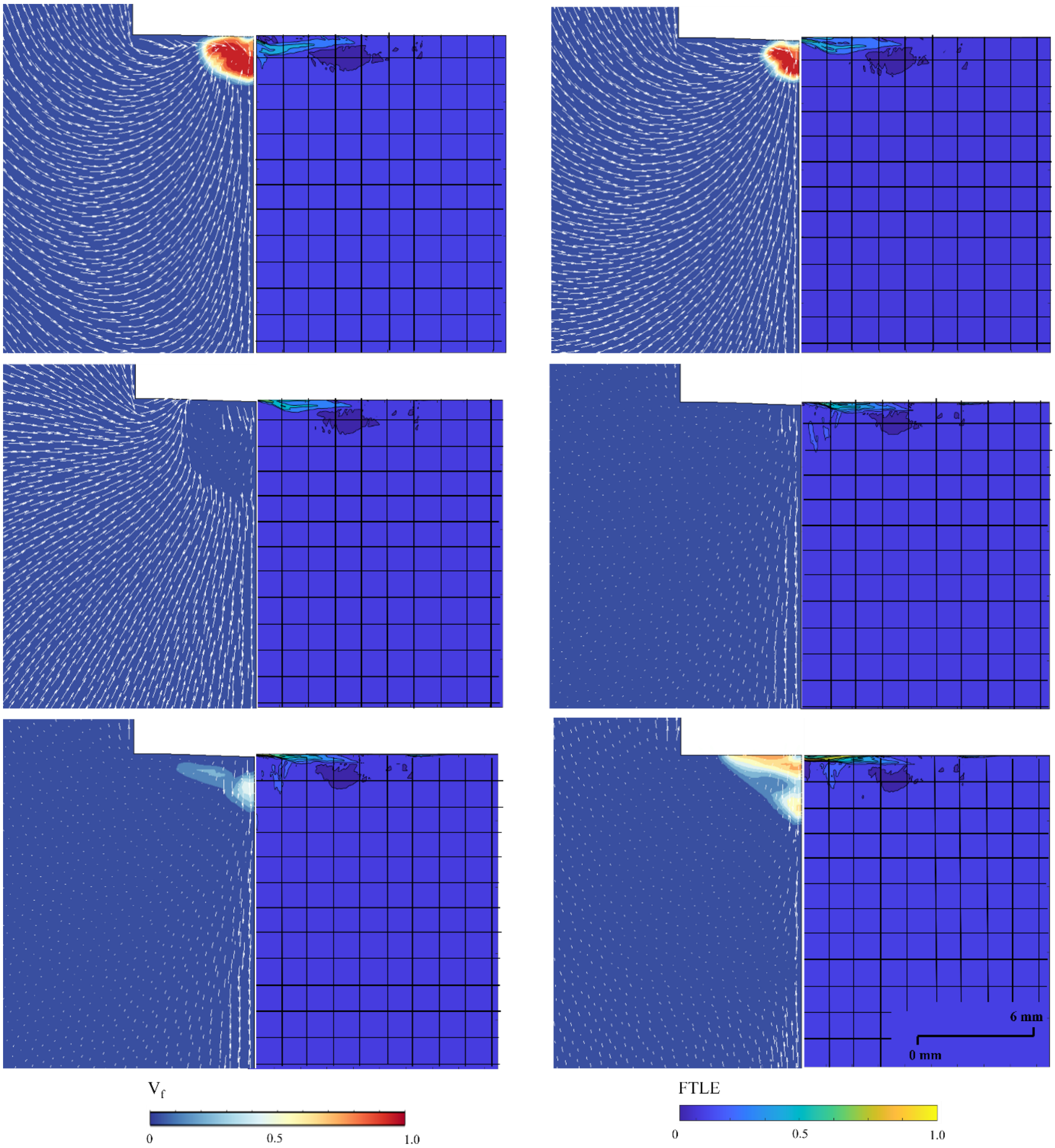

Figure 5.8: Diagram of a 9.5 x 19 mm region in proximity of the horn (Kirchhoff Model) illustrating the vector and contour plots of flow direction and vapor volume fraction on the left and FTLE on the right where (a-e) represent flow times at t = 0.00043, 0.00049, 0. 000535, 0.000585, 0.000635, and 0.000695 s, respectively.

5.4 Conclusion

In summary, the study concludes that the Kirchhoff-based vibration model leads to significant underprediction of cavitation growth and collapse in which it has been associated with low-pressure peaks and higher cycle frequencies. Moreover, the study delved deeper to find the induced differences in flow behavior within the proximity of the tip and the attached cavitation by visualizing LCS using FTLE. As it turned out, an impinging jet is formed near the tip with both vibration models, however, it is important emphasize that the development direction of the jet is rather distinct. The Kirchhoff-based model manipulates the proximal flow in which the jet develops diagonally to the tip surface and penetrates the center cavity inducing its collapse and subsequent splitting into two smaller cavities near the tip edges. These also end up collapsing upon reaching the following pressure peak. Meanwhile, the uniform vibration model shows the jet impinging the entire cavity horizontally forcing the attached structure into a complete collapse. It could be argued that the reason behind the different jet formations could be related to the position and eccentricity of the Karman vortex formed downstream of the tip. With the Kirchhoff model, the vortex is primarily positioned under the horn while the uniform model has its vortex appearing on its side. Interestingly, all these differences begin to dissolve with the increase of the tip diameter. Perhaps, it is a strong indication that the influence of the first mode shape of the horn tip's vibration gradually loses significance with larger surface areas. The finding of this underlying relationship between the vibration model and the diameter highlights the significance of the choice of the model when defining the vibration of the horn tip, as it strongly manipulates the cavitation collapse mechanisms. Generally, a new window for acoustic cavitation controllability may accompany this discovery that may offer new approaches to location-specific surface processing. In retrospect, the uniform vibration model appears to be more suitable universally in modelling ultrasonic horns of small tip diameters, while the Kirchhoff-based vibration model performs better in larger tip diameters, as it captures the influence of displacement's radial distribution on radial flow velocity and pressure distribution.

6 Analyzing the influence of toroidal vortex development on acoustic multi-bubble macrostructures under different ultrasonic horn tip diameters

6.1 Introduction

In this chapter, deeper scrutiny of the flow dynamics instigated by the irradiation of ultrasonic acoustic waves within an aqueous domain is conducted based on the aforementioned observations on the toroidal vortex made in Chapter 5. Here, a numerical study was conducted on a two-dimensional horn-type reactor domain in aims to explore the different acoustically driven flow types induced by varying horn tip diameters of horns oscillating at 20 kHz in an aqueous solution. The diameters that were considered in the said exploration were 3, 6, 13, 16, and 19 mm.

Notably, with such investigations on different horn geometries and operating conditions, many observations have surfaced on the resemblance of the cavity structures formed under the horn, namely, streamers, clusters, CBS, and MBS [161-163]. It has been reported that governance of the aforementioned cavity structures is strongly influenced by multiple factors, be it working fluid properties or horn geometry. It was widely accepted that a higher vaporization pressure, for instance, would result in an encouraging fluidic environment that facilitates the formations of cavitation. However, Žnidarčič et al. [128] delved further into different liquid properties, namely liquid temperature, surface tension, and viscosity. While it has been reported that none of the properties had any substantial role in the cavitation formation dynamics, it has been established that surface tension and viscosity relatively share a notable effect on the cavity's collapse intensity. In particular, the main cavity collapse demonstrated a potential cushioning effect with higher viscosity. Similar observations were made by Tzanakis et al. [68], where they added that the damping effect induced by the viscosity led to an increase in the bubble oscillation period. However, unlike Žnidarčič et al. [109, 128], significant differences in the cavity structure and its respective dynamics were observed. It has been suggested that a primary reason behind this is the attenuation of acoustic energy due to high viscosity. The different cavity structures witnessed in the investigation were categorized as either conical or spherical. In the case of the low surface tension fluid (ethanol), it was noted that no continuous structure was formed.

In more recent studies, similar qualitative observations were made on the cavity structure; however, these were all found in aqueous media [164, 165]. As a matter of fact, these were the qualitative conclusions of studies scrutinizing different horn tip diameters. For instance, Moussatov et al. [166] considered three tip diameters of 20, 80 and 120 mm, in which bubble clusters were shown to self-arrange into the stable cone-like macrostructure. Upon examining the macrostructure under the three tips at a constant acoustic intensity of $I = 8.2\frac{W}{cm^2}$, it is concluded that the increase in the diameter results in a more prominently localized cone-like structure under the horn tip. Other studies have found that the said structure can also be attained with intermediate horn diameters, typically within the range of 10-12 mm [161, 167, 168]. However, any further decrease in the horn diameter transfigures this cavity structure into a mushroom-like attached cavity, namely acoustic supercavitation [128, 116]. In an attempt to establish an understanding behind the different structures, some studies have initially tried to identify the flow field dynamics. Previous studies suggested that this may be due to the direction reversal of the Bjerknes force [169-171] that is induced by the formulated high pressure proximal regions near the horn axis. This unfolds into a series of repulsive and attractive bubble regions that in turn shape the cone. On a more recent note, Biasiori-Poulanges et al. [161] have utilized high-speed X-RAY imaging to precisely visualize the proximal flow field and understand its role in the formation of the conical structure. Here, the investigation concluded that the conical shape formation is simply due to a multi-stage cavitation development sequence in which it begins with the splitting of single bubbles into 'daughter' bubbles forming clouds that later merge down the horn tip center. Complementing this stage, radial pressure at the center then molds the clouds into what is known as CBS.

While the aforementioned studies have successfully been able to justify the development of such structures, the sudden geometry-induced transformation from CBS to MBS with the decrease of the horn tip diameter has had limited scrutiny in literature. Ma et al. [164] hinted at the fragility of CBS in highly turbulent flows induced in smaller diameters, while other studies have added, based on their consistent observations of proximal toroidal vortices, that their formations within the vicinity of the cavity may play a role in the cavity's dynamics [104, 172]. However, the role of the flow manipulations induced by these vortices has not been explored and remains unclear. Therefore, the presented study is a numerical exploration of the origin of the toroidal vortex and its development in aims to uncover any underlying relationships with the cavity's development and structure. The investigative methodology is a computational fluid dynamic (CFD) assessment of cavitation development and its proximal flow field that considers five horn tip diameters that are typically categorized in literature as small-diameter and large-diameter ultrasonic horns. As such, this is to capture any behavioral changes by the proximal vortex upon changing the horn's diameter. In addition, this study aims to uncover a more elaborate understanding of the nonlinear variation in the cavity macrostructures' shape and the proximal toroidal vortex's locomotion and size.

6.2 Ultrasonic Computational Modelling

The presented study adopts a numerical methodology that facilitates two stages of the investigation: a structural modal analysis of considered ultrasonic transducers to assess the adopted mode shape during a 20 kHz oscillation, and a computational fluid dynamics (CFD) analysis to define the proximal flow generated by the chosen myriad of horn diameters. Each segment of the methodology describes the geometries considered, and the equations that govern the physics of the solid and fluid domains.

6.2.1 Modal Analysis Setup

6.2.1.1 Establishing ultrasonic transducer domains and defining boundary conditions

As it has been established by the previous literature, the horn diameter appears to play a crucial role in defining the cavity structure generated underneath its tip. Initially, this can be taken as an indicator of a possible change in the longitudinal vibration mode shape the horn tip experiences with an increase in its diameter. However, to scrutinize this and be able to rule out such change, two transducer geometries were generated based on dimensional extractions from physical transducer models found in published literature [173, 173, 174]. It is of extreme importance to replicate the geometries to an exact scale to ensure that the acoustic energy transmission throughout the transducer body is replicated as well [175]. Therefore, the two geometries constructed, illustrated and dimensioned in Figure 6.1, were assigned Ti-6Al-4V as the material. Table 6.1 tabulates the respective isotropic elastic material properties.

Table 6.1: Ti-6Al-4V material properties describing its isotropic elasticity.

Material	*Temperature, ∘C*	*Young's Modulus, Pa*	*Poisson's Ratio*	*Bulk Modulus, Pa*	*Shear Modulus, Pa*
Ti-6Al-4V	20	1.07×10^{11}	0.323	1.0075×10^{11}	4.0438×10^{10}

Furthermore, the geometries were discretized using a structured mesh. The modal analysis deals with free vibration characteristics, as such, no external loads were applied. The horn geometries were left free to oscillate in their unconstrained state. The modal analysis considered is in fact a linear dynamics analysis, in which the general equation of motion is taken into consideration. This was solved using ANSYS Modal as the finite element solver. Moreover, the damping effects have been ignored for simplicity, and thus, they have been zeroed out in the equation of motion. Lastly, these reconsiderations of the equation of motion result in the definition of a free and undamped system that is expressed in Eq. 6.1 below.

$$[M]\{\ddot{u}\} + [K]\{u\} = \{0\} \tag{6.1}$$

Here, M is the mass matrix, $\ddot{u}$ is the vector of acceleration, K is the global stiffness matrix, and u is the displacement vector. The equation was solved for its eigenvalues and eigenvectors that correspond to the mode shapes of the geometries. These mode shapes were used to assess the influence of the horn geometry, specifically the diameter, on the longitudinal vibration mode.

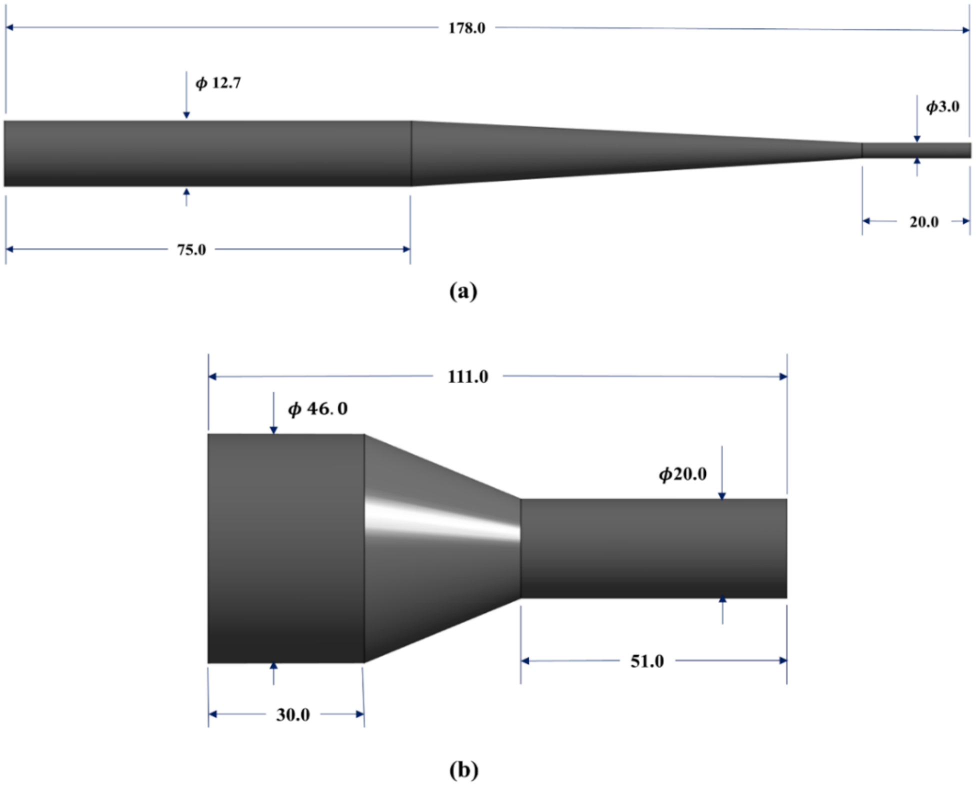

Figure 6.1: Dimensioned solid domains of the two ultrasonic horns considered (in mm) with (a) a horn tip diameter of 3 mm [11, 34] and (b) a horn tip diameter of 20 mm [35].

6.2.2 Computational Fluid Dynamics Domain

6.2.2.1 Creation of the Calculation Domain

In the investigation presented in this chapter, the numerical setup previously constructed in Chapters 4 and utilized in Chapter 5, is implemented here as well. This generalized domain has been further extrapolated in the presented study to consider a range of horn diameters; the values of ϕ_h chosen are 3 mm, 6 mm, 13 mm, 16 mm, and 19 mm. The axisymmetric condition defined in the CFD solver essentially solves the flow equations for the domain slice then implicitly rotates the 2D plane around the axis of symmetry to account for the full volume.

6.2.2.2 Extended Numerical Setup Validation

Given that the study investigates larger tip diameters compared to Chapters 4 and 5, extensions in the flow time and number of timesteps may be required to ensure that the numerical setup is still able to capture slower cavitation cycle in larger tip diameters. Therefore, the simulation was run for double the flow time specified to ensure that all cavitation behaviors are well-captured within the 3 ms timeframe. The pressure signal was extracted, as shown in Figure 6.2, and the near-subharmonic frequency of the cavitation cycle was obtained in aims to compare it with the previously obtained 5990 Hz oscillation frequency. From Figures 4.13 and 6.3, it seems that the signal and its frequency of oscillation obtained closely resemble the previous signal obtained. This ensures that using a longer flow time for all considered horn tip diameters will still guarantee capturing the two-phase flow behaviour.

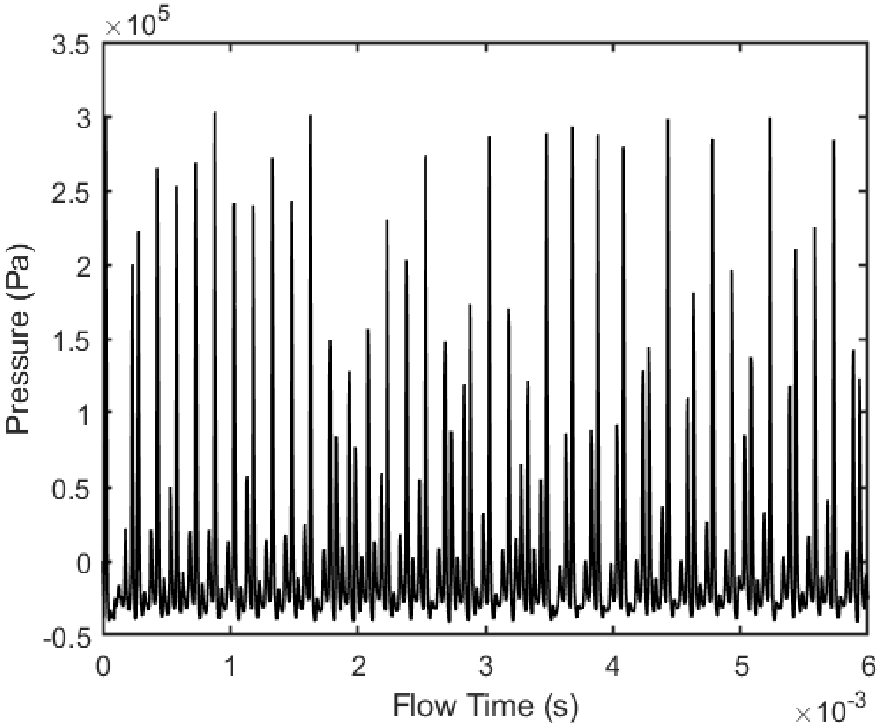

Figure 6.2: Time evolution of pressure signal obtained from a monitor point positioned next to the 3 mm horn tip running for 12 ms.

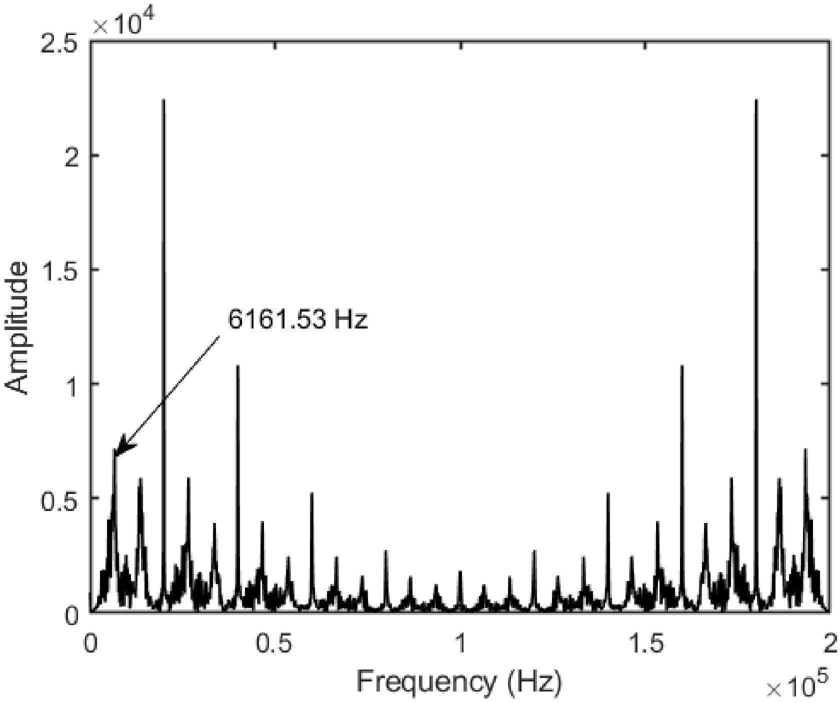

Figure 6.3: Frequency response plot of the pressure signal obtained in Fig. 3.5.

6.3 Analysis Methodology and Results Discussion

6.3.1 Modal Analysis of Ultrasonic Transducers and Categorizing their Mode Shapes

In the presented modal analysis, two reasonably distinct ultrasonic transducer models were selected in order to extract any potentially underlying structural changes to the horn tip oscillation at their expected oscillation frequency. It has been assumed that the two transducers are comprised of a Titanium alloy (Ti-6Al-4V), as the material is found to be rather common in the production of physical ultrasonic transducer models [176-178]. Highlighted in Figure 6.4 are shared observations made in the two transducers of first mode shape occurring at distinct frequencies. While it is easily observed that the two mode shapes exist in both transducer models, their general trends attributed to each mode are also the same. Interestingly, the longitudinal mode shape (Mode Shape 1) occurs within a tight frequency range around 20 kHz. Moreover, the longitudinal mode shape in both transducers is seen to experience very similar, if not exact, shape transfiguration, where the horn tip is seen to extend uniformly forward. This emphasizes that despite the geometry distinction, the mode shape maintains its behavior with both small and large diameters.

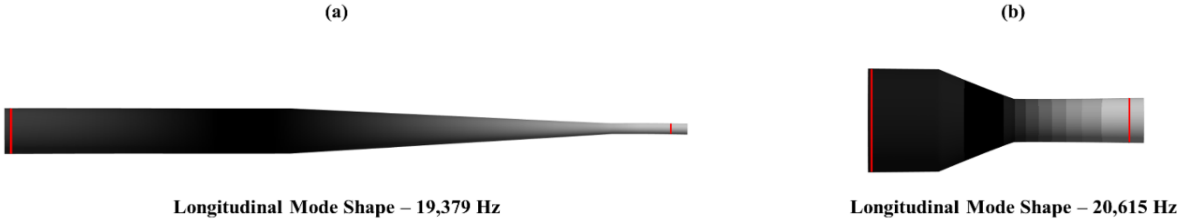

Figure 6.4: Longitudinal mode shapes and their respective frequencies observed in (a) the transducer geometry with a 3 mm tip diameter and (b) the transducer geometry with a 20 mm tip diameter. The red lines highlight the shape and position of the transducer edges prior to deformation.

6.3.2 Analysis of Cavity Structural Behaviour under Different Horn Tip Diameters

Upon establishing the consistent mode shape during the transducer's longitudinal vibration, the horn tip was numerically programmed to oscillate accordingly by introducing Eq. 2.36 in UDF form to govern its oscillation throughout the CFD simulations. Multiple diameters have been examined in aims to track the potential differences in development of acoustic cavitation. Figures 6.5 through 6.9 illustrate the cavity development and its structural formations during a single cycle consisting of its growth and collapse stages.

With the 3 mm horn tip, a clear set of sub-cycles of minor growths and collapses make up the single lifecycle of the attached cavity is initially observed. At its first few moments, from t_0 to $t_0 + 6\Delta T$, the attached cavity structure emerges in the form of a thin sheet about the horn tip, starting from the center of the tip, which later is seen to transfigure into an inverse mushroom upon reaching its growth climax, at $t_0 + 16\Delta T$. However, with its cycle's progression, the structure begins to gradually shrink radially and flatten against the horn tip until it bursts from its center, splitting it into two small-sized clouds. These clouds take position on the sides of the horn tip, where they are lastly seen to be unable to sustain their shape leading to their eventual collapse. On a similar note, this observation has also been found in the case of the 6 mm horn tip diameter, as shown in Figure 6.6. However, two notable differences lie at the attached center of the cavity. The first divergence in the 3 mm trend is apparent during the early onset cavitation, where the cavity is seen to gradually take form on the sides of the horn, unlike the 3 mm horn tip where the cavity began at the center. This can be clearly observed during the early stages of growth from $t_0 + 4\Delta T$ till $t_0 + 22\Delta T$.

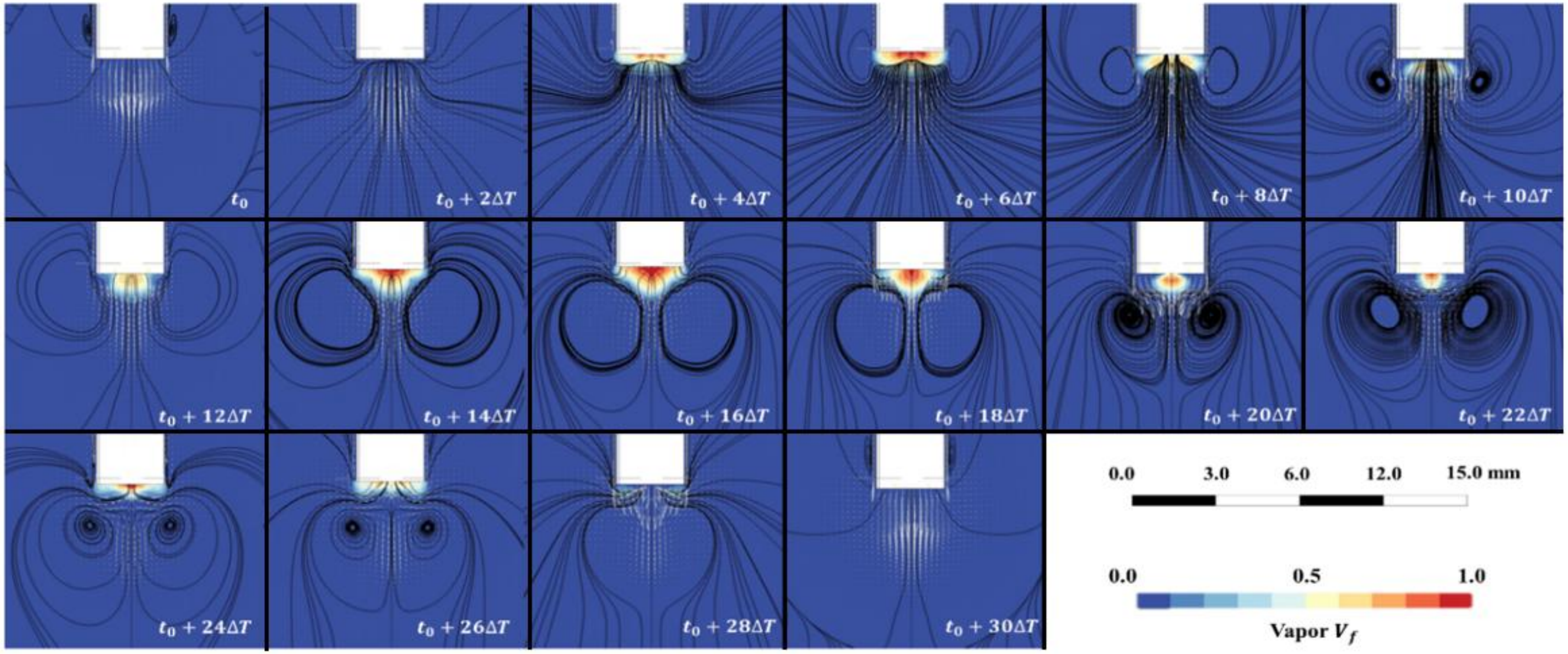

Figure 6.5: A series of vapor volume fraction contour plots that demonstrate a single cycle of the growth and collapse of acoustic cavitation under a 3 mm horn tip diameter. Surface streamline and vector plots were also highlighted in the contour plots to visualize the proximal flow behaviour and direction.

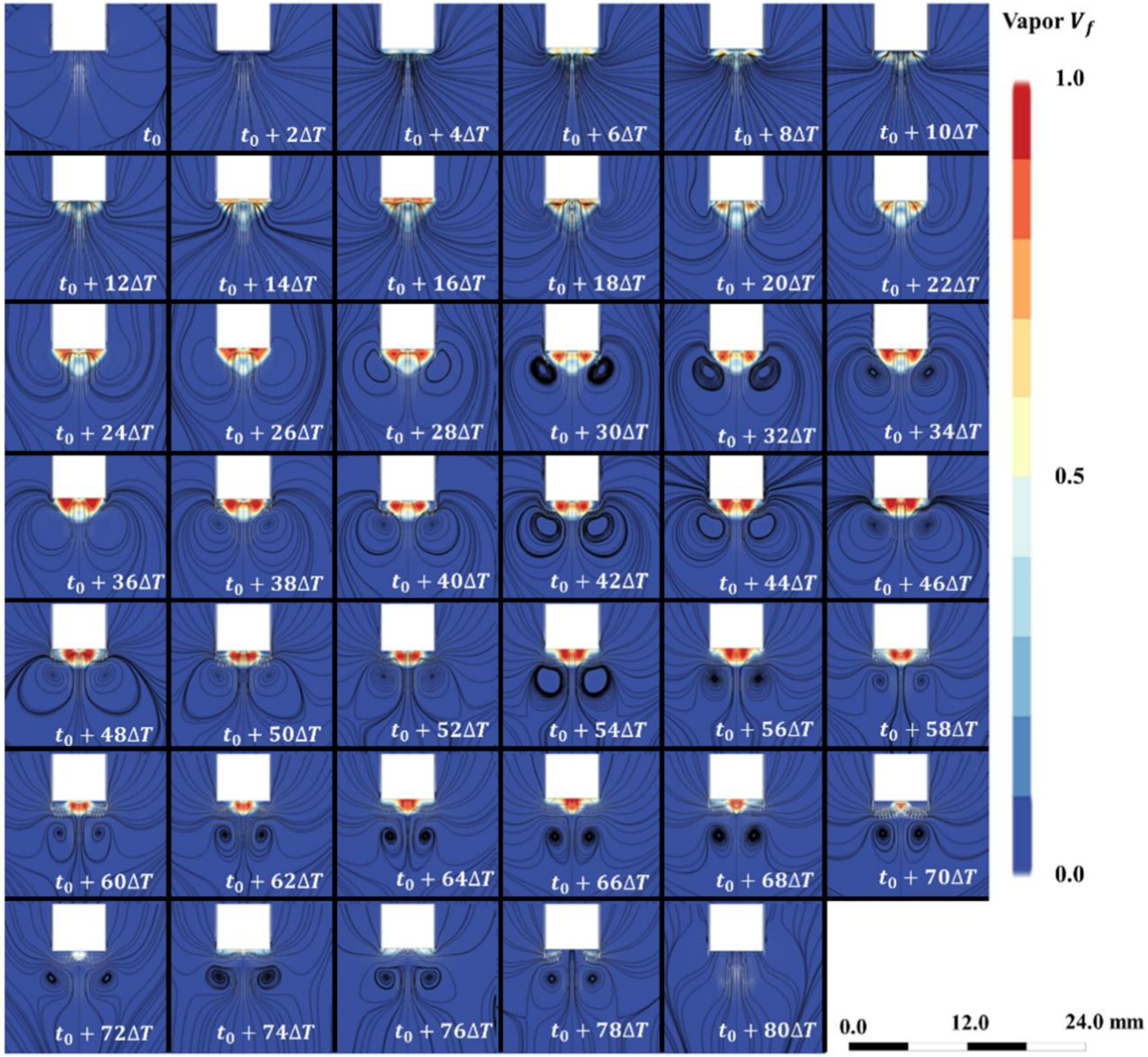

Figure 6.6: A series of vapor volume fraction contour plots that demonstrate a single cycle of the growth and collapse of acoustic cavitation under a 6 mm horn tip diameter. Surface streamline and vector plots were also highlighted in the contour plots to visualize the proximal flow behaviour and direction.

With the progression of its growth, highlighted at times $t_0 + 24\Delta T$ to $t_0 + 34\Delta T$, the two cavities expand radially towards one another until they merge completely forming one continuous MBS cavity. However, this in turn creates a minute condensation region that situates a buffer zone between the horn tip and the cavity center. In other words, this kink in the cavity center appears to slightly levitate and detach the cavity structure from the horn tip; however, this small condensation remains rather static and does not develop any further. Nevertheless, this structural deformation eventually alleviates and is backfilled by vapor, as shown at time $t_0 + 56\Delta T$. From this point onwards, the cavity's collapse stage commences by closely following the collapse mechanism observed in the 3 mm case in Figure 6.5. Essentially, the cavity's collapse is observed as an initial radial shrinkage until the small circular-like cavity is pushed against the horn tip, where it is seen to split into two smaller cavities positioned on the horn tip sides. Lastly, these cavities eventually collapse marking the end of the cavitation lifecycle. Interestingly, it seems that horn tips industrially categorized as 'small horn tips' share very similar cavitation growth-collapse structural progression. These aforementioned observations made on the two horn tip diameters are in full agreement with observations and conclusions made in previous studies on small horn tips, where CBS is hardly pronounced throughout the lifecycle [147, 179]. However, it has been argued that CBS is rather a common cavitation structural formation under horn tips with considerably larger diameters. Thus, Figure 6.7 demonstrates the cavity structures predicted under a 13 mm horn tip.

The cavitation formation observed under the 13 mm horn tip essentially maintains the same point of growth, in which an attached sheet of cavitation is seen to collectively form about the tip's center. However, shortly after, the cavity begins to take shape by centralizing and expanding axially from the tip. This can be clearly observed from $t_0 + 10\Delta T$ to $t_0 + 22\Delta T$. Interestingly, the first significant deviation in the previously noted cavitation development trend is observed, where the centrally concentrated cavity experiences a wave of temporary shrinkage; generally, the center cavity gradually dissipates, as minor nucleation sites are initialized along the tip's surface. It is important to note that in the following growth cycle instances, from $t_0 + 42\Delta T$ to $t_0 + 54\Delta T$, highlights a struggle in the regrowth of the center cavity. More specifically, the cavity does not reattain the equivalent saturation of the center bubble region previously observed at early stages of the lifecycle. Instead, cavitation clouds established in proximity to each attached cavity site were dragged towards the center region and molded into CBS. This, in turn, marks the second deviation in the aforementioned small horn cavitation trends. This cavity development sequence aligns with conclusions made by previous studies on large horns [165, 180].

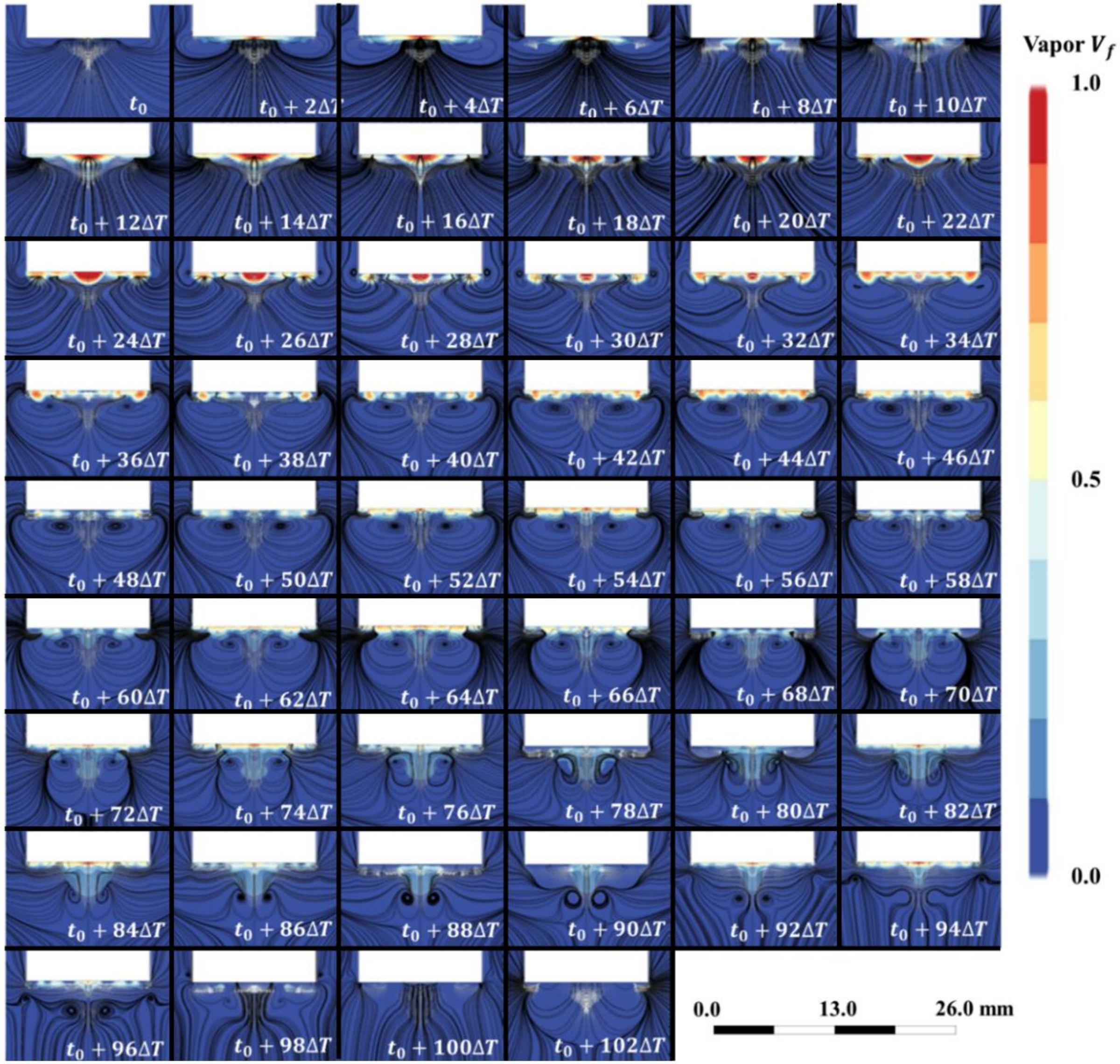

Figure 6.7: A series of vapor volume fraction contour plots that demonstrate a single cycle of the growth and collapse of acoustic cavitation under a 13 mm horn tip diameter. Surface streamline and vector plots were also highlighted in the contour plots to visualize the proximal flow behavior and direction.

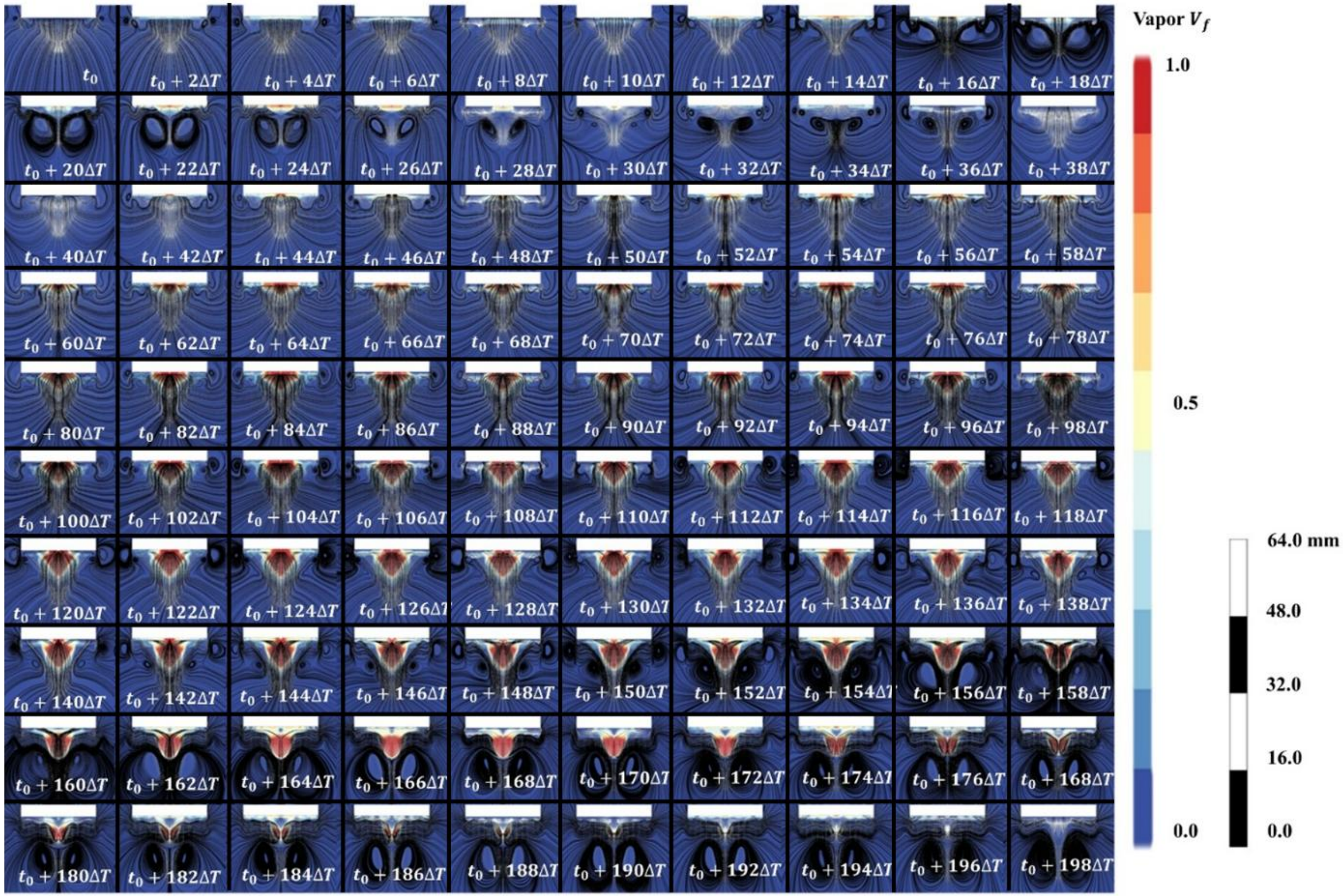

Figure 6.8: A series of vapor volume fraction contour plots that demonstrate a single cycle of the growth and collapse of acoustic cavitation under a 16 mm horn tip diameter. Surface streamline and vector plots were also highlighted in the contour plots to visualize the proximal flow behavior and direction.

Parallel observations and recurring nucleation themes are examined with larger horn tip diameters. Upon observing the cavitation dynamics under the 16 mm horn tip, it can be safely said that the cavitation dynamics maintain the same relative growth mechanism in terms of cavitation centralization and CBS adaptation. However, the collapse mechanism under the governance of such large horn tip is instead dissimilar. The contours illustrated in Figure 6.8 stretching from $t_0 + 160\Delta T$ to $t_0 + 196\Delta T$ demonstrate an alternate initialization and proceeding of the collapse cycle. Initially, the conical cavity structure is seen to stretch axially leading to the narrowing of its body's midsection. This is seen to continue until the attached section is thinned out completely and the stretching cavity head is 'pinched off'. Furthermore, the detached cavity experiences a post-detachment deformity from its top side as it is launched towards the downstream vortex, eventually leading to its collapse. Notably, based on qualitative inspection, this collapse can be analogous to the collapse of a near-wall cavity. Knowing that the vortex pressure distribution is highest at its ends, it could perhaps be assumed that vortex region acts as a wall. Thus, the detached cavity is seen to be impinged by a jet through its center. Meanwhile, shortly after this instance, the attached sheet cavity follows with its own collapse.

With the last case of a 19 mm horn tip diameter, Figure 6.9 presents that neither the cavitation growth nor collapse mechanisms witnessed any significant divergence from what has been observed in the 16 mm case. However, a minute difference has been noted to exist in the pinched cavity; the cavity head is seen to have a plunged top, rather than the parabolic top demonstrated in the 16 mm case. As it has been observed, these transformations of the cavity structure have had an eventual significant impact on the growth and collapse mechanism. Typically, this could be a solid indicator to an underlying change in the cavitation-induced extremities in the proximal flow properties, i.e. transmission of the pressure shockwave upon collapse. It is understood that collapse intensity is crucial for many process-intensification ultrasonic methodologies [181], and thus to better understand the significance of each cavity structure, a proper quantification of the frequency of cavity collapse and the resultant pressure peaks that follow becomes important to assess the extent of their respective cavitation collapse intensities.

Figure 6.9: A series of vapor volume fraction contour plots that demonstrate a single cycle of the growth and collapse of acoustic cavitation under a 16 mm horn tip diameter. Surface streamline and vector plots were also highlighted in the contour plots to visualize the proximal flow behavior and direction.

6.3.3 Quantifying Cavitation-induced Proximal Flow Conditions

The quantification of these flow attributes has been numerically performed by tracing pressure variations at the monitor point highlighted in Figure 6.2 and by quantifying the vapor volume generated under each horn tip. The vapor volume was calculated by cycling through the meshed domain and summing the products of the vapor volume fraction and the respective mesh cell volume. Figure 6.10 below illustrates the constructed pressure and volume signals obtained from each horn tip geometry.

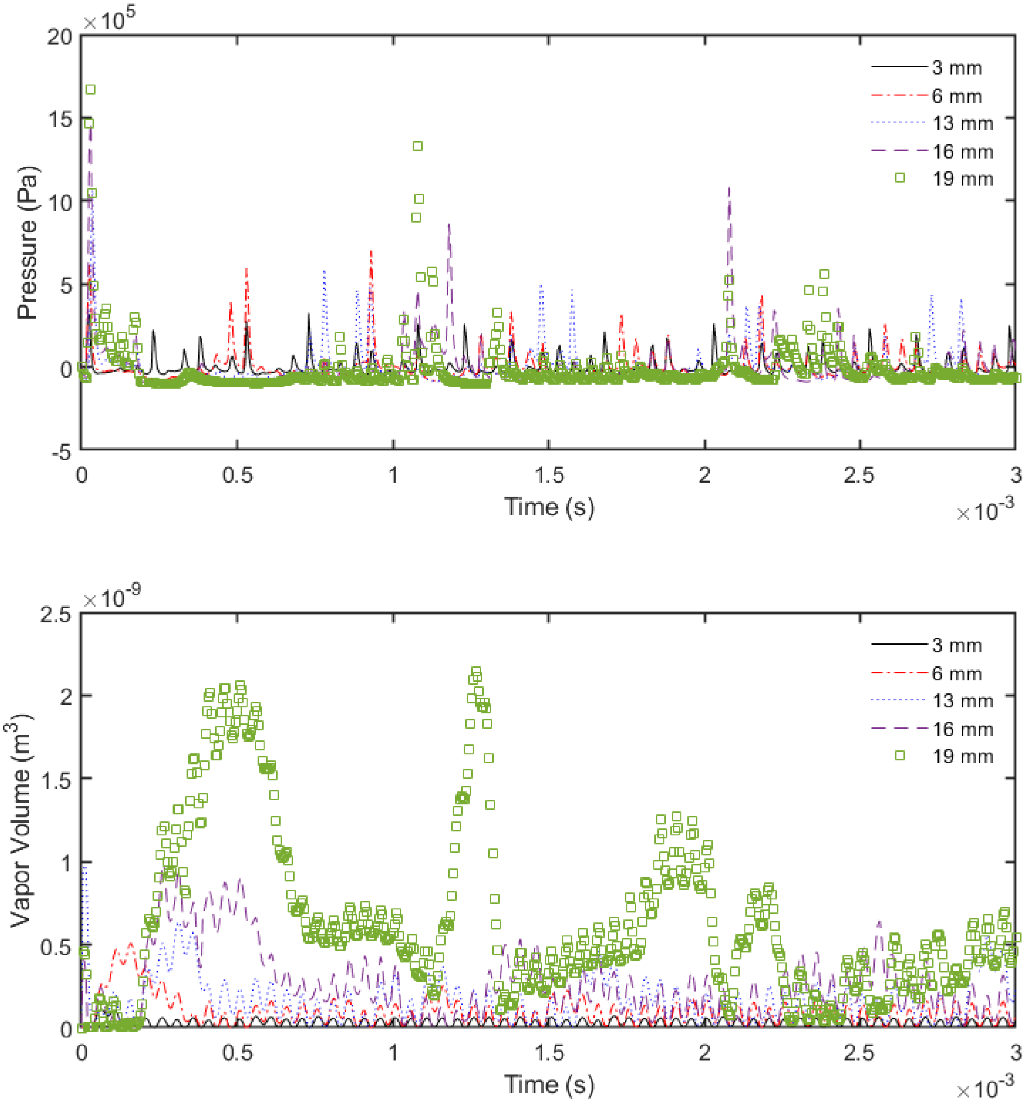

Figure 6.10: Comparative plots of pressure signals (top) and vapor volume signals (bottom) for different horn tip diameters.

Initial observations of the two graphs show that the pressure and volume peaks incrementally increase with the increase of the horn tip diameter, while keeping the horn oscillation amplitude, oscillation frequency, and aqueous environment constant. However, this is no new behavior and rather much expected; the increase in the horn tip diameter facilitates further cavitation growth by increasing the number of nucleation sites, which can be seen by the large vapor volume peaks.

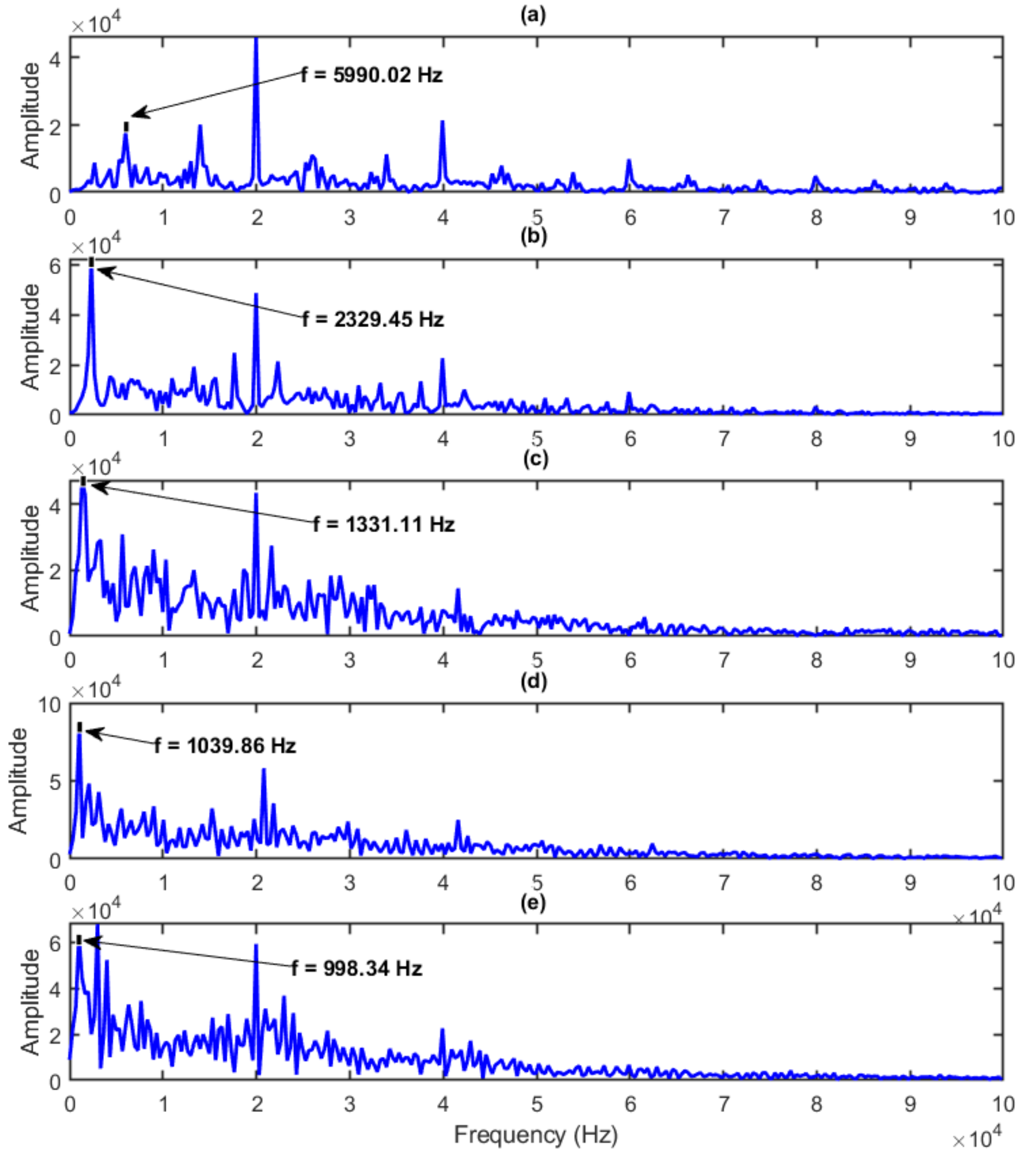

Figure 6.11: FFT plots of the vapor volume signals obtained from (a) 3 mm (b) 6 mm (c) 13 mm (d) 16 mm and (e) 19 mm horn tips.

Moreover, with the expansion of the cavitation region, its proceeding collapse would then naturally be of higher intensity, thus, this is reflected as larger pressure peaks. With the consideration of the previously observed cavity structures, this increase in cavitation collapse intensity can also be justified by the collapse mechanism. As it seems, MBS tends to produce a less intense pressure shockwave compared to cases with CBS. Recalling the cavity structures present during the collapse sequences illustrated in Figures 6.5 – 6.9, it has been observed that the collapse of MBS induces a sub-cavity positioned at the sides of the horn tip. It could be suggested that the pressure wave induced by the collapse of the center cavity is dampened by those temporary side cavities. Perhaps, this potentially can be analogous to the shielding effect discussed in [182, 183]. This is because during the cases of CBS, these side cavities no longer govern the collapse of the center cavity, as the collapse mechanism detaches the center cavity from the horn surface. Therefore, this facilitates the radial traveling of the pressure shockwave without experiencing any of the said damping effects.

Evidently, another key difference illustrated between the different diameters is the gradual change of phase and frequency induced by the increase in diameter, as shown in Figure 6.11. It appears that the structural integrity of MBS is rather unstable and thus, it is seen that the growth-collapse cycle occurs quite frequently. Meanwhile, the CBS that appears under the 13 mm, 16 mm, and 19 mm horn tips demonstrates a longer lifecycle, where the structure grows gradually but rather steadily. Previous studies have argued that small horns tend to experience highly aggressive and turbulent flows proximal to the horn tip [152, 184]. Therefore, it would be reasonable to suggest that the cavity structures found under small horns are frequently broken down due to high turbulence.

6.3.4 Analysis of the Toroidal Vortex Lifecycle

To garner further insight on the source of this turbulence and its flow attributes, initial qualitative observations must be made to develop a preliminary idea of the type of flow proximal to the horn tip. Referring back to Figures 6.5 – 6.9, a recurring theme can be deduced and that there always exists a strong presence of some toroidal vortex within the vicinity of the horn tips. Interestingly, this vortex tends to morph and experience a series of transfigurations in its eccentricity and size depending on the horn tip size. After examining the progression of the toroidal vortex in each of the horn tip cases, two general vortex development trends were extracted and summarized in Figure 6.12 below.

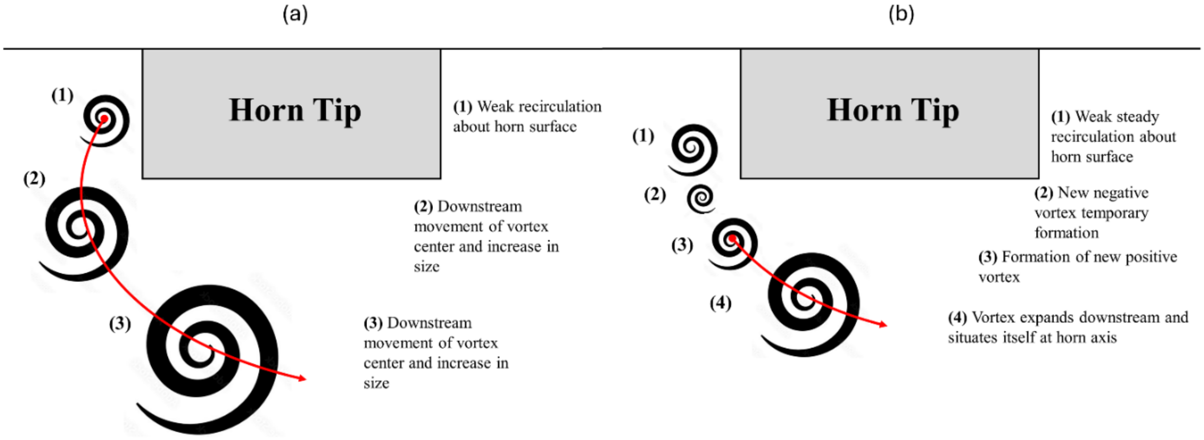

Figure 6.12: A schematic diagram of the fluid subdomain within the vicinity of the horn tip showing the progression of the toroidal vortex in cases of (a) small horn tip diameters, namely 3, 6 mm and 13 mm and (b) large horn tip diameters, such as 16 and 19 mm. The red arrow in both diagrams highlights the trajectory of the vortex.

In the case of small horn tip diameters, it has been observed that the toroidal vortex maintains a consistent behavior. Generally, the toroidal vortex starts as an attached minute recirculation zone on the horn wall due to the ramming oscillatory motion of the horn tip in the aqueous medium. This recirculation then begins to gradually expand in size and march downstream towards the horn tip axis of symmetry. The vortex finally settles at the horn tip axis and reaches its maximum size threshold, before beginning abruptly dissipating at the end of the cavitation collapse phase. On the other hand, the vortex found under larger horn tips behaves quite differently. Essentially, the vortex initialization still sources from the recirculation zone induced by the horn tip motion; however, with the expansion of the vortex, it is seen to stay in place instead. This recirculation then generates a short-lived vortex rotating counterclockwise. With its gradual dissipation, a new vortex emerges closer to the horn tip axes, where it is seen to grow. Though, an important feature to note is that the initial side recirculation remains present during the growth of the secondary vortex near the horn axis.

Upon establishing the general fact that the toroidal vortex has a dynamic behavior of expanding and relocating, the vortex center and the vortex size were tracked against dimensionless time, as demonstrated in the MATLAB code in Appendix E, to draw signals that highlight the vortex trajectory, vortex dimensionless length, and frequency of motion. These signals have been compiled and presented in Figures 6.13 and 6.14 below. The normalized vortex diameter has been evaluated by taking the recirculation length (ϕ_v), measured by the distance between two inflection points of high radial velocity along the axial direction, and normalizing it against the respective horn tip diameter (ϕ_h) of the evaluated case.

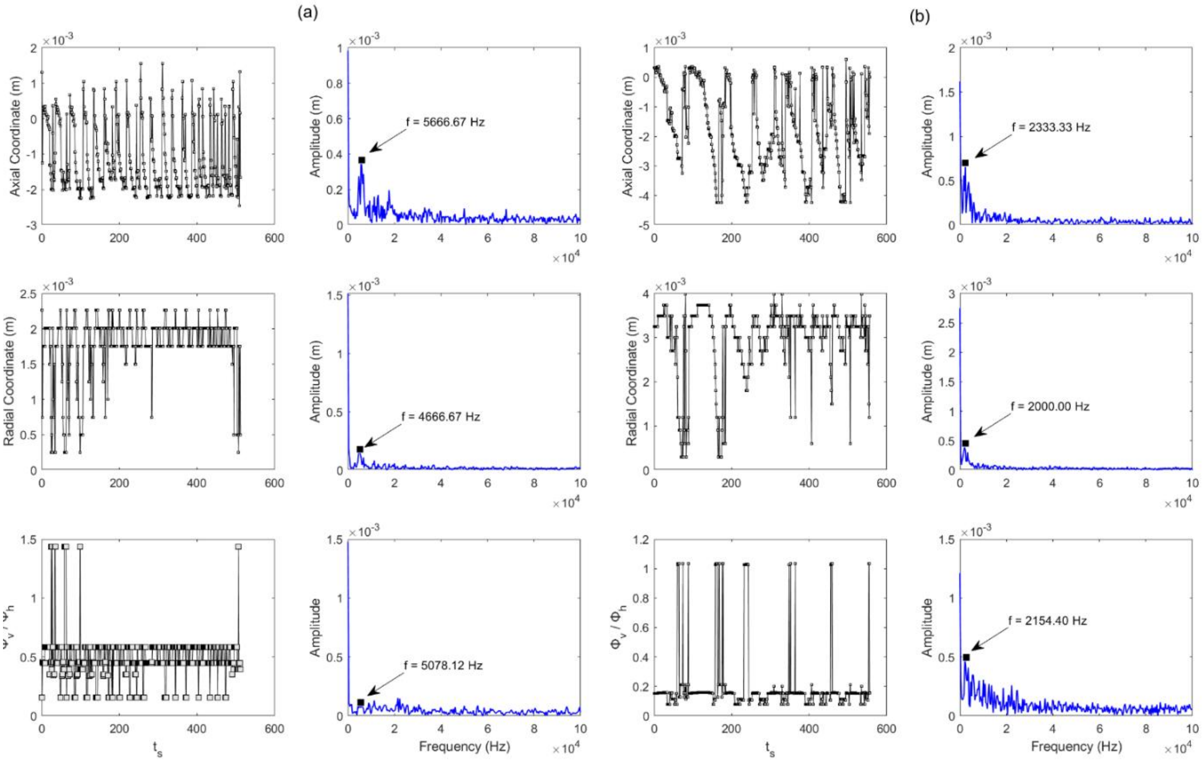

Figure 6.13: Plots of transient signals of vortex center cylindrical coordinates and normalized vortex diameter drawn for cases (a) 3 mm horn tip and (b) 6 mm horn tip. The frequencies of each of the complex signals were extracted through implementations of FFT.

At first glance, a few obvious trends can be immediately spotted, for instance, both the vortex movement, in the radial and axial direction, and its expansion-contraction cycle decrease in frequency with increasing horn diameters. Furthermore, an increasingly apparent jitter appears in the motion and development of the vortex with the increase in size of the horn tip. These observations are qualitatively represented by the surface streamlines in Figures 6.5 – 6.9, where the vortices formed in proximity to small horn tips appear rather steady in their growth. In other words, the trajectory of their development does not involve any form of sub-expansionary-contractionary cycles, instead, the vortex continues to expand in size and move downstream in position until it settles at its final location before dissipating and marking the end of its lifecycle. Interestingly, vortices of small horn tips tend to frequently march in the axial direction downstream of the horn relative to the radial direction. With the 3 mm horn tip, the vortex center moves in the axial direction at a frequency of 5.67 kHz, compared to the 4.67 kHz locomotion frequency in the radial direction. Similarly, the vortices under the 6 mm horn tip are shown to march axially at a frequency of 2.33 kHz compared to the 2.00 kHz radially. However, the reversal of this trend occurs upon enlarging the horn tips. This transition is marked by the 13 mm horn tip, where surprisingly, the vortex moves in both directions at the same exact frequency of 1.33 kHz. However, moving forward, the 16 mm and the 19 mm horn tips demonstrate a bias towards the radial direction where their oscillation maintained a frequency of 1.67 kHz and 2.33 kHz, respectively. Interestingly, the effect of this directional preference is seen to govern the growth of the vortex.

It is rather intriguing to observe that the vortices under the small horn tips are significantly larger than those formed under large horn tips. Under the 3 mm and 6 mm tips, the vortices can reach a size ranging from 1.0 to 1.5 times the tip diameter. However, with larger tips, the vortices maximum lengths become limited to a range between 0.3 to 0.6 times their respective tip diameters. Recalling that these values of vortex diameters represent the vortices' axial expansion, it is then understood that the decreasing trend observed can indicate a change in the vortices' eccentricity. As a matter of fact, the streamlines in Figures 6.5 – 6.9 do indicate changing vortex morphology. It is rather intriguing to observe that the vortices respective to the small horn tips appear rather symmetrical and do not present any significant asymmetry or eccentricity during their lifecycle. Meanwhile, the vortices present under larger horn tips demonstrate more volatility in shapeshifting. Initially, these vortices form symmetrically and share a circular shape, however, with their progression, the vortices are seen to fidget and stretch radially in parallel to the horn tip surface, as they relocate underneath the tip surface. Finally, the vortex is then observed to stretch in the axial direction [172, 185]. A potential explanation of this categorized vortex behaviour is its strong attribution to the presence and sustenance of the negative pressure gradient under the horn tip. With larger horn tips, the attached cavity appears flatter and appears to sustain the instantaneous negative pressure gradient for longer periods of time. The flow motion dynamic composed of a 'push' by the ultrasonic horn and a 'pull' by the negative pressure gradient field, sustains the presence of the vortex and positions it at the horn axis, where the pressure nodes are most prominent.

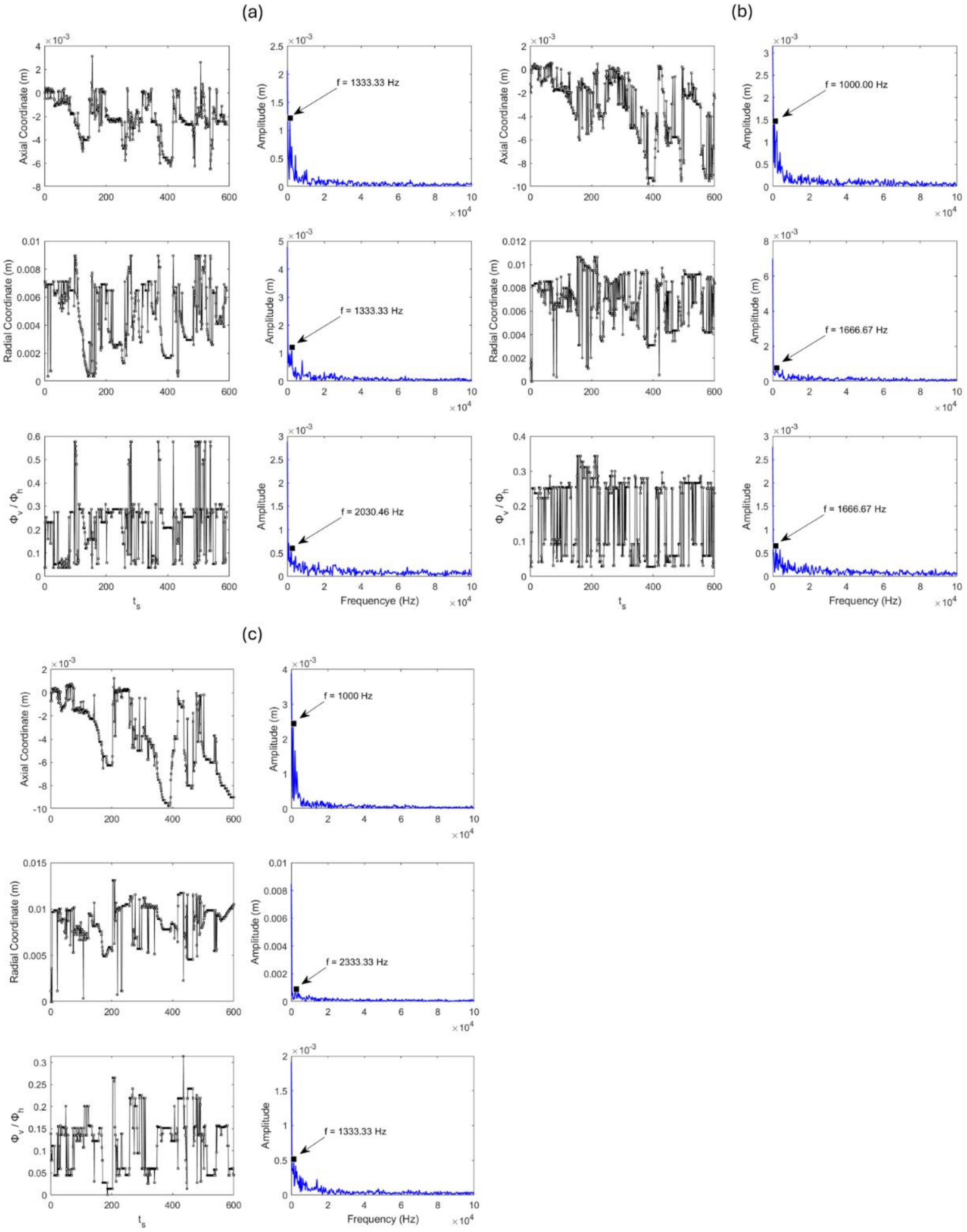

Figure 6.14: Plots of transient signals of vortex center cylindrical coordinates and normalized vortex diameter drawn for cases (a) 13 mm horn tip (b) 16 mm horn tip and (c) 19 mm horn tip. The frequencies of each of the complex signals were extracted through implementations of FFT.

6.3.5 Uncovering the Influence of the Toroidal Vortex Morphology on Cavitation Growth

Based on the previous observations made in Section 3.2, the difference between MBS and CBS is the diameter of the cavity's base and the axial length of the cavity's downstream reach. Essentially, MBS is described as having a small length-to-diameter ratio while CBS is vice versa. Therefore, the maximum growth of the cavities observed can be generalized by the drawing presented in Figure 6.15.

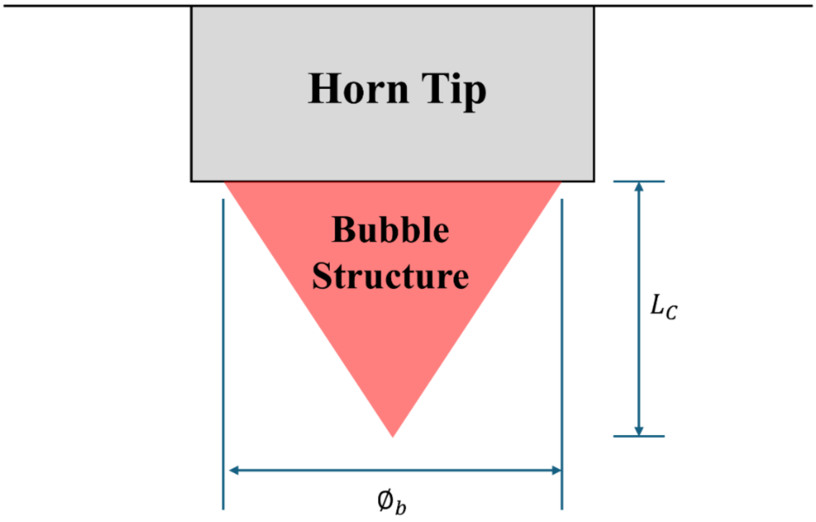

Figure 6.15: A generalized schematic of the common bubble macrostructure observed under the horn tips illustrating key geometrical features, namely the axial length of reach, l, and diameter of attached cavity's base, ϕ_b.

Thus, in an attempt to align the trends observed by the cavitation and vortex structures under small and large horn tips, the maximum vortex and cavitation sizes have been extracted for each horn tip geometry to assess the existence of an underlying trend between the vortex and the cavitation sizes. This was performed by extracting a series of vortex diameter and cavitation volume maxima under each horn tip and plotting the trends, as shown in Figure 6.16.

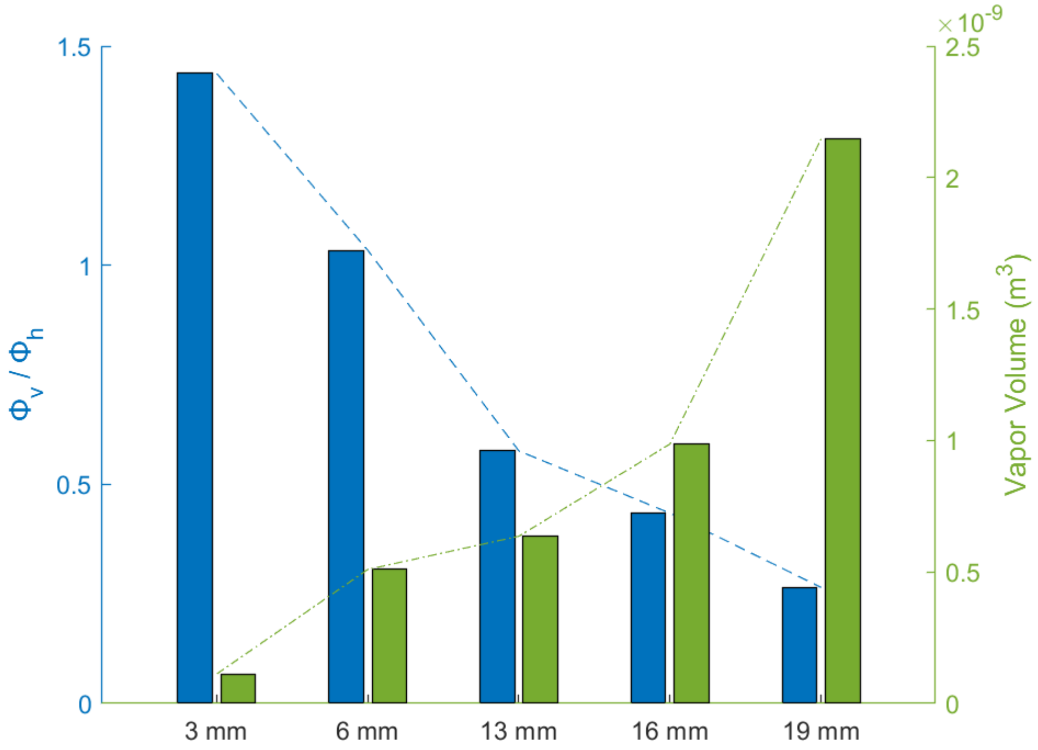

Figure 6.16: Bar graphs and trendlines highlighting the change in the maximum normalized vortex diameter and maximum vapor volume for each respective horn tip size.

From what it seems, the vortex diameter maintains an inversely proportional relationship with the vapor volume produced under the horn tip. To reiterate previously mentioned conclusions, the increase of the horn tip diameter induces a gradual, linear-like decrease in the vortex size. Moreover, this increase in horn tip size leads to an increased vapor-filled volume under the horn tip. In reference to the aforementioned bubble structures, namely MBS and CBS, in Section 6.1, it can be categorically said that the large symmetrical vortex structures mold the cavity structure into this mushroom-like bubble structure. Perhaps, the equidistant extension of the vortex structure in the radial and axial directions exerts significant axial pressure on the bubble structure, limiting its growth in the axial direction and depressing it against the horn tip surface. However, the bubble structure takes form by expanding radially instead. In retrospect to Section 6.1, these observations of cavitation structure transitions were observed in prior works, where such transitions were initialized by the medium content and its temperature under the same horn tip diameter [173]. With the presented study, the underlying role of the horn tip diameter in assisting this transition is uncovered upon increasing the diameter while keeping remaining control variables constant. This strongly indicates that the diameter plays a role in the acoustic energy distribution about the radiating surface area, which ultimately manipulates the pressure distribution and flow structures in proximity to the horn.

When moving from 3 mm to 13 mm, the trend begins to noticeably differ. In Figure 6.16, it is highlighted that the vapor structure increases in volume upon a drastic drop in the vortex size. This is also reflected in Figure 6.7, in which the vortex seems to examine its first dynamic in eccentricity. The vortex initially appears symmetrical when forming itself on the side, however, it becomes progressively eccentric in the radial direction as it progresses in front of the horn tip. During that stage, the cavitation structure appears to struggle to grow outward and remains flattened against the tip surface. However, the vortex changes the direction of its eccentricity shifting it from eccentrically radial to axial. Upon that occurrence, the pressure exerted on the cavity structure is gradually released, and the cavity center is allowed to grow axially. Interestingly, this growth formation appears to take a cone-shape, as discussed earlier. This may be due to the radial pressure exerted on the cavity structure molding it the bubble structure into a cone. In similar fashion, the same vortex-cavitation structural dynamic is observed in the 16 mm and the 19 mm horn tips. This is also reflected in the trendlines in Figure 6.16, in which vapor volume proceeds to increase, while vortex size continues to decrease. However, away from qualitative deduction, Figure 6.17 quantifies the dimensions of the cavity structures indicated in Figure 6.15, at their maximum instances, observed under each horn tip and tracks the change in dimensions with respect to the size of the vortex.

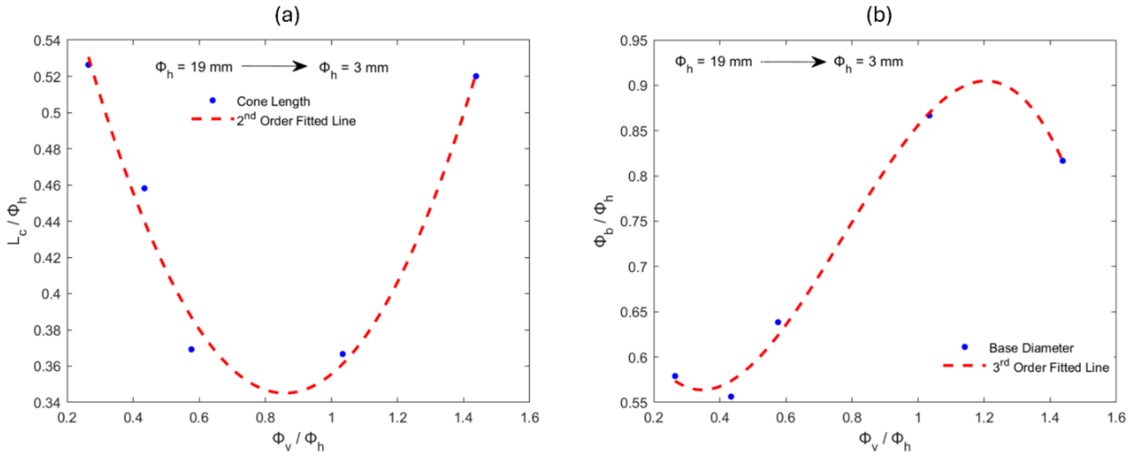

Figure 6.17: Diagrams of fitted lines along datapoints plotted for (a) normalized structure length and (b) normalized structural base diameter against the normalized vortex diameter. Each point represents the dimension of the maximum cavity structure obtained under its respective horn tip size. The normalization was performed using varying ϕ_h. The points represent a decreasing horn tip from left to right.

Interestingly, it appears that the vortex structure affects the cavity structure very distinctly. The influence of the vortex size on the base diameter and the length of the bubble structure is rather different. Looking at the structure length, based on the fittings of the datapoints, it seems that the increase in the vortex size, with respect to the respective horn size, has a parabolic effect on the cavity's length. Furthermore, the normalized structure length seems to be rather equivalent approximately equating to $L_C/\phi_h = 0.53$ at $\phi_V/\phi_h = \begin{cases} 0.22, & \phi_h = 19\ mm \\ 1.43, & \phi_h = 3\ mm \end{cases}$. However, based on the observations made in the previous sections, this increase in in the length when $\phi_V/\phi_h = 0.22$ can be interpreted as it being due to the decrease in the vortex's eccentricity in the axial direction and expanding in the radial direction instead. This coincides with the observations made for the case of $\phi_V/\phi_h = 1.43$, thus, highlighting the role of the vortices' eccentricity in influencing the cavity's axial length. Moving forward, the decrease in the vortex size seems to lead to a temporary drop in the vortex length, before it rises again.

However, looking at the influence of the vortex diameter on the base diameter of the attached cavity, a distinctly different trend is observed. It seems that the increase in the vortex size induces a general growth in the cavity base diameter. Similar to the previous analysis, the radial eccentricity here seems to play its role in controlling the base diameter, as well. Interestingly, the parabolic trend previously observed does not carry forward when examining the base diameter, despite similar eccentricities for the small and large vortices. However, upon factoring in the horn tip diameter, things become much clearer. In supplement to the qualitative observations made, the vortices present at large tip diameters are relatively smaller, and thus their radial eccentricity is considered local to the center of the horn tip. As such, the radial pressure applied by the vortex is seen to strongly contain the cavity structure within the horn tip center. On the other hand, smaller horn tips, i.e. 3 mm and 6 mm, are seen to experience relatively larger vortices, in which their radial eccentric structure expands beyond the horn tip, approximately 1.0 to 1.5 times the horn tip size for the 6 mm and 3 mm horn tips, respectively. Therefore, the radial pressure is no longer localized and is seen to spread the cavity against the entire horn tip surface. To examine the overall effect of the vortex on the cavity structure, Table 6.2 summarizes the vortex and cavity structure dimensions and evaluates the resultant aspect ratio (AR) of the cavity structure found under each horn tip calculated as follows. This highlights that MBS is essentially a lumped cone-like structure with a small AR.

$$AR = {}^{L_c}/_{\phi_B} \quad (6.2)$$

The insight provided by this term is the decreasing trend increase in symmetricity of the cavity structure with the increase of the horn tip diameter.

Table 6.2: Summary of the vortex and cavity structural dimensions with respect to the horn tip diameter.

ϕ_h, mm	${}^{\phi_V}/_{\phi_h}$	${}^{\phi_B}/_{\phi_h}$	${}^{L_c}/_{\phi_h}$	ϕ_V, mm	ϕ_B, mm	L_C, mm	AR
3	1.44	0.82	0.52	4.31	2.50	1.56	0.62
6	1.03	0.87	0.37	6.20	5.20	2.20	0.42
13	0.58	0.64	0.37	7.49	8.30	4.80	0.58
16	0.43	0.55	0.46	6.95	8.90	7.33	0.82
19	0.26	0.58	0.53	5.03	11.00	10.00	0.91

6.3.6 Examining the Governance of the Toroidal Vortex on Cavitation Collapse

It has been established that the vortex structure has a significant potential role in governing the growth of the cavity structure under the horn tip in ways that set specific limits in its growth direction and extension. However, the role of the vortex in the cavity's collapse remains ambiguous. Based on the shared conclusions of many previous studies, the collapse of the cavitation structure generated under the horn tip is typically initialized by a dent induced by the formation of an impinging jet. However, the source and formation of this jet is yet unknown. It can be speculated that due to the nature of the vortex and its consistent proximal position near the horn tip surface, the vortex may play a role in redirecting flow. Therefore, a set of vector plots to track the flow field is shown in Figure 6.18.

Figure 6.18 illustrates a couple of frames for each horn tip size, where the frames in the left column represent the instance at which cavitation reaches a maximum in the growth-collapse cycle. Meanwhile, the right column shows a set of frames that shows the instance at which the collapse cycle first commences. The focus here is to highlight the vortex structure in each of the cycle scenarios under each horn tip. At maximum growth, the vortices appear to contour around the attached cavity creating a dent into the vortex structure. In other words, the flow directed by the vortex curves around the borders of the cavity. This observation is found to be consistent in all cavity formations found under every horn tip. However, during the initiation of the cavity collapse phase, the vortex is simultaneously seen to redirect flow through the vapor zone and impinging the cavity structure. It is crucial to note that the cavitation's structural scattering in larger horn tip groups, such as 13 mm and above, may be due to the designated displacement shape of the horn tip. Recalling that the horn tip motion was defined as a uniformly displacing sinusoidal motion for all cases, this eliminates any potentially significant effects from the neglected flexural motion on the acoustic energy distribution. In turn, its influence on the radial behaviour of the cavitation structure is not captured. Additionally, judging from the velocity contour plots, the consistent congregation of these counter-rotating vortices about the horn axis appears to be due to the axial acoustic streaming flow (discussed further in Section 7) and its resultant radial pressure gradient driving the flow inward. This is facilitated by the axisymmetric geometry of the horn tip, as any off-axis vortex would be unstable and decay, while the central vortex pair is self-sustained by the streaming field.

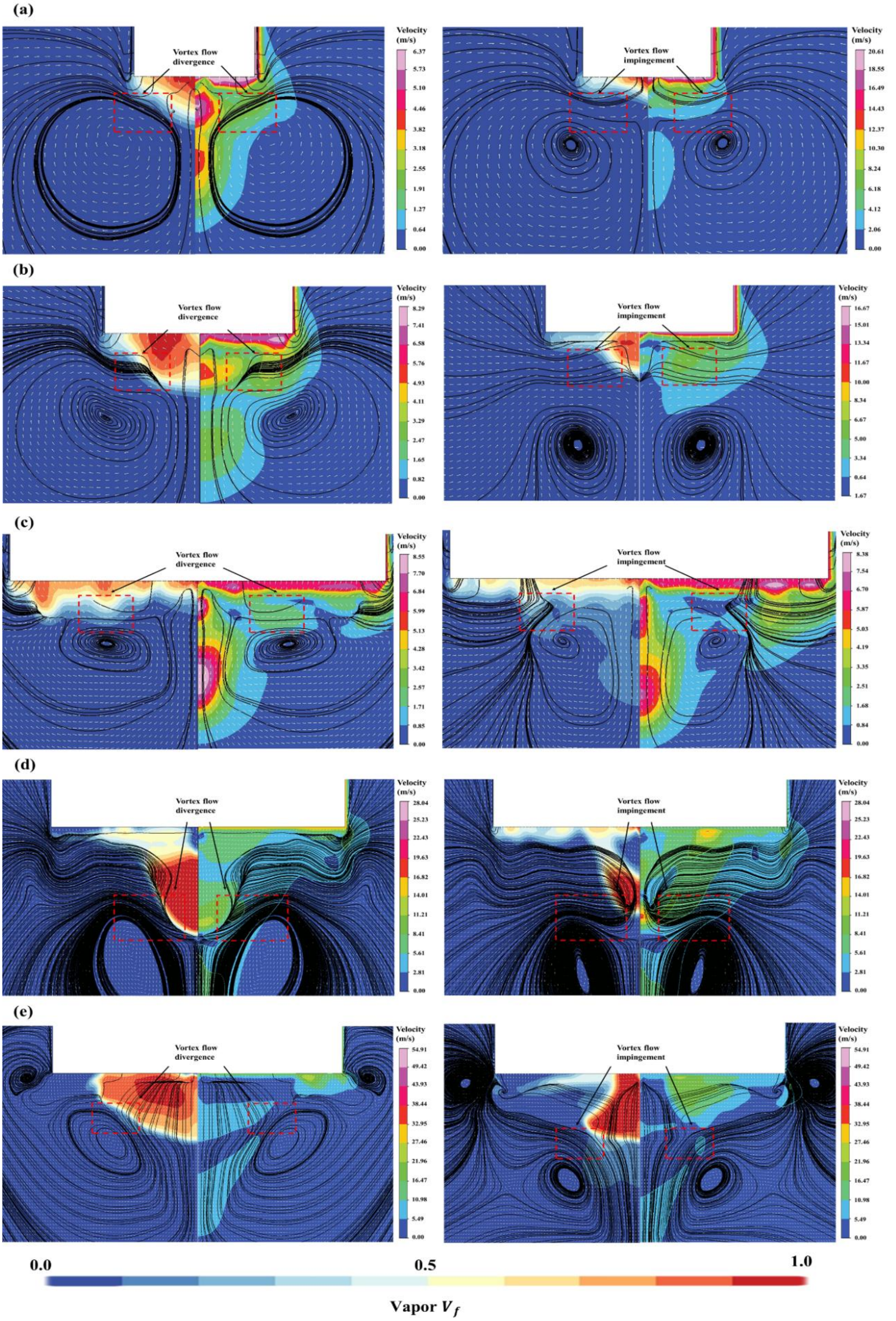

Figure 6.18: Vector and streamline plots at instances of maximum cavity growth (left column) and cavity collapse (right column) for each of (a) 3 mm (b) 6 mm (c) 13 mm (d) 16 mm (e) and 19 mm.

This divergence and impingement flow behavior of the liquid phase can perhaps be justified by a potential compressibility effect of the vapor phase. However, in attempts to justify this flow behavior, an analogous method taken from coaxial flow analyses has been adopted here. More specifically, the momentum ratio (MR) has been calculated to evaluate the vortex-directed flow's ability to impinge the cavity structure. MR here is defined as [186]:

$$MR = \frac{\rho_{vapor} U_{a,vapor}{}^2}{\rho_{liquid} U_{a,liquid}{}^2} \tag{6.3}$$

Where ρ_{vapor} and ρ_{liquid} are the water vapor and water liquid phase densities, respectively. $U_{a,vapor}$ and $U_{a,liquid}$ here are the axial velocities for the vapor and liquid phase, respectively. The extraction of these velocity values was performed by identifying the first point of contact between the two phases, namely the liquid and vapor, and extracting the axial component of velocity for each phase. With these values, MR is then calculated and plotted against horn tip diameter to observe the trendlines in Figure 6.19. The trendlines observed for both the diverging and impinging jet instances demonstrate similar trends; however, each with a different meaning. The diverging line refers to the scenario in which the vortex is seen to curve or 'diverge' around the cavity structure, while the impinging line refers to the scenario in which the vortex flow penetrates the cavity structure. The decreasing diverging trendline, with the increase of the horn tip diameter, indicates that the cavity structure's ability in diverting the vortex-directed jet drops. Relatively, the decreasing trend of the impinging line dictates that the vortex-directed jet increases in strength.

As such, the momentum ratio highlights a possible explanation of the role of the vortex in redirecting flow into the cavity structure, in which it initializes the collapse phase of the cavity. It is crucial to note that the vortex expansion-contraction frequencies highlighted in Figures 6.13 and 6.14 almost always tend to fall close within the subharmonic frequency range of the cavitation pressure and volume signals provided in Figure 6.10. This could in fact be a solid indicator for the strong underlying correlation the vortex development has with the cavitation structural development. However, while it is typically known that correlation does not automatically mean causation, however, the vortex has been seen to hold a share in governing the collapse mechanism of the acoustic cavity.

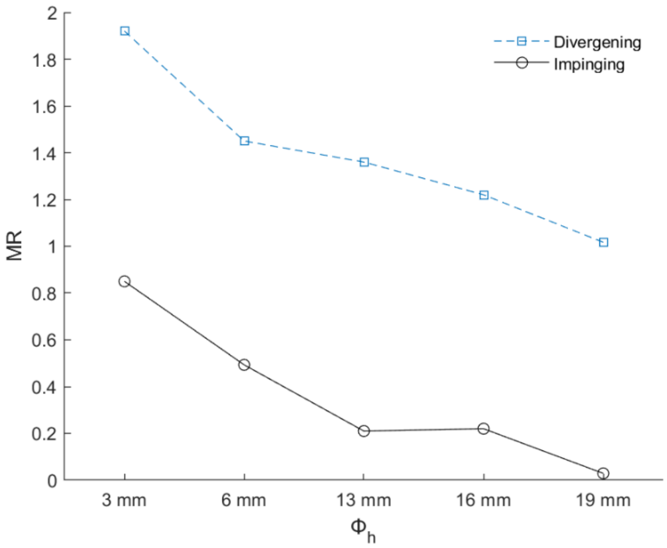

Figure 6.19: Momentum ratio trendlines for cases of diverging and impinging water liquid jet flows.

6.4 Conclusion

The present study has demonstrated a thorough numerical investigation that scrutinized the role of the typically observed toroidal vortex in governing the cavitation structure produced under the ultrasonic horn tip. Multiple horn tip diameters, categorically labelled as small and large horn tips, have been explored to identify the role and behaviour of the vortex in molding the cavity. This was inspired by the recurring observations made in previous studies where small horn tips tend to establish a mushroom-like bubble structure while larger horn tips facilitate the growth of a cone-like bubble structure. Thus, it was of great interest to observe whether the toroidal vortex has any involvement in this phenomenon.

This chapter delved into the origin of the toroidal vortex by conducting a modal analysis of the horn tip and identifying the mode shape at the typical vibration frequency of 20 kHz. Moreover, the parametric analysis conducted has identified the general vortex structural progression trends under small and large horn tips. It has been observed that the vortex tends to initialize at the side of the horn as a recirculation zone induced by the horn tip vibration, where it later enlarges and marches around the horn tip and toward the horn tip axis. The primary differences in the vortex behaviour in small and large horn tips fell within the vortex size and eccentricity. Under small horn tips, the toroidal vortex tends to be symmetrical and significantly large with respect to the horn tip size. Meanwhile, large horn tips witness toroidal vortices that undergo two stages of eccentricity changes, starting with eccentricity in the radial direction followed by eccentricity in the axial direction.

It has been determined that these structural behaviours govern the cavity structure's shape, growth, and collapse. The MBS adopted by cavities under small horn tips is partially due to the vortex's occupation of the axial space downstream of the cavity. Thus, the cavity's axial expansion is limited, and instead, the cavity is seen to extend radially covering the horn tip surface. Meanwhile, CBS observed under large horn tips is plausibly molded by the eccentric vortex present within its vicinity. Based on the orientation of the vortex eccentricity, the cavity structural growth is limited accordingly. Upon having the vortex take up a radially eccentric stance, the cavity structure is seen strongly depressed against the horn tip surface limited from growing outwards. However, with the gradual axial shift in vortex position and eccentricity, the cavity clouds are pushed and pinched toward the horn axis forming the commonly witnessed cone-like structure.

Moreover, the collapse of the cavity structure, both MBS and CBS, is shown to be governed by the impinging jet directed by the proximal toroidal vortex. An attempt to justify the instance of impingement was conducted by evaluating the momentum ratio between the vapor and water liquid momentum. Once the vapor structure is seen to lose momentum and the vortex gaining momentum, the impingement becomes successful agitating the cavity structure and initializing its collapse.

7 Time-averaged Early Stagnation Point Formations during Transient Acoustic Cavitation

7.1 Introduction

The aforementioned CFD results have highlighted that the sonoreactor geometry plays a major role in inhibiting or enhancing sonochemical reactions, which is essentially in line with a multitude of pervious observations [187-189]. Thus, in the previous CFD studies, the underlying influence of the horn tip surface area on the inertial bubble self-organizing capacity during the transient state of the reactor was scrutinized [190]. Generally, the role of the proximal toroidal vortex, a product of a developing acoustic streaming, on the inertial cavitation development was hypothesized. As observed, one of the key observations made was the dimensional variation of the cluster's shape; the aspect ratio (AR) approaches unity with larger diameters, as the dimensionless vortex length shortens, with the increase of the horn tip diameter (D). While this is rather an eye-catching trend, it is crucial to note that these instantaneous readings have been recorded at transient cavitation growth amplitudes and may not precisely reflect the reality of the trend.

Therefore, as part of a deeper scrutiny of the phenomenon, we have attempted time-averaging the flow. To our surprise, however, we found that the extent at which the stream-linked vortex produced under all reactor cases reached their respective stagnation plane at a distance of 2D away from the horn tip. We have therefore, in addition to reporting our own results, attempted what we hope to be a numerical justification of the observed phenomenon through a mathematical formulation based on the Stuart streaming conservation of momentum and its respective definition of the acoustic force ($\overrightarrow{F_a}$). What follows is a comparison between a parametric one-dimensional iterative calculation and the two-dimensional computational fluid dynamics (CFD) simulation conducted in our aforementioned work. We are keen to hypothesize that there exists a two-way coupling between the time-averaged bubble cluster shape and the said distance of stagnation. More specifically, the one-dimensional model will facilitate the unravelling of the underlying role of effective cavitation-based attenuation on the acoustic wave propagation that may justify the halting of axial flow and the development of the stagnation plane. This investigation would, in turn, provide further insight on the flow mechanism and transportation of inertial cavity bubbles, which are commonly known to play a vital role in facilitating ultrasonic-assisted process intensification [191-193].

7.2 Streaming Modelling and Flow Dynamics

The inherent nonlinear behaviour a fluid adopts, upon the imposition of an ultrasonic field, has been enriched with decades of research. This scrutiny of the underlying two-way coupling between acoustics and hydrodynamics has led to the definition of a well-developed area of acoustofluidics known as acoustic streaming. Essentially, the term refers to the steady Stokes drift component upon decomposing the fluid's reaction to some periodic stimulation. In simple terms, it is the establishment of a steady-state vortical jet, or 'stream', accompanying the ultrasonic wave propagation to some point of stagnation [194]. With the extensive scrutiny acoustic streaming underwent, many authors have made key contributions to stitch up a string of governing equations that, in turn, provides a complete general solution of the flow problem. Rayleigh [195], for instance, has made an attempt on this multi-physics flow problem by resolving the second-order average velocity produced by the proximal behaviour of the fluid near a plate. Adhering to that, both Nyborg [196] and Westervelt [197] highlighted a multitude of cases where Rayleigh's base interpretation of streaming holds true. Essentially, it has been highlighted that this type of streaming is typically observed in standing wave systems with wavelength-scale channels ($L/\lambda \approx 1$) [198]. However, the nature of the said Rayleigh-Nyborg-Westervelt (RNW) streaming theory is its negligence of fluid inertia effects and thus making this theory exclusively applicable to slow flows, otherwise known as 'creeping motion' [199-201]. It is known that this kind of streaming is only observed in reactors with significantly low acoustic power sources falling within micro-watts [202]. In aims to capture the streaming's large Reynolds asymptotic behaviour, Lighthill [203] established the Reynolds stress approach by linking the flow turbulence with acoustic perturbations defining what is known now as 'Stuart streaming'.

Practically speaking, Stuart streaming is more commonly found in industrial applications of sonochemical reactors, as such systems operate at relatively high acoustic power. The nature of this streaming is justified as a steady flow that is induced by the attenuation of transverse acoustic waves in the present fluid domain [202, 204]. While streaming is a ubiquitous acoustofluidic phenomenon, the nature of the fluid can influence the strength of the presence of acoustic streaming. Primarily, a strong damping effect of acoustic streaming was clearly observed in inhomogeneous fluids due the presence of a density gradient caused by a solute concentration field [194, 205]. Such damping can also occur in homogeneous fluids, however, it would require specifically shaped confinements, or channels, for this to occur [206]. Nevertheless, the acoustic attenuation that drives this streaming sources from all composites of the fluid domain; it can be the compound absorption property of a multi-phase fluid domain, for instance. More specifically, the bubbly phase generated as a byproduct of the ultrasonic source's periodic stimulation has been shown to be a primary contributor to the acoustic attenuation.

Given that these resonating bubbles heavily influence both density and compressibility of the domain, the viscous losses are deemed negligible. Therefore, this implied variation in the speed of sound then induces the reflection, absorption, and scattering of the acoustic energy away from the initial sound beam directed from the ultrasonic source [207]. Surely, the present quantity of resonating bubbles within the vicinity of the sound beam is a decisive factor on the degree of its attenuation; however, the question that arises is, what are the factors that then influence the concentration of bubbles about an ultrasonic transducer? Well, the concentrations of bubble cluster formation positively follow an increasing trend in acoustic power. Interestingly, this is based on an established sonochemical fact agreed upon by many, as it has been observed that sonochemiluminiscence (SCL) decreases with the increase in input power [188, 208, 209]. This tends to indicate that there exists a decrease in sonochemical active region volumes [171]. It has been noted that the bubble cluster formations tend to adopt specific shapes at instantaneous times, such as MBS, volcano-like bubble structures (VBS), and more commonly CBS [161]. Biasiori-Poulanges et al. [161], in their investigation, have scrutinized the transient cavity generated under a 12 mm horn-type reactor in aims to visualize and identify the mechanism responsible for the commonly observed CBS.

It has been previously understood that there exists an interaction between neighbouring bubbles where one applies a force, known as the Bjerknes force, on another. Considering that two neighbouring bubbles exist in a strong acoustic field, it can be said that the pressure gradient field is the source of the Bjerknes forces acting from the first bubble on the second bubble. This force can be quantified as $F_{1,2} = -V_2 \nabla P$. It has been deduced that primary and secondary Bjerknes forces play a role the self-organizing 'streamers' and 'acoustic Lichtenberg figures'

[166, 170] at anti-nodal regions [169, 210], and thus it has been analogized to the bubble behaviour during transient cavitation. Conclusions on its step mechanism were that (i) existing single bubbles oscillate at amplitudes overcoming their interface repelling force, (ii) single bubbles then deform and merge with one another to form a cloud, (iii) and lastly the cloud is molded into the cone shape due to the radial pressure distribution along the horn tip.

7.3 One-dimensional Mathematical Formulation

This section focuses on translating the fluid problem tackled in Chapter 6 to a one-dimensional problem by considering the proximal flow induced by the horn vibration, as shown in Figure 7.1. The developing flow, attributed to the transient cavitation state, was observed to consistently flow towards some stagnation point, z = 0, positioned at l = 2D and proceed to outwardly flow in the radial direction with axial symmetry to form the proximal toroidal vortices. However, we reiterate that this observation has been made upon time-averaging the flow for each geometrical case. Thus, it is desired to unfold this trend by focusing on developing a one-dimensional formulation to track the variation in the axial flow. Essentially, this formulation isolates axial flow dynamics and its variation with acoustic forcing sourcing from the radiating surface, while neglecting azimuthal and radial flow instabilities. As such, any radial flow variations, sourcing from the previously acknowledge counter-rotating vortices are assumed negligible. Upon eliminating the transient term, we utilize definitions of continuity and conservation of momentum for a steady flow with the aforementioned fluid mixture properties. We have also safely assumed a no-slip boundary at the horn tip based on many observations made on the radial profile [171, 201]. Lastly, the flat profile nature of the axial velocity was approximated for our case for mathematical modelling convenience [184].

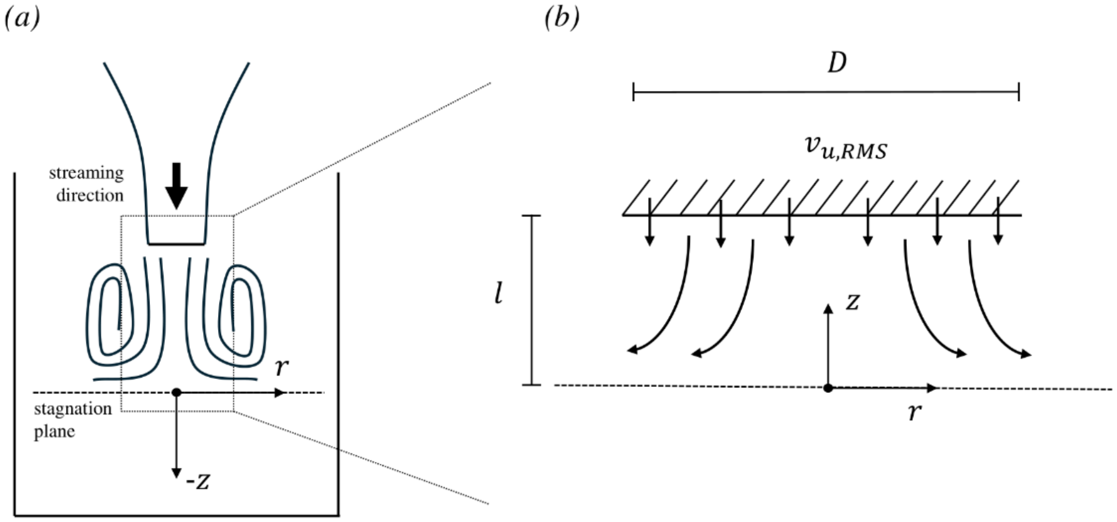

Figure 7.1: A schematic of the axisymmetric flow configuration, with respect to the cylindrical coordinate system, observed in all considered horn diameter cases. (a) An overview of the time-averaged flow during transient cavitation highlighting the developing acoustic streaming and the stagnation plane encountered. (b) A detailed picture of the flow profile in proximity to the horn tip of diameter D and the position of the stagnation plane at a distance l from the horn tip surface.

The flow field and pressure distribution governing equations are then laid out as the continuity

$$\frac{1}{r}\frac{\partial}{\partial r}(r\,v_r)+\frac{\partial}{\partial z}v_z=0 \tag{7.1}$$

conservation of r-momentum

$$\rho_m\left(v_r\frac{\partial v_r}{\partial r}+v_z\frac{\partial v_r}{\partial z}\right)=-\frac{\partial p}{\partial r}+\mu_m\left[\frac{\partial}{\partial r}\left(\frac{1}{r}\frac{\partial}{\partial r}(rv_r)\right)+\frac{\partial^2 v_r}{\partial z^2}\right] \tag{7.2}$$

and conservation of z-momentum

$$\rho_m\left(v_r\frac{\partial v_z}{\partial r}+v_z\frac{\partial v_z}{\partial z}\right)=-\frac{\partial p}{\partial z}+\mu_m\left[\frac{1}{r}\frac{\partial}{\partial r}\left(r\frac{\partial v_z}{\partial r}\right)+\frac{\partial^2 v_z}{\partial z^2}\right]+\rho_m\vec{g}+\overrightarrow{F_a} \tag{7.3}$$

The θ-momentum equation has been neglected due to the initial two-dimensional assumption of the domain. Here, v_z is the flow velocity in the z-direction, ρ_m and μ_m are the fluid mixture density and the fluid mixture dynamic viscosity. The z-momentum equation shows two additional force terms, namely the gravitational force $\rho_m\vec{g}$ and the acoustic force $\overrightarrow{F_a}$. For this problem, however, we neglect the role of the gravitational force on the flow and only consider the propagating acoustic force in the axial domain. Based on Lighthill [211], the acoustic force, in the case of a downstream moving plane wave, is defined as

$$\vec{F_a}=-\frac{\partial\overline{\rho v^2}}{\partial z} \tag{7.4}$$

With the expression of acoustic intensity, I, and establishing the relationship between spatial variation of I and streaming, I is then represented as

$$I=\rho\,c\overline{v^2}=I_0e^{-2\alpha z} \tag{7.5}$$

where ρ is the fluid density, c is the speed of sound, v is the flow velocity, and α is the compound attenuation of the acoustic wave. One can then translate $\overrightarrow{F_a}$ in terms of I where

$$\overrightarrow{F_a}=-\frac{1}{c}\frac{dI}{dz}=\frac{2\alpha}{c}I_0e^{-2\alpha z} \tag{7.6}$$

in which

$$I_0=\frac{P_{a,0}^2}{2\rho c} \tag{7.7}$$

$P_{a,0}$ here is the acoustic pressure at the horn tip surface. Like many acoustic properties in the fluid domain, P_0 experiences adverse attenuation as the plane wave progresses away from the horn tip. Its spatial distribution has been modeled by Yasui et al. [118] about the axis of symmetry such that

$$P_a(z) = \rho c v_{z,0} \left| 2\beta \sin\frac{\pi}{\lambda}\left(\sqrt{z^2 + \left(\frac{D}{2}\right)^2} - z\right)\right| \tag{7.8}$$

Upon taking P_a at z = 0 and replacing in equation 6.6, $\overrightarrow{F_a}$ finally becomes

$$\overrightarrow{F_a} = 4\beta\alpha\rho v_{u,RMS}^2 sin^2\frac{D\pi}{2\lambda}e^{-2\alpha z} \tag{7.9}$$

where $v_{u,RMS}$ is the time-averaged flow velocity, D is the horn tip diameter, and λ is the acoustic wavelength. Taking note of β, it is essentially defined as an under-relaxation term, introduced by Yasui et al. [118], to correct the attenuation of the acoustic wave. This factor was inspired by a comparative study investigating the variation in local bubble radii under an acoustic horn. In our case, however, we have obtained a set of β values through a fitting algorithm, implementing least squares, to satisfy the curve-fitting criterion that ensures the predicted boundary conditions from the two-dimensional CFD simulation are met. Essentially, the criterion was obtained by conducting a validation simulation comparing the numerical results we obtained of a horn reactor of D = 10 mm to the pressure model Yasui et al. [118] obtained. The small resultant percentage error was then extracted and implemented as a benchmark for fittings of the curves of the remaining diameters.

$$v_r = 0 \qquad at\ z = 0 \tag{7.10}$$

$$\frac{\partial v_r}{\partial z} = 0 \qquad at\ z = 0 \tag{7.11}$$

$$\frac{\partial v_r}{\partial z} = 0 \qquad at\ z = l \tag{7.12}$$

$$v_z = -v_{u,RMS} \qquad at\ z = l \tag{7.13}$$

$$P = P_0 \qquad at\ z = 0, r = 0 \tag{7.14}$$

Equations 7.10, 7.11, and 7.12 arise based on observations made in our CFD study, which will be discussed later in section 4 of this chapter, on the extensions of the induced vortical structures during the transient state of the reactor. The stagnation point predicted by our CFD model has revealed that the velocity radial flow profile converges to 0, with respect to the axial coordinate, before accelerating in the radial direction. Interestingly, a strong analogy can be drawn out from the assumed uniformity of the boundary conditions constraining the reactor system to the porous plate system established by Chapman & Bauer [212]. As such, we have adopted the following proven relationship where

$$v_r = r\phi(z) \tag{7.15}$$

Upon replacing this definition in Eq. 7.1, the following definition of v_z is obtained

$$\frac{\partial v_z}{\partial z} = -2\phi(z) \tag{7.16}$$

in which

$$v_z = -2\int_0^z \phi(z)dz \tag{7.17}$$

This way, we have isolated v_z's definition to be only in terms of z. Ultimately, this transforms our boundary conditions to

$$\frac{\partial v_z}{\partial z} = 0 \qquad at\ z = 0 \tag{7.18}$$

$$\frac{\partial^2 v_z}{\partial z^2} = 0 \qquad at\ z = 0 \tag{7.19}$$

$$\frac{\partial^2 v_z}{\partial z^2} = 0 \qquad at\ z = l \tag{7.20}$$

$$v_z = -v_{u,RMS} \qquad at\ z = l \tag{7.21}$$

Furthermore, as our intended model is one-dimensional in the axial direction, Eq. 7.3 is nondimensionalized using the following dimensionless quantities

$$\theta = \frac{v_z}{v_{u,RMS}} \tag{7.22}$$

$$\zeta = \frac{z}{D} \tag{7.23}$$

$$Re = \frac{\rho v_{u,RMS} D}{\mu_m} \tag{7.24}$$

Equation 7.3 then becomes

$$\theta\frac{\partial\theta}{\partial\zeta} - \frac{\mu_m}{\rho_m v_{u,RMS} D}\frac{d^2\theta}{d\zeta^2} = -\frac{1}{\rho_m v_{u,RMS}^2}\frac{\partial p}{\partial\zeta} + 4\beta\alpha D sin^2\left(\frac{\pi D}{2\lambda}\right)e^{-2\alpha D\zeta} \tag{7.25}$$

or

$$\theta\theta' - \frac{1}{Re}\theta'' = D_P + \Gamma C e^{\Gamma\zeta} \tag{7.26}$$

Notably, the process of deriving the nondimensional momentum equation has resulted in the surfacing of three additional nondimensional numbers that are

$$D_P = -\frac{1}{\rho_m v_{u,RMS}^2}\frac{\partial p}{\partial \zeta} \tag{7.27}$$

$$\Gamma = -2\alpha D \tag{7.28}$$

and

$$C = 2\beta sin^2\left(\frac{\pi D}{2\lambda}\right) \tag{7.29}$$

These dimensionless numbers were taken as model constants governed by fluid mixture properties. Firstly, Piercy & Lamb [213] have suggested that the first-order differential term $\frac{\partial p}{\partial z}$ is insignificant, as any observed pressure variation in the system is essentially radiation pressure driven by $\overrightarrow{F_a}$. Thus, the nondimensional pressure D_P here is considered a negligible, yet potentially corrective, constant. Similarly, C resembles an under-relaxation factor for a given D. Based on the nature of the function when taking its limit at $\lim_{D \to 0.016} C(D) = C_{min}$, $\overrightarrow{F_a}$ experiences reduced amplification with the increase of D. Lastly, Γ consists of two terms, α being the compound attenuation coefficient [214] and D. As such, it is defined as the dimensionless compound attenuation.

The solution of Eqns. 7.18 to 7.26 provides the complete analytical solution of the present flow problem. However, the approach we have taken to obtain the exact solution is a more iterative approach, in which we solved Eqn. 7.26 numerically with a finite-differencing method where we created a system of coupled differential equations of an order no greater than one by modifying Eq. 7.26 as such. That is, we define the coupled system starting with a new dimensionless partial differential equation of some function $f(\zeta)$

$$f(\zeta) = \theta'(\zeta) \tag{7.30}$$

such that Eqn. 7.26 becomes

$$\theta f - \frac{1}{Re}f' = D_P - \Gamma C e^{-\Gamma\zeta} \tag{7.31}$$

Additionally, recalling that D_P is a constant,

$$\frac{D_P}{\zeta} = 0 \tag{7.32}$$

Meanwhile, Re, Γ, and C are varied parametrically from case to case. The three equations were then linearized about a trial solution to, ultimately, implement the numerical method designed by Newmann [215]. This facilitates iterative computation of the trial solution until the solution finally meets the residual criterion of 10^{-10}. It is noteworthy to state that convergence has been achieved within 7-50 steps depending on the initial guess used upon initialization. The implementation of this subroutine can be found in Appendix F.

7.4 Results and Discussion

7.4.1 Two-dimensional Flow Approximation

Building upon the previous study's observations [190], we considered the following geometrical variation in horn-type reactors, tabulated in Table 7.1, to assess their overall acoustic and cavitation performances during their transient states. We have fixed the power input, operational frequency, and oscillation amplitude at 49 W, 20 kHz, and 164 μm, respectively, for all cases to isolate the influence of the horn tip diameter on the flow. To draw out this comparison, we performed the transient CFD calculation on all cases to monitor and extract instantaneous velocities at every discretized point along the horn axis. This was followed by computing the RMS velocity at each mesh point of the axis to, ultimately, normalize it against $v_{u,RMS}$. These normalized velocity values were then plotted against the normalized axial length ζ, as it is illustrated in Figure 7.2a. Here, it becomes clear that there exists an unusual flow trajectory, where the agitated flow eventually reaches some point of stagnation $\zeta = 2$ along the axis. Recalling that D sustains a relationship with the acoustic power density P_D such that

$$P_D = \frac{P}{V} = \frac{P}{\frac{1}{4}\pi D^2 H} \tag{7.33}$$

This strikingly highlights that regardless of the size of the volume of influence V the acoustic power transmission reaches, the stagnation plane remains positioned at a distance 2D. It is arguable that the usage of an unsteady RANS model, like SST $k - \omega$, might facilitate this trend by averaging out the turbulent acoustic streaming structures and increasing the rate of decay of the acoustic pressure wave. However, the consistency of this trend under different horn diameters highlights that the effect of the turbulence model is not as pronounced. Ultimately, the only impact the change in D, or P_D, had on flow is the rate of exponential decay the flow experiences as it approaches the said stagnation. In an attempt to garner deeper insight to this trend, we monitored the averaged variation in the RMS vapor volume fraction α_v along the same axial distance to identify any coupled effect, if any, of the vapor structure on the point of stagnation, as shown in Figure 7.2b. Interestingly, and as highlighted by the two instances of inset plots, it was revealed that the vapor structure has no definitive influence on the stagnation point either. The two distinct vapor structure profiles are highlighted in Figure 7.3, where MBS is prominent under the 3 and 6 mm horn tips, while CBS takes shape under the 13 and 16 mm horn tips. However, upon examining the vapor structures' axial extension, we were able to capture the endpoints of cavitation dissipation for each case, as numbered from (1) - (4). It was revealed that these endpoints unanimously coincide with the velocity decay curves' kinks towards $\theta = 0$ for all cases. Such observation reinforced the extent of attenuation the inertial bubbles have on this acoustic force-driven flow. Therefore, we have decided to further scrutinize the vapor-induced attenuation role in influencing the time-averaged flow through a one-dimensional approximation of the axial flow.

Table 7.1: Tabulation of time-averaged velocity, vapor volume fraction for each of the marked points in figure 22 and the power density of each horn geometry.

Marked Points	D (mm)	θ^* (-)	α_v^* (-)	P_D (W/cm^3)
1	3	-0.0434	0.00087	64.785
2	6	-0.0539	0.00065	16.196
3	13	-0.0779	0.00079	3.45
4	16	-0.0881	0.00079	2.278

*extracted values at respective marked points highlighted in Figure 7.2.

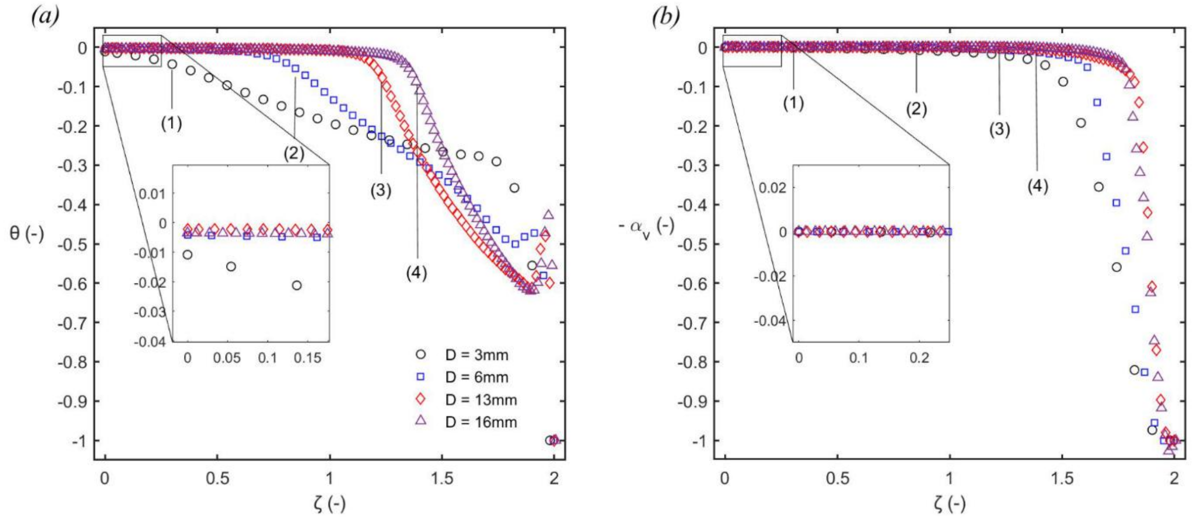

Figure 7.2: (a) Variation of normalized RMS velocity plotted against the downstream axial distance normalized with respect to the horn tip diameter of the respective geometrical case (D = 3, 6, 13, and 16 mm). The inset plot highlights the observed stagnation. (b) Variation of RMS vapor volume fraction along the horn axis, with an inset plot showing the convergence of α_v to 0 at the stagnation point for all cases. Points (1) - (4) highlight the points at which α_v first reaches 0 for cases D = 3 - 16 mm, respectively. ζ is the dimensionless z-position normalized with respect to the tip diameter D for each case.

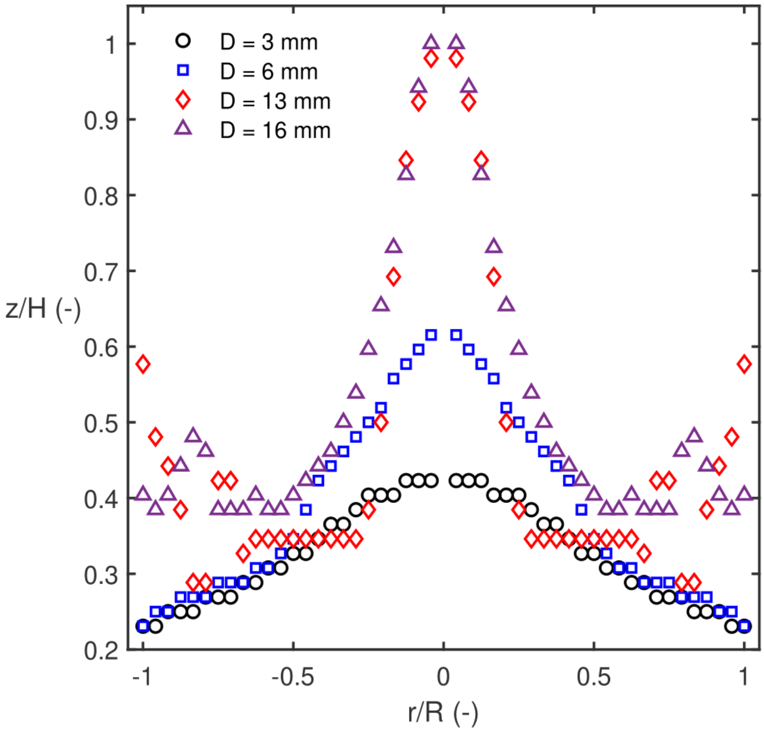

Figure 7.3: Comparative plots illustrating time-averaged bubble cluster structure radial profiles, dimensioned based on their normalized radial and axial position under horn tips of diameters D = 3, 6, 13, and 16 mm. Here, the axial position z is normalized against the maximum height H reached by the profile formed under D = 16 mm, while the radial position r is normalized against the horn tip radius R.

7.4.2 One-dimensional Axial Flow Interpretations

7.4.2.1 Complete Numerical Simulation

Equations 7.30 – 7.32 were solved by constraining the system with their respective boundary conditions from Eqns. 7.18 – 7.21. Moreover, the initialization of the one-dimensional iterative calculation consists of inputting the desired acoustic and domain phase properties, in addition to a set of initial guesses for the equations' unknowns, namely $\frac{d\theta}{d\zeta}$, θ, and D_P. Meanwhile, Re and C were kept as model constants governed by the given flow properties induced in each case; they are computed as per the D of the considered case. As for Γ, while in practice $\Gamma(\alpha, D) = -2\alpha D$, we have manually controlled its variation from case to case through artificially varying α. This is to observe its contribution to the flow behaviour, especially to the stagnation point position, within our numerical region. However, to obtain α of each case, we have utilized the least squares fitting method to essentially optimize the dimensionless attenuation coefficient ensuring a satisfactory fitting of the one-dimensional calculated flow to the numerically-extracted trends shown in Figure 7.4. Technically, we have fixed $\theta = 0$ as a boundary condition at $\zeta = 2$ while keeping the boundary at $\zeta = 0$ free-floating to maintain its dependency on the attenuation coefficient.

In that sense, as the one-dimensional model neglects the plausible effects of bubble-bubble interactions and flows in the radial direction and thus α here may carry underpredicted values that are underpredicted the amplified scattering and attenuation effects induced by bubbles radially positioned about the horn axis. Moreover, various mesh sizes were tested to extrapolate the calculation towards the horn tip boundary. Based on that, we have settled on a discretization composed of 1,000 points. Considering the fact that all our horn-type reactor geometries induce largely turbulent flows, such mesh size was required to capture the boundary layer phenomenon at $\zeta = l$. Mathematically, this is justified by the diminishing effect of the highest-order term due to the high Re.

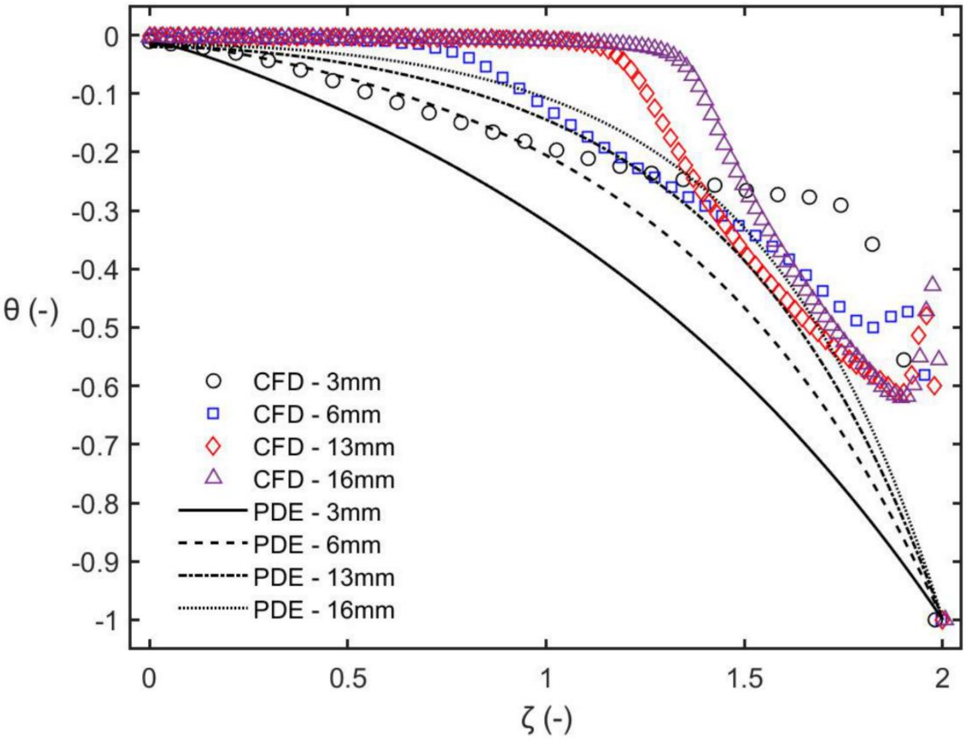

Figure 7.4: Comparative plot between the variation of normalized RMS velocity against the normalized downstream axial predicted by the CFD computation and the one-dimensional (PDE) calculation for various horn reactor cases, D = 3, 6, 13, and 16 mm. ζ is the dimensionless z-position normalized with respect to the tip diameter D for each case.

As demonstrated in Figure 7.4, we performed a validation comparing the trends predicted by the one-dimensional steady flow model and the two-dimensional time-averaged transient CFD model. While the predicted one-dimensional trends do in fact come across as reasonably satisfactory, it seems, however, that there is a noticeable discrepancy in the θ magnitudes. This can be potentially justified by the one-dimensional model's dismissal of any small, yet noticeable, transient, or more specifically turbulent, components of the acoustically-driven flow [216]. Moreover, this justification is complicit with the results presented in the numerical exploration conducted by Dentry et al. [217], where they observed that a turbulent-dominant jet tends to lead to a marginally faster streaming decay. However, as the curves' slopes are, nevertheless, well-captured within the region $0.75 < \zeta < 2$, we speculate that the steady component here does in fact play a major role in the overall axial flow examined under the horn.

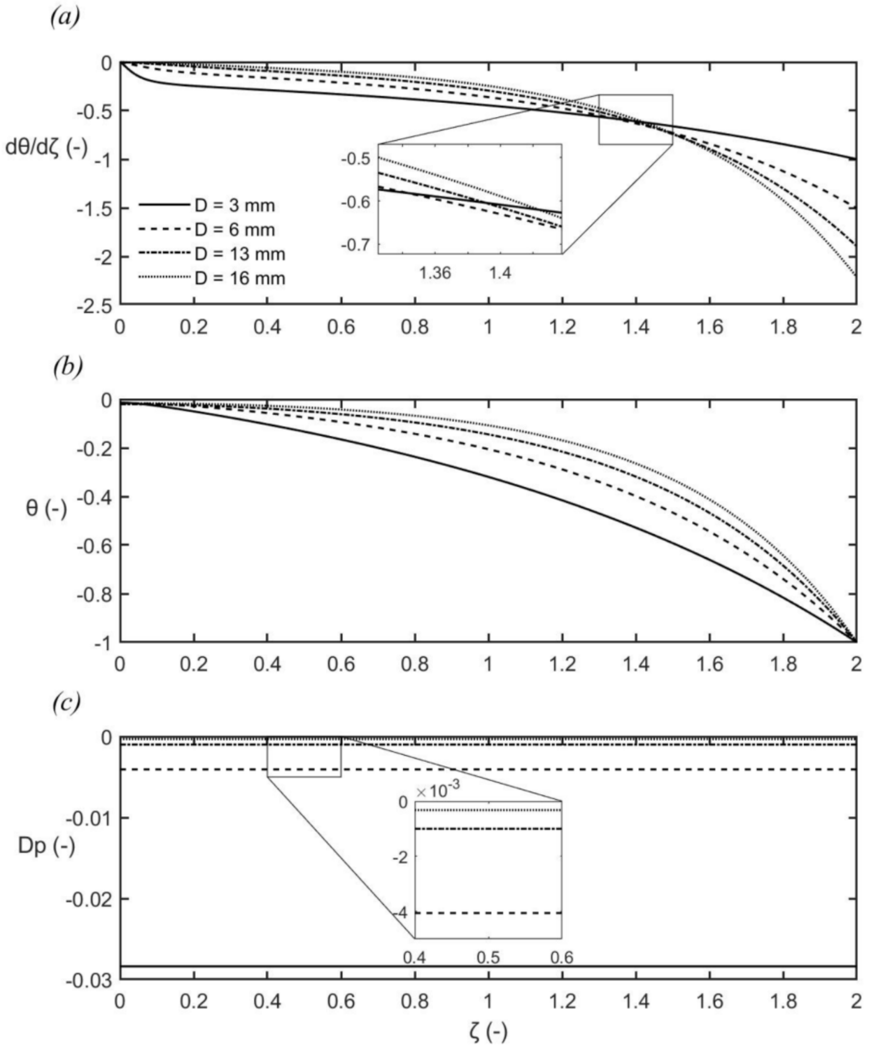

Figure 7.5: A series of comparative plots, produced by the one-dimensional iterative calculation, summarizing the predicted trends of (a) the normalized RMS flow deceleration, (b) the normalized RMS flow velocity, and (c) the dimensionless pressure gradient plotted against the downstream axial distance normalized with respect to the horn tip diameter of the respective geometrical case (D = 3, 6, 13, and 16 mm). The two inset plots highlight regions of interest and clarify the variation of $\frac{d\theta}{d\zeta}$ and D_P values. ζ is the dimensionless z-position normalized with respect to the tip diameter D for each case.

Table 7.2: Tabulation of values of artificially fitted model coefficients (C, β, α, and Γ) for each horn tip diameter D and its respective Re_B.

D (mm)	Re_B (-)	D_P (-)	C (-)	β (-)	α (m^{-1})	α (dB/cm)	$\lvert\Gamma\rvert$ (-)
3	61 692	0.0284	0.0158	2.0000	299.52	0.495	1.797
6	123 381	0.0041	0.0014	0.0435	246.92	0.479	2.963
13	267 326	0.001	0.0003	0.0018	145.4	0.433	3.780
16	329 106	0.0003	0.0001	0.0003	138.33	0.428	4.427

Observing the predicted flow behaviours in Figures 7.5a and 7.5b, it becomes clear that the flow decelerates much faster towards the $\theta = 0$ stagnation point with larger horn diameters. This is perhaps due to the amplified 'push' effect of the steady component of flow on the acoustic wave in relation to the growing Re. Figure 7.5a has highlighted this trend, however, it unveils an interesting trend in the initial flow acceleration at the horn surfaces. It initially appeared that with the doubling of the horn diameter from 3 mm to 6 mm, $\frac{d\theta}{d\zeta}$ increases by a factor of 1.5. However, upon further doubling the diameter, $\frac{d\theta}{d\zeta}$ was amplified by a rather noticeably reduced factor of 1.24. the further increase in diameter would still induce a heightened acceleration by the same factor of approximately 1.24, despite the diameter increase being a factor of 1.23. Moreover, the inset plot in Figure 7.5a magnifies the junction of deceleration curves where it amplifies the 3 mm horn flow deceleration as an anomaly due to its relatively exaggerated gradual decline towards the stagnation point. We speculate that the formulation of this junction may be due to the attached cavitation axial extension, this is further discussed in detail in section 7.5 of this chapter. However, the deceleration trends of the remaining tip diameters all show similar decelerating trends with a joint intersection at $\zeta = 1.46$.

Furthermore, when it came to scrutinizing these trends with respect to the model coefficients, we were able to uncover potential correlations with what has been observed in the flow velocity and deceleration. As per the tabulated data in Table 7.2, we noticed that the effects of the dimensionless pressure gradient D_P becomes more and more insignificant with the increase of D. Judging by the flow type induced under each horn tip, this could be potentially due to significantly increased turbulence of the acoustically-driven flow. Thus, recalling the conclusive suggestion made by Piercy & Lamb [213], this leads us to believe that the observation aligns with their justification. However, what is rather eye-catching, is the sharp shrinkage of D_P upon initially doubling the diameter, which is later followed by a more continuous and gradual decrease of D_P's influence on flow.

It is hypothesized that, perhaps, there exists an underlying non-linearity in the influence of turbulent flow properties on the acoustic wave behaviour. This was based on conclusions drawn from Miller & Comings [218], in which they illustrated the amplification of the static pressure's insignificance on the axial flow due to the large disparity between longitudinal mean momentum and static pressure. Thus, we have taken their case as an analogy to our case of acoustically-driven flow. On another note, coefficients related to the governance of the acoustic force, namely C, β, and α, demonstrate inverse proportionality to the increase in Re. It is unsurprising to see that both C and β share the same effect due to their coupled nature shown in Eq. 7.29. Here, β primarily plays the role of under-relaxing the amplification effect of C on the force. Physically, this indicates a reduction in strong interference effects, that is typically experienced by the axial pressure during acoustic radiation from a cylindrical piston, governed by the Rayleigh Length [207].

As for α, its trend can be attributed to the observations previously made in our study, where we recorded a decrease in the active cavitation zones proximal to the horn tip, as the inertial bubbles self-assemble into a CBS [190]. The values obtained for α do in fact align with observations made by Feuillade [219], however, a slight underprediction is noticeable. What is interesting, though, is the opposing Γ trend, despite its direct correlation with α. As clearly shown, Γ marches upward by an increment of approximately unity with the doubling of D. This eventually highlights the possible role of the factor 2D that arose during nondimensionalization, as it introduces direct proportionality of the horn tip diameter to the attenuation induced by the multiphase medium downstream. Acknowledging the high Re with larger D, we are led to believe that the flow becomes inertia-dominated, therefore, minimizing the losses due the mixture viscosity. We have thus interpreted 2D as a corrective term for attenuation and defined Γ as a corrected dimensionless attenuation coefficient.

7.4.2.2 Small Re Number Asymptotic Behaviour

Thus far, our investigation demonstrated a strong focus on practical cases of horn-type reactors, where 'fast-streaming' dominated our flow observations. As we have scrutinized the trends of compound attenuation effects of the fluid composition on the acoustically-driven flow, it would of great importance to explore the nature of attenuation during 'creeping motion'. Typically, 'near-field' flow behaviour becomes the primary focus during such flows, and such proximal flow is seen to form when the Rayleigh length is $\frac{D}{\lambda} \geq 1$. Taking the unity of $\frac{D}{\lambda}$ is then reflected in the value of C as it also converges to unity. With that said, Eq. 7.26 then becomes

$$\theta\theta' - \frac{1}{Re}\theta'' = D_P - \Gamma e^{-\Gamma\zeta} \tag{7.34}$$

We then solved this expression analytically through a regular perturbation procedure, that considers a small parameter $\epsilon = Re \ll 1$, using the following coefficient expansions:

$$\theta(\zeta) = \theta_0 + \theta_1 Re + \theta_2 Re^2 + O(Re^3) \tag{7.35}$$

$$\theta'(\zeta) = \theta_0' + \theta_1' Re + \theta_2' Re^2 + O(Re^3) \tag{7.36}$$

$$\theta''(\zeta) = \theta_0'' + \theta_1'' Re + \theta_2'' Re^2 + O(Re^3) \tag{7.37}$$

$$D_P = D_{P,0} + D_{P,1} Re + D_{P,2} Re^2 + O(Re^3) \tag{7.38}$$

$$\Gamma = \Gamma_0 + \Gamma_1 Re + \Gamma_2 Re^2 + O(Re^3) \tag{7.39}$$

We went with applying the aforementioned boundary conditions in section 7.3, with the exception of the boundary condition in Eq. 7.11. Instead, we have replaced that boundary condition with another that constrains the flow at $\zeta = 0$ to ensure that $\theta = 0$. This way, we reach the following small Re approximations below. Their derivations are demonstrated in Appendix G.

$$\begin{aligned}\theta = -\frac{1}{4}\zeta^2 + \left(-\frac{1}{20}\zeta^2 - 0.057709\zeta^3 - 0.008489\zeta^4 + \frac{1}{160}\zeta^5\right)Re \\ + \left(0.141961\zeta^2 - 0.0689317\zeta^3 - 0.014967\zeta^4 + \frac{1}{400}\zeta^5 + 0.0024106\zeta^6 \right. \\ \left. + 0.0003032\zeta^7 - \frac{1}{5120}\zeta^8\right)Re^2\end{aligned} \tag{7.40}$$

$$\begin{aligned}\theta' = -\frac{1}{2}\zeta + \left(-\frac{1}{10}\zeta - 0.173127\zeta^2 - 0.033958\zeta^3 + \frac{1}{32}\zeta^4\right) Re \\ + \left(0.283922\zeta - 0.206795\zeta^2 - 0.059869\zeta^3 + \frac{1}{80}\zeta^4 + 0.0144634\zeta^5 \right. \\ \left. + 0.00212242\zeta^6 - \frac{1}{640}\zeta^7\right) Re^2\end{aligned} \tag{7.41}$$

$$\begin{aligned}\theta'' = -\frac{1}{2} + \left(-\frac{1}{10} - 0.311847\zeta - 0.087073\zeta^2 + \frac{1}{8}\zeta^3\right) Re \\ + \left(0.283922 - 0.4135901\zeta - 0.179609\zeta^2 + \frac{1}{20}\zeta^3 + 0.072137\zeta^4 \right. \\ \left. + 0.0127345\zeta^5 - \frac{7}{640}\zeta^6\right)\end{aligned} \tag{7.42}$$

$$D_P = \frac{1}{2} - 0.767250 Re - 0.641065 Re^2 \tag{7.43}$$

$$\Gamma = -0.579026\mathrm{Re} - 0.357143\mathrm{Re}^2 \tag{7.44}$$

Table 7.3: Tabulation of time-averaged flow profile, cavitation axial region, and bulk Reynolds number of each horn geometry.

	Re = 0.25		Re = 0.5		Re = 0.75		Re = 1.0	
ζ (-)	θ (-)	θ' (-)	θ (-)	θ' (-)	θ (-)	θ' (-)	θ (-)	θ' (-)
0.0	0.0000	0.0000	0.0000	0.0000	0.0000	0.0000	0.0000	0.0000
0.1	-0.0026	-0.0513	-0.0024	-0.0493	-0.0022	-0.044	-0.0017	-0.0355
0.2	-0.0103	-0.1038	-0.01	-0.1016	-0.009	-0.0933	-0.0074	-0.0791
0.3	-0.0234	-0.1575	-0.0299	-0.1569	-0.021	-0.1481	-0.0178	-0.1312
0.4	-0.0418	-0.2124	-0.0414	-0.2153	-0.0388	-0.2084	-0.0339	-0.1919
0.5	-0.0659	-0.2686	-0.066	-0.2768	-0.0629	-0.2744	-0.0565	-0.2615
0.6	-0.0956	-0.326	-0.0969	-0.3414	-0.0939	-0.3460	-0.0865	-0.3398
0.7	-0.1311	-0.3846	-0.1344	-0.4089	-0.1323	-0.4229	-0.1247	-0.4265
0.8	-0.1726	-0.4442	-0.1788	-0.4791	-0.1786	-0.5048	-0.1721	-0.5212
0.9	-0.2200	-0.5048	-0.2303	-0.5519	-0.2334	-0.5913	-0.2292	-0.623
1.0	-0.2735	-0.5662	-0.2892	-0.6267	-0.297	-0.6817	-0.2969	-0.7311
1.1	-0.3333	-0.6282	-0.3557	-0.7033	-0.3698	-0.7753	-0.3756	-0.8442
1.2	-0.3992	-0.6907	-0.4299	-0.7811	-0.4521	-0.8712	-0.4658	-0.9611
1.3	-0.4714	-0.7534	-0.5119	-0.8595	-0.5441	-0.9684	-0.5679	-1.0800
1.4	-0.5499	-0.816	-0.6018	-0.9379	-0.6458	-1.0657	-0.6818	-1.1992
1.5	-0.6346	-0.8784	-0.6995	-1.0157	-0.7572	-1.1618	-0.8077	-1.3168
1.6	-0.7255	-0.9402	-0.8049	-1.092	-0.8781	-1.2555	-0.9451	-1.4306
1.7	-0.8226	-1.0011	-0.9178	-1.1661	-1.0081	-1.3453	-1.0936	-1.5384
1.8	-0.9257	-1.0607	-1.038	-1.2372	-1.1469	-1.4297	-1.252	-1.638
1.9	-0.9883	-1.1187	-1.1651	-1.3045	-1.2938	-1.5073	-1.4208	-1.7272
2.0	-1.0000	-1.1748	-1.2987	-1.367	-1.4481	-1.5767	-1.5975	-1.8038
	$D_p = 0.2681$		$D_p = -0.0439$		$D_P = -0.4360$		$D_P = -0.9083$	
	$\|\Gamma\| = 0.1671$		$\|\Gamma\| = 0.3788$		$\|\Gamma\| = 0.6352$		$\|\Gamma\| = 0.9362$	

Considering the following small increments of Re = 0.25, 0.5, 0.75, and 1.0, we tabulate each coefficient at each Re to track their trends and visualize the corresponding flow behaviours, as shown in Table 7.3. The overall trends are quite consistent with each increase in Re; we observe that the $|\theta|$ and $|\theta'|$ increase upon approaching the horn tip in all cases of Re. However, interestingly, we have noticed the surfacing of an underlying non-linearity within the field proximal to the horn tip surface. It initially becomes prominent at Re = 0.5 in which the velocity values begin to slightly overshoot at $1.8 \leq \zeta \leq 2.0$. Moreover, this trend minutely develops, in which it begins to be expand downstream, such that at Re = 0.75 onwards, the region becomes constraint within $1.7 \leq \zeta \leq 2.0$. This could be analogous to the variation in the axial velocity profile between a low and a high acoustic frequency setting[217]. However, soon enough, with the progression of Re, this discrepancy surfaces as a probable accuracy limitation of the small perturbation assumption of Re. On the other hand, D_P and Γ here demonstrate direct proportionality with Re. It is speculated the gradual rise of Γ is an indicator of an expanding cavitation region within the proximal axial direction, and thus an increase in attenuation is to be expected. However, to compare its value marching trend with the trend observed in Table 7.2, we have taken into account the proportionality of increase in value of Γ with Re in both the laminar and turbulent regimes. Here, we observe that in the previously explored turbulent regime, Γ presented a slow decay in the factor increase upon doubling Re. For instance, the factor rise of Γ from Re = 61,692 to Re = 123,381 demonstrates an increase by a factor of ≈ 1.65. However, the further doubling of Re has led to an increase by a factor of ≈ 1.26 instead. This trend does not exist in the laminar regime, as we consistently witness doubling in Γ upon doubling Re. The rise of D_P, however, hints at the presence of some nonlinear trend when compared to its progression in larger Re, as shown in Table 7.2. However, this requires further scrutiny to validate this trend.

7.4.3 Bubble Cluster Shape-driven Acoustic Attenuation

Nevertheless, it has been interestingly observed that the general trends of both α and Γ remain true to the exact solution in both laminar and turbulent regimes, where α is seen to decrease, while Γ increases, with the increase in turbulence of the flow regime. While this points in the direction of a proper explanation to the constant location of the observed stagnation point, however, the justification remains inconclusive. Specifically, it is not yet understood as to why the acoustically-driven flow is strongly attenuated with the presence of MBS compared to the cases with the presence of CBS. Therefore, in an attempt to scrutinize this relationship, we took the initial step to delve deeper into justifying the bubble structure arrangements. By acknowledging the horn-proximal flow features, specifically its vorticity, it can be suggested that the arrangement of bubbles can be induced by nature of the flow recirculation. Related studies conducted by Stommel [220], Toobey et al. [221], Manton [222], and Maxey [223] all explore the gravitational settling of heavy particles within vortex flows. All of Stommel [220], Toobey et al. [221], and Manton [222] have explored the entrapment of assumingly small spherical particles in two-dimensional, incompressible cellular flows. Maxey [223], however, has further defined the importance of accounting the compound effect induced by particle inertia and virtual mass on the gravitational settling of these spherical particles. In situations of coherent vortical structures, Tio et al. [224] and Ganan-Calvo and Lasheras [225] have investigated the long-term evolution of particle dynamics. Based on a four-parameter, and later five-parameter, dynamical system they have developed by accounting for the effects of particle size, turbulent intensity, vorticity distribution, and gravity, they were able to categorize the suspension mechanisms of particles of different densities. Effectively, a particle-path function was defined as

$$\phi \equiv \Psi\big(x_p(t), y_p(t)\big) \tag{7.45}$$

to represent a stream function Ψ evaluated at a given instantaneous particle position $\big(x_p(t), y_p(t)\big)$ along its respective trajectory. From that, they have further derived a rate of change of Φ as follows

$$\frac{\mathrm{d}\Phi}{dt} = \frac{\partial \Psi}{\partial x}\bigg|_P \frac{dx_p}{dt} + \frac{\partial \Psi}{\partial y}\bigg|_P \frac{dy_p}{dt} = u_y\, V_x - u_x\, V_y \tag{7.46}$$

However, in the case of buoyant particles, such as bubbles, it has been well-established that bubbles released in rotational flow fields tend to be entrapped by a series of equilibrium points, if their rise speed in still fluid Q is below a given threshold based on an observation made by Maxey [223] when investigating Langmuir cellular flow fields. Upon exceeding the threshold value of Q, bubbles may escape this 'captivity' and to rise and accumulate along asymptotic paths. As such, this observation was later modeled and confirmed by Tio et al. [224] by numerically showing the instantaneous locations of a grid of bubbles that entered and escaped captivity of the vortex and highlighting their accumulated suspension points above the vortex. Aside from the primary and secondary Bjerknes forces, it can be argued that the buoyant nature of bubbles can be a primary factor that governs their accumulation and formation into the variety of bubble structures witnessed under the acoustic horn. While this grants us a good indicator of the underlying role the proximal vortex has on the bubble structure, this justification may not be applicable for our numerical results, as the modified ZGB model does not model vapor as particulates but more as local nucleation governed by the local pressure gradient. As such, we have dissected the time-averaged flow behaviours observed in each case that are categorically attributed to the vortex presence and its core position.

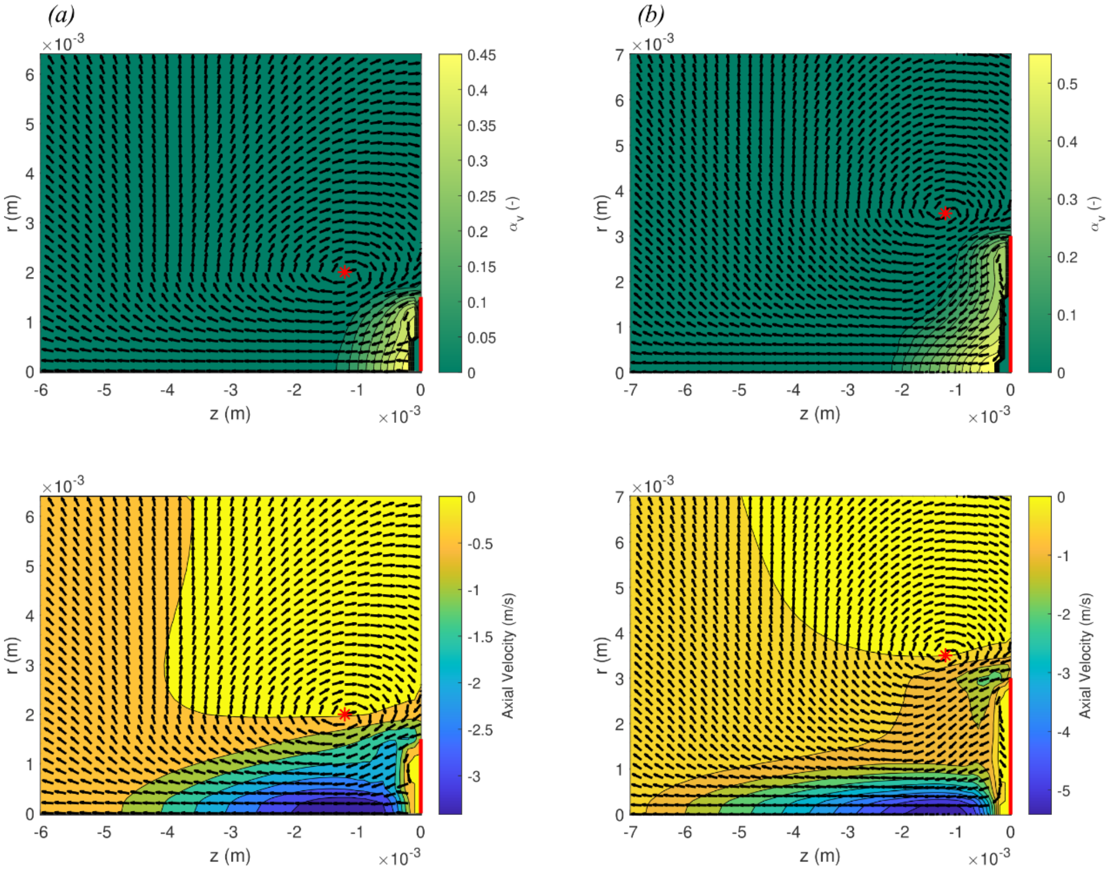

Figure 7.6: Time-averaged axisymmetric contour and vector plots of (up) vapor volume fraction and (down) axial velocity for flows driven by (a) the 3 mm horn tip and (b) the 6 mm horn tip. The red vertical line outlines the horn tip and the red asterisk marks the vortex core center.

As shown in Figure 7.6 and Figure 7.7, contours and vector plots of the time-averaged flow field were extracted for the aforementioned horn-type reactor cases of D = 3, 6, 13, and 16 mm horn tips. Upon initial observation, a primary vortex consistently positioned ≈ 0.5 mm above the horn tip edge appears in all horn-type reactors. However, a secondary vortex surfaces under the larger horn tips, namely the 13 and 16 mm horn tips, positioning itself relatively closer to the horn axis. Categorically, cases with bubble structures resembling MBS sustain the primary vortex only, while cases with CBS are seen to sustain both the primary and secondary vortices. It is crucial, however, to note that both primary and secondary vortices were only observed to shift radially but never axially. with the increase of the horn tip diameter. Perhaps, this may only emphasize the locality of the vortices effect on the bubble structures and its negligible effects on the freestream flow. Another general trend observed, regardless of the diameter size and the bubble structural shape, is the flow behavior from within the bubble structure itself. Upon axially examining the progression of the bubble structure, a velocity gradient is revealed. Specifically, the velocity at the tip surface unanimously starts at v_{RMS}, however, it begins to gradually decrease to a minimum velocity. Interestingly, the initialization of the velocity recovery phase coincides with the interface of the cavitation structure. While the phenomenon itself has been observed across all reactor geometries, a deeper qualitative observation would reveal that the extent of this velocity gradient varies from one reactor to the other. Looking at the axial velocity contour plots about the horn axis, one can qualitatively note an offset distance following the negative velocity gradient from the horn tip surface, where maximum velocity is achieved, till the instance where the lowest velocity. When comparing this offset distance and marking it on the vapor volume fraction contour plots, we find that this marks the bubble structures' core length.

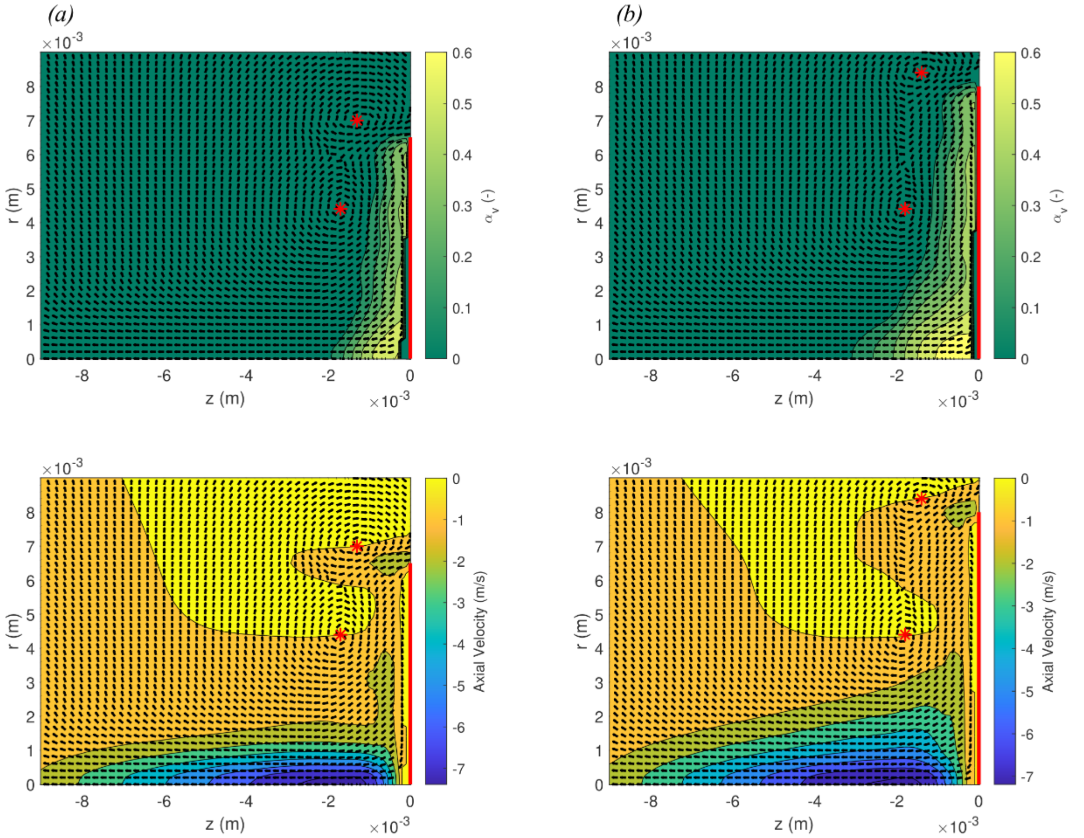

Figure 7.7: Time-averaged axisymmetric contour and vector plots of (up) vapor volume fraction and (down) axial velocity for flows driven by (a) the 13 mm horn tip and (b) the 16 mm horn tip. The red vertical line outlines the horn tip and the red asterisk marks the vortex core center.

To quantitatively scrutinize this, Figure 7.8 plots the velocity gradients achieved about the axes of all four horn reactors. By nondimensionalizing the z-axis with respect to the diameter of the respective horn reactor, the offset distance appears to shrink with the increase of D. From Figure 7.8, the offset distances are measured at 0.27, 0.20, 0.12, and 0.11 for cases of D = 3, 6, 13, and 16 mm, respectively. In retrospect, however, this offset distance increases instead from 0.81 mm, 1.2 mm, 1.56 mm to 1.76 mm for the aforementioned diameters, respectively. Nevertheless, by taking scaling into account, we notice that the core size increase is rather insignificant compared to the increase in size of the horn reactor. Furthermore, another interesting trend in the curves drawn in Figure 7.8 was the hump that occurs marking a maximum change in velocity before reaching a steady-state velocity value downstream of the horn. The insights provided by this hump lies in its midpoint, as it highlights the velocity gradient and recovery marking the axial length of the bubble structure from the horn tip. Surprisingly, the maxima reached at each hump is very consistent, as it equates to $\approx 0.1\ \mathrm{ms}^{-1}$. Moreover, with nondimensionalizing its axial length, we do notice the significant recession in the bubble structure extension when put into perspective with the tip diameter of the horn reactor. Once again, this does not necessarily indicate that the cavity itself is shrinking, as it shown that the contrary is true in Figures 7.6 and 7.7. However, all this begs the question as to whether this variation in the velocity gradient is indicative of the bubble distribution within the bubble structure under the horn.

Therefore, Figure 7.9 has been plotted to illustrate the progression of the bubble population within each of the bubble structures generated under all considered horn reactors. The bubble population was calculated within mesh cell n by multiplying the volume of the cell V_C by the interpolated vapor volume fraction occupying cell n and dividing it by the volume of the bubble, given that the implemented modified ZGB model assumes a constant equivalent bubble radius R. One of the prominent trends one may notice is the linearity and nonlinearity of the bubble distribution within MBS and CBS, respectively. The nonlinearity witnessed within CBS closely resembles an exponential distribution. Moreover, judging by their slopes, it seems that CBS tends to experience a sharp drop in bubble population density within the structure's center and the interface, meanwhile, MBS seems to relatively sustain the bubble population density throughout most of its structure. Generally, it can be said that any increase in the horn tip diameter tends to increase the rate of decay of bubble population about both structure types. Interestingly, however, this is compensated for by a drastic increase in the bubble population near the horn tip. This may indicate the growth in the bubble structure core size and density, with CBS cores being much denser. However, despite that, all bubble structures' interfaces seem to sustain the same amount of bubbles of approximately n_B = 7,573. As it has been mentioned that the interface marker, based on the velocity gradient plot in Figure 7.8 is rather equivalent in all cases, it can be speculated that there exists some form relationship between the velocity gradient and the bubble density. Perhaps, it can be boiled down to a possible generation of similar pressure fields at the interface regions that governs the presence of bubbles. With this explanation, it can be suggested that the different rates of bubble population decay is due to the different pressure fields induced by the position of the primary vortex. As aforementioned in Figures 7.6 and 7.7, the primary vortex core consistently positions itself about the corner of the horn tip edge, and thus, the vortex position is only up-scaled radially with the increase of D. Ultimately, the vortex core is found to be positioned further away from the bubble structure axis leading to a relatively high pressure field about the axis.

In retrospect, this may be a potential justification for the attenuation trend captured by the exact solution of the one-dimensional mathematical formulation of the acoustically-driven axial flow. It seems that a more linear bubble population distribution throughout the bubbly structure has the tendency to increase the acoustic attenuation of flow, as opposed to a more biased bubble distribution towards the near-horn region demonstrated by the CBS found under the 13 and 16 mm horn reactors.

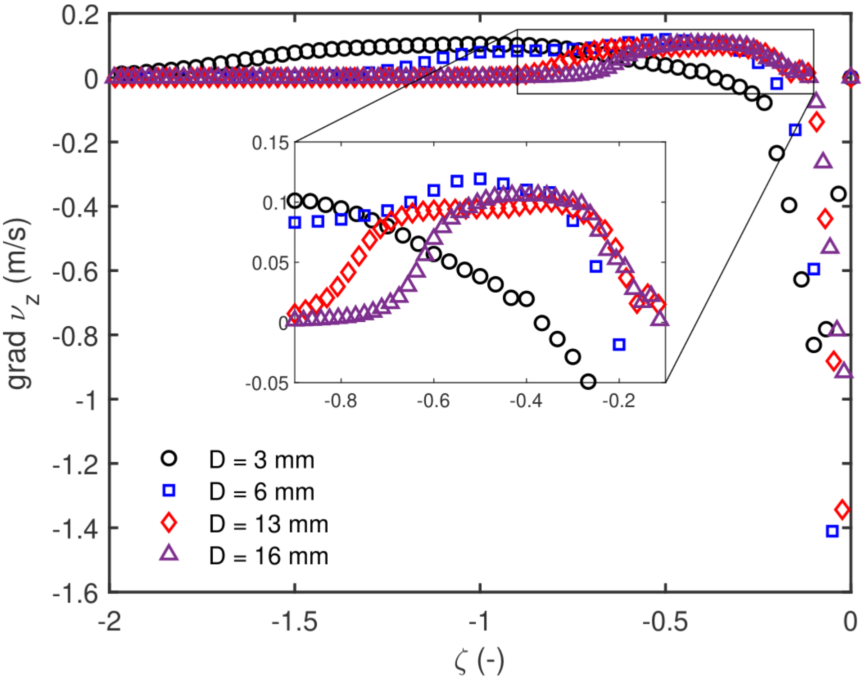

Figure 7.8: Axial velocity gradients about the horn axis plotted against the dimensionless axial coordinate for cases of D = 3, 6, 13, and 16 mm. ζ is the dimensionless z-position normalized with respect to the tip diameter D for each case.

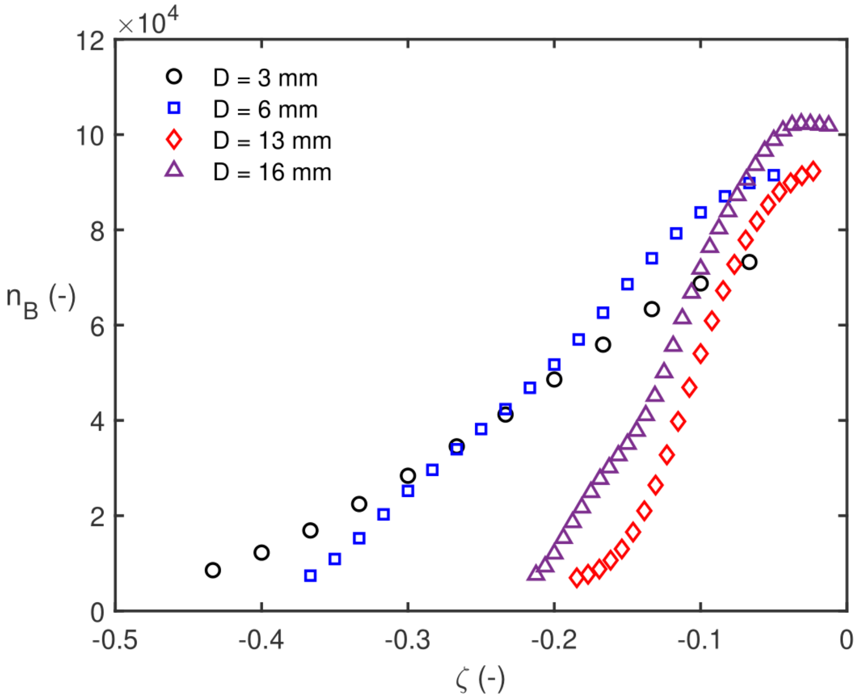

Figure 7.9: Number of bubbles n_B plotted against the dimensionless axial coordinate along the horn axis for cases of D = 3, 6, 13, and 16 mm. ζ is the dimensionless z-position normalized with respect to the tip diameter D for each case.

7.5 Conclusion

This chapter presented a numerical study that delves deeper into understanding the averaged flow behavior under each of the horn tips considered in order to establish a better idea on the steady-state two-way coupling between the toroidal vortex and the cavity structure. Upon time-averaging the flow, an early stagnation point was revealed at a point 2D away from the horn tip with a diameter D.

A 2D axisymmetric simulation was conducted to predict the flow about the horn's axis of multiple horn-type reactor geometries, D = 3, 6, 13, and 16 mm. With respect to that, we have tracked the trends of dimensionless quantities, such as the dimensionless velocity θ, to highlight demonstrate its convergence to 0 at a non-dimensional axial distance of $\zeta = 2D$. We numerically obtained the exact solution of a non-dimensional conservation of momentum equation governing the flow in the axial direction. This involved resolving newly emerged dimensionless model coefficients, such as the dimensionless absorption coefficient α and the under-relaxation factor C. These factors were artificially fitted into the equation based on the least square fitting method that aims to match the curves computed from the CFD calculation. An odd trend was demonstrated by the coupled absorption coefficients, α and Γ.

We witnessed a steady drop in α with the increase of the horn tip diameter, or Re, while Γ was seen to steadily increase instead. We hypothesize that this factor's gradual prominence sources from the fact the flow is inertia-dominated, as the flow becomes more turbulent with larger D. Upon comparing between the behavior of Γ in a laminar regime and a turbulent regime, we observed that Γ sustains direct proportionality with Re in which a double in the value of Re, in turn, induces a double in the value of Γ. On the contrary, this was not observed in turbulent regimes, as Γ's increase gradually decays with the increase in Re. Based on these accounts, we are keen to hypothesize that the attenuation factor 2D does not only attribute attenuation to the flow regime, but it also sustains an underlying link to the cloud bubble structure and self-organization.

While most cases of horn-type reactors operate under the ‘fast streaming’ category, the nondimensionalized equation obtained provides a level of controllability of proximal flow about the horn through manipulation of the empirical constants of both α and β. Despite that, it is still crucial to conduct a set of experiments to validate the observed trends and strengthen confidence in the proposed scaling law.

8 The Two-way Coupling between Acoustically Generated Vortical Flows and Bubbly Activity Zone Dispersion

8.1 Introduction

In Chapters 5, 6 and 7, the acoustically generated vortical-type flows were introduced as phenomena specific to horn-type reactors. Chapter 6 has scrutinized the source of their formations and their development to ultimately describe the generated vortical flow's lifecycle. Moreover, Chapter 7 takes on the underlying effect of the presence of such vortical structures, and that is the establishment of a scalable stagnation plane with respect to the horn tip diameter. The mutual theme in these two chapters, however, is the underlying influence between the attached bubbly structures along the horn tip on the attenuation of the acoustic flow. It was made clear that different cavitation structures have different attenuation capabilities and mechanisms that alter the propagation of the acoustic wave throughout the medium. This can potentially have a significant impact on the performance of the reactor. Therefore, in this chapter, further scrutiny of the acoustofluidic mechanism of this attenuation takes place in aims to provide the missing link to justify the nonlinear variety in performance, and more specifically, reactivity of horn-type reactors.

The fundamental mechanism of the resultant reactivity of a horn-type reactor has been extensively discussed, in Chapter 2, where the collective collapse of acoustic bubbles produces local pressure and temperature conditions that satisfy the formation of hydroxyl ($OH\,\cdot$), hydrogen ($H\,\cdot$) and hydroperoxyl ($HO_2\,\cdot$) radicals in a given water medium. The presence of these volatile radicals then creates active zones that react with compounds and substrates within their vicinity. As such, it has been agreed that there exists an underlying correlation between the concentration of free radicals and the dispersion of bubble populations within the domain [149]. Therefore, many studies have explored horn-type reactor optimization based on the premise of 'taming' the formation of bubbles within the system [149, 209, 226]. Several investigations have noted the influence of a multitude of deterministic parameters that impact the formation of cavitation bubbles, such as acoustic power, oscillation frequency, domain temperature, and even the geometry of the ultrasonic horn, specifically the tip diameter. For instance, Hatanak et al. [227] and Kojima et al. [226] investigated the underlying dependency of sonochemical efficiency on the acoustic power. Both have observed nonlinearity in the efficiency trends with the linear increase in acoustic power that starts off as quenching and ultimately ends as extinguishing. Both studies have suggested that this trend could potentially be due to the increase in active bubble population per unit volume.

This nonlinear behaviour was further carried forward in the observations made by Viciconte et al. [228], however, conclusions made here diverge away from the aforementioned suggestion on the bubble population. In this exploration, the authors have scrutinized the reactivity of multiple ultrasonic horns of different tip diameters. Essentially, horns of larger tip diameters appear to produce larger concentrations of the fluorescent product $7OHC$, and ultimately, achieving a higher chemical efficiency, defined as:

$$\eta_{chem} = \frac{C_{7OHC} \times BDE_{OH}}{\Delta u} \tag{8.1}$$

where C_{7OHC} is the concentration of this fluorescent product, which is assumed to be an indicator to the concentration OH radicals, BDE_{OH} is the bond dissociation energy, and Δu is the internal energy absorbed by the reactor. However, the nonlinearity finally surfaces in the vapor volume trends. While generally, an increase in the horn tip diameter from 3 mm to 40 mm does in fact increase the vapor volume produced, however, an inflection point emerges at the 14 mm diameter in which there is a noticeable drop in the vapor volume in comparison to the 7 mm tip before increasing along with the diameter to 40 mm. This leaves sufficient room to assume that the present differences in the cavitation structure and dynamics have an underlying impact on the reaction rate of the reactors. Viciconte et al. [228], along with Rivas et al. [229] and Ashokkumar [230], have reached the same conclusion suggesting that smaller dispersed bubbles induce a dissipation of higher energy density upon their collapse in comparison to larger bubbles. In turn, this leads to a higher production of radicals. Given that larger tip diameters sustain the presence of such small bubbles, this phenomenon is then reflected in the increasing η_{chem} with the increase of the tip diameter.

As it appears, there is a lot of speculation on the reason behind the nonlinear performance trends that are seen to converge towards the role of the cavitation structure. Based on the previous investigations in Chapters 6 and 7, we understand that the proximal vortical flow field about the horn tip maintains some governing role over the cavitation structure structural characteristics. This then provides us with a strong foundation to scrutinize the interplay between proximal vortex characteristics and the cavitation structural and flow dynamics. Similar to the methodology followed in the aforementioned explorations, the investigative methodology is an extrapolation of the CFD configuration described in the previous chapters to facilitate the assessment of the cavitation structure and its accompanied proximal velocity and pressure fields under horn geometries summarized in Table 8.1. This parametric analysis is inspired by Viciconte et al.'s experimental work [228] and initialized by a collaboration with the authors to further scrutinize their observed trends.

8.2 Ultrasonic Horn Geometries and Reactor Configurations

The range of reactor geometries and operating configurations considered in the presented exploration in this Chapter are fundamentally based on the experimental setup implemented in Viciconte et al. [228] in which a 200 mL aqueous solution is ultrasonically irradiated by titanium probes, of varying diameters tabulated in Table 8.1, submerged 25 mm into the domain. These probes are excited by a Hielscher ultrasonic transducer UP400S that operates at an oscillation frequency of 24 kHz and sustains a maximum power of 400 W. With this configuration, controllability of the oscillation amplitude is facilitated through the power regulation of the device, represented as percentage powers with respect to the maximum power. Experimentally, this percentage is translated to a metric amplitude and a calorimetric power. Furthermore, an immersed thermocouple in the solution, specifically positioned at the corner of the cylindrical container, to monitor the solution temperature without interfering with the ultrasonic multiphase flow field and wave propagation. Lastly, the electric power extracted by the ultrasonic transducer was recorded using a socket-type multimeter. Numerically, on the other hand, this experimental setup was replicated by exactly implementing the same domain created and utilized in Chapter 6, with the oscillation amplitude being governed by a UDF implementing Eq. 2.36. It is important to note that the experimental study scrutinized only ϕ_D= 3, 7, 14, and 40 mm. However, based on the aforementioned nonlinearity observed between the 14 mm and the 40 mm horn tips, we have interpolated two additional configurations, namely the 24 mm and the 32 mm horn tips to deeply explore and characterize this inflection. Figure 8.1 illustrates the fitted trendlines obtained based on the configurations implemented experimentally to define the interpolation scheme.

Table 8.1: Different ultrasonic horn reactor configurations and operating conditions. The ***bold text*** *refers to the interpolated operating horn reactor geometries and their respective oscillating parameters.*

ϕ_D (μm)	A_{nom} (%)	A_r (μm) ± 2.35	ϕ_D (μm)	A_{nom} (%)	A_r (μm) ± 2.35
3	30	23.54	**24**	30	14.70
	50	25.89		50	26.48
	70	47.08		70	30.52
	90	62.38		90	41.09
	100	64.74		100	41.87
7	30	-	**32**	30	9.13
	50	36.39		50	16.76
	70	50.47		70	18.83
	90	64.55		90	25.37
	100	64.08		100	25.65
14	30	19.95	40	30	2.35
	50	29.34		50	2.35
	70	39.91		70	4.70
	90	53.99		90	5.88
	100	55.16		100	5.88

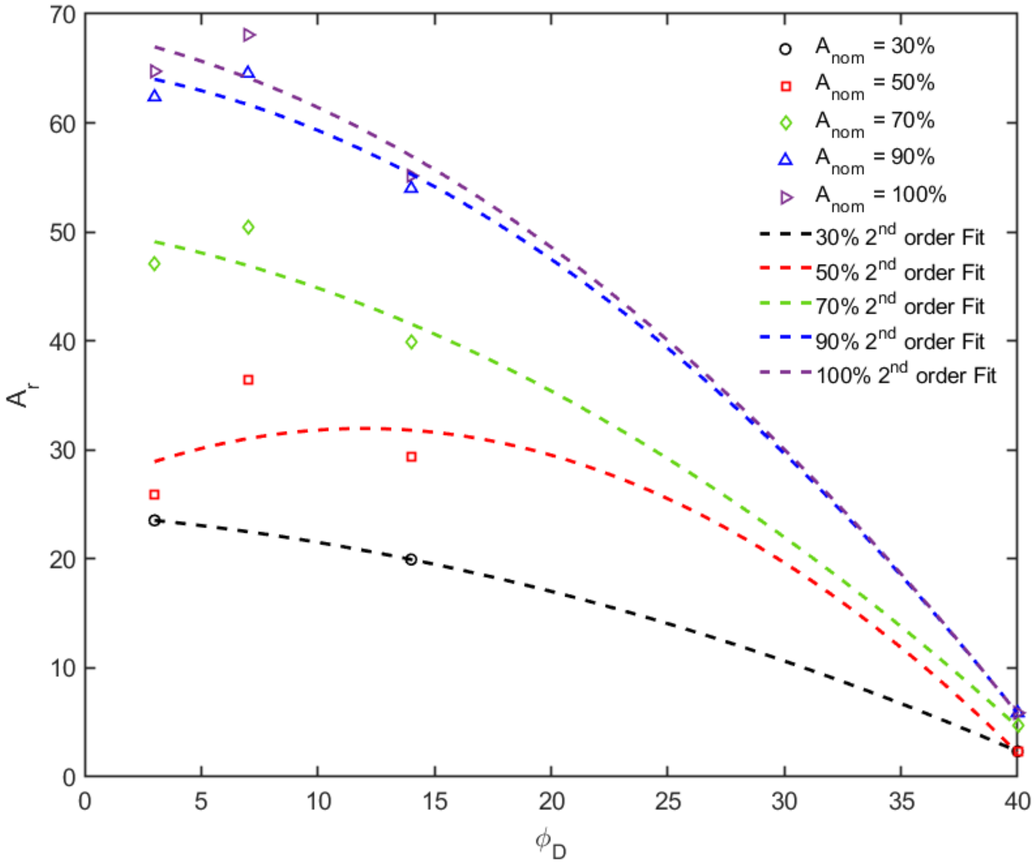

Figure 8.1: Fitted trend lines plotting the variation of horn tip displacement amplitude A_r (in μm) with respect to the horn tip diameter ϕ_D (in mm) operating at different power level conditions.

A second-order line fitting scheme was used to facilitate the interpolation of the acoustic configurations of horn diameters between 14 mm and 40 mm. For the case of $A_{nom} = 30\%$, it is understood that there is relatively limited number of data points, this single-point absence is due to the lack of experimental measurements at that operating condition. Nevertheless, the same polynomial fit was applied uniformly to all cases to maintain a consistent interpolation methodology across different power levels and to ensure comparability of trends. Despite this being a limitation of the presented dataset, the fitting still provides reasonable interpolation within the measured range, while avoiding introducing additional bias through the use of different fitting methods.

Moreover, a secondary consistent trend noticeable in Figure 8.1 is the slight increase in the displacement amplitude of the 7 mm horn tip at all power levels alike. Given a constant power level, this hike could be the interplay between impedance matching, resonant frequency tuning and radiation damping. At this intermediate diameter, an impedance match between the horn and the liquid was established and thus allowing for efficient energy transfer and maximum displacement. Meanwhile, at the small tip diameter, a poor impedance matching might have limited achieving displacement amplitude. On a similar note, the increased radiation resistance and modal redistribution with larger tip diameters led to a continuous reduction in their displacement amplitude.

8.3 Results and Discussion

8.3.1 Attached Cavitation Macrostructural Dynamics

Building on what was previously observed in Chapters 6 and 7, the observed time-averaged radial profiles sustained by the attached cavitation macrostructures overlap with the aforementioned trends, shown in Figure 7.3, by similarly demonstrating the same transition from MBS to CBS when moving from small horn tip diameters to larger diameters. However, observations of this trend begin to gradually diverge when reducing the power input into the ultrasonic transducer. Essentially, MBS found in smaller diameters remain present even at lower acoustic powers, however, they do shrink in size. However, upon climbing towards the 14 mm horn tip, the attached macrostructure begins to flatten instead, merely resembling a layered cushion placed on the larger horn tips. With further increasing the diameter from 14 mm to 40 mm, this cushion proceeds to become incrementally thinner.

Nevertheless, the cavitation structure shape here is merely a shallow comparison between the cavitation performance of the horn-type reactors and do not reveal much about their influence on the reactor's reaction rate. Instead, we speculate that perhaps the size of the cavitation and its oscillating frequency may reveal underlying correlations between the structure and the reactor chemical performance, as they may act as indicators to the extent of active zone presence within the domain. The typical lifecycle of an acoustic cavitation bubble disclosed in Chapter 2.2.1 summarizes the expansion of micronuclei through rectification diffusion or even coalescence with one another due to secondary Bjerknes forces, followed by reaching their resonance size that eventually leads to their collapse. This mechanism then disperses smaller active bubbles that undergo the same process [231]. By taking inspiration of this well-established mechanism, we attempted to draw analogous themes from the single-bubble lifecycle with the attached cavitation cluster. It was assumed that the bubble cluster attached to the horn tip is a single, continuous cavitation body – more like a large single bubble with an interface defined by its outermost layer that maintains a vapor volume fraction equal to 0.1. To mirror the dynamic behaviour of a bubble, we equivalently translated the cavitation structure attached to the horn tip of diameter D into a single spherical bubble structure with a constant equivalent radius R_{eq} that retains the same vapor volume V_B, as shown in Figure 8.2.

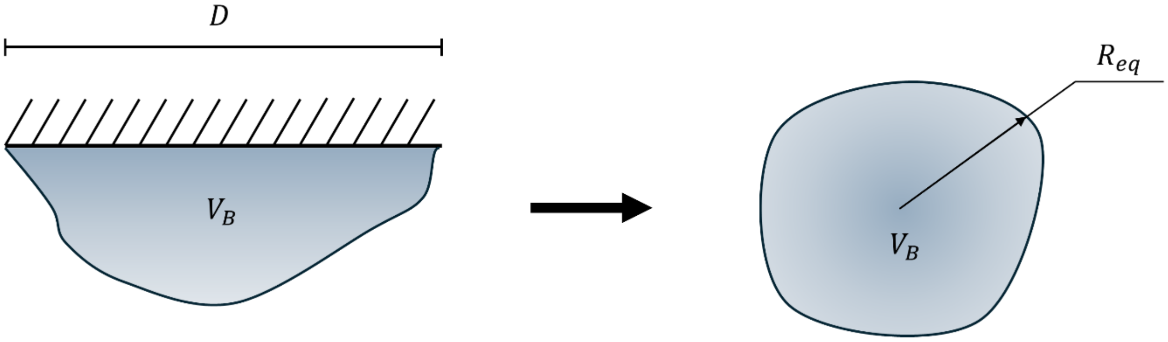

Figure 8.2: The translation procedure of the attached cavitation macrostructure on a horn tip surface of diameter D to an equivalent single spherical bubble of constant equivalent radius R_{eq} and vapor volume V_B.

Moreover, the dynamic oscillation, and specifically the resonance, of this equivalent bubble is assessed by adopting the previously established bubble natural frequency generalized model by Brennen et al. [30]. To derive the said model, Brennen et al. [30] started by neglecting both the thermal and compressibility effects and decomposing p_∞ in the Rayleigh-Plesset equation, stated in Eq. 2.3, into a mean value $\bar{p}_\infty$ and a small perturbation of the pressure amplitude $\tilde{p}$ with a radian frequency ω, such that

$$p_\infty = \bar{p}_\infty + Re\{\tilde{p}e^{j\omega t}\} \tag{8.2}$$

the bubble linear dynamic response becomes

$$R = R_E[1 + Re\{\varphi e^{j\omega t}\}] \tag{8.3}$$

where R_E is the equilibrium bubble radius sustained at $\bar{p}_\infty$ and φ is the bubble radius response in the form of a complex number. This way, $Re|\varphi|$ is simply the oscillation amplitude of the bubble radius. Moreover, φ phase represents the difference between p_∞ and R. In that regard, by replacing Eqns. 8.2 and 8.3 into Eq. 2.3, an expression that defines the bubble radius frequency is formulated as follows

$$\omega^2 - j\omega\frac{4\nu_l}{R_E^2} + \frac{1}{\rho_l R_E^2}\left[\frac{2S}{R_E} - 3kp_{GE}\right] = \frac{\tilde{p}}{\rho_l R_E^2 \varphi} \tag{8.4}$$

where

$$p_{GE} = \bar{p}_\infty - p_v + \frac{2S}{R_E} = \frac{3m_G T_B K_G}{4\pi R_E^3} \tag{8.5}$$

For a given perturbed pressure amplitude $\tilde{p}$, the maximum amplitude response appears to occur at a frequency ω_P, which can be evaluated by the minimum radius value in the left-hand side (LHS) of Eq. 8.4. This, in turn, gives us the following

$$\omega_P = \left[\frac{\left(3kp_{GE} - \frac{2S}{R_E}\right)}{\rho_l R_E^2} - \frac{8\nu_l^2}{R_E^4}\right]^{\frac{1}{2}} \qquad (8.6)$$

With this equation, and assuming negligible damping of the bubble radius oscillation induced by viscous effects, one can ultimately obtain an expression for the natural frequency of the bubble

$$\omega_N = \left[\frac{1}{\rho_l R_E^2}\left\{3k(\bar{p}_\infty - p_v) + 2(3k-1)\frac{S}{R_E}\right\}\right]^{\frac{1}{2}} \qquad (8.7)$$

where S is the liquid surface tension and k is a constant equal to 1 in our case, assuming that the bubble oscillation is an isothermal process. Here, it becomes noticeable that the natural frequency ω_N becomes solely dependent on the pressure gradient $(\bar{p}_\infty - p_v)$. More popularly, Minnaert [277] reduced this equation to

$$\omega_N = \frac{3.26}{R_E} \qquad (8.8)$$

given that the single bubble is present in an aqueous domain at atmospheric conditions. In that regard, we have utilized the said equivalencies and frequency definitions on the acoustic cavitation structures observed in the stated cases in Table 8.1. Specifically, we started with extracting the monitored vapor volume signal and implementing FFT on each of them to obtain the underlying oscillation frequency, assuming that this represents the resonance frequency of the macrostructure. This assumption sources from the natural frequency definition in Eq. 8.7 in which it expresses that bubble resonance occurs when zero viscous damping is assumed on the bubble radius. Likewise, the modified ZGB cavitation model derived in Chapter 4 is based on a simplified Rayleigh-Plesset equation, expressed in Eq. 4.13, that neglects the influence of viscosity on the bubble radius progression. Following that, the vapor signals and their respective FFT are summarized in Figures 8.3 – 8.7.

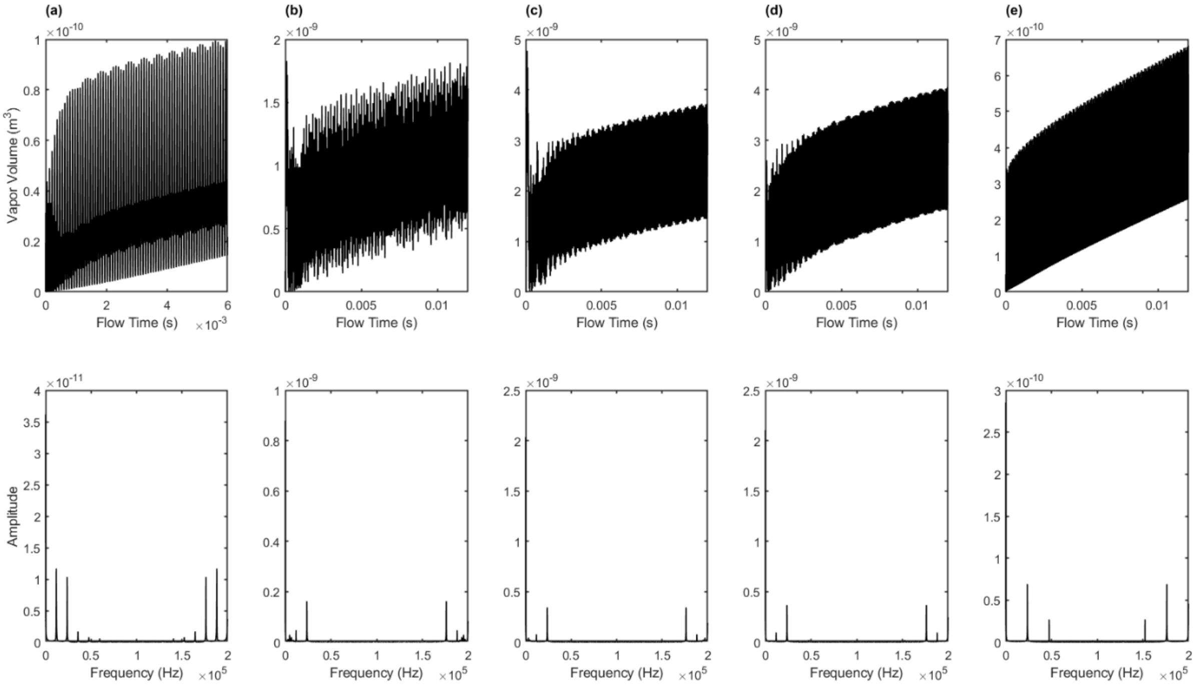

Figure 8.3: Vapor volume signals and their respective frequency response plots for all cases of A_{nom} = 30% where (a) - (e) represent the 3 mm case to 40 mm case.

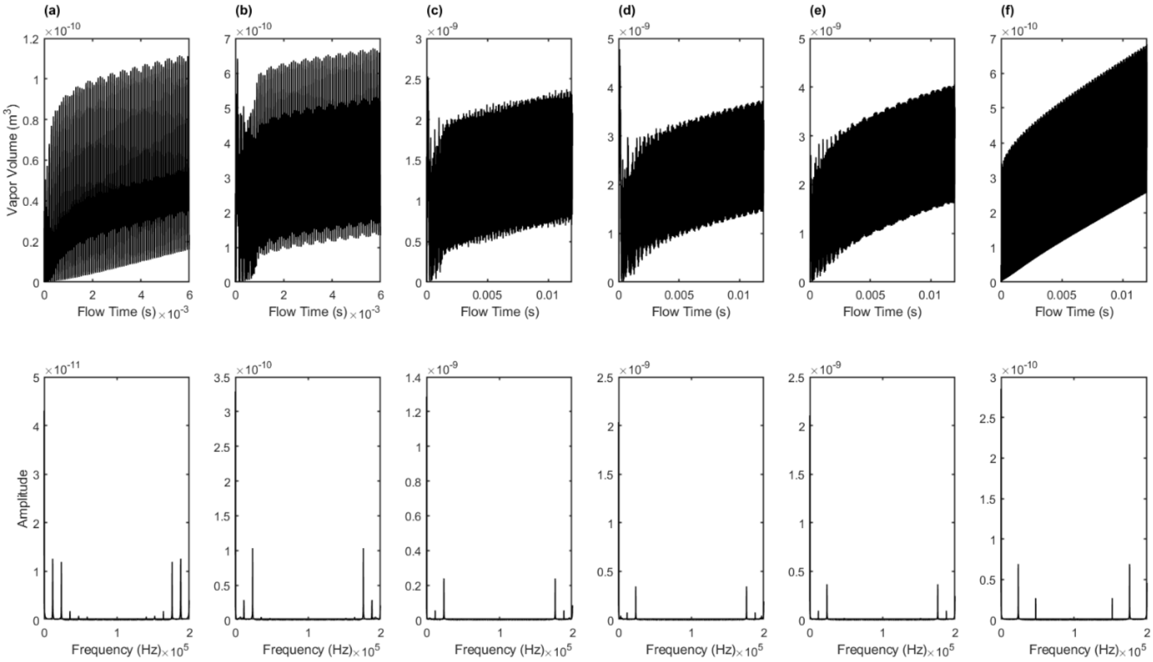

Figure 8.4: Vapor volume signals and their respective frequency response plots for all cases of A_{nom} = 50% where (a) - (e) represent the 3 mm case to 40 mm case.

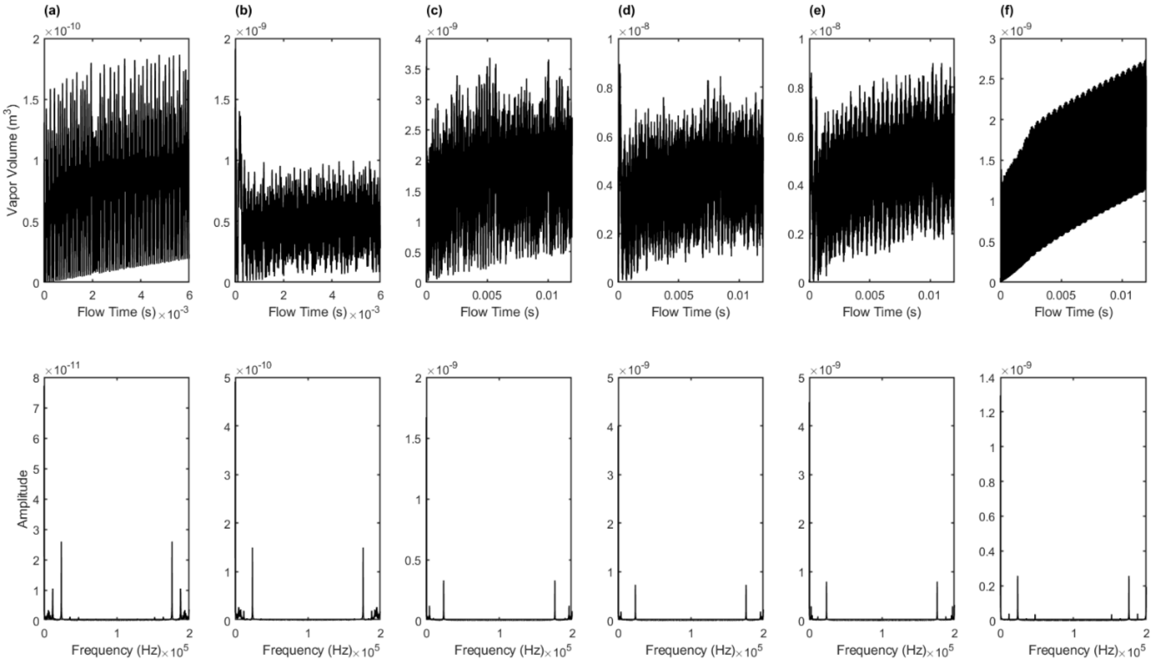

Figure 8.5: Vapor volume signals and their respective frequency response plots for all cases of A_{nom} = 70% where (a) - (e) represent the 3 mm case to 40 mm case.

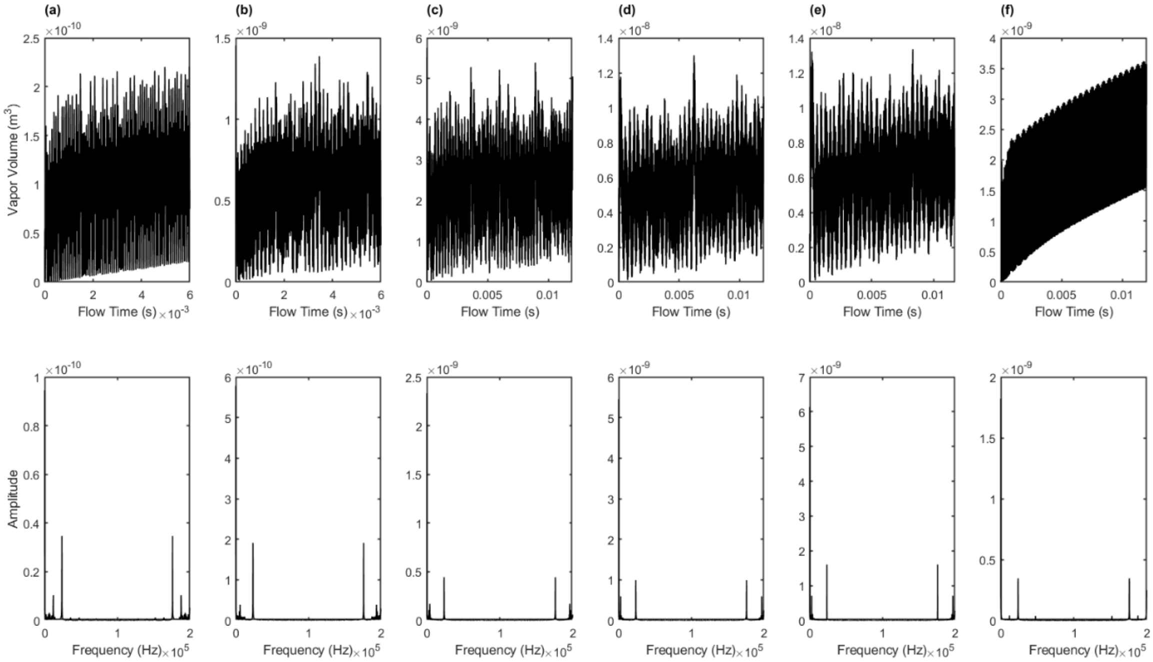

Figure 8.6: Vapor volume signals and their respective frequency response plots for all cases of A_{nom} = 90% where (a) - (e) represent the 3 mm case to 40 mm case.

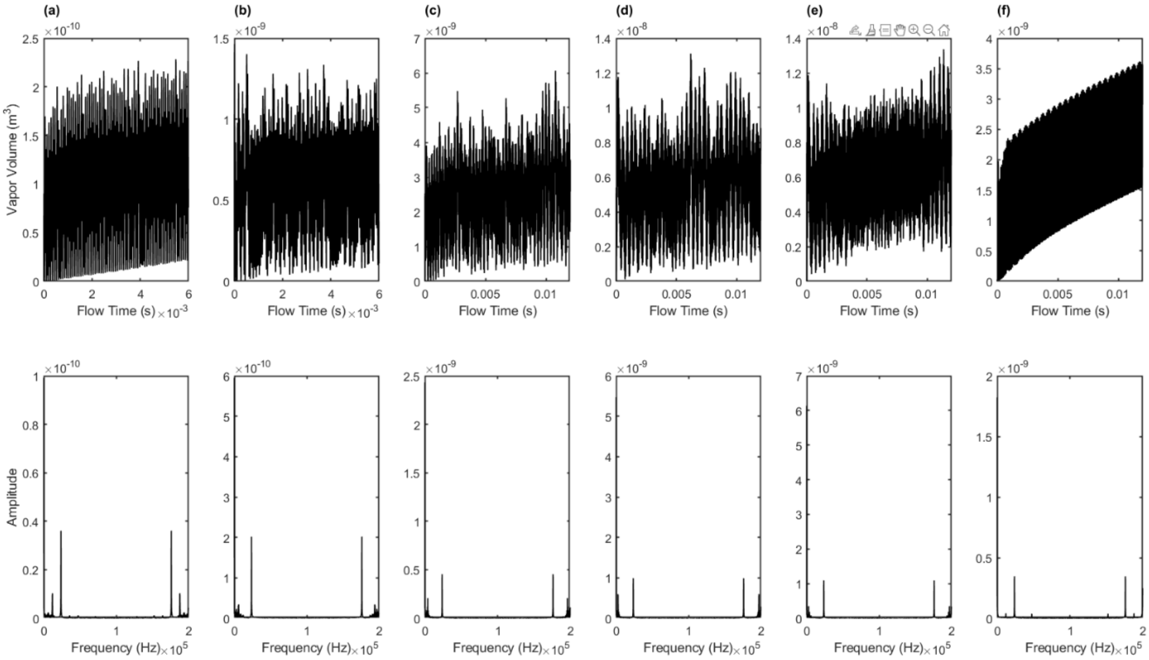

Figure 8.7: Vapor volume signals and their respective frequency response plots for all cases of A_{nom} = 100% where (a) - (e) represent the 3 mm case to 40 mm case.

Furthermore, by calculating the RMS of the vapor volume signal, we can then evaluate the time-averaged equivalent radius of each case by utilizing the following volume equation of the sphere.

$$V_B = \frac{4}{3}\pi R_{eq}^3 \tag{8.9}$$

With both frequency and radius data obtained, data points were plotted alongside the Minnaert resonance curve to compare the potential overlap or translation of the data points obtained from the established Minnaert resonance curve. These datapoints were categorized based on the horn tip diameter they were generated under. Therefore, based on Eq. 8.8, we have fitted a curve similar to the Minnaert resonance curve along each category of points to illustrate the differences. This comparison is highlighted in Figure 8.8 below. Generally, it is shown that with the increase of the horn tip diameter, the curve translates upward deeming that the cavitation structures generated are ultimately larger in size and oscillate at increasing bandwidths. Interestingly, the 3 mm tip diameter almost overlaps with the Minnaert resonance curve suggesting that the structure under such horn tip acts as a bubble at atmospheric conditions.

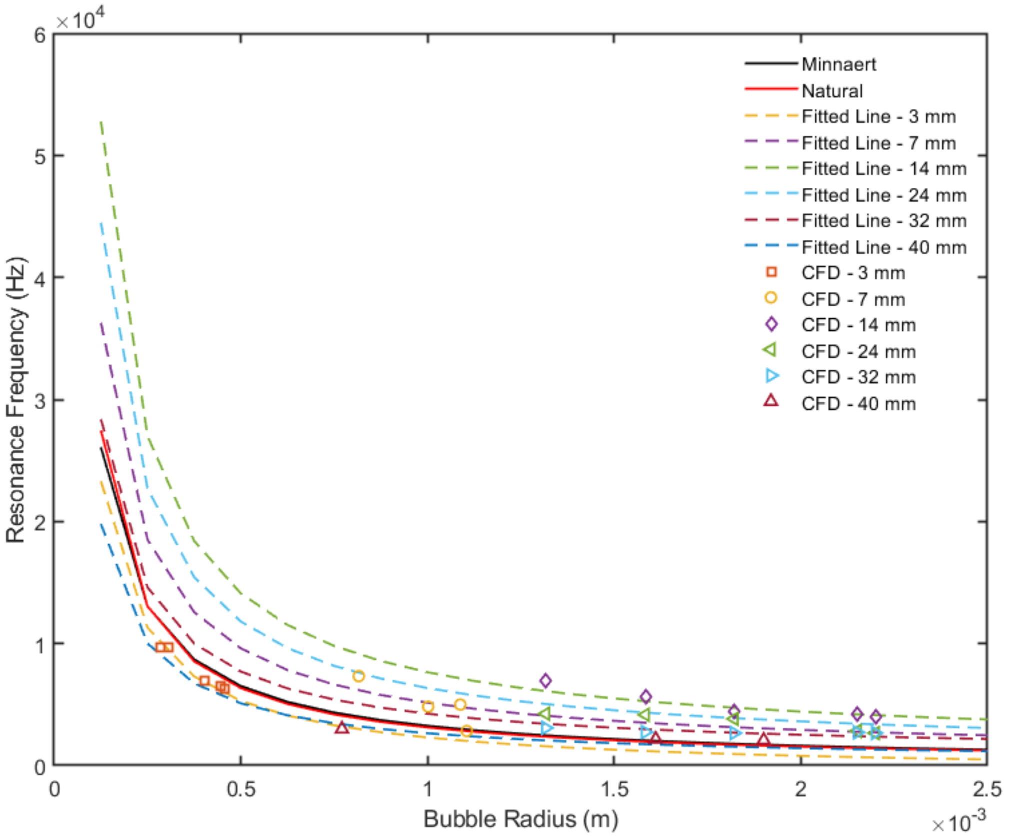

Figure 8.8: Comparative plot showing the resonance frequency of each cavitation macrostructure obtained under each horn tip diameter.

Furthermore, another interesting trend revealed is the nonlinearity that occurs past the 14 mm horn tip. With the increase of the tip diameter from 14 to 40 mm, the curve begins to translate downwards instead indicating lower oscillation frequencies, however, with larger cavitation structures. Essentially, the large cavitation structures observed under the 14 mm to the 40 mm horn tips are not due to their axial extensions but their flat spreading along a larger surface area of the horn tip. Therefore, vapor within their respective domains occupy more volume. These trends were in fact obtained numerically for each case, however, to ensure confidence in these trends, we have extracted experimental data and plotted them alongside the numerical results, as shown in Figure 8.9. Given that the numerical setup used is the same setup validated in Sections 4, 5 and 6, this plot acts as an extended validation and reinforces the capability of this configuration to comparatively capture the experimentally observed oscillatory behaviours of generated cavitation structures. While additional quantitative comparisons could further enrich the validation, the comparative plot here focuses on demonstrating the model's ability to reproduce the frequency scaling behaviour with respect to the horn tip geometry, which is the physical phenomenon of interest. Ultimately, this provides sufficient ground to assess the reactors' performance from a purely hydrodynamic perspective.

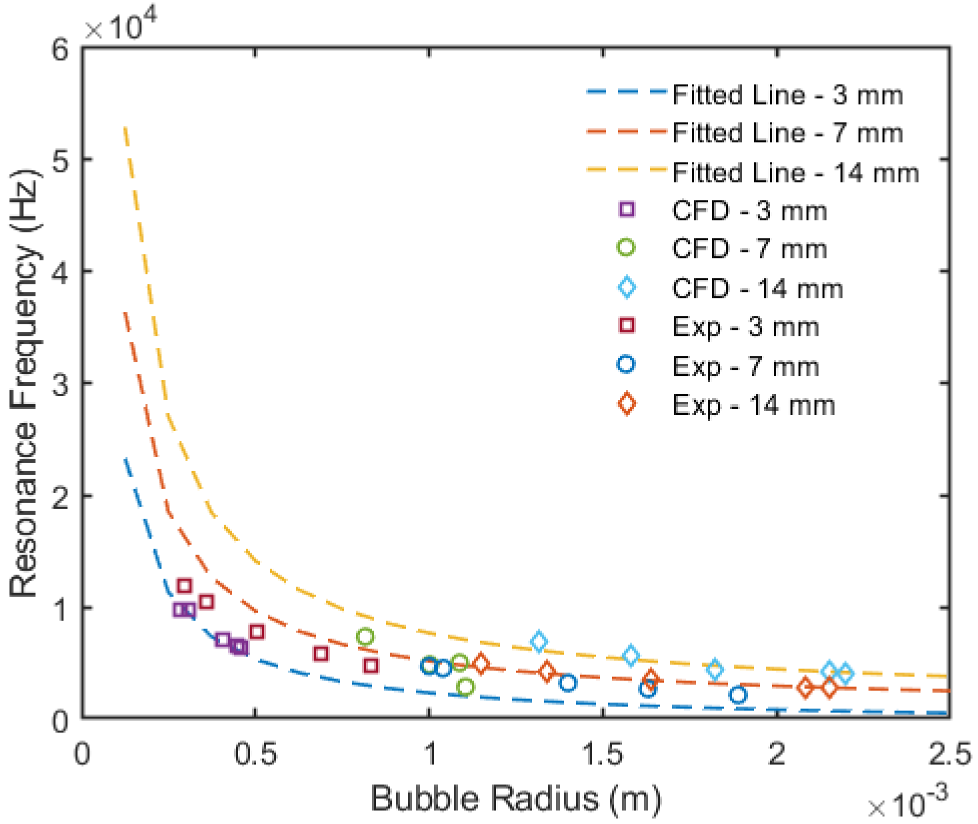

Figure 8.9: Validation plot comparing the numerical results with the experimental results by showing the resonance frequency of each cavitation macrostructure obtained under each horn tip diameter.

Here, a small discrepancy between the numerical and the experimental results can be seen highlighting the numerical simulation's relatively small underprediction of the frequency trends. Nevertheless, the fitted lines generally precisely capture matching trends and dynamic behaviours of all bubbly structures. The fitted trendline translations were plotted using the following generalized function of the Minnaert resonance expression

$$\omega_n = \frac{a}{R_{eq}} + b \tag{8.10}$$

where a and b are fitting coefficients, where $a = 3.26$ and $b = 0$ for Minnaert resonance equation. As mentioned earlier, this is generally obtained by solving the natural frequency equation expressed in Eq. 8.7 by assuming atmospheric conditions. This way, it can be said that the manipulation of these coefficients for the different trendlines indicate a possible shift in the value of the pressure gradient in Eq. 8.7 away from atmospheric conditions. To prove this, we have attempted to replot the fitted trendlines using Eq. 8.7 to quantify the exact change in the pressure gradient term, as shown in Figure 8.10.

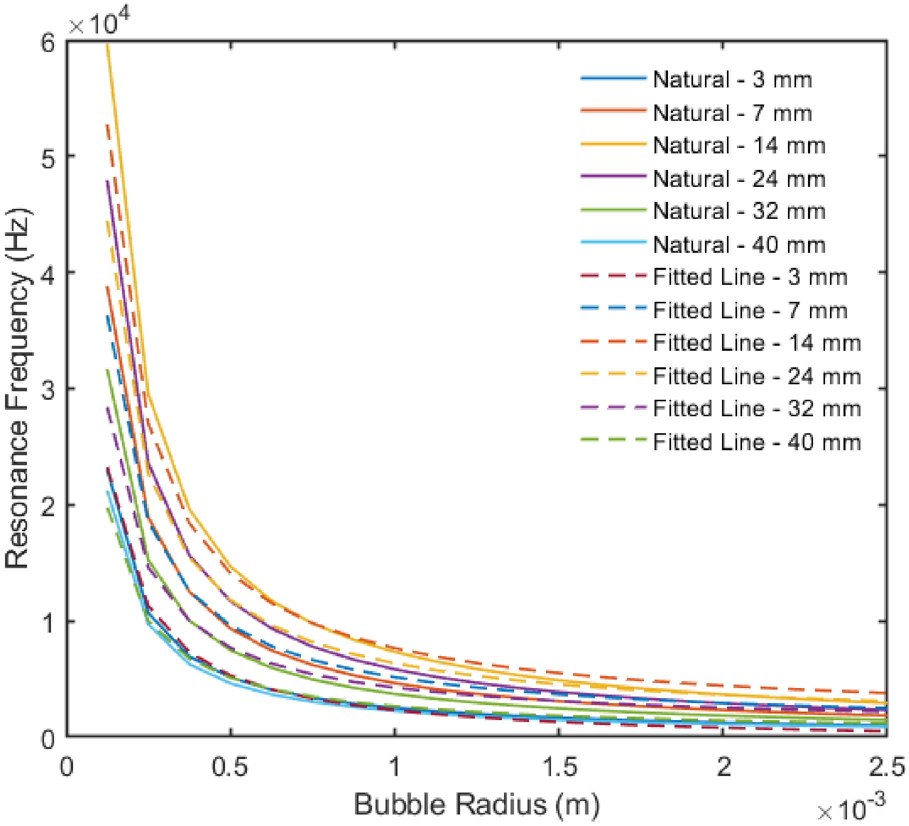

Figure 8.10: Comparison between trendlines fitted using the generalized Minnaert equation and the natural frequency equation.

With trial and error, the pressure gradient values were chosen to fit as closely as possible to the fitted lines. These pressure gradient values were then recorded for each diameter, as illustrated in Figure 8.11, and plotted against the inlet Reynolds number of each horn tip. What was rather eye-catching is the remerging of the said nonlinearity in the pressure gradient values as well. Initially, the pressure gradient seems to increase drastically with the increase in the horn tip diameter from 3 mm to 14 mm. Afterwards, the inflection point becomes apparent with short stepdown in the pressure gradient when moving from a 14 mm to a 24 mm horn tip, until it ultimately, and rather surprisingly, reaches a value almost equivalent to the value observed at 3 mm horn tip. Another interesting point is the overlap of this nonlinearity with the nonlinearity observed in progression of the Reynolds number. This could be a potential indicator towards the role of the flow field on the generation of these pressure gradient values. Recalling that $\Delta P = p_\infty - p_v$, where p_v is a constant material property referring to the vaporization pressure, this typically means that it is p_∞ that governs the value of ΔP. Essentially, Brennen et al. [30] defines this term as the ambient pressure of the container a single bubble is settled in. However, it is obvious that perhaps this definition does not exactly apply for the case of acoustic cavitation. Instead, it was found that p_∞ here is defined as the RMS pressure of the domain. Therefore, p_∞ will be referred as p_{RMS} from this point onwards. As such the questions that rise from these observations are as follows: (i) what are the factors that govern the value of p_{RMS}? (ii) to what extent is the influence of cavitation's presence on p_{RMS}? (iii) If so, what governs the structural dynamics of the cavitation structure? The following sections will answer the raised questions.

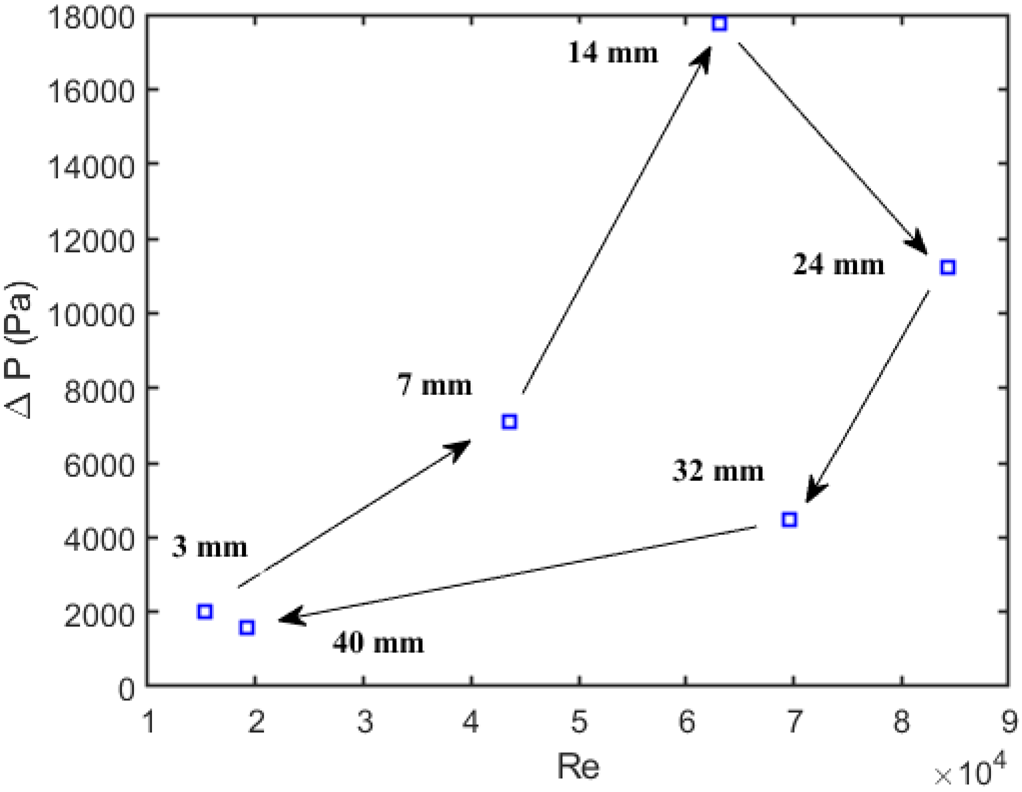

Figure 8.11: The generated pressure gradient by different inlet Reynolds number under different horn tips.

8.3.2 Proximal Acoustic Multiphase Flow Field

As preliminary measures taken to answer the stated queries, we started by isolating this section's scrutiny to the triangular inflection region observed in Figure 8.11 formed by the 14 mm, 24 mm, and the 32 mm points. This is to shine light on the underlying factors that play a role in the establishment of this nonlinear region. Based on the exploration in Chapter 7, it has been understood that the acoustic wave tends to experience attenuation due to a multitude of factors, such as the material property of the fluid domain, the presence of impurities, and in our case, the presence of homogenous phases within the continuous domain. We have already concluded that the larger the axial presence of cavitation is the more refracted, and eventually attenuated, the acoustic wave will be. While the conclusion was consistent with our observations in multiple cases, however, it fails to justify the present nonlinearity here. It is crucial to note that the investigation conducted in Chapter 7 was a mere change of diameter while keeping all horn operating conditions constant, i.e. the oscillation amplitude was kept constant for horn tips considered, while not necessarily physically possible. In the present case, on the other hand, the oscillation amplitude changes from one tip diameter to another, since the parameters are based on an experimental setup. Furthermore, the selection of the oscillation amplitude varies with respect to the power level set for the ultrasonic transducer. As such, the cavitation flow fields were analysed in both amplitude variation directions.

8.3.2.1 Flow Field Variations with Tip Diameter Changes

For the first case, we have scrutinized the flow fields of the three diameters during their operation at 30% power. In a similar fashion conducted in Chapter 7, the flow field parameters for each case were time-averaged, as shown in Figure 8.12. Going by the shape of the cavitation structure, it seems as though the macrostructure sustains this sheet-like structure about the horn tips, only that it appears to get thinner with larger horn tip diameters. This becomes clearer in Figure 8.13, where the position of the hump starts off the furthest at around $\zeta = 0.25$ for the 14 mm case and begins to recede until $\zeta = 0.1$ for the 32 mm case. This attribution between the $grad\ v_z$ hump location and the cavitation axial extension was proven in Chapter 7. The slight resemblance of a cone-like structure with the cavitation's axial extension under the 14 mm tip clearly defines itself as the turning point for the cavitation structure towards a flatter structure with larger horn tips.

Making preliminary judgements, based on the variation in the operating conditions of the considered horn tips, the appearance of these flatter structures might be due to the fact that the same percentage acoustic energy is being distributed over a larger surface area, ultimately, forcing the horn tip into a smaller amplitude oscillation. In other words, the amount of acoustic energy transferred to the fluid domain is gradually decreasing with increase in the diameter, as previously discussed by Viciconte et al. [228]. This also is reflected in the axial velocity contour plots, in which a gradual deceleration in the acoustically excited flow is demonstrated when moving from the 14 mm horn towards the 32 mm horn, which may justify the hump size variation observed in Figure 8.13. However, what is rather eye catching is the pressure distribution about the horn tip; it appears as though the high-pressure interface perfectly overlaps the attached cavitation structure wavy interface. This perhaps can be taken as a hint towards uncovering the correlation between the two.

Recalling the attenuation trends computed using the one-dimensional model in Chapter 7, it is understood that attenuation of the acoustic wave is in fact governed by the cavitation, however, it is not governed by its overall size but by its bubble density. With larger horns, we have observed, both here and in the previous chapter, that the cavitation structure is generally larger, whether it adopts a sheet-like structure or a cone-like structure. Nevertheless, the attenuation was proven to be greatest under the smaller horn tip diameters, i.e. 3 mm and 6 mm tips. We have suggested then that this is probably due to the bubble density and distribution within the macrostructure. This suggestion is shown to apply in the present case as well, judging by the trends plotted in Figure 8.14, which were obtained by following the same methodology discussed in Section 7.4.3. A general overview of the trends will reveal that the rate of decay of the bubble population within the structures increases significantly under larger tip diameters, which, in turn, further highlights the shortened axial extension of the cavitation structure. Moreover, the bubble density, specifically within the structure's core, seem to sharply drop at the 32 mm case, while it was quite comparable between the 14 mm and 24 mm cases. In reference to the pressure distribution observed in Figure 8.12, the acoustic pressure wave transverses further downstream when faced with a smaller bubble population, and in turn, the ultrasonic radiation has more influence over the domain. This could be a plausible explanation to the noted variation in p_{RMS} from one case to another, however, it is important to see if these observations hold true in the remaining power levels before making any ultimatums.

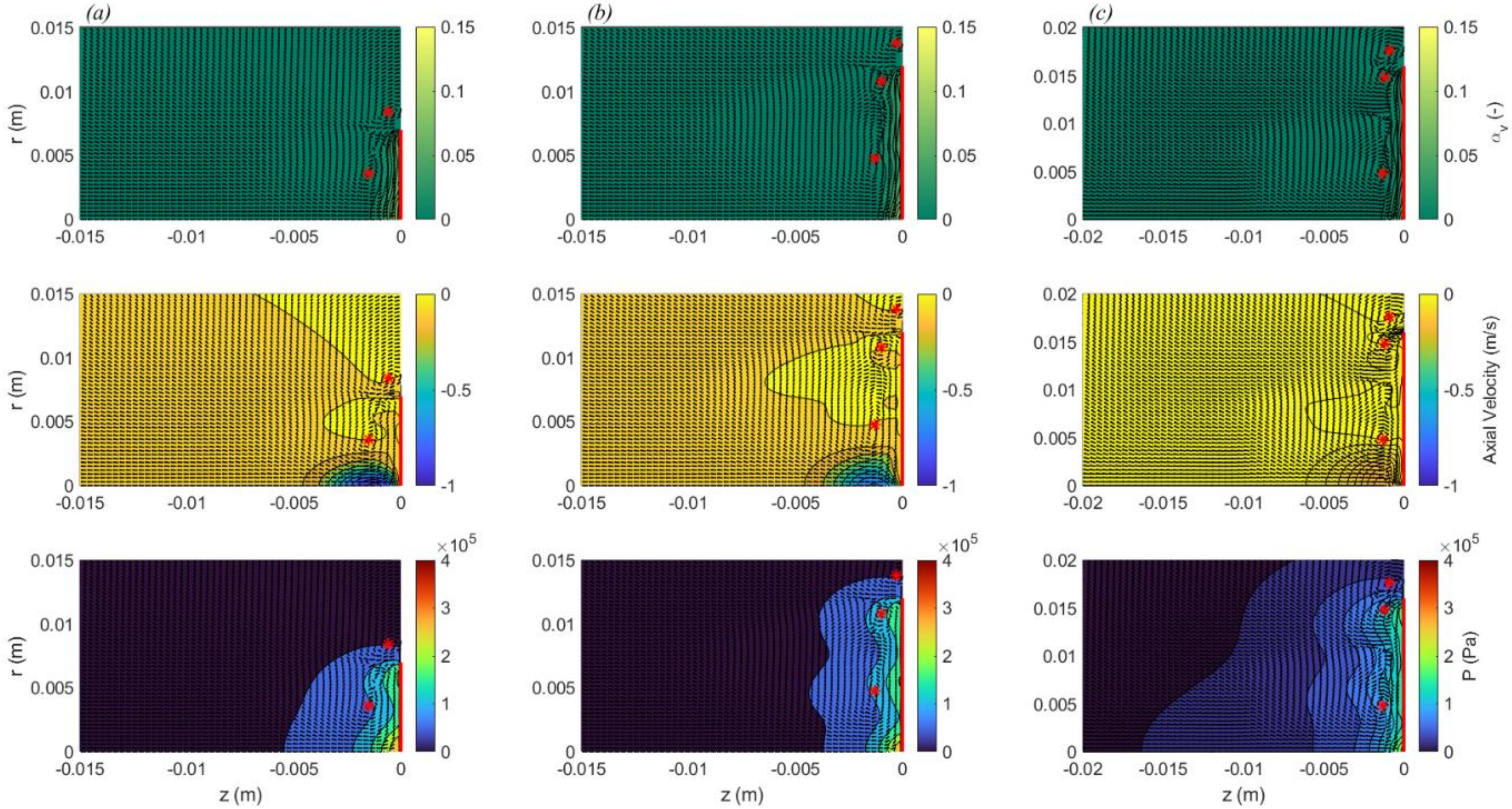

Figure 8.12: Axisymmetric contour-vector plots of the time-averaged (top) vapor volume fraction (center) axial velocity and (bottom) pressure of the proximal flow about (a) a 14 mm tip (b) a 24 mm tip and (c) a 32 mm tip all operating at 30% power. The red vertical lines represent the horn tip, and the red asterisks label the vortex centers.

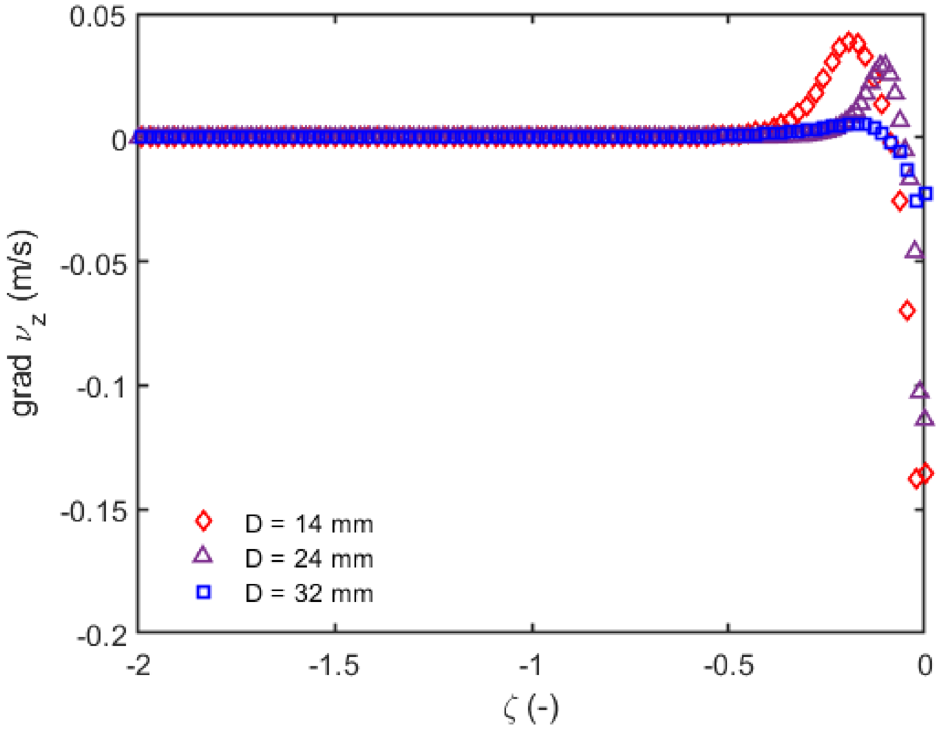

Figure 8.13: Axial velocity gradients about the horn axis plotted against the dimensionless axial coordinate for cases of D = 14, 24, and 32 mm. ζ is the dimensionless z-position normalized with respect to the tip diameter D for each case.

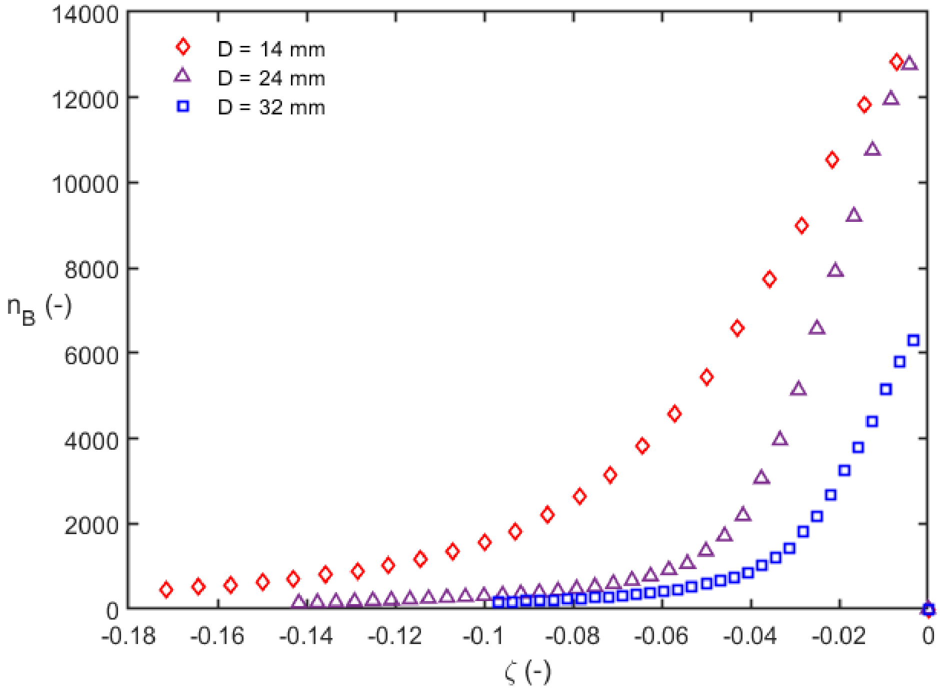

Figure 8.14: Number of bubbles n_B plotted against the dimensionless axial coordinate along the horn axis for cases of D = 14, 24, and 32 mm. ζ is the dimensionless z-position normalized with respect to the tip diameter D for each case.

8.3.2.2 Flow Field Variations with Power Level Changes

In this subsection, we have taken the 14 mm horn tip and scrutinized all its power levels to explore the potential impact the increase in amplitude with the same diameter has on the proximal flow field. At first glance, we can immediately observe that the cavitation structure gradually grows in size and morph into a closer shape resembling CBS. This axial growth downstream is highlighted in both Figure 8.15 and Figure 8.16. In Figure 8.16, specifically, the axial extension can be quantified by the shift in the maximum point of the hump. Interestingly, the structural extensions of cavitation seem comparable enough in such a way that one can categorize them in the following groups: (i) low power range (ii) mid-power range and (iii) high power range. At 30% power, the axial extension reaches 0.25D, while the structure's axial extension reaches at about 0.45D at both 50% and 70% power. Lastly, at 90% and 100%, the axial extension ultimately reaches 0.75D. Moreover, the axial flow seems to drastically accelerate with the increase of power, which is justified due to the proportional increase in acoustic energy density distributed about the same horn tip surface area, moreover, this induces a higher energy concentration being transmitted into the fluid domain through the radiation column created under the acoustic horn. Using Eq. 7.33, we tabulated the acoustic intensity I_A and the acoustic power density P_D trends for each power level, as shown in Table 8.2.

Table 8.2: Acoustic horn oscillation conditions and acoustic energy concentration parameters for the 14 mm horn tip at each power level.

$\phi_D\ (\mu m)$	A_{nom} (%)	$A_r\ (\mu m)\ \pm 2.35$	P (W)	$I_A\ (W/mm^2)$	$P_D\ (W/mm^3)$
14	30	19.95	120	0.21	0.009
	50	29.34	200	0.35	0.015
	70	39.91	280	0.53	0.021
	90	53.99	360	0.81	0.024
	100	55.16	400	0.90	0.030

It is expected to observe that the trends of both I_A and P_D are collinear in nature and increasing with the increase in the power input P, as it shows that the increase acoustic energy concentration on the surface of the horn tip will eventually dissipate to the fluid radiation column under the horn tip. One may notice that the energy density within the fluid column is substantially less than the acoustic energy density about the surface area of the horn tip, however, this trend surely complies with the simple fact that the energy is being distributed over a larger volume, and thus the energy concentration is spread thin.

Despite that, the flow field particularly demonstrates a significant change in its behaviour within the system through the change in the pressure distribution about the horn tip. Essentially, the once curvy pressure interface appears to smoothen out with a power level increase from 30% to 70%. As what was discussed earlier, this new pressure interface falls in-line with the smoothened cavitation interface, as well. This gradual transfiguration from a sheet-like structure to CBS is also reflected in the bubble distribution, plotted in Figure 8.17, based on the yet another deduction made in Chapter 7 stating that CBS tends to sustain a highly nonlinear bubble distribution. This is particularly observed for 70%, 90%, and 100% power. Furthermore, and as one can already predict, a higher power level induces a higher bubble density within the macrostructure. However, it now becomes of great significance to understand the governing factors of the bubble distribution and population. Conclusions drawn previously suggesting that the bubble distribution is a consistent indicator to the cavitation macrostructure's shape provides a solid platform to build on in our current case; the question ultimately boils down to, what governs the bubble structure shape?

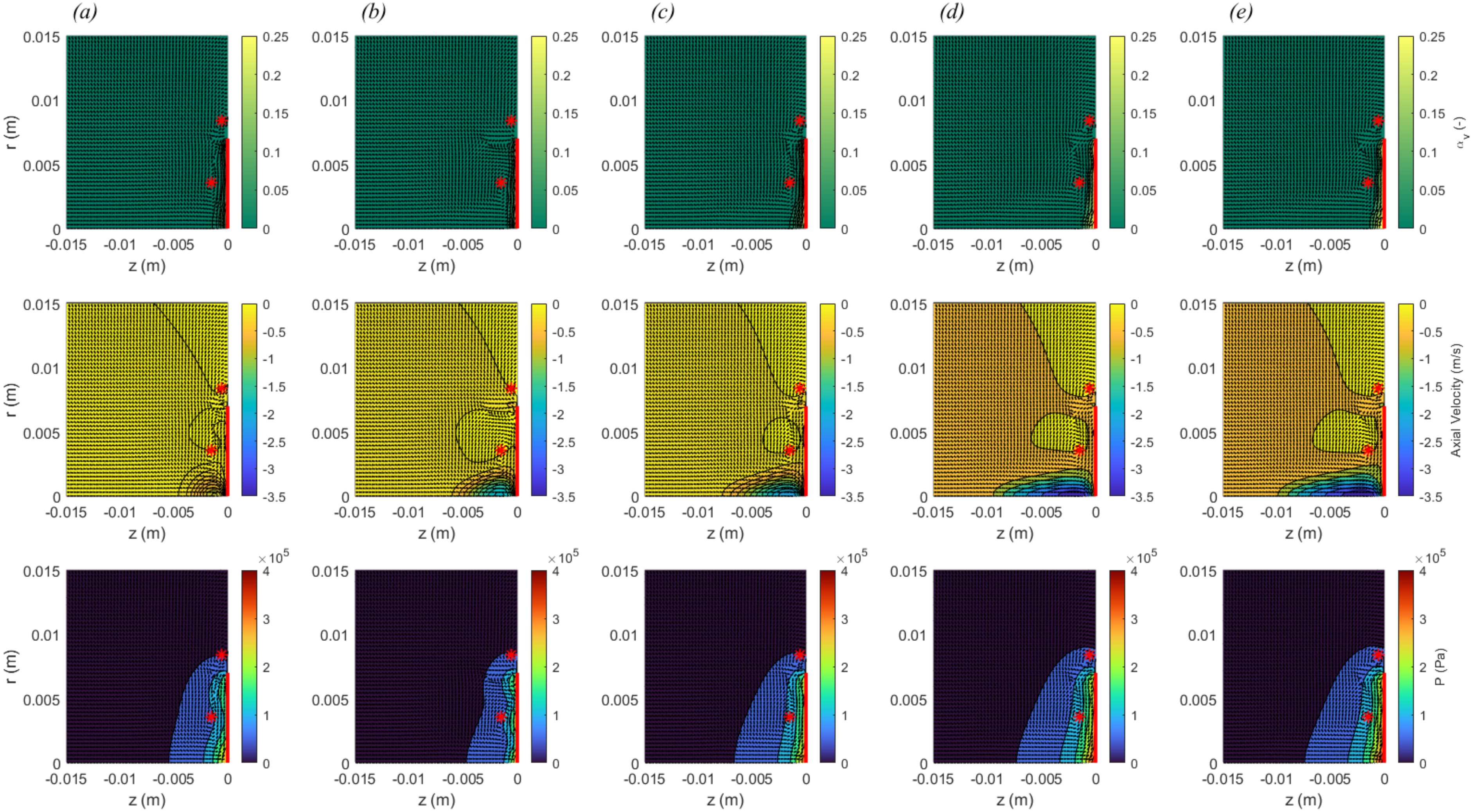

Figure 8.15: Axisymmetric contour-vector plots of the time-averaged (top) vapor volume fraction (center) axial velocity and (bottom) pressure of the proximal flow about a 14 mm tip operating at (a)-(e) 30% - 100% power, respectively The red vertical lines represent the horn tip, and the red asterisks label the vortex centers.

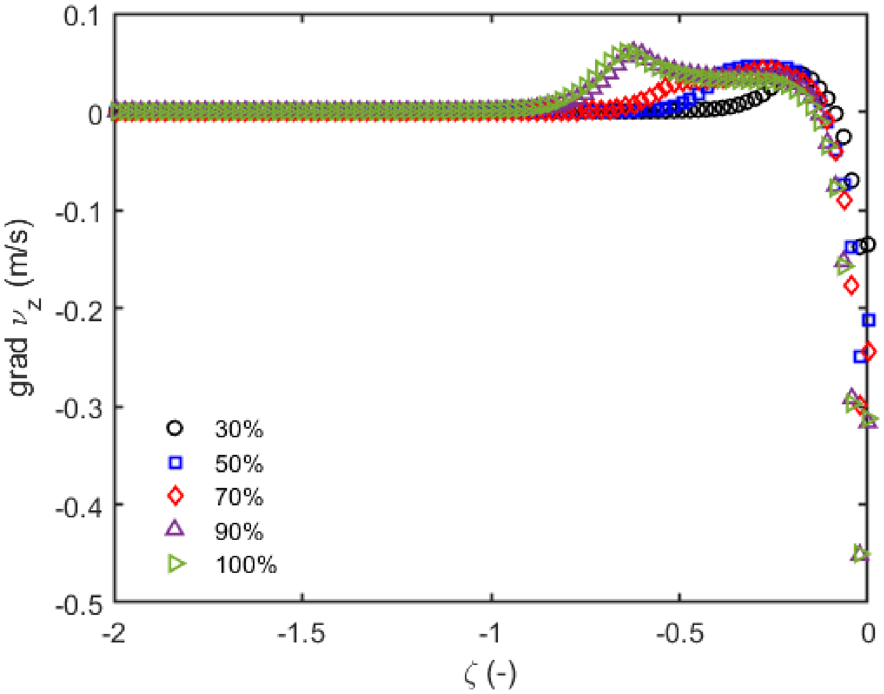

Figure 8.16: Axial velocity gradients about the horn axis plotted against the dimensionless axial coordinate for the horn tip D = 14 mm operating at different power levels. ζ is the dimensionless z-position normalized with respect to the tip diameter D.

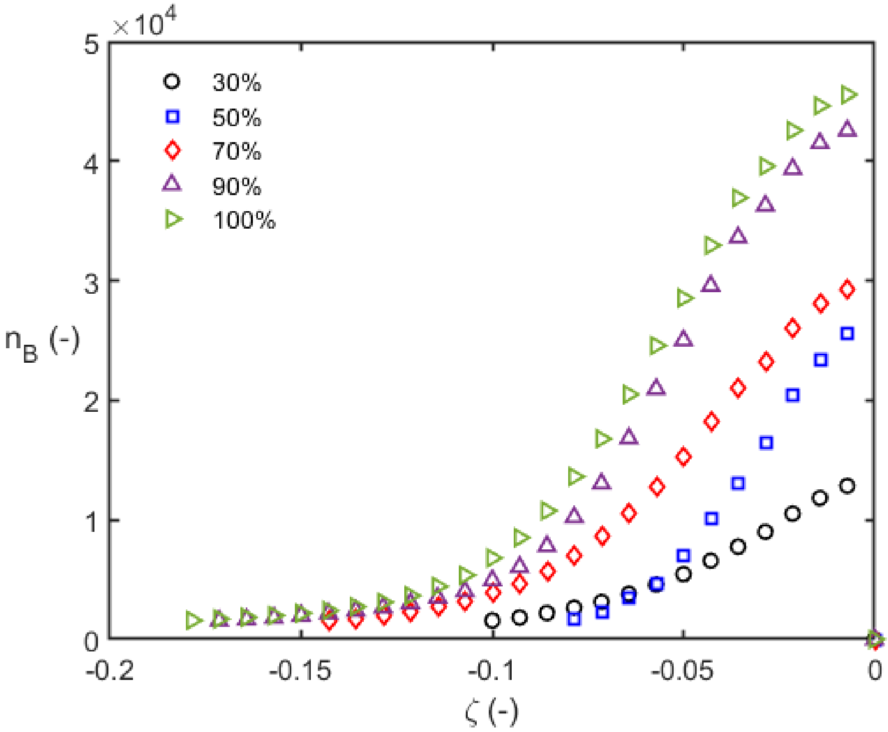

Figure 8.17: Number of bubbles n_B plotted against the dimensionless axial coordinate along the horn axis for the horn tip D = 14 mm operating at different power levels. ζ is the dimensionless z-position normalized with respect to the tip diameter D.

8.3.3 Vortical Structural Behaviours

In both Chapters 5 and 6, we have established that there exists a generative locomotive toroidal vortex produced by the periodic motion of the horn as a recirculation zone on both its sides, initially. These then reposition themselves downstream along the horn axis forming a couple of counter-rotating vortices. In Chapter 6, specifically, we have placed major focus vortex-bubble interaction and ultimately concluded that the vortex has some hand in governing the lifecycle of the transient cavitation structure through flow manipulations and ultimately forming an impinging jet that breaks down the continuous structure. As we are currently scrutinizing the steady structure of cavitation, the role of the time-averaged vortices in the manipulation of the cavitation structure remains unknown. In Figure 8.12, this primary counter-rotating vortex seems to be actively present under all three horn tips, of course with different sizes, eccentricities, and lengths. Moreover, the aforementioned side recirculation is also present in the steady domain. However, what was rather interesting was the formations of new secondary vortices along the tip surface of the larger horn tips. Noticing the overlap between the scattering of these vortices, the pressure distribution, and the flatter appearance of the cavitation structure hint at a potential coupled effect between them all. In aims to look further into the change in the vortex property and position with respect to its correlative occurrence with different cavitation structures, Figure 8.18 zooms into the recurring primary vortex and plots the respective pressure distribution and the flow curl within the chosen confined subdomain for the same cases shown in Figure 8.12.

The purpose of this figure is to shine light on what was hinted at in Figure 8.12, and that is the variation in the pressure distribution and interface is being governed by the presence of the vortex. One can notice from the previous figure, and the current figure below, that the vortex centre appears as though it is initially positioned at low pressure node in the 14 mm case, however, this immediately begins to gradually change with the increase of the tip diameter. Moreover, upon plotting the curl of the velocity vector field, the vector field within the confinement of the vortex core comes across as initially very rotational, however, its vorticity begins to dissipate with the increase in the tip diameter hinting at a possible weakening of the vortex. Usually, when a vortex core loses its vorticity, it starts to slow down leading it to shift from its inertial-dominated behaviour to a more viscous-dominated behaviour. At this point, its circulation begins to significantly dissipate, and its vorticity is seen to diffuse. However, to quantify this effect and precisely judge the transformation of the primary vortex under scrutiny, the vortex Reynolds number has been computed for each case through the following expression

$$Re_V = \frac{\Gamma}{\nu} \tag{8.11}$$

where Γ is the circulation around the vortex confined region, which is evaluated by

$$\Gamma = \oint_C \vec{v} \cdot d\vec{s} = \iint_S \omega_z \, dA \tag{8.12}$$

Here, Γ is defined in two ways, the first being the line integral of the velocity field $\vec{v}$ over a closed curve C, where $d\vec{s} = \vec{v}\, dt$. Moreover, this is equivalent to the double integration of the angular momentum in the z-direction over a closed surface S. Provided the curl in Figure 8.18, ω_z can directly be computed using the following relationship

$$\omega_z = \frac{1}{2}\nabla \times v \tag{8.13}$$

Ultimately, this way, we can use the second definition of Γ to interpret the value of circulation and replace it in Eq. 8.11 to obtain Re_V. The vortex Reynolds number for each case in Figure 8.18 are 32.6, 14.6, and 4.57 for the 14 mm, 24 mm, and the 32 mm tips, respectively. The obvious trend is that the viscous effects gradually overcome the inertial effects on the vortex causing its vorticity to dissipate much faster. This in turn justifies the pressure change in the low-pressure node at which the vortex centres lie in, since the insufficient sustenance of vortex rotation prevents the creation of a low-pressure node proximal to the horn tip. As a result, this may be the reason behind the flattening of the cavitation structure; the proximal pressure field is insufficiently low to encourage any further nucleation downstream of the horn tip.

On the other hand, however, a change in the power input into the 14 mm horn tip resulted in what was already observed in Figure 8.15. In Figure 8.19, the incremental increases in the power level were generally observed to facilitate larger steady high-pressure zones proximal to the horn tip, however, no significant change to the vortex position was observed at all. Instead, the vortex was seen sustaining its high vorticity and minimizing its viscous dissipation, almost acting like an ideal vortex. Interestingly as well, the vortex core seems to consistently appear at a low-pressure node, which appears to partially facilitate the axial extension of the cavitation structure observed in Figure 8.15. This is of course a compound effect of a more inertia-dominated vortex behaviour and a higher amplitude of oscillation of the acoustic wave that generated these low-pressure nodes. This observation is supported by the computed values of Re_V for each power level where it was found that Re_V = 32.60, 611.17, 549.67, 782.00, and 941.14 for power levels 30% through 100%, respectively. As it was concluded that the cavitation structural shape influences the propagation of the acoustic wave throughout the domain, it leads us to think that the said variation in the vortex structural behaviour does in fact have moulding capabilities over the cavitation structure through manipulations of the pressure field. As such, this ultimately controls the equivalent radius obtained for each case. Moreover, manipulations of the size and shape of the cavitation structure then allow for the control of the extent of attenuation of the acoustic wave that, in turn, influence the value of p_{RMS}. Therefore, this directly influences the observed variation in the resonance frequency of the macrostructure's oscillation.

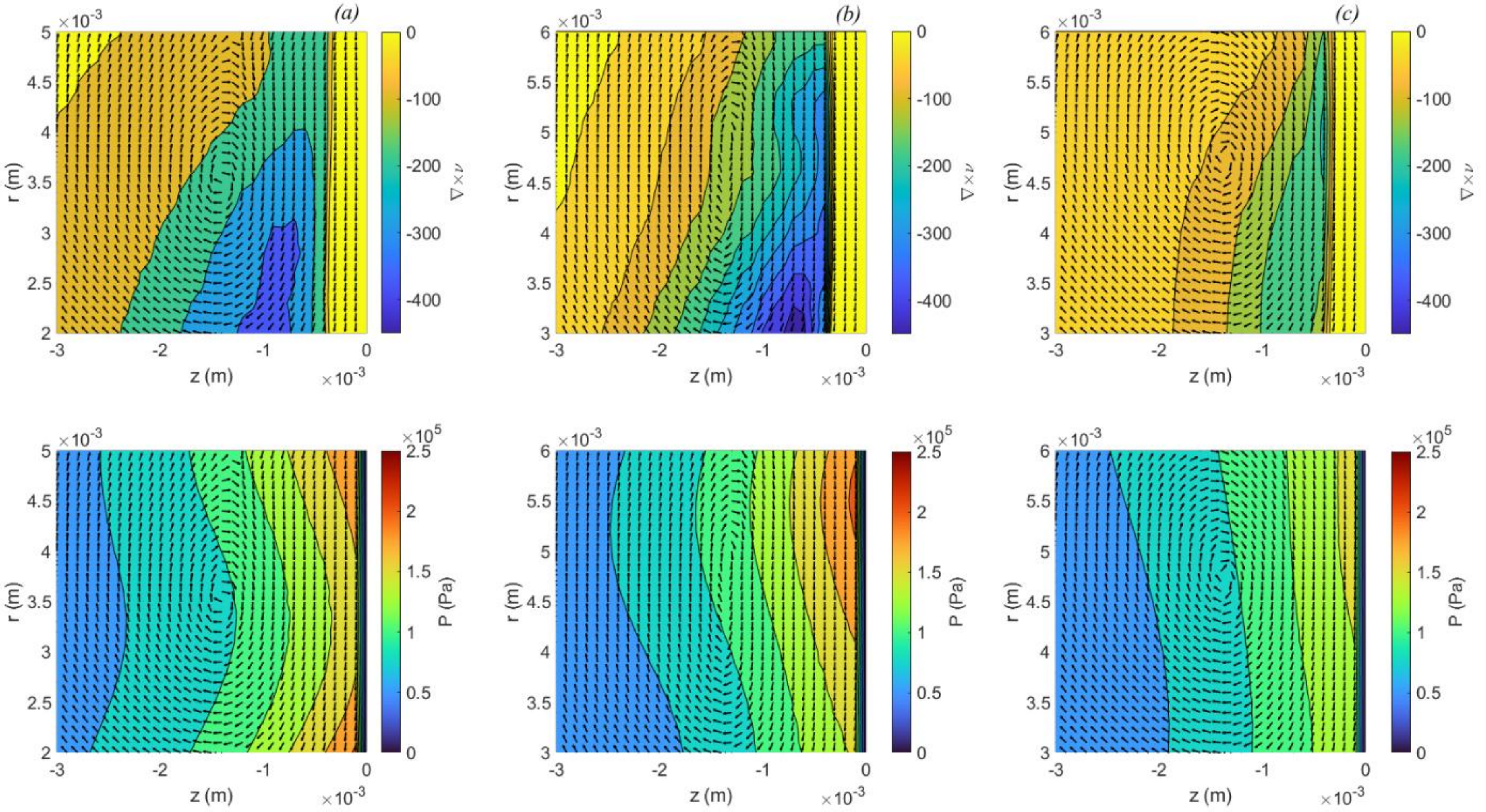

Figure 8.18: Axisymmetric contour-vector plots of the time-averaged (top) curl and (bottom) pressure of the proximal flow about the closest vortex to the horn axis of the (a) 14 mm tip (b) 24 mm tip and (c) 32 mm tip cases all operating at 30% power.

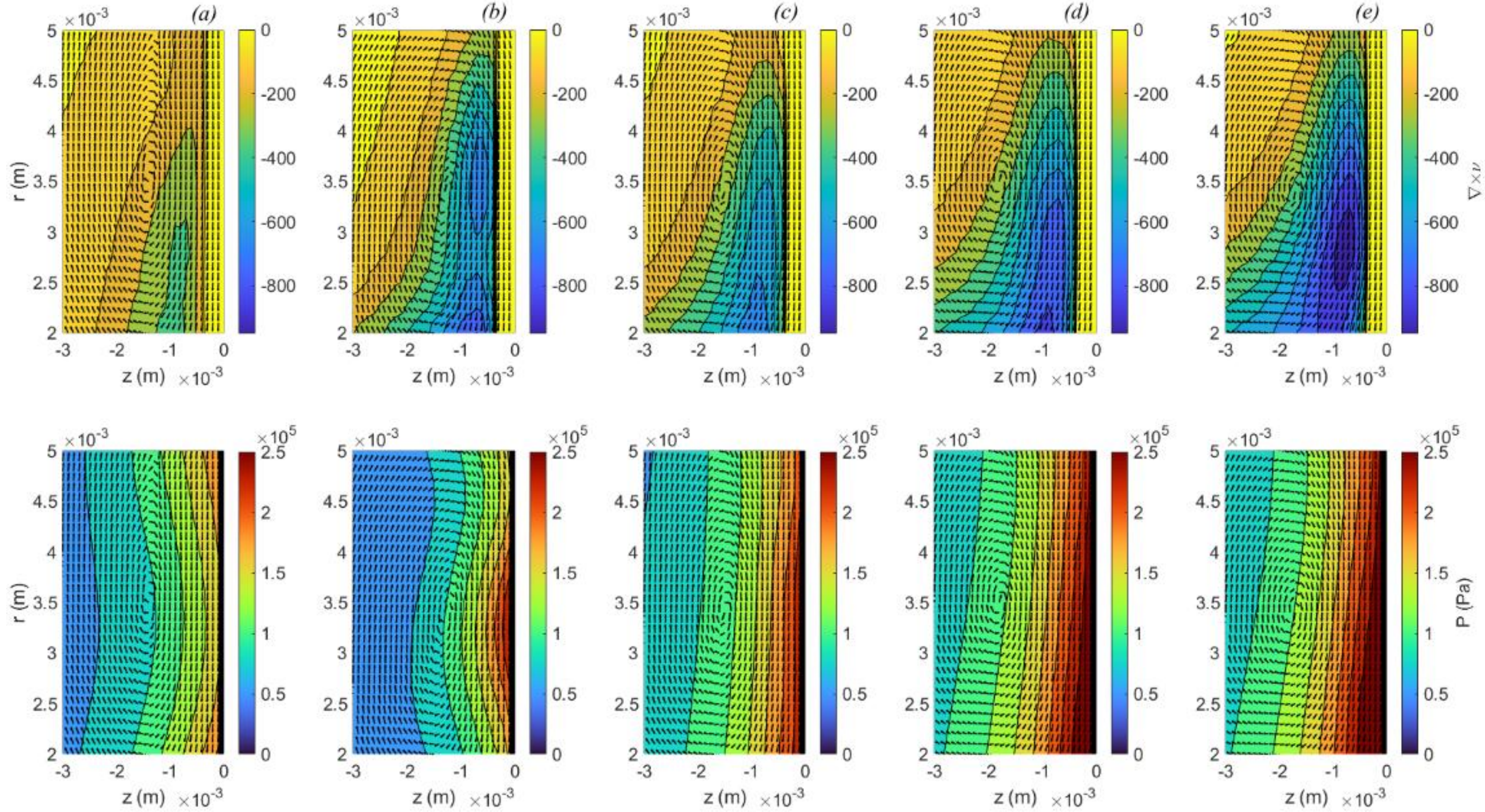

Figure 8.19: Axisymmetric contour-vector plots of the time-averaged (top) curl and (bottom) pressure of the proximal flow about the closest vortex to the horn axis of the 14 mm tip operating at (a) – (e) 30% to 100% power respectively.

8.3.4 Bubble Dispersion and Active Zone Creation

Moving slightly downstream from the horn tip and the attached cavitation, we experimentally uncover yet another major difference in the transversion of acoustic cavitation bubbles, summarized in Figure 8.20. As it appears that the vapor far-field comprises of relatively smaller bubbles in comparison to the bubbles agglomerated within the attached cavitation macrostructure, the presented numerical configuration is unable to capture the vapor nucleation in the downstream region. Specifically, this inaccuracy sources from the implemented cavitation model, where it assumes that the nucleating bubbles typically attain a constant equivalent radius of 25×10^{-3} m. As such, anything smaller is averaged out and neglected. Essentially, the difference observed was that with smaller horns, 3 mm and 7 mm tips, the far-field cavitation bubbles appear as nanoscale bubbles that independently transverse downstream without any traces of coalescence. However, upon observing the far-field under larger horns, 14 mm and 40 mm tips, we observe that these bubbles begin to decelerate in their downstream motion, as shown specifically under the 14 mm horn, and instead begin to coalesce and agglomerate in place, as shown under the 40 mm horn.

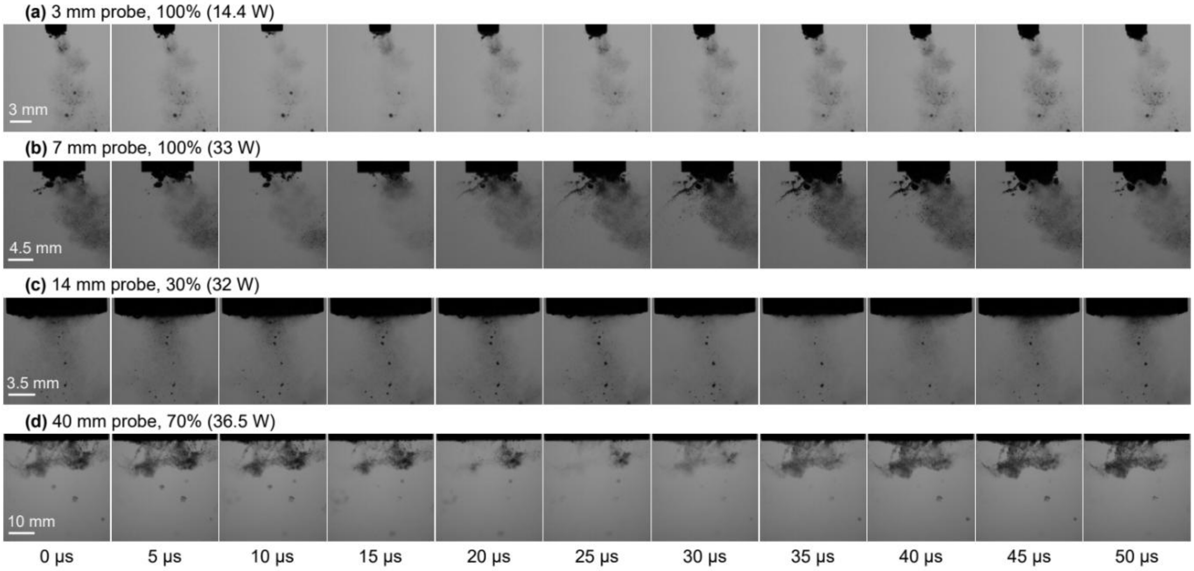

Figure 8.20: Sequential high-speed frames of instantaneous transient cavitation under (a) 3 mm horn tip operating at 100% power, (b) 7 mm horn tip operating at 100% power, (c) 14 mm horn tip operating at 30%, and (d) 40 mm horn tip operating at 70% power [228].

Additionally, an interesting attribute that was observed lies within these bubbles' oscillations, as their oscillation frequency appear in line with that of their respective macrostructure's oscillation. Therefore, we are keen to hypothesize that there exists an underlying interaction, or at least a correlation, between the macrostructure and the far-field vapor. As we have already established, the toroidal vortex tends to be more turbulent and ideal with smaller horn tips, while it is more viscous-dominant with larger tips. Considering that the vortex found under smaller tips tend to sustain their high-speed recirculation, it could probably be said the observed bubbles transverse along the established path by the vortex downstream of the horn tip. As for larger horns, the vortex tends to viscous dominant resulting in a slower, more dissipative recirculation. Therefore, these nanobubbles appear rather stationary, which facilitates their agglomeration and coalescence. Furthermore, if we were to draw parallels between the observed far-field bubble motion and the bubble distribution streamlines discussed in Chapter 7, one can further highlight the potentially bigger role the vortex has over the far-field behaviour of these bubbles. It was essentially discussed that buoyant particles, i.e. cavitation bubbles, tend to follow path lines established by the proximal vortex [221-223]. However, these types of particles end up getting entrapped at equilibrium points within the vortex if their rise speed does not exceed a given threshold Q empirically defined by the vortical flow field [223]. In a previous study scrutinizing Stuart vortices, these bubbles were seen accumulating at equilibrium points in such a way that remarkably resembles a ’cat’s eye’, ultimately matching the shape of the Stuart vortex [224]. The three main equilibrium points are highlighted in Figure 8.21.

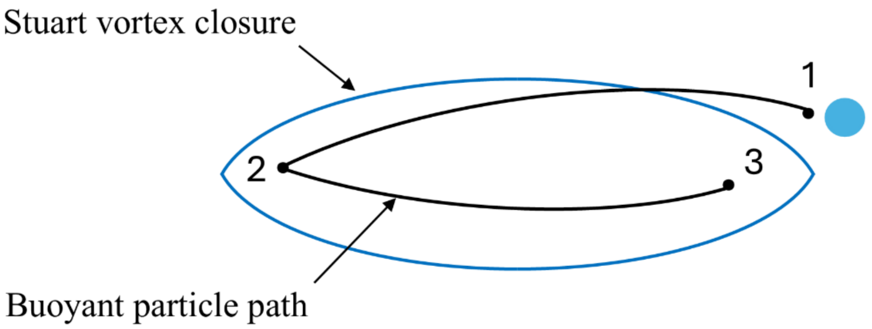

Figure 8.21: A boundary streamline of a Stuart vortex, or ‘cat’s eye’, showing the typical path of a buoyant particle takes within the vortex. Points labelled 1, 2, and 3 represent the equilibrium points observed by Tio et al. [224].

This comes across as potentially analogous to what we observed in the far-field of the 40 mm case. The agglomerations of bubbles formed, represented by the darkened clusters, downstream of the horn tip may just be stable equilibrium points at which bubble coalescence and agglomeration is strongly encouraged. Additionally, this falls in line with the position of the vortex resolved in the numerical simulation in Figures 8.18 and 8.19, where the primary vortex falls within approximately 2-3 mm axially away from the tip. This can then justify the distributions of vapor zones areas under the different horn tips observed by Viciconte et al. [228], as summarized in Figure 8.22. Given that Viciconte et al. [228] have observed a more polydisperse stationary vapor regions in the far-field under the more chemically efficient horn-type reactor, i.e. 40 mm case, it can be added that the additional low frequency oscillation of these agglomerates may further facilitate the production of OH radicals and enhance the treatment of water pollutants.

(a) 7 mm, 100% (33 W)

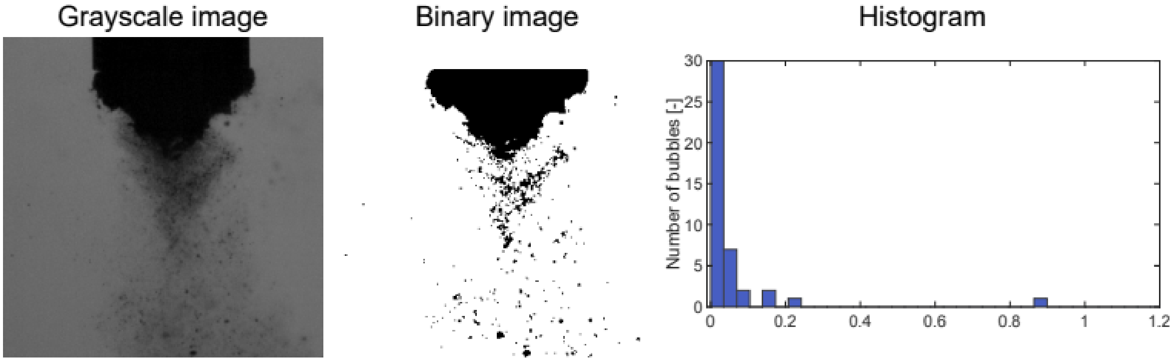

(b) 14 mm, 30% (32 W)

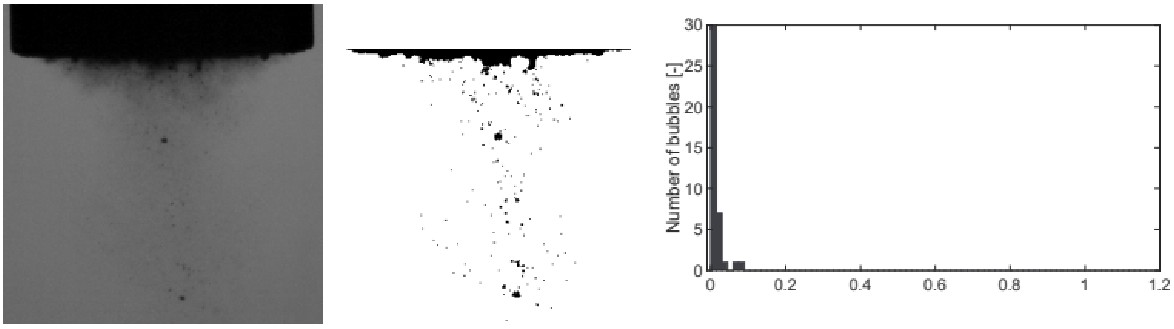

(c) 40 mm, 70% (36.5 W)

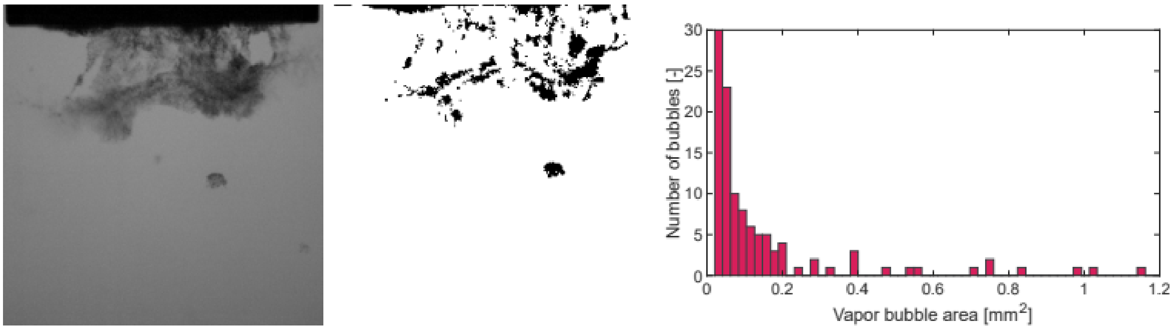

Figure 8.22: Sequential processing of high-speed frames to extract the histogram distribution of far-field vapor regions areas under the (a) 7 mm tip operating at 100% power, (b) 14 mm tip operating at 30%, and (c) 40 mm tip operating at 70% power [228].

8.4 Conclusion

This chapter presented both a numerical study that explores the structural dynamics of the attached cavitation macrostructure and its relationship with production of hydroxyl radicals. Through leveraging previously observed multiphase flow dynamics, this chapter generally provided a practical perspective of the primary role of acoustically induced proximal flow in governing the overall performance and reactivity of the horn-type reactor. Based on experimental observations made by Viciconte et al. [228], it was initially detected that the production of radicals had achieved the highest yield under the 40 mm horn tip, although the attached cavitation structure was the thinnest, in comparison to the structures observed under smaller horns, and had no axial presence downstream of the domain.

As a means to scrutinize this behaviour, the same two-dimensional axisymmetric numerical setup configured in Chapters 6 and 7, was utilized to conduct a parametric analysis considering multiple horn tip sizes, namely 3-, 7-, 14-, 24-, 32-, and 40-mm horn tips operating at five different power levels, 30%, 50%, 70%, 90%, and 100% power. As such, a two-way analysis examining the performance variation of the horn-type reactor with respect to both the tip diameter and the oscillation amplitude. By considering the attached cavitation macrostructure as one continuous bubbly body, we have assumed equivalency between the attached structure and the structure of a perfectly spherical bubble. Well-established structural models and attributes of a spherical bubble were assumed applicable to the observed macrostructures, specifically, the bubble oscillation models were implemented to describe the oscillation of the macrostructure within each design point.

Generally, the macrostructures observed appeared to be rather in-line with what was observed previously in Chapters 6 and 7; small horn tips facilitate MBS while larger horn tips produce CBS. However, with the change in the horn's amplitude, it was noted that both MBS and CBS tend to initially adopt a sheet-like structure at low power levels but eventually achieve their respective fully developed structures at higher power levels. Moreover, by following the generalized bubble resonance model and the Minnaert resonance model, we have observed that small MBS oscillates at a much higher bandwidth when compared to the larger CBS observed under larger horn tips. Justifications of this trend sourced from the vortical flows predicted by the numerical simulations. It appeared as though the vortex gradually becomes viscous dominated, as its core's vorticity dissipates at higher rates. This loss of rotation in the vortex core leads to the inability of generating a low-pressure node at the vortex location, and thus, preventing the attached cavity from further nucleating and expanding downstream from the horn tip. As it is noted that the oscillation frequency is governed by the pressure gradient within the domain, the shrinking in the cavitation structure decreased the attenuation of the acoustic wave propagation, ultimately, facilitating the proportional decrease in the resonance frequency of the cavitation structure. As a result, correlation conclusions can be drawn suggesting that low frequency oscillations of the sheet-like structure, in addition to the stationary polydisperse vapor regions, can facilitate larger yields of hydroxyl radicals and create more activity regions throughout the domain.

9 Conclusions and Future Works

The presented thesis had dedicated aims and objectives to precisely define the working principle of horn-type ultrasonic reactors and to generalize the flow field produced under those types of reactors. Following these investigative targets, the thesis has presented a series of sequential numerical studies that aimed to tackle the research objectives stated in Section 1.4 as follows: (1) build and experimentally validate a complete numerical configuration coupled with a new cavitation model to accurately predict acoustically generated cavitation structures, (2) explore different horn oscillation modelling techniques and their influence on flow field, (3) identify key flow attributes and properties of the acoustically induced multiphase flow proximal to the horn, (4) generalize the time-averaged multiphase flow, and (5) investigate the two-way interactions between the cavitation macrostructure produced and the proximal flow field about the horn tip. In that manner, a set of key conclusions were drawn for each stage of the investigation.

9.1 Conclusions

Initially, a multi-bubble cavitation model was derived on the assumptions that the multiphase domain is a continuous homogenous mixture between the water liquid and the water vapor phases.

- As such, the new model was derived from the Rayleigh-Plesset equation through a ZGB-inspired simplification of the equation. However, deviating away from the ZGB model's derivation, the new model accounts for inertial effects on the development of the bubble interface. This resulted in a mathematical expression the development of the bubble interface based on four empirical constants, namely the equivalent bubble radius, the nucleation site volume fraction, the vaporization constant, and the condensation constant.
- Based on a stepwise regression and response optimization, through the desirability approach, achieved a set of optimized values, 25×10^{-6} m, 5×10^{-4}, 17.35988, and 0.1, for each aforementioned constant, respectively.
- The optimized model was successfully validated against previous experimental results of a 3 mm horn-type reactor operating at 20 kHz and set at a 164 μm oscillation amplitude.

This directly addresses Objective 1, establishing a validated numerical foundation capable of predicting cavitation structure formation and behaviour under ultrasonic excitation. Carrying forward with the new model, and as a final step for configuring the full numerical model, a comparative exploration was conducted to draw parallels between the uniform and the Kirchhoff-based vibration models used to oscillate the horn geometry in the domain. The basis of the comparison lied within the different flow features induced under each model, and this was studied by visualizing the LCS using FTLE.

- It appeared that the Kirchhoff-based model led to significant underprediction of cavitation growths and collapses in which it has been associated with low-pressure peaks and higher cycle frequencies.

- This was justified by the model's facilitation of the formation of a diagonally impinging jet that penetrates the centre of the cavitation macrostructure leading to its two-step collapse.
- It was argued that this jet formation is governed by the instantaneous position and eccentricity of the toroidal vortex downstream of the horn, as the vortex is primarily positioned under the horn under the Kirchhoff-based vibration, while the uniform model has its vortex offset to the horn's side.
- The vortex-cavitation interaction is reflected in the frequency response of both the pressure and vapor volume signals; the collapse of the cavitation structure is observed to occur at a frequency of 7966.69 Hz under the Kirchhoff-based model, while it occurs at 4991.68 Hz frequency under the uniform model.
- This doubling in magnitude of oscillation frequency is a strong indicator that this is due to the two-step collapse that occurs under the Kirchhoff-based vibration. Interestingly however, all these differences begin to dissolve with the increase of the tip diameter. Perhaps, it is a strong indication that the influence of the first mode shape of the horn tip's vibration gradually loses significance with larger surface areas.

This fulfils Objective 2 by demonstrating how the choice of horn oscillation modelling influences cavitation morphology and dynamics. As the underlying significance of the vortex-cavitation interaction was revealed, a numerical parametric analysis followed that scrutinized the general vortex structural progression trends under a set of small and large horn tips comprised of 3-, 6-, 13-, 16-, and 19-mm horns. The primary differences in the vortex behaviour in small and large horn tips fell within the vortex size and eccentricity.

- Under small horn tips, the toroidal vortex tends to be symmetrical and significantly large with respect to the horn tip size. Meanwhile, large horn tips witness toroidal vortices that undergo two stages of eccentricity changes, starting with eccentricity in the radial direction followed by eccentricity in the axial direction.
- Regarding the vortex-cavitation interaction, the first indicator of potential correlation was the equivalency of the vortex expansion–contraction frequency and the cavity's sub-harmonic frequency. It has been found that the cavity structure is molded into MBS by the presence of a symmetric locomotive vortex structure that extends up to 1.5 times the horn tip diameter. Meanwhile, CBS is observed to take shape in the presence of an eccentric locomotive vortex that attains a size within 0.2–0.6 times the horn tip diameter.
- The significance of the vortex size and position is also observed in the cavity's collapse, as the vortex appears to govern the ability of the cavity impinging jet to initialize the collapse phase. An attempt to justify the instance of impingement was conducted by evaluating the momentum ratio between the vapor and water liquid momentum. Once the vapor structure is seen to lose momentum and the vortex gaining momentum, the impingement becomes successful agitating the cavity structure and initializing its collapse.

This addresses Objective 3 by identifying vortex topology, eccentricity evolution, and frequency coupling as key flow attributes governing cavitation structure behaviour. It was clearly shown that the vortex size in the time domain tends to oscillate rather rapidly and behave distinctly from one horn-type reactor to the other. Therefore, this acted as an obstacle to the acoustic flow generalization that this investigation intended to achieve in aims of building a foundation for optimization. As such, a follow-up numerical study was conducted to obtain the time-averaged behaviour of the vortices observed.

- This ultimately demonstrated the emerging early stagnation point that consistently positions itself at a distance of two times the ultrasonic horn tip diameter $2D$, regardless of the tip size. Referring back to the established vortex-cavitation coupling, cavitation attenuation was scrutinized by mathematically modeling the time-averaged axial flow during the cavitation transient state and solving the flow using Newman's subroutine.
- During fast streaming, acoustic force attenuation decreases exponentially at a maximum rate of ≈ 1.70 with the doubling of Re. However, an inverse trend was demonstrated by the dimensionless attenuation $\Gamma = -2\alpha D$, as it increased by a factor of ≈ 1.28. Similarly, Γ exponentially increased with the doubling of Re during slow streaming suggesting direct proportionality between Γ and Re. This emphasized the underlying role of the term $2D$ in amplifying attenuation induced by morphing structures of inertial bubble clusters.
- Moreover, tracking the bubble population along the horn axis revealed that mushroom-like structures formed under small horn tips have a linear bubble distribution, while cone-like structures under larger tips maintained an exponential distribution. This may suggest that a linear distribution may enhance attenuation and justify the aforementioned trends.

This directly responds to Objective 4 by providing a scalable, geometry-independent flow feature useful for modelling and design. Lastly, insights on the vortex significance on the intra-structural bubble distribution and acoustic wave attenuation provided a strong platform to properly assess the reactivity performance of the horn-type reactor.

- Experimentally, a trend has been identified demonstrating that the production of radicals had achieved the highest yield under the 40 mm horn tip, although the attached cavitation structure was the thinnest, in comparison to the structures observed under smaller horns, and had no axial presence downstream of the domain.
- A parametric analysis considering multiple horn tip sizes, namely 3-, 7-, 14-, 24-, 32-, and 40-mm horn tips operating at five different power levels, 30%, 50%, 70%, 90%, and 100% power was conducted. By considering the attached cavitation macrostructure as one continuous bubbly body, we have assumed equivalency between the attached structure and the structure of a perfectly spherical bubble.
- Generally, by following the generalized bubble resonance model and the Minnaert resonance model, we have observed that small MBS oscillates at a much higher bandwidth when compared to the larger CBS observed under larger horn tips. The vortex gradually becomes viscous dominated, which appeared to drop its vorticity. As a result, the slow-down in the vortex core rotation induced a high-pressure node, instead of the typical low-pressure node observed in smaller horn tips, ultimately, preventing the attached cavity from further nucleating and expanding downstream from the horn tip. Moreover, this induced shrinking in the cavitation structure decreased the attenuation of the acoustic wave and decreased the resonance frequency of the cavitation structure.

- As a result, this suggests that the sheet-like polydisperse cavitation structure can achieve resonance at a much lower frequency, ultimately, leading to the facilitation of a larger amount of activity zones and higher radical concentrations.

This addresses Objective 5 by linking cavitation–vortex coupling to functional performance metrics such as the reactor reaction rate.

9.2 Contributions to Literature and Future Works

With that study, the investigation achieves all research aims and objectives that primarily revolve around numerically modelling acoustically induced multiphase flow in horn-type reactors in hopes to provide a deeper understanding of the generalized working principle of horn-type reactors and to build a solid foundation for optimization of these reactors depending on the usage intended. Prominent contributions to literature made from the aforementioned series of investigations are as follows:

- A new homogenous mixture cavitation model was developed and optimized specifically for capturing bubble cluster inertia-dominant development in an ultrasonically irradiated environment.
- The two-way coupled nature of the horn-tip proximal toroidal vortex and the attached acoustic cavitation is identified and generalized in horn-type reactors operating at the low-to-mid range bandwidth.
- Under different horn geometries, the initial role of the acoustic attenuation induced by the preliminary attached cavity was revealed to facilitate acoustic streaming that births the proximal toroidal vortex. In turn, the vortex' ability to 'mold' the attached cavitation structure during its proceeding growth stages was demonstrated.
- This revealed a resultant dynamic attenuation of ultrasonic wave propagation throughout the medium that effectively controls the chemical performance of the horn-type reactor.
- Ultimately, a set of control parameters, responsible for dictating the reaction rate of the horn-type reactor, was defined and compiled.

The series of studies have advanced the fundamental understanding of the proximal vortical flow, its lifecycle, and its governing significance of the number of chemically active sites created throughout the domain. This, however, hints at the next research steps that should follow this extended investigation.

- Firstly, it would be great to carry out a deeper optimization of the new cavitation model through testing and examining the performance of each empirical constant in cases of different flow conditions and high bandwidths of ultrasonic radiation, such as frequencies of 1 MHz and above. This would refine the modularity of the model and enhance its prediction of bubble dynamics nonlinearities that may arise in cases of high frequencies. Possibly, this may facilitate the usage of the model as a predictive tool in biomedical applications. However, the proposed extension should be viewed as a long-term development direction, as new numerical modelling challenges arise within that frequency range. Specifically, complexities such as nonlinear acoustic propagation, strong viscous and thermal attenuation and overall higher computational costs would require to be addressed as prerequisites.

- Similarly, to better generalize the flow about a wider range of horn-type reactors, a further optimization study must be conducted to adjust the relaxation factors set in the one-dimensional mathematical model. This would then facilitate another study that explores a wider range of operation conditions and bandwidths of the horn reactors, such as 1 MHz and above, that are typically exclusively used in the medical field in a variety of treatment procedures.
- Moreover, recalling that the numerical model is configured to only capture fluid dynamic behaviors within the horn-type reactors' domains, it would be of great improvement to the accuracy of the numerical model to couple the current setup with a chemical model that would capture the radical formations and dissipation that occurs within the acoustically nucleated bubbles. This way, a more concise relationship between the acoustic flow features and the reactor performance can be established and assessed, respectively.

APPENDIX A: Modified Cavitation Model Source Code

As discussed in Chapter 4, the new cavitation model derivation was essentially inspired by the ZGB interpretation of the relationship between the equivalent bubble radius, the vapor volume fraction, and the nucleation site volume fraction. The source code below summarizes the optimized implementation of the derived cavitation model into ANSYS FLUENT as a multiphase homogeneous mixture model.

```
#include <udf.h>
#include <stdio.h>
#include <math.h>

//Modified Zwart et al. Cavitation Model

#define F_vap (17.35988) //Vaporization Constant
#define F_cond (0.1) // Condensation Constant

#define dt (0.000005) //Time Step Size

#define r (25.*pow(10,-6)) //Bubble Radius Constant
#define r_nuc (5.*pow(10,-4)) //Nucleation Volume Fraction

#define rhoV (C_R(c,vap)) //Vapor Density

DEFINE_LINEARIZED_MASS_TRANSFER(zwart_mod,c,t,from_index,from_species_index,
to_index, to_species_index, d_mdot_d_vof_from,d_mdot_d_vof_to)
{

//Definitions
real m_dot;
real m_source;

real ts = N_TIME; //Current Time Step
real final_ts = 500; //Final Time Step

real p_vap = 2808; //Vapor Pressure

real p_op = RP_Get_Real ("operating-pressure"); //Operating Pressure
real press = C_P(c, t) + p_op; //Absolute Pressure
real dp = p_vap-press; //Pressure Difference
real dp0 = ABS(dp); //Absolute Value
// dp0 = MAX(dp0, 1e-4);

Thread *liq = THREAD_SUB_THREAD(t, from_index);
Thread *vap = THREAD_SUB_THREAD(t, to_index);

real rhoL = C_R(c,liq); //Liquid Density
real rl = C_VOF(c,liq); //Liquid Volume Fraction
real rv = C_VOF(c,vap); //Vapor Volume Fraction
real r_rho_lv = 1./rhoV - 1./rhoL;

//Growth Rate and Acceleration at t = 0
real dr_2 = dp0/(rhoL*r);
real dr = dr_2*dt;
```

```
real source = sqrt(2./3.*dp0/C_R(c,liq));
m_dot = 0.;
m_source = 0.0;

C_UDMI (c,t,0) = dp0/(rhoL*r);
C_UDMI (c,t,1) = dr_2*dt;

//Source Terms at Remaining Time Steps
if (dp > 0){
m_dot = F_vap*(3.*r_nuc*(1.-C_VOF(c,vap))/r)*rhoV*C_UDMI (c,t,1);
m_source = m_dot * rl;
*d_mdot_d_vof_from  = m_dot;
*d_mdot_d_vof_to    = -m_dot;
} else {
m_dot = -F_cond*(3.*C_VOF(c,vap)*rhoV/r)*C_UDMI (c,t,1);
m_source = m_dot * rv;
*d_mdot_d_vof_from = m_dot;
*d_mdot_d_vof_to = -m_dot;
}
C_UDMI (c,t,0) = dp0/(rhoL*r) - (3./(2.*r))*pow(C_UDMI (c,t,1),2);
C_UDMI (c,t,1) = C_UDMI (c,t,1) + (C_UDMI (c,t,0)*dt);

/*  ++++++++++ ds/dp term ++++++++++++++   */
if(NNULLP(THREAD_STORAGE(t, SV_MT_DS_DP)))
C_STORAGE_R(c,t,SV_MT_DS_DP) = ABS(r_rho_lv*m_source/(2*dp0));

return m_source;
}
```

APPENDIX B: Uniform Vibration Model Source Code

In Chapter 5, the equation of the uniform sinusoidal vibration of the ultrasonic horn boundaries is translated as a ANSYS FLUENT-compatible boundary condition. This custom boundary condition is fed as a 'rigid boundary' dynamic meshing algorithm, as it allows ANSYS FLUENT to automatically accommodate for any excessively deformed mesh cells caused by the motion of the horn walls.

```
#include <udf.h>
#include <stdio.h>
#include <stdlib.h>
#include <math.h>

DEFINE_CG_MOTION(uniformVib, dt, vel, omega, time, dtime)
{
Thread *t; /*is the pointer to the structure that stores*/
real A= 164*pow(10,-6); /* Assign amplitude*/
real H= 20000; /* Assign frequency*/
real ω = 2. * M_PI * H; /*Calculate the omega*/
real v = A*ω*sin(ω*time); /*Calculate velocity*/
/* reset velocities . The linear and angular velocities are returned to FLUENT
by overwriting the
arrays vel and omega, respectively*/
NV_S (vel, =, 0.0);
NV_S (omega, =, 0.0);
/* obtain the thread pointer for which this motion is defines */
t = DT_THREAD(dt);
/* compute velocity */
v = A*ω*cos(ω*time);
vel[1] = v;
}
```

APPENDIX C: Kirchhoff-based Vibration Model Source Code

In a different implementation manner to that shown for the uniform vibration model in Chapter 5, the Kirchhoff-based vibration equation is described by the DEFINE_GRID_MOTION ANSYS FLUENT-specific macro that typically defines the motion of mesh nodes along the selected boundary. In the source code below, the nodes were selected and displaced with time according to Eq. 2.61. However, similar to the uniform vibration source code, the boundary condition is introduced as a 'rigid boundary' dynamic meshing algorithm, to facilitate the remeshing of the excessively deformed mesh cells during the defined deformation of the boundary.

```
#include <udf.h>
#include <stdio.h>
#include <stdlib.h>
#include <math.h>

DEFINE_GRID_MOTION(kirchVib,domain,dt,time,dtime)
{
Thread *tf = DT_THREAD(dt);
face_t f;
Node *v;
real NV_VEC(omega), NV_VEC(axis), NV_VEC(dx);
real NV_VEC(origin), NV_VEC(rvec);
real r, disp;
real R = 0.0015;
real dis_max= 164*pow(10,-6);
real h = 20000;
real delta = 0.000001;
real w = 2. * M_PI * h; int n;

real axis_multi = -1;
real NV_VEC(axis_neutral);

SET_DEFORMING_THREAD_FLAG(THREAD_T0(tf)); //set pointer to reference point at
adjacent cell zone
NV_D(axis, =, 1.0, 0.0, 0.0);
NV_D(axis_neutral, =, 0.0, 0.0, 0.0);

begin_f_loop(f,tf)
{
f_node_loop(f,tf,n)
{
v = F_NODE(f,tf,n);
if (NODE_POS_NEED_UPDATE (v) && NODE_Y(v) >= 0) //update node only if the node
has not been previously updated
{
NODE_POS_UPDATED(v); //label current node as updated
r = (NODE_Y(v))/R; //non-dimensionalize the poisiton
```

```
Message ("Node Number = %f\n", NODE_Y(v));
disp = dis_max*(1-pow((r),2)+2*pow((r),2)*log(r+delta/R))*sin(w*time);
NODE_X(v) = disp;
Message ("Node Coord (x) = %f\n", NODE_X(v));
}
}
}
end_f_loop(f,tf);
}
```

APPENDIX D: Finite Time Lyapunov Exponent MATLAB Code

The Finite Time Lyapunov Exponent procedure summarized by Eqs. 5.2 – 5.3 in Chapter 5 was applied and solved in a step-by-step process coded on MATLAB. The object-oriented program simply consists of two files, the main code, otherwise known here as FTLE.m, and the FTLE calculation function, labelled as calculate_ftle.m that is called by FTLE.m. The program simply discretizes a subdomain, extracted from the CFD domain, with a clutter of particles of a specific resolution. Afterwards, these particles are advected across the subdomain with an imported velocity field from the CFD simulation. Ultimately, by calling calculate_ftle.m, Eq. 5.3 is solved to obtain the FTLE across the subdomain.

FTLE.m

```
clc
clear
tic

% Creating the grid of particles

xBound = [-0.005 0];
yBound = [0 0.005];

gridResX = 2.5e-05;
gridResY = 2.5e-05;

xInt = floor((xBound(2) - xBound(1))/gridResX)+1;
yInt = floor((yBound(2) - yBound(1))/gridResY)+1;

x = linspace(xBound(1), xBound(2), xInt);
y = linspace(yBound(1), yBound(2), yInt);

gridResX_1 = x(2)-x(1);
gridResY_1 = y(2)- y(1);

[X,Y] = meshgrid(x,y);

nP = xInt*yInt; % Total number of particles

% Create interpolation function
% Backward integration

dt = 575;

while dt <= 600

    tEnd = 1;
    tStart = tEnd + dt;
    % tLength = 499;
    % tStart = 600; % Integration start time
    % %     tEnd = tStart - tLength;
    % tEnd = 1; % Integration end time
    tStepSize = 5e-06; % Step size
    % Nt = tStart-tEnd-1;
    Nt = tEnd-tStart-1; % Number of time steps
```

```
xVect = X(1:end)'; % Inital x-coordinate vector
yVect = Y(1:end)'; % Initial y-coordinate vector

xCoord = zeros(nP,3); % Matrix to store new and old x coordinates
yCoord = xCoord; % Matrix to store new and old y coordinates

xCoord(:,3) = xVect; % x-coordinate at t = 0
yCoord(:,3) = yVect; % y-coordinate at t = 0
xCoord(:,2) = xVect; % x-coordinate at t = t-1
yCoord(:,2) = yVect; % y-coordinate at t = t-1

check = sqrt(xVect.^2+yVect.^2)>= 0.025;
s = sum(check);
if s > 0
    error('particles sided outside of domain')
end

loadBar = waitbar(0, 'Calculating flow map');

for tStep=tStart:-1:tEnd
    if tStep < 10
        name = ['FFF-6-000' num2str(tStep)];
    elseif tStep < 100
        name = ['FFF-6-00' num2str(tStep)];
    elseif tStep < 1000
        name = ['FFF-6-0' num2str(tStep)];
    else
        name = ['FFF-6-' num2str(tStep)];
    end

    sol_data0=dlmread(name,'',1,0);

    % create interpolation function
    x0=sol_data0(:,2);
    y0=sol_data0(:,3);
    vx0=sol_data0(:,4);
    vy0=sol_data0(:,5);
    VIx0=scatteredInterpolant(x0,y0,vx0);
    VIy0=scatteredInterpolant(x0,y0,vy0);

    % interpolate new positions
    vi_x = VIx0(xCoord(:,2),yCoord(:,2));
    vi_y = VIy0(xCoord(:,2),yCoord(:,2));
    % Calculate x-coordinate at t = t + tstep
    xCoord(:,1)=xCoord(:,2) + tStepSize*vi_x;
    % Calculate y-coordinate at t = t + tstep
    yCoord(:,1)=yCoord(:,2) + tStepSize*vi_y;

    if tStep > tEnd
        xCoord(:,2)=xCoord(:,1);
        yCoord(:,2)=yCoord(:,1);
    end
    waitbar((tStart + 1 - tStep)/(tStart + 1 - tEnd))
    clear x0 y0 z0 vx0 vy0 vz0 VIx0 VIy0 VIz0 sol_data0 name m Zrel
end
```

```
run=1;
delete(loadBar)
name1=['flow_map-bt-' num2str(tStart) '-x-' num2str(run) '.txt'];
name2=['flow_map-bt-' num2str(tStart) '-y-' num2str(run) '.txt'];
save(name1,'X','-ascii','-double')
save(name2,'Y','-ascii','-double')
clear i h tstep tstart tend tcrit t name1 name2 run

% Create flow map
flowMap=zeros(nP,2,2);
flowMap(:,:,1)=[xCoord(:,end) yCoord(:,end)];
flowMap(:,:,2)=[xCoord(:,1) yCoord(:,1)];

writematrix(flowMap,'flowMap.csv')

FTLE_v = zeros(nP,1); % Matrix to store FTLE values for each particle
tol = 0.000001; % Reference tolerance

% Indexing and storing neighboring particles' coordinates

loadBar = waitbar(0, 'Calculating FTLE');

for p = 1:nP

    xSelect = flowMap(p,1,1);
    ySelect = flowMap(p,2,1);
    parNeighCoord1 = zeros(4,2);
    parNeighCoord2 = zeros(4,2);

    disp(p);

    pn = 1;

    while pn <= 4

        if pn == 1
            x_i_m1 = xSelect - gridResX_1;

            [Rx,Cx] = find(abs(flowMap(:,1,1)-x_i_m1) < tol);
            [Ry,Cy] = find(flowMap(:,2,1) == ySelect);

            Rx_check = size(Rx);

            if Rx_check(1,1) == 0
                pn = pn + 1;
            end

        end

        if pn == 2
            x_i_m1 = xSelect + gridResX_1;

            [Rx,Cx] = find(abs(flowMap(:,1,1)-x_i_m1) < tol);
            [Ry,Cy] = find(flowMap(:,2,1) == ySelect);
```

```
    Rx_check = size(Rx);

    if Rx_check(1,1) == 0
        pn = pn + 1;
    end

end

if pn == 3
    x_i_m1 = xSelect;
    y_j_m1 = ySelect + gridResY_1;

    [Rx,Cx] = find(flowMap(:,1,1) == xSelect);
    [Ry,Cy] = find(abs(flowMap(:,2,1)-y_j_m1) < tol);

    Ry_check = size(Ry);

    if Ry_check(1,1) == 0
        pn = pn + 1;
    end

end

if pn == 4
    x_i_m1 = xSelect;
    y_j_m1 = ySelect - gridResY_1;

    [Rx,Cx] = find(flowMap(:,1,1) == xSelect);
    [Ry,Cy] = find(abs(flowMap(:,2,1)-y_j_m1) < tol);

    Ry_check = size(Ry);

    if Ry_check(1,1) == 0
        pn = pn + 1;
    end

end

rXs = size(Rx);
rYs = size(Ry);

if rXs(1,1) >= rYs (1,1)
    sizeDiff = rXs(1,1) - rYs(1,1);
    Ry = [Ry ; zeros(sizeDiff,1)];
    for i = 1:rXs(1,1)
        for j = 1:rXs(1,1)
            if Ry(i,1) == Rx(j,1)
                reqXCoordLoc = Rx(j,1);
                reqYCoordLoc = Ry(i,1);
                disp('Match Found!')
                %                 break
            else
                %                 disp('Match Not Yet Found.')
                continue
            end
        end
```

```
                end
            end

            if rYs(1,1) > rXs(1,1)
                sizeDiff = rYs(1,1) - rXs(1,1);
                Rx = [Rx ; zeros(sizeDiff,1)];
                for i = 1:rYs(1,1)
                    for j = 1:rYs(1,1)
                        if Rx(i,1) == Ry(j,1)
                            reqXCoordLoc = Rx(i,1);
                            reqYCoordLoc = Ry(j,1);
                            disp('Match Found!')
                            %                 break
                        else
                            %                 disp('Match Not Yet Found.')
                            continue
                        end
                    end
                end
            end

            if pn < 5
                parNeighCoord1(pn,1) = flowMap(reqXCoordLoc,1,1);
                parNeighCoord1(pn,2) = flowMap(reqYCoordLoc,2,1);

                parNeighCoord2(pn,1) = flowMap(reqXCoordLoc,1,2);
                parNeighCoord2(pn,2) = flowMap(reqYCoordLoc,2,2);
            end

            if pn < 6
                pn = pn + 1;
            end

        end
        T=Nt*0.000001;
        FTLE = calculate_ftle(parNeighCoord1(1,1),parNeighCoord1(1,2),
parNeighCoord1(2,1) ...
            , parNeighCoord1(2,2), parNeighCoord1(3,1), parNeighCoord1(3,2),
parNeighCoord1(4,1), ...
            parNeighCoord1(4,2), parNeighCoord2(1,1), parNeighCoord2(1,2), ...
            parNeighCoord2(2,1), parNeighCoord2(2,2), parNeighCoord2(3,1),
parNeighCoord2(3,2), ...
            parNeighCoord2(4,1), parNeighCoord2(4,2), T); % Calculating FTLE

        FTLE_v(p,1) = FTLE; % Store FTLE in a vector
        waitbar((p-1)/(nP-1));
    end

    delete(loadBar);

    % Convert vector into matrix to store FTLE to its corresponding particle
coordinate

    FTLE_m = zeros(xInt,yInt);
    r = 1;
```

```
    for v = 1:yInt
        FTLE_m(:,v) = FTLE_v(r:r+xInt-1,1);
        r = r + xInt;
    end

    % Plot FTLE wrt x and y

    contourf(X,Y,FTLE_m)
    colorbar
    xlabel('x')
    ylabel('y')
    title('FTLE contour plot')

    contName = ['FTLE_' num2str(dt) '.tif'];
    saveas(gcf, contName);

    dt = dt + 1;

end
toc
```

calculate_ftle.m

```
function out=calculate_ftle(x_in1j_0, y_in1j_0, x_ip1j_0, y_ip1j_0, x_ijn1_0,
y_ijn1_0,...
    x_ijp1_0, y_ijp1_0, x_in1j_T, y_in1j_T, x_ip1j_T, y_ip1j_T, x_ijn1_T,
y_ijn1_T, x_ijp1_T, y_ijp1_T, T)

A11 = (x_ip1j_T - x_in1j_T)/(x_ip1j_0 - x_in1j_0);
A12 = (x_ijp1_T - x_ijn1_T)/(y_ijp1_0 - y_ijn1_0);
A21 = (y_ip1j_T - y_in1j_T)/(x_ip1j_0 - x_in1j_0);
A22 = (y_ijp1_T - y_ijn1_T)/(y_ijp1_0 - y_ijn1_0);

A = [A11 A12;A21 A22];
B = A'*A;
disp(A);

delta = max(eig(B));
out = -log(delta)/(2*T);
end
```

APPENDIX E: Vortex Analysis MATLAB Code

The fluctuation of the vortex size observed under different horn tips in Chapter 6 was measured by initially assuming that the proximal toroidal vortex behaves like a Rankine vortex, where the vortex core is imagined as a cylinder embodying a solid-body rotation. Thus, the radius of this cylinder r_0 is interpreted as the vortex core size. As such, the vortex size is highlighted by the length of the line joining two local tangential velocity maxima passing through a zero-velocity point representing the vortex centre. To illustrate this, Fig. A1 plots the tangential velocity distribution within the vortex along the radial coordinate.

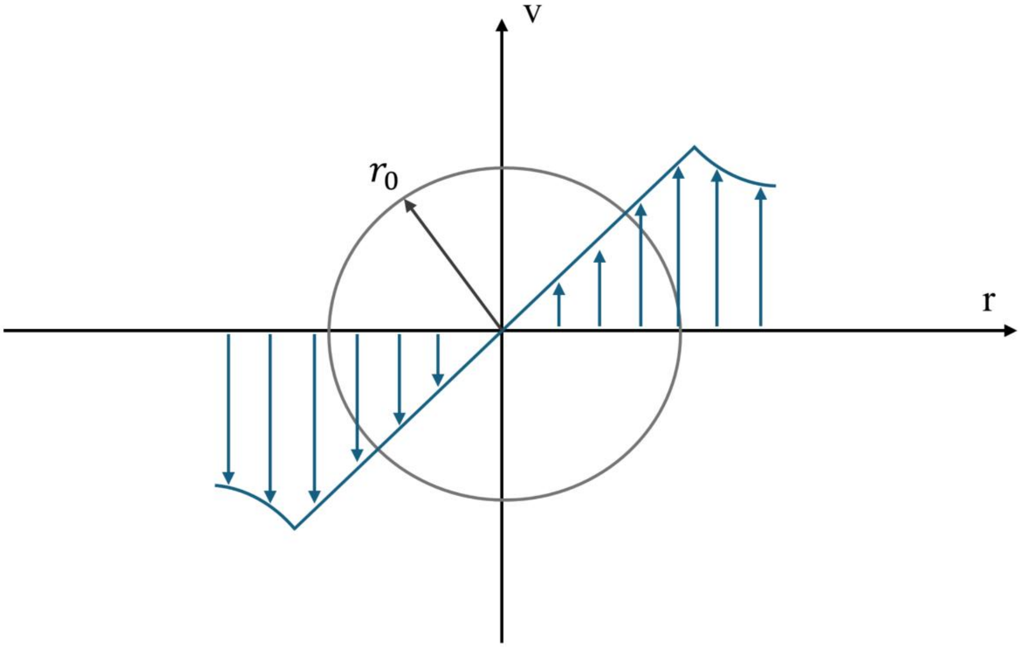

Figure A1: Tangential velocity distribution within the Rankine vortex against the radial coordinate.

With that said, the MATLAB code below was written to take in the tangential velocity from the velocity field exported from ANSYS FLUENT, plot its distribution in the subdomain proximal to the horn tip, and detect any distribution patterns resembling the one illustrated in Fig. A1. Afterwards, the diameter of the toroidal vortex is evaluated by seeking two directional changes in the slope of the linear line of the tangential distribution plot and measuring the distance between these two points.

```
clear
clc
close all

cd 'C:\Users\basel\OneDrive\Documents\DPhil Work\Publications\Ultrasonic Horn
Modelling\Updated Work\FTLE Toolkit\Velocity_files\16mm\Corrected TxtFiles 1'
files = dir;
filesCell = struct2cell(files);
fileNames = filesCell(1,3:602);

[R_fN, C_fN] = size(fileNames);
vortexCenterMat = zeros(C_fN,2);
```

```
hornDia = 0.019;

for i = 1:C_fN
    f = readtable(fileNames{1,i});
    xCoord = f{:,2};
    yCoord = f{:,3};
    u = f{:,4};
    v = f{:,5};
    f = f{:,:};
    vortexRegion = f;
    vortexRegion = f((f(:,2) >= -0.01) & (f(:,2) <= 0.00149513), :);
    vortexRegion = vortexRegion((vortexRegion(:,3) >= 0.00025) &
(vortexRegion(:,3) <= 0.0131167), :);
    vortexRegion(:,6) = sqrt((vortexRegion(:,4).^2) + (vortexRegion(:,5).^2));

    [R_vMat, C_vMat] = size(vortexRegion);

    for j = 1:R_vMat
        vortexCenterVel = min(vortexRegion(:,6));
        [R_vC, C_vC] = find(vortexRegion(:,6) == vortexCenterVel);

        leftVectRow = R_vC - 1;
        rightVectRow = R_vC + 1;

        if leftVectRow ~= 0 & rightVectRow ~= 0 & leftVectRow <= R_vMat &
rightVectRow <= R_vMat
            if vortexRegion(leftVectRow,5) > 0 & vortexRegion(rightVectRow,5)
< 0
                vortexCenterMat(i,1) = vortexRegion(R_vC(1,1),2);
                vortexCenterMat(i,2) = vortexRegion(R_vC(1,1),3);
                break
            elseif j == R_vMat
                continue
            else
                vortexRegion(R_vC,:) = [];
                [R_vMat, C_vMat] = size(vortexRegion);
                continue
            end
        else
            vortexRegion(R_vC,:) = [];
            [R_vMat, C_vMat] = size(vortexRegion);
        end

    end

end

[R_vCM, C_vCM] = size(vortexCenterMat);
```

```
figure
scatter(vortexCenterMat(:,1), vortexCenterMat(:,2))
figure
plot([1:R_vCM], vortexCenterMat(:,1));
figure
plot([1:R_vCM], vortexCenterMat(:,2));

Y1 = fft(vortexCenterMat(:,1));
Y2 = fft(vortexCenterMat(:,2));
L = R_vCM;
Fs = 1/5e-06;
fs = Fs/L*(0:(L/2));

figure
P2 = abs(Y1/L);
P1 = P2(1:L/2+1);
P1(2:end-1) = 2*P1(2:end-1);
plot(fs,P1,"LineWidth",2)
title("Single-Sided Amplitude Spectrum of X(t)")
xlabel("f (Hz)")
ylabel("|P1(f)|")

figure
P2 = abs(Y2/L);
P1 = P2(1:L/2+1);
P1(2:end-1) = 2*P1(2:end-1);
plot(fs,P1,"LineWidth",2)
title("Single-Sided Amplitude Spectrum of X(t)")
xlabel("f (Hz)")
ylabel("|P1(f)|")

[R_cM, C_cM] = size(vortexCenterMat);
recircLengthVect = zeros(R_cM,1);
vortexPlot = f;

figure
hold on
for x = 1:R_cM
    selectedY = vortexCenterMat(x,2);
    selectedRows = find(vortexPlot(:,3) == selectedY);
    [R_sR, C_sR] = size(selectedRows);
    radialVelVect = zeros(R_sR,1);
    xCoordVect = zeros(R_sR,1);

    for y = 1:R_sR
        radialVelVect(y,1) = vortexPlot(selectedRows(y,1),5);
        xCoordVect(y,1) = vortexPlot(selectedRows(y,1),2);
    end
```

```
    plot(xCoordVect./hornDia, radialVelVect)

    gradVect = gradient(radialVelVect);
    [R_gV, C_gV] = size(gradVect);
    for z = 1:R_gV
        if z < R_gV
            if gradVect(z + 1) < 0 && gradVect(z) > 0
                point1 = xCoordVect(z,1);
            elseif gradVect(z) < 0 && gradVect(z + 1) > 0
                point2 = xCoordVect(z+1,1);
            else
                continue
            end
        else
            break
        end
    end

    recircLength = abs(point2 - point1);
    recircLengthVect(x,1) = recircLength;

end
hold off

[R_rLV, C_rLV] = size(recircLengthVect);

figure
plot([1:R_rLV], recircLengthVect./hornDia)

Y3 = fft(recircLengthVect);
L = R_rLV;
Fs = 1/5e-06;
fs = Fs/L*(0:(L/2));

figure
P2 = abs(Y3/L);
P1 = P2(1:L/2+1);
P1(2:end-1) = 2*P1(2:end-1);
plot(fs,P1,"LineWidth",2)
title("Single-Sided Amplitude Spectrum of X(t)")
xlabel("f (Hz)")
ylabel("|P1(f)|")

recircLengthMax = abs(max(recircLengthVect))/hornDia;
recircLengthMin = abs(min(recircLengthVect))/hornDia;
```

APPENDIX F: Newman BAND Python Code

The Newman BAND subroutine was used to solve a system of three partial differential equations, namely Eqs. 7.30 – 7.32, that emerged from our attempt in linearizing Eq. 7.26 through the use of trial solutions, as discussed in Chapter 7.

```
from scipy.sparse import coo_matrix
from scipy.sparse.linalg import spsolve
from numpy import *
from pylab import *
import math

# N is number of unknowns
# NJ is number of mesh points

# non-dimensional axial acceleration, f, is c1
# non-dimnesional axial velocity, theta, is c2
# non-dimensional acoustic attenuation, Dp, is c3

saveOn = True    # saving generated data in .csv file

N = 3
NJ = 1000

# Set convergence tolerance and max number of iterations
tol = 1e-10
itmax = 100

# Constants for the problem
L = 2
f = 20e03           # oscillation freq. (Hz)
c_l = 1500          # speed of sound (m/s) in water
c_v = 477.5         # spead of sound (m/s) in  vapor
alphaC_l = 4/4      # 1D volume fraction of liquid in domain (speed of sound)
c = alphaC_l*c_l + (1 - alphaC_l)*c_v  # domain speed of sound
la = c/f            # wavelength (m)
A = 164e-06         # oscillation amp. (m)
w = 2*pi*f          # angular velocity (rad/s)
v = A*w           # axial oscillation velocity (m/s)

D = 3e-3           # horn tip dia. (m)
g = 9.81            # gravitational acceleration (m/s^2)

rho_l = 998.3        # water density (kg/m^3)
rho_v = 0.0173       # vapor density (kg/m^3)
mu_l = 0.0010003     # water dynamic viscosity (Pa.s)
```

```
mu_v = 1.34e-05      # vapor dyanmic viscosity (Pa.s)
alpha_l = 4/4        # 1D volume fraction of liquid in domain
rho = alpha_l*rho_l + (1 - alpha_l)*rho_v                       # domain
density
mu = alpha_l*mu_l + (1 - alpha_l)*mu_v                          # domain
dynamic viscoisty

B_con = 0.05*10                              # slope correction factor
R_con = rho*v*D/mu                          # reynolds number
C_con = 2/B_con*(sin(pi*D/(2*la)))**2       # constant
G_con = -2*299.52*D                         # non-dimensional acoustic
attenuation

# R = 10
dC = 1e-04
# dC2 = dC

# Makes the mesh
xx = linspace(0,L,NJ)
h = L/(NJ-1)

# INITIAL GUESSES

def initguess():
    cold = ones([N,NJ])
    cold[0,:]= 0
    cold[1,:]= 0
    cold[2,:]= 0

    return cold

# FILLMAT

def fillmat(cold):
    # first column is equation
    # second column is position
    # third column is species

    # initialize matrices

    sma = zeros([N,NJ,N])
    smb = zeros([N,NJ,N])
    smd = zeros([N,NJ,N])
    smg = zeros([N,NJ])

    # fill matrices

    smb[0,:,1] = -1
```

```
smb[1,:,0] = -1/R_con
smb[2,:,2] = 1

smd[0,:,0] = 1
smd[1,:,0] = (cold[1,:] + dC)
smd[1,:,2] = -1

for l in range(NJ):
    # smg[1,l] = -G_con*C_con*exp(-2.*G_con*(L/NJ)*l)
    smg[1,l] = -G_con*C_con*exp(-G_con*(L/NJ)*l)

# Boundary condition 1

smp = zeros([N,N])
sme = zeros([N,N])
smf = zeros([N,1])

# smp[0,1] = -1
sme[0,0] = 1
smp[1,0] = 1
# sme[1,1] = 1
smp[2,2] = 1
# smf[1] = -0.05

# Insert (sme smp smf) into (smb smd smg)

smb[:,0,:] = smp[:,:]
smd[:,0,:] = sme[:,:]
smg[:,0] = transpose(smf)

# Boundary condition 2

smp = zeros([N,N])
sme = zeros([N,N])
smf = zeros([N,1])

smp[0,1] = -1
sme[0,0] = 1
smp[1,0] = 1
sme[2,1] = 1
smf[2] = -1
# smf[0] = 100

# Insert (sme smp smf) into (smb smd smg)

smb[:,NJ-1,:] = smp[:,:]
smd[:,NJ-1,:] = sme[:,:]
smg[:,NJ-1] = transpose(smf)
```

```
    # print(smg)
    return sma, smb, smd, smg

# ABDGXY

def abdgxy(sma, smb, smd, smg):
    sma = transpose(sma, (0, 2, 1))
    smb = transpose(smb, (0, 2, 1))
    smd = transpose(smd, (0, 2, 1))

    A = sma-h/2.0*smb
    B = -2.0*sma+h**2*smd
    D = sma+h/2.0*smb
    G = h**2*smg

    B[:,:,0] = h*smd[:,:,0]-1.5*smb[:,:,0]
    D[:,:,0] = 2.0*smb[:,:,0]
    G[:,0]=h*smg[:,0]
    X = -0.5*smb[:,:,0]

    A[:,:,NJ-1]=-2.0*smb[:,:,NJ-1]
    B[:,:,NJ-1]=h*smd[:,:,NJ-1]+1.5*smb[:,:,NJ-1]
    G[:,NJ-1]=h*smg[:,NJ-1]
    Y=0.5*smb[:,:,NJ-1]

    ABD = concatenate((A, B, D), axis=1)
    BC1 = concatenate((B[:,:,0] , D[:,:,0] , X), axis=1)
    BC2 = concatenate((Y , A[:,:,NJ-1] , B[:,:,NJ-1]), axis=1)
    ABD[:,:,0] = BC1
    ABD[:,:,NJ-1] = BC2
    # print(G)
    return ABD, G

# BAND

def band(ABD, G):

    BMrow = reshape(arange(1,N*NJ+1), (NJ,N))
    BMrow = BMrow[:, :, newaxis]
    BMrow = transpose(BMrow, (1, 2, 0))
    BMrow = BMrow[:,[0 for i in range(3*N)],:]

    a = arange(1,3*N+1)
    a = a[newaxis,:]
    a = repeat(a,N,0)
    a = a[:,:,newaxis]
    a = repeat(a,NJ,2)
```

```
    b = arange(0,(N)*(NJ-3)+N,N)
    b = hstack((b[0], b, b[len(b)-1]))
    b = b[newaxis,newaxis,:]
    b = repeat(b,N,0)
    b = repeat(b,3*N,1)

    BMcol = a + b
    BMcol = BMcol - 1
    BMrow = BMrow - 1
    BMrow = ravel(BMrow)
    BMcol = ravel(BMcol)
    ABD = ravel(ABD)
    BigMat = coo_matrix((ABD, (BMrow, BMcol)), shape=(N*NJ, N*NJ)).tocsc()
    BigG = transpose(G)
    BigG = ravel(BigG)
    # print BigMat.todense()
    delc = spsolve(BigMat, BigG)
    return delc

# MAIN PROGRAM

cold = initguess()
it = 1
did = False

for it in range(1,itmax):

    sma, smb, smd, smg = fillmat(cold)
    ABD, G = abdgxy(sma, smb, smd, smg)
    delc = band(ABD, G)
    delc = delc.reshape((NJ, N))
    delc = transpose(delc)
    error = cold - delc
    maxerror = amax(abs(error))
    print (it, ', ', maxerror)
    cold = delc
    if maxerror < tol:
        did = True
        print ('Converged in ' +str(it)+ ' iterations.')
        break

if not did:
    print ('The program did not converge.')

# Plots

fig, (ax1,ax2,ax3) = plt.subplots(3,1,figsize=(6, 6))
```

```
fig.subplots_adjust(left=0.15)

params = {'mathtext.default': 'regular' }
rcParams.update(params)

xs = xx
c1 = cold[0,:]
c2 = cold[1,:]
c3 = cold[2,:]
ax1.plot(xs,c1,'-', color='black', markeredgecolor='k')
# ax1.legend(['$C_{1G$'],loc='center right')
ax1.set_ylabel('dϑ/dζ', loc="top", rotation='horizontal')
ax2.plot(xs,c2,'-', color='black', markeredgecolor='k')
# ax2.legend(['$C_{1}$'],loc='center right')
ax2.set_ylabel('ϑ', loc="top", rotation='horizontal')
ax3.plot(xs,c3,'-', color='black', markeredgecolor='k')
# ax3.legend(['$C_{1}$'],loc='center right')
ax3.set_ylabel('Dp', loc="top", rotation='horizontal')

ax1.tick_params(axis='both', direction='in', bottom=True, top=True, left=True,
right=True)
ax2.tick_params(axis='both', direction='in', bottom=True, top=True, left=True,
right=True)

print(R_con)
show()

diaSave = math.trunc(D*1000)
# print(diaSave)

if saveOn:
    saver = [xs, c1, c2, c3]
    diaSave = f"{diaSave:04d}"
    savetxt('C:/Users/basel/Documents/DPhil Work/Publications/Horn Tip
Concavity/MATLAB/Python_Newman/data_exports/' + str(diaSave) + '.csv', saver,
delimiter=",")
else:
    pass
# saver = zip(*saver)
close('all')
```

APPENDIX G: Regular Perturbation of Small Re

To simplify the regular perturbation solution, the exponential term in Eq. 7.34 has been substituted with Taylor series expansion, assuming a truncation error of order $O(3)$, such that

$$e^{-\Gamma\zeta} = 1 - \Gamma\zeta + \frac{\Gamma^2\zeta^2}{2} + O(3) \tag{A1}$$

As such, the force term then becomes:

$$\Gamma e^{-\Gamma\zeta} = \Gamma\left(1 - \Gamma\zeta + \frac{\Gamma^2\zeta^2}{2}\right) \tag{A2}$$

By substituting this, alongside equation 7.39, the force term then becomes:

$$\begin{aligned}\Gamma \mathrm{e}^{-\Gamma\zeta} &= (\Gamma_0\mathrm{Re} + \Gamma_1\mathrm{Re}^2 + \Gamma_2\mathrm{Re}^3)\left(1 - (\Gamma_0 + \Gamma_1\mathrm{Re} + \Gamma_2\mathrm{Re}^2)\zeta + \frac{1}{2}(\Gamma_0 + \Gamma_1\mathrm{Re} + \Gamma_2\mathrm{Re}^2)^2\zeta^2\right) \\ &= (\Gamma_0\mathrm{Re} + \Gamma_1\mathrm{Re}^2 + \Gamma_2\mathrm{Re}^3)\left(1 - \Gamma_0\zeta - \Gamma_1\zeta\mathrm{Re} - \Gamma_2\zeta\mathrm{Re}^2 + \frac{1}{2}\Gamma_0^2\zeta^2 + \frac{1}{2}\Gamma_0\Gamma_1\zeta^2\mathrm{Re}\right. \\ &\quad + \frac{1}{2}\Gamma_0\Gamma_2\zeta^2\mathrm{Re}^2 + \frac{1}{2}\Gamma_0\Gamma_1\zeta^2\mathrm{Re} + \frac{1}{2}\Gamma_1^2\zeta^2\mathrm{Re}^2 + \frac{1}{2}\Gamma_1\Gamma_2\zeta^2\mathrm{Re}^3 + \frac{1}{2}\Gamma_0\Gamma_2\zeta^2\mathrm{Re}^2 \\ &\quad \left. + \frac{1}{2}\Gamma_1\Gamma_2\zeta^2\mathrm{Re}^3 + \frac{1}{2}\Gamma_2^2\zeta^2\mathrm{Re}^4\right) \\ &= \Gamma_0\mathrm{Re} - \Gamma_0^2\zeta\mathrm{Re} - 2\Gamma_0\Gamma_1\zeta\mathrm{Re}^2 + \frac{1}{2}\Gamma_0^3\zeta^2\mathrm{Re} + \frac{3}{2}\Gamma_0^2\Gamma_1\zeta^2\mathrm{Re}^2 + \Gamma_1\mathrm{Re}^2 + \mathrm{O}(\mathrm{Re}^3)\end{aligned} \tag{A3}$$

Moreover, to obtain the complete equation, equations 7.35 – 7.39 are substituted into equation 7.34, which then formulates:

$$\begin{aligned}&-\theta_0'' + (\theta_0\theta_0' - \theta_1'')\mathrm{Re} + (\theta_0\theta_1' + \theta_1\theta_0' - \theta_2'')\mathrm{Re}^2 + \mathrm{O}(\mathrm{Re}^3) \\ &\quad = \mathrm{D}_{\mathrm{P},0} + \mathrm{D}_{\mathrm{P},1}\mathrm{Re} + \mathrm{D}_{\mathrm{P},2}\mathrm{Re}^2 - \Gamma_0\mathrm{Re} + \Gamma_0^2\zeta\mathrm{Re} - \Gamma_0^3\zeta\mathrm{Re} - \frac{1}{2}\Gamma_0^3\zeta^2\mathrm{Re} - \Gamma_1\mathrm{Re}^2 \\ &\quad + 2\Gamma_0\Gamma_1\zeta\mathrm{Re}^2 - \frac{3}{2}\Gamma_0^2\Gamma_1\zeta^2\mathrm{Re}^2 + \mathrm{O}(\mathrm{Re}^3)\end{aligned} \tag{A4}$$

Upon grouping up the orders of Re, in aims to resolve all terms of each of equations 7.35 – 7.39, we obtain for $O(1)$:

$$\theta_0'' = -\mathrm{D}_{\mathrm{P},0} \tag{A5}$$

$O(Re)$

$$\theta_1'' = -D_{P,1} + \Gamma_0 - \Gamma_0^2\zeta + \frac{1}{2}\Gamma_0^3\zeta^2 + \theta_0\theta_0' \tag{A6}$$

$O(Re^2)$

$$\theta_2'' = -D_{P,2} + \Gamma_1 - 2\Gamma_0\Gamma_1\zeta + \frac{3}{2}\Gamma_0^2\Gamma_1\zeta^2 + \theta_1\theta_0' + \theta_0\theta_1' \tag{A7}$$

Furthermore, the resolved boundary conditions, as mentioned in section 7.3, translate to the following:

$$\theta'(0) = 0 = \theta_0'(0) + \theta_1'(0)\mathrm{Re} + \theta_2'(0)\mathrm{Re}^2 \tag{A8}$$

where $\theta_0'(0) = \theta_1'(0) = \theta_2'(0) = 0$

$$\theta(0) = 0 = \theta_0(0) + \theta_1(0)\mathrm{Re} + \theta_2(0)\mathrm{Re}^2 \tag{A9}$$

$\theta_0(0) = \theta_1(0) = \theta_2(0) = 0.$

$$\theta''(2) = 0 = \theta_0''(2) + \theta_1''(2)\mathrm{Re} + \theta_2''(2)\mathrm{Re}^2 \tag{A10}$$

$\theta_0''(2) = \theta_1''(2) = \theta_2''(2) = 0$, and

$$\theta(2) = -1 = \theta_0(2) + \theta_1(2)\mathrm{Re} + \theta_2(2)\mathrm{Re}^2 \tag{A11}$$

in which $\theta_0(2) = -1$ while $\theta_1(2) = \theta_2(2) = 0$. With that said, the boundary conditions were then applied to equations A5 - A7 where applicable to ultimately obtain the values of each term in D_P and Γ and the expressions of each term in θ, θ', and θ''. From $O(1)$, we deduce that:

$$D_{P,0} = \frac{1}{2} \tag{A12}$$

$$\theta_0'' = -\frac{1}{2} \tag{A13}$$

$$\theta_0' = -\frac{1}{2}\zeta \tag{A14}$$

$$\theta_0 = -\frac{1}{4}\zeta^2 \tag{A15}$$

And from $O(Re)$:

$$D_{P,1} = -0.767250 \tag{A16}$$

$$\Gamma_1 = -0.579026 \tag{A17}$$

$$\theta_1'' = 0.767250 - 0.579026 - 0.335271\zeta - 0.097065\zeta^2 + \frac{1}{8}\zeta^3 \tag{A18}$$

$$\theta_1' = 0.767250\zeta - 0.579026\zeta - 0.167636\zeta^2 - 0.032355\zeta^3 + \frac{1}{32}\zeta^4 \tag{A19}$$

$$\theta_1 = 0.383625\zeta^2 - 0.289513\zeta^2 - 0.055925\zeta^3 - 0.008088\zeta^4 + \frac{1}{160}\zeta^5 \tag{A20}$$

and, lastly, from $O(Re^2)$:

$$D_{P,2} = -0.641065 \quad \text{(A21)}$$

$$\Gamma_2 = -0.641065 \quad \text{(A22)}$$

$$\begin{aligned}\theta_2'' = {} & 0.641065 - 0.357143 - 0.413590\zeta - 0.179609\zeta^2 + \frac{1}{20}\zeta^3 + 0.072137\zeta^4 \\ & + 0.0127345\zeta^5 - \frac{7}{640}\zeta^6\end{aligned} \quad \text{(A23)}$$

$$\begin{aligned}\theta_2' = {} & 0.641065\zeta - 0.357143\zeta - 0.206795\zeta^2 - 0.059869\zeta^3 + \frac{1}{80}\zeta^4 + 0.0144634\zeta^5 \\ & + 0.00212242\zeta^6 - \frac{1}{640}\zeta^7\end{aligned} \quad \text{(A24)}$$

$$\begin{aligned}\theta_2 = {} & 0.3205325\zeta^2 - 0.1785715\zeta^2 - 0.0689317\zeta^3 - 0.014967\zeta^4 + \frac{1}{400}\zeta^5 + 0.0024106\zeta^6 \\ & + 0.0003032\zeta^7 - \frac{1}{5120}\zeta^8\end{aligned} \quad \text{(A25)}$$

These were then replaced back into the perturbation expansions stated in 7.35 – 7.39 to give the final approximations of each term, as shown in 7.40 – 7.44.

REFERENCES

[1] M. Falkenmark, J. Lundqvist, C. Widstrand, Macro-scale water scarcity requires micro-scale approaches. Aspects of vulnerability in semi-arid development, Natural Resources Forum, 13 (1989).

[2] M. Kummu, J. Guillaume, H.d. Moel, S. Eisner, M. Florke, M. Porkka, S. Siebert, T.I.E. Veldkamp, P.J. Ward, The world's road to water scarcity: shortage and stress in the 20th century and pathways towards sustainability, Scientific Reports, 6 (2016).

[3] D. Chen, C. Zhang, H. Rong, C. Wei, S. Gou, Experimental study on seawater desalination through supercooled water dynamic ice making, Desalination, 476 (2020).

[4] M. Sheng, Y. Yang, X. Bin, S. Zhao, C. Pan, F. Nawaz, W. Que, Recent advanced self-propelling salt-blocking technologies for passive solar-driven interfacial evaporation desalination systems, Nano Energy, 89 (2021).

[5] J. Kim, S. Hong, Optimizing seawater reverse osmosis with internally staged design to improve product water quality and energy efficiency, Journal of Membrane Science, 568 (2018) 76-86.

[6] E. Curcio, G. Di Profio, Membrane Crystallization, in: Current Trends and Future Developments on (Bio-) Membranes, 2019, pp. 175-198.

[7] K. Tado, F. Sakai, Y. Sano, A. Nakayama, An analysis on ion transport process in electrodialysis desalination, Desalination, 378 (2016) 60-66.

[8] D.U. Lawal, N.A.A. Qasem, Humidification-dehumidification desalination systems driven by thermal-based renewable and low-grade energy sources: A critical review, Renewable and Sustainable Energy Reviews, 125 (2020).

[9] H. Frank, K.E. Fussmann, E. Rahav, E. Bar Zeev, Chronic effects of brine discharge form large-scale seawater reverse osmosis desalination facilities on benthic bacteria, Water Res, 151 (2019) 478-487.

[10] A. Panagopoulos, K.J. Haralambous, Environmental impacts of desalination and brine treatment - Challenges and mitigation measures, Mar Pollut Bull, 161 (2020) 111773.

[11] T. Saeed, S. Muntaha, M. Rashid, G. Sun, A. Hasnat, Industrial wastewater treatment in constructed wetlands packed with construction materials and agricultural by-products, Journal of Cleaner Production, 189 (2018) 442-453.

[12] N.T. Giao, Surface Water Quality Influenced by Industrial Wasterwater Effluent in An Giang Province, Vietnam, Journal of Science and Technology Research, 4 (2022).

[13] D. Parde, A. Patwa, A. Shukla, R. Vijay, D.J. Killedar, R. Kumar, A review of constructed wetland on type, treatment and technology of wastewater, Environmental Technology & Innovation, 21 (2021).

[14] G. Palani, A. Arputhalatha, K. Kannan, S.K. Lakkaboyana, M.M. Hanafiah, V. Kumar, R.K. Marella, Current Trends in the Application of Nanomaterials for the Removal of Pollutants from Industrial Wastewater Treatment-A Review, Molecules, 26 (2021).

[15] S.K. Sela, A.K.M.N.-U. Hossain, S.Z. Hussain, N. Hasan, Utilization of prawn to reduce the value of BOD and COD of textile wastewater, Cleaner Engineering and Technology, 1 (2020).

[16] F. Yalcinkaya, E. Boyraz, J. Maryska, K. Kucerova, A Review on Membrane Technology and Chemical Surface Modification for the Oily Wastewater Treatment, Materials (Basel), 13 (2020).

[17] N.Y. Donkadokula, A.K. Kola, I. Naz, D. Saroj, A review on advanced physico-chemical and biological textile dye wastewater treatment techniques, Reviews in Environmental Science and Bio/Technology, 19 (2020) 543-560.

[18] A. Shahedi, A.K. Darban, F. Taghipour, A. Jamshidi-Zanjani, A review on industrial wastewater treatment via electrocoagulation processes, Current Opinion in Electrochemistry, 22 (2020) 154-169.

[19] P.R. Rout, T.C. Zhang, P. Bhunia, R.Y. Surampalli, Treatment technologies for emerging contaminants in wastewater treatment plants: A review, Sci Total Environ, 753 (2021) 141990.
[20] A. Ullah, S. Hussain, A. Wasim, M. Jahanzaib, Development of a decision support system for the selection of wastewater treatment technologies, Sci Total Environ, 731 (2020) 139158.
[21] R. Alizadeh, L. Soltanisehat, P.D. Lund, H. Zamanisabzi, Improving renewable energy policy planning and decision-making through a hybrid MCDM method, Energy Policy, 137 (2020).
[22] H.T. Nguyen, U. Safder, X.Q. Nhu Nguyen, C. Yoo, Multi-objective decision-making and optimal sizing of a hybrid renewable energy system to meet the dynamic energy demands of a wastewater treatment plant, Energy, 191 (2020).
[23] W. Qiao, R. Li, T. Tang, A.A. Zuh, Removal, distribution and plant uptake of perfluorooctane sulfonate (PFOS) in a simulated constructed wetland system, Frontiers of Environmental Science & Engineering, 15 (2020).
[24] L. Qin, M. Gao, M. Zhang, L. Feng, Q. Liu, G. Zhang, Application of encapsulated algae into MBR for high-ammonia nitrogen wastewater treatment and biofouling control, Water Res, 187 (2020) 116430.
[25] P. Gao, J. Cui, Y. Deng, Direct regeneration of ion exchange resins with sulfate radical-based advanced oxidation for enabling a cyclic adsorption – regeneration treatment approach to aqueous perfluorooctanoic acid (PFOA), Chemical Engineering Journal, 405 (2021).
[26] E. Yakamercan, A. Aygün, Fate and removal of pentachlorophenol and diethylhexyl phthalate from textile industry wastewater by sequencing batch biofilm reactor: Effects of hydraulic and solid retention times, Journal of Environmental Chemical Engineering, 9 (2021).
[27] J.-P. Jalkanen, L. Johansson, M. Wilewska-Bien, L. Granhag, E. Ytreberg, K.M. Eriksson, D. Yngsell, I.-M. Hassellöv, K. Magnusson, U. Raudsepp, I. Maljutenko, H. Winnes, J. Moldanova, Modelling of discharges from Baltic Sea shipping, Ocean Science, 17 (2021) 699-728.
[28] L. Pasquina-Lemonche, J. Burns, R.D. Turner, S. Kumar, R. Tank, N. Mullin, J.S. Wilson, B. Chakrabarti, P.A. Bullough, S.J. Foster, J.K. Hobbs, The architecture of the Gram-positive bacterial cell wall, Nature, 582 (2020) 294-297.
[29] J.I. Thornycroft, S.W. Barnaby, Torpedo Boat Destroyers, Journal of the American Society for Naval Engineers, 7 (1985) 771-736.
[30] C.E. Brennen, Cavitation And Bubble Dynamics, Oxford University Press, 1995.
[31] X. Sun, J.J. Park, H.S. Kim, S.H. Lee, S.J. Seong, A.S. Om, J.Y. Yoon, Experimental investigation of the thermal and disinfection performances of a novel hydrodynamic cavitation reactor, Ultrason Sonochem, 49 (2018) 13-23.
[32] B. Wang, H. Su, B. Zhang, Hydrodynamic cavitation as a promising route for wastewater treatment – A review, Chemical Engineering Journal, 412 (2021).
[33] B. Boyd, S. Becker, Numerical modeling of the acoustically driven growth and collapse of a cavitation bubble near a wall, Physics of Fluids, 31 (2019) 032102.
[34] S. Begmatov, A.G. Dorofeev, V.V Kadnikov, A.V. Beletsky, N.V. Pimenov, N.V. Ravin, A.V. Mardanov, The structure of microbial communities of activated sludge of large-scale wastewater treatment plants in the city of Moscow, Scietific Reports, 12 (2022) 3458.
[35] Y. Han, T. Yang, G. Xu, L. Li, J. Liu, Characteristics and interactions of bioaerosol microorganisms from wastewater treatment plants, J Hazard Mater, 391 (2020) 122256.
[36] K.P. Mishra, P.R. Gogate, Intensification of degradation of Rhodamine B using hydrodynamic cavitation in the presence of additives, Separation and Purification Technology, 75 (2010) 385-391.
[37] M. Sežun, J. Kosel, M. Zupanc, M. Hočevar, J. Vrtovšek, M. Petkovšek, M. Dular, Cavitation as a Potential Technology for Wastewater Management – An Example of Enhanced

Nutrient Release from Secondary Pulp and Paper Mill Sludge, Strojniški vestnik – Journal of Mechanical Engineering, 65 (2019) 641-649.

[38] L.M. Cerecedo, C. Dopazo, R. Gomez-Lus, Water disinfection by hydrodynamic cavitation in a rotor-stator device, Ultrason Sonochem, 48 (2018) 71-78.

[39] M. Badve, P. Gogate, A. Pandit, L. Csoka, Hydrodynamic cavitation as a novel approach for wastewater treatment in wood finishing industry, Separation and Purification Technology, 106 (2013) 15-21.

[40] B. Maršálek, Š. Zezulka, E. Maršálková, F. Pochylý, P. Rudolf, Synergistic effects of trace concentrations of hydrogen peroxide used in a novel hydrodynamic cavitation device allows for selective removal of cyanobacteria, Chemical Engineering Journal, 382 (2020).

[41] H. Kim, B. Koo, X. Sun, J.Y. Yoon, Investigation of sludge disintegration using rotor-stator type hydrodynamic cavitation reactor, Separation and Purification Technology, 240 (2020).

[42] P. Wu, L. Bai, W. Lin, X. Wang, Mechanism and dynamics of hydrodynamic-acoustic cavitation (HAC), Ultrason Sonochem, 49 (2018) 89-96.

[43] O. Johansson, T. Pamidi, V. Shankar, Extraction of tungsten from scheelite using hydrodynamic and acoustic cavitation, Ultrason Sonochem, 71 (2021) 105408.

[44] Y. Gu, Y. Li, X. Li, P. Luo, H. Wang, Z.P. Robinson, X. Wang, J. Wu, F. Li, The feasibility and challenges of energy self-sufficient wastewater treatment plants, Applied Energy, 204 (2017) 1463-1475.

[45] J. Drewnowski, A. Remiszewska-Skwarek, S. Duda, G. Łagód, Aeration Process in Bioreactors as the Main Energy Consumer in a Wastewater Treatment Plant. Review of Solutions and Methods of Process Optimization, Processes, 7 (2019).

[46] L. Rayleigh, VIII. On the pressure developed in a liquid during the collapse of a spherical cavity, The London, Edinburgh, and Dublin Philosophical Magazine and Journal of Science, 34 (1917) 94-98.

[47] P. Aursand, M.A. Gjennestad, E. Aursand, M. Hammer, Ø. Wilhelmsen, The spinodal of single- and multi-component fluids and its role in the development of modern equations of state, Fluid Phase Equilibria, 436 (2017) 98-112.

[48] E.N. Harvey, W.D. McElroy, A.H. Whiteley, On Cavity Formation in Water, Journal of Applied Physics, 18 (1947) 162-172.

[49] J. Frenkel, Kinetic theory of liquids, Dover, New York, 1955.

[50] K.A. Morch, Cavitation nuclei and tensile strength of water, International Symposium on Cavitation, (2018).

[51] Z. Gao, W. Wu, B. Wang, The effects of nanoscale nuclei on cavitation, Journal of Fluid Mechanics, 911 (2021).

[52] A.A. Atchley, A. Prosperetti, The crevice model of bubble nucleation, The Journal of the Acoustical Society of America, 86 (1989).

[53] K.K. Tanaka, Y. Kimura, Theoretical analysis of crystallization by homogeneous nucleation of water droplets, Phys Chem Chem Phys, 21 (2019) 2410-2418.

[54] F. Yang, Homogeneous nucleation in a Poiseuille flow, Phys Chem Chem Phys, 23 (2021) 3974-3982.

[55] S.N. Lvov, D.M. Hall, A.V. Bandura, I.K. Gamwo, A semi-empirical molecular statistical thermodynamic model for calculating standard molar Gibbs energies of aqueous species above and below the critical point of water, Journal of Molecular Liquids, 270 (2018) 62-73.

[56] J.W. Gibbs, The Scientific Papers, Nature, 1 (1907).

[57] W. Zhou, C. Wu, H. Lv, B. Zhao, K. Liu, L. Ou, Nanobubbles heterogeneous nucleation induced by temperature rise and its influence on minerals flotation, Applied Surface Science, 508 (2020).

[58] X. Huang, C. Li, K. Zuo, Q. Li, Predominant Effect of Material Surface Hydrophobicity on Gypsum Scale Formation, Environ Sci Technol, 54 (2020) 15395-15404.

[59] L. Lu, J. Zhang, J. Xu, Microscopic visualization of heterogeneous nucleation process on smooth spherical particle: Method and results, Chemical Engineering Science, 213 (2020).

[60] H. Guo, Y. Xing, H. Yuan, R. Zhang, Y. Zhang, P. Deng, Improving the anti-icing performance of superhydrophobic surfaces by nucleation inhibitor, Surface Engineering, 36 (2019) 621-627.

[61] J.F. Lu, X.F. Peng, Dynamical evolution of heterogeneous nucleation on surfaces with ideal cavities, Heat and Mass Transfer, 43 (2006) 659-667.

[62] W. Wang, Z. Li, M. Liu, X. Ji, Influence of water injection on broadband noise and hydrodynamic performance for a NACA66 (MOD) hydrofoil under cloud cavitation condition, Applied Ocean Research, 115 (2021).

[63] T.Q. Bui, H.T.M. Ngo, H.T. Tran, Surface-protective assistance of ultrasound in synthesis of superparamagnetic magnetite nanoparticles and in preparation of mono-core magnetite-silica nanocomposites, Journal of Science: Advanced Materials and Devices, 3 (2018) 323-330.

[64] K. Yasui, Dynamics of Acoustic Bubbles, 2015.

[65] J. Cui, Z. Zhang, X. Liu, L. Liu, J. Peng, Studies on viscosity reduction and structural change of crude oil treated with acoustic cavitation, Fuel, 263 (2020).

[66] S.S. Rashwan, I. Dincer, A. Mohany, An investigation of ultrasonic based hydrogen production, Energy, 205 (2020).

[67] G.S. Nhivekar, V.K. Rathod, Acoustic cavitation assisted lipase B catalysed synthesis of polyethylene glycol stearate in a solvent free system via esterification: synthesis and optimization, Journal of Chemical Technology & Biotechnology, 94 (2019) 2465-2474.

[68] I. Tzanakis, G.S. Lebon, D.G. Eskin, K.A. Pericleous, Characterizing the cavitation development and acoustic spectrum in various liquids, Ultrason Sonochem, 34 (2017) 651-662.

[69] A. Žnidarčič, R. Mettin, C. Cairós, M. Dular, Attached cavitation at a small diameter ultrasonic horn tip, Physics of Fluids, 26 (2014) 023304

[70] R. Altay, A.K. Sadaghiani, M.I. Sevgen, A. Şişman, A. Koşar, Numerical and Experimental Studies on the Effect of Surface Roughness and Ultrasonic Frequency on Bubble Dynamics in Acoustic Cavitation, Energies, 13 (2020) 1126.

[71] D. Suo, B. Govind, S. Zhang, Y. Jing, Numerical investigation of the inertial cavitation threshold under multi-frequency ultrasound, Ultrason Sonochem, 41 (2018) 419-426.

[72] L. Ye, X. Zhu, Y. He, T. Song, Effect of frequency ratio and phase difference on the dynamic behavior of a cavitation bubble induced by dual-frequency ultrasound, Chemical Engineering and Processing - Process Intensification, 165 (2021).

[73] L. Jiang, H. Ge, F. Liu, D. Chen, Investigations on dynamics of interacting cavitation bubbles in strong acoustic fields, Ultrason Sonochem, 34 (2017) 90-97.

[74] H. Wu, H. Zheng, Y. Li, C.D. Ohl, H. Yu, D. Li, Effects of surface tension on the dynamics of a single micro bubble near a rigid wall in an ultrasonic field, Ultrason Sonochem, 78 (2021) 105735.

[75] L.A. Crum, Surface Oscillations and Jet Development in Pulsating Bubbles, Le Journal de Physique Colloques, 40 (1979) C8-285-C288-288.

[76] K.S. Suslick, D.J. Flannigan, Inside a collapsing bubble: sonoluminescence and the conditions during cavitation, Annu Rev Phys Chem, 59 (2008) 659-683.

[77] T. Yamamoto, S.V. Komarov, Dynamic behavior of acoustic cavitation bubble originated from heterogeneous nucleation, Journal of Applied Physics, 128 (2020) 004702.

[78] E. Ezzatneshan, H. Vaseghnia, Dynamics of an acoustically driven cavitation bubble cluster in the vicinity of a solid surface, Physics of Fluids, 33 (2021).

[79] D. Qin, Q. Zou, S. Lei, W. Wang, Z. Li, Cavitation Dynamics and Inertial Cavitation Threshold of Lipid Coated Microbubbles in Viscoelastic Media with Bubble-Bubble Interactions, Micromachines, 12 (2021) 1125.
[80] P. Koukouvinis, M. Gavaises, O. Supponen, M. Farhat, Numerical simulation of a collapsing bubble subject to gravity, Physics of Fluids, 28 (2016).
[81] C. Yuan, J. Song, L. Zhu, M. Liu, Numerical investigation on cavitating jet inside a poppet valve with special emphasis on cavitation-vortex interaction, International Journal of Heat and Mass Transfer, 141 (2019) 1009-1024.
[82] L.T. Liu, X.B. Chen, W.Q. Zhang, A.M. Zhang, Study on the transient characteristics of pulsation bubble near a free surface based on finite volume method and front tracking method, Physics of Fluids, 32 (2020).
[83] R. Temam, Navier Stokes Equations: Theory and Numerical Analysis, AMS Chelsea Publishing, Rhode Island, USA, 2001.
[84] X. Ye, X. Yao, R. Han, Dynamics of cavitation bubbles in acoustic field near the rigid wall, Ocean Engineering, 109 (2015) 507-516.
[85] B. Rahmatizadeh, M.T.H. Beheshti, M. Azadegan, M. Najafi, Stability analysis and sliding mode control of a single spherical bubble described by Keller–Miksis equation, International Journal of Dynamics and Control, 9 (2021) 1757-1764.
[86] K. Kerboua, O. Hamdaoui, A. Alghyamah, Energy balance of high-energy stable acoustic cavitation within dual-frequency sonochemical reactor, Ultrason Sonochem, 73 (2021) 105471.
[87] M.S. Plesset, A. Prosperetti, Bubble Dynamics and Cavitation, Annual Review of Fluid Mechanics, 9 (1977) 145-185.
[88] S. Frikha, O. Coutier-Delgosha, J.A. Astolfi, Influence of the Cavitation Model on the Simulation of Cloud Cavitation on 2D Foil Section, International Journal of Rotating Machinery, 2008 (2008) 1-12.
[89] A. Kubota, H. Kato, H. Yamaguchi, A new modelling of cavitating flows: a numerical study of unsteady cavitation on a hydrofoil section, Journal of Fluid Mechanics, 240 (1991) 59-96.
[90] C.L. Merkle, L. Feng, P.E.O. Buelow, Computational modeling of the dynamics of sheet cavitation, in: 3rd International Symposium on Cavitation, Grenoble, France, 1998.
[91] R.F. Kunz, D.A. Boger, D.R. Stinebring, T.S. Chyczewski, J.W. Lindau, H.J. Gibeling, S. Venkateswaran, T.R. Govindan, A Preconditioned Navier-Stokes Method for Two-phase Flows with Application to Cavitation Prediction, Computers and Fluids, 29 (2000).
[92] G.H. Schnerr, J. Sauer, Physical and Numerical Modeling of Unsteady Cavitation Dynamics, in: 4th International Conference on Multiphase Flow, ICMF, 2001.
[93] P.J. Zwart, A.G. Gerber, T. Belamri, A Two-Phase Flow Model for Predicting Cavitation Dynamics, in: 5th International Conference on Multiphase Flow, ICMF, 2004.
[94] A.K. Singhal, M.M. Athavale, H. Li, Y. Jiang, Mathematical Basis and Validation of the Full Cavitation Model, Journal of Fluids Engineering, 124 (2002) 617-624.
[95] M. Frobenius, R. Schiling, R. Bachert, B. Stoffle, G. Ludwig, THREE-DIMENSIONAL UNSTEADY CAVITATION EFFECTS ON A SINGLE HYDROFOIL AND IN A RADIAL PUMP – MEASUREMENTS AND NUMERICAL SIMULATIONS, in: 5th International Symposium on Cavitation, Osaka, Japan, 2003.
[96] L. Rayleigh, Theory of Sound, Dover Publications, New York, 1896.
[97] W.L. Nyborg, Acoustic streaming due to attenuated plane waves, The Journal of the Acoustical Society of America, 25 (1953) 68-75.
[98] P.J. Westervelt, The theory of steady rotational flow generated by a sound field, The Journal of the Acoustical Society of America, 25 (1953) 60-67.

[99] S. Tjotta, Theoretical investigation of heat and streaming generated by high intensity ultrasound, Acustica, 85 (1999) 19-25.
[100] J.T. Stuart, Unsteady Boundary Layers, Oxford University Press, London, 1963.
[101] H. Schilichting, Boundary Layer Theory, McGraw-Hill, 1979.
[102] J. Klima, A. Frias-Ferrer, J. Gonzalez-Garcia, J. Ludvik, V. Saez, J. Iniesta, Optimisation of 20 kHz sonoreactor geometry on the basis of numerical simulation of local ultrasonic intensity and qualitative comparison with experimental results, Ultrason Sonochem, 14 (2007) 19-28.
[103] V. Saez, A. Frias-Ferrer, J. Iniesta, J. Gonzalez-Garcia, A. Aldaz, E. Riera, Characterization of a 20 kHz sonoreactor. Part I: analysis of mechanical effects by classical and numerical methods, Ultrason Sonochem, 12 (2005) 59-65.
[104] M. Rahimi, S. Movahedirad, S. Shahhosseini, CFD study of the flow pattern in an ultrasonic horn reactor: Introducing a realistic vibrating boundary condition, Ultrason Sonochem, 35 (2017) 359-374.
[105] J.A. Gallego-Juarez, Piezoelectric cermaics and ultrasonic transducers, Journal of Physics E: Scientific Instruments, 22 (1989).
[106] E. Ventsel, T. Krauthammer, Thin Plates and Shells: Theory, Analysis, and Applications, CRC Press, 2001.
[107] J. Kim, J.N. Reddy, Analytical solutions for bending, vibration, and buckling of FGM plates using a couple stress-based third-order theory, Composite Structures, 103 (2013) 86-98.
[108] J. Du, F. Chen, Cavitation dynamics and flow aggressiveness in ultrasonic cavitation erosion, International Journal of Mechanical Sciences, 204 (2021).
[109] A. Znidarcic, R. Mettin, M. Dular, Modeling cavitation in a rapidly changing pressure field - application to a small ultrasonic horn, Ultrason Sonochem, 22 (2015) 482-492.
[110] B. Al Bishtawi, K.B. Mustapha, G. Scribano, Modeling the mass transfer at acoustically generated bubble interface using Rayleigh–Plesset equation second-order derivatives, Physics of Fluids, 34 (2022).
[111] H. Zhang, C. Baschman, H. Fasel, Reynolds-averaged Navier-Stokes calculations of unsteady turbulent flow, in: AIAA 2000, Reno, NV, USA, 2000.
[112] A. Hellsten, S. Laine, Extension of the k-w-SST turbulence model for flows over rouch surfaces, American Institute of Aeronautics and Astronautics, 98 (1997).
[113] D.C. Wilcox, Reassessment of the Scale-Determining Equation for Advanced Turbulence Models, AIAA Journal, 26 (1988) 1299-1310.
[114] W.P. Jones, B.E. Launder, The calculation of low-Reynolds-number-phenomena with a two-equation model of turbulence, Int. J. Heat Mass Transf., 16 (1973) 1119-1130.
[115] V.S. Nanda, R. Simha, Theoretical Interpreation of Tait Equation Parameters, The Journal of Chemical Physics, 41 (2004).
[116] L. Yusuf, M.D. Symes, P. Prentice, Characterising the cavitation activity generated by an ultrasonic horn at varying tip-vibration amplitudes, Ultrason Sonochem, 70 (2021) 105273.
[117] P. Muleki Seya, C. Desjouy, J.C. Bera, C. Inserra, Hysteresis of inertial cavitation activity induced by fluctuating bubble size distribution, Ultrason Sonochem, 27 (2015) 262-267.
[118] K. Yasui, Y. Iida, T. Tuziuti, T. Kozuka, A. Towata, Strongly interacting bubbles under an ultrasonic horn, Phys Rev E Stat Nonlin Soft Matter Phys, 77 (2008) 016609.
[119] S. Lesnik, A. Aghelmaleki, R. Mettin, G. Brenner, Modeling acoustic cavitation with inhomogeneous polydisperse bubble population on a large scale, Ultrasonics Sonochemistry, (2022).
[120] J.B. Keller, M. Miksis, Bubble oscillations of large amplitude, The Journal of the Acoustical Society of America, 68 (1980) 628-633.

[121] R. Altay, A.K. Sadaghiani, M.I. Sevgen, A. Şişman, A. Koşar, Numerical and Experimental Studies on the Effect of Surface Roughness and Ultrasonic Frequency on Bubble Dynamics in Acoustic Cavitation, Energies, 13 (2020).
[122] F.R. Gilmore, The Growth or Collapse of a Spherical Bubble in a Viscous Compressible Liquid, in, California Institute of Technology, Pasaden, California, 1952.
[123] S. Popinet, S. Zaleski, A front-tracking algorithm for accurate representation of

surface tension, International Journal for Numerical Methods in Fluids, 30 (1999) 775-793.
[124] A.I. Eller, L.A. Crum, Instability of the Motion of a Pulsating Bubble in a Sound Field, 47 (1970) 762–767.
[125] W. Lauterborn, Numerical investigation of nonlinear oscillations of gas

bubbles in liquids, The Journal of the Acoustical Society of America, 59 (1976) 283–293.
[126] S.S. Rashwan, I. Dincer, A. Mohany, Investigation of acoustic and geometric effects on the sonoreactor performance, Ultrason Sonochem, 68 (2020) 105174.
[127] S. Zhao, C. Yao, L. Liu, G. Chen, Parametrical investigation of acoustic cavitation and extraction enhancement in ultrasonic microreactors, Chemical Engineering Journal, 450 (2022).
[128] A. Žnidarčič, R. Mettin, C. Cairós, M. Dular, Attached cavitation at a small diameter ultrasonic horn tip, Physics of Fluids, 26 (2014).
[129] O. Louisnard, A simple model of ultrasound propagation in a cavitating liquid. Part I: Theory, nonlinear attenuation and traveling wave generation, Ultrason Sonochem, 19 (2012) 56-65.
[130] R. Mettin, P. Koch, W. Lauterborn, Modeling Acoustic Cavitation With Bubble Redistribution, in: Sixth International Symposium on Cavitation,, Wageningen, The Netherlands, 2006, pp. 1-5.
[131] K. Kerboua, O. Hamdaoui, A. Alghyamah, Numerical Characterization of Acoustic Cavitation Bubbles with Respect to the Bubble Size Distribution at Equilibrium, Processes, 9 (2021).
[132] R.I. Cukier, R. Kapral, J.R. Lebenhaft, J.R. Mehaffey, On the microscopic origin of Stokes' law, The Journal of Chemical Physics, 73 (1980) 5244-5253.
[133] J. Sauer, Instationär kavitierende Strömungen - Ein neues Modell, basierend auf Front Capturing (VoF) und Blasendynamik, in: Fakultät für Maschinenbau (MACH), Universität Karlsruhe (TH), Karlsruhe, Germany, 2000.
[134] C.A.R. Duarte, F.J. de Souza, Dynamic mesh approaches for eroded shape predictions, Wear, 484-485 (2021) 203438.
[135] ANSYS, Dynamic Mesh Update Methods, in, ANSYS, 2009.
[136] R. Hooke, Lecture de potentia restitutiva, or of spring, explaining the power of springing bodies to which are added some collections, John Martyn, 1678.

[137] D. Montgomery, Design and Analysis of Experiments, Sixth Edition ed., Wiley, 2004.
[138] L. Geng, X. Escaler, Assessment of RANS turbulence models and Zwart cavitation model empirical coefficients for the simulation of unsteady cloud cavitation, Engineering Applications of Computational Fluid Mechanics, 14 (2019) 151-167.
[139] J.-H. Bae, K. Chang, G.-H. Lee, B.-C. Kim, Bayesian Inference of Cavitation Model Coefficients and Uncertainty Quantification of a Venturi Flow Simulation, Energies, 15 (2022) 4204.
[140] X. Escaler, R. Roig, V. Hidalgo, Sensitivity Analysis of Zwart-Gerber-Belamri Model Parameters on the Numerical

Simulation of Francis Runner Cavitation, in: 10th International Symposium on Cavitation, Baltimore, Maryland, USA, 2018.

[141] F. Reuter, S. Lesnik, K. Ayaz-Bustami, G. Brenner, R. Mettin, Bubble size measurements in different acoustic cavitation structures: Filaments, clusters, and the acoustically cavitated jet, Ultrason Sonochem, 55 (2019) 383-394.

[142] Minitab, Getting Started with Minitab Statistical Software, in, 2022.

[143] J. B. Hirkude, A.S. Padalkar, Performance optimization of CI engine fuelled with waste fried oil methyl ester-diesel blend using response surface methodology, Fuel, 119 (2014) 266-273.

[144] G. Kozmus, J. Zevnik, M. Hocevar, M. Dular, M. Petkovsek, Characterization of cavitation under ultrasonic horn tip - Proposition of an acoustic cavitation parameter, Ultrason Sonochem, 89 (2022) 106159.

[145] H. Lais, P.S. Lowe, L.C. Wrobel, T.-H. Gan, Investigation of Ultrasonic Sonotrode Design to Improve the Performance of Ultrasonic Fouling Removal, IEEE Access, 7 (2019) 148897-148912.

[146] J. S.V, G. Natarajan, K.S. S, Numerical investigation of ultrasonic cavitation in stir cast aluminium matrix melt composites, Applied Physics of Condensed Matter (Apcom 2022).

[147] M. Petkovšek, M. Dular, Cavitation dynamics in water at elevated temperatures and in liquid nitrogen at an ultrasonic horn tip, Ultrasonics Sonochemistry, 58 (2019).

[148] P.B. Patil, S. Raut-Jadhav, A.B. Pandit, Effect of intensifying additives on the degradation of thiamethoxam using ultrasound cavitation, Ultrason Sonochem, 70 (2021) 105310.

[149] K. Fattahi, E. Robert, D.C. Boffito, Numerical and experimental investigation of the cavitation field in horn-type sonochemical reactors, Chemical Engineering and Processing - Process Intensification, 182 (2022).

[150] M. Abedini, F. Reuter, S. Hanke, Corrosion and material alterations of a CuZn38Pb3 brass under acoustic cavitation, Ultrason Sonochem, 58 (2019) 104628.

[151] N.B. Suryawanshi, V.M. Bhandari, L.G. Sorokhaibam, V.V. Ranade, Investigating Adsorptive Deep Desulfurization of Fuels Using Metal-Modified Adsorbents and Process Intensification by Acoustic Cavitation, Industrial & Engineering Chemistry Research, 58 (2018) 7593-7606.

[152] S. Mottyll, R. Skoda, Numerical 3D flow simulation of ultrasonic horns with attached cavitation structures and assessment of flow aggressiveness and cavitation erosion sensitive wall zones, Ultrason Sonochem, 31 (2016) 570-589.

[153] Y. Huang, M. Feng, X. Chen, Pull-in instability and vibration of quasicrystal circular nanoplate actuator based on surface effect and nonlocal elastic theory, Archive of Applied Mechanics, 92 (2022) 853-866.

[154] J. Zhou, P. Lu, Y. Xue, C. Lu, A third-order plate model with surface effect based on the Gurtin–Murdoch surface elasticity, Thin-Walled Structures, 185 (2023).

[155] J.A. Morton, M. Khavari, A. Priyadarshi, A. Kaur, N. Grobert, J. Mi, K. Porfyrakis, P. Prentice, D.G. Eskin, I. Tzanakis, Dual frequency ultrasonic cavitation in various liquids: High-speed imaging and acoustic pressure measurements, Physics of Fluids, 35 (2023).

[156] L. Ye, X. Zhu, X. Wei, S. Wu, Damage characteristics and surface description of near-wall materials subjected to ultrasonic cavitation, Ultrason Sonochem, 67 (2020) 105175.

[157] S.L. Brunton, C.W. Rowley, Fast computation of finite-time Lyapunov exponent fields for unsteady flows, Chaos, 20 (2010) 017503.

[158] Y. Long, X. Long, B. Ji, LES investigation of cavitating flows around a sphere with special emphasis on the cavitation–vortex interactions, Acta Mechanica Sinica, 36 (2020) 1238-1257.

[159] S.J. Lighthill, Acoustic Streaming, Journal of Sound and Vibration, 61 (1978).

[160] F.J. Trujillo, K. Knoerzer, A computational modeling approach of the jet-like acoustic streaming and heat generation induced by low frequency high power ultrasonic horn reactors, Ultrason Sonochem, 18 (2011) 1263-1273.
[161] L. Biasiori-Poulanges, C. Bourquard, B. Lukic, L. Broche, O. Supponen, Synchrotron X-ray imaging of the onset of ultrasonic horn cavitation, Ultrason Sonochem, 92 (2023) 106286.
[162] T. Pozar, V. Agrez, R. Petkovsek, Laser-induced cavitation bubbles and shock waves in water near a concave surface, Ultrason Sonochem, 73 (2021) 105456.
[163] X. Wang, Z. Ning, M. Lv, C. Sun, The Investigation of Ultrasonic Energy Attenuation in Aqueous Solutions, Journal of the Physical Society of Japan, 90 (2021).
[164] X. Ma, B. Huang, G. Wang, M. Zhang, Experimental investigation of conical bubble structure and acoustic flow structure in ultrasonic field, Ultrason Sonochem, 34 (2017) 164-172.
[165] K.L. Tan, S.H. Yeo, Bubble dynamics and cavitation intensity in milli-scale channels under an ultrasonic horn, Ultrason Sonochem, 58 (2019) 104666.
[166] A. Moussatov, C. Granger, B. Dubus, Cone-like bubble formation in ultrasonic cavitation field, Ultrason Sonochem, 10 (2003) 191-195.
[167] A. Jayaprakash, J.-K. Choi, G.L. Chahine, F. Martin, M. Donnelly, J.-P. Franc, A. Karimi, Scaling study of cavitation pitting from cavitating jets and ultrasonic horns, Wear, 296 (2012) 619-629.
[168] S. Singh, J.-K. Choi, G.L. Chahine, Characterization of Cavitation Fields From Measured Pressure Signals of Cavitating Jets and Ultrasonic Horns, Journal of Fluids Engineering, 135 (2013).
[169] B. Avvaru, A.B. Pandit, Oscillating bubble concentration and its size distribution using acoustic emission spectra, Ultrason Sonochem, 16 (2009) 105-115.
[170] R. Mettin, S. Luther, C.-D. Ohl, W. Lauterborn, Acoustic cavitation structures and simulations by a particle model, Ultrason Sonochem, 6 (1999) 25-29.
[171] D. Schieppati, M. Mohan, B. Blais, K. Fattahi, G.S. Patience, B.A. Simmons, S. Singh, D.C. Boffito, Characterization of the acoustic cavitation in ionic liquids in a horn-type ultrasound reactor, Ultrason Sonochem, 102 (2024) 106721.
[172] A. Priyadarshi, M. Khavari, S. Bin Shahrani, T. Subroto, L.A. Yusuf, M. Conte, P. Prentice, K. Pericleous, D. Eskin, I. Tzanakis, In-situ observations and acoustic measurements upon fragmentation of free-floating intermetallics under ultrasonic cavitation in water, Ultrason Sonochem, 80 (2021) 105820.
[173] BANDELIN, MS 73 Titanium Microtip Product Information SONOPLUS Accessories, in, BANDELIN, 2005.
[174] M. Roopa Rani, R. Rudramoorthy, Computational modeling and experimental studies of the dynamic performance of ultrasonic horn profiles used in plastic welding, Ultrasonics, 53 (2013) 763-772.
[175] K. Hornisova, P. Billik, Some properties of horn equation model of ultrasonic system vibration and of transfer matrix and equivalent circuit methods of its solution, Ultrasonics, 54 (2014) 330-342.
[176] E. Sahinoglu, T. Uslu, Effects of various parameters on ultrasonic comminution of coal in water media, Fuel Processing Technology, 137 (2015) 48-54.
[177] A. Thiemann, F. Holsteyns, C. Cairos, R. Mettin, Sonoluminescence and dynamics of cavitation bubble populations in sulfuric acid, Ultrason Sonochem, 34 (2017) 663-676.
[178] J. Yu, H. Luo, T.V. Nguyen, L. Huang, B. Liu, Y. Zhang, Eigenfrequency characterization and tuning of Ti-6Al-4V ultrasonic horn at high temperatures for glass molding, Ultrasonics, 101 (2020) 106002.

[179] A. Hajnorouzi, M.S. Rahmanifar, P. Yaghoubi, Effects of Increasing Acoustic Power at a Small-Diameter Ultrasonic Horn Tip on the Synthesis and Characteristics of MnO2 Nanoparticles, Journal of the Korean Physical Society, 77 (2020) 153-160.
[180] L. Bai, W. Xu, J. Deng, C. Li, D. Xu, Y. Gao, Generation and control of acoustic cavitation structure, Ultrason Sonochem, 21 (2014) 1696-1706.
[181] S.S. Arya, P.R. More, M.R. Ladole, K. Pegu, A.B. Pandit, Non-thermal, energy efficient hydrodynamic cavitation for food processing, process intensification and extraction of natural bioactives: A review, Ultrason Sonochem, 98 (2023) 106504.
[182] P. Wu, X. Wang, W. Lin, L. Bai, Acoustic characterization of cavitation intensity: A review, Ultrason Sonochem, 82 (2022) 105878.
[183] T. Yamamoto, K. Kubo, S.V. Komarov, Characterization of acoustic streaming in water and aluminum melt during ultrasonic irradiation, Ultrasonics Sonochemistry, 71 (2021).
[184] M.C. Schenker, M.J. Pourquie, D.G. Eskin, B.J. Boersma, PIV quantification of the flow induced by an ultrasonic horn and numerical modeling of the flow and related processing times, Ultrason Sonochem, 20 (2013) 502-509.
[185] S. Lesnik, A. Aghelmaleki, R. Mettin, G. Brenner, Modeling acoustic cavitation with inhomogeneous polydisperse bubble population on a large scale, Ultrason Sonochem, 89 (2022) 106060.
[186] M.A. Habib, J.H. Whitelaw, Velocity Characteristics of a Confined Coaxial Jet, Journal of Fluids Engineering, 101 (1979) 521-529.
[187] Y. Fang, T. Yamamoto, S. Komarov, Cavitation and acoustic streaming generated by different sonotrode tips, Ultrason Sonochem, 48 (2018).
[188] K. Fattahi, G. Dodier, E. Robert, D.C. Boffito, Flow effects on sonochemical oxidation acitivity in a 20kHz ultrasonic horn system, Chem Eng J, 489 (2024).
[189] R. Jamshidi, B. Pohl, U.A. Peurker, G. Brenner, Numerical investigation of sonochemical reactors considering the effect of inhomogeneous bubble clouds on ultrasonic wave propagation, Chem Eng J, 189 (2012) 364-375.
[190] B. Al Bishtawi, K.B. Mustapha, G. Scribano, Molding the acoustic cavity - analyzing the influence of toroidal vortex development on acoustic multi-bubble macrostructures under different ultrasonic horn tip diameters, Phs Fluids, 36 (2024) 043336.
[191] N. Brezhneva, N.V. Dezhkunov, S.A. Ulasevich, E.V. Skorb, Characterization of transient cavitation activity during sonochemical modification of magnesium particles, Ultrason Sonochem, 70 (2021) 105315.
[192] J. Dulle, S. Nemeth, E.V. Skorb, D.V. Andreeva, Sononanostructuring of zinc-based materials, RCS Adv., 2 (2012).
[193] E. Kuvyrkov, N. Brezhneva, S.A. Ulasevich, E.V. Skorb, Sonochemical nanostructuring of titanium for regulation of human mesenchymal stem cells behavior for implant development, Ultrason Sonochem, 52 (2019) 437-445.
[194] J.T. Karlsen, W. Qiu, P. Augustsson, H. Bruus, Acoustic streaming and its suppression in inhomogenous fluids, Phys Rev Lett, 120 (2018).
[195] Rayleigh, On the circulation of air observed in Kundt's tubes and on some allied acoustical problems, Philos Trans R Sco, 175 (1884).
[196] W.L. Nyborg, Acoustic streaming near a boundary, J Acoust Soc Am, 30 (1958).
[197] P.J. Westervelt, The theory of steady rotational flow generated by a sound field, J Acoust Soc Am, 25 (1953).
[198] K. Kolesnik, P. Hashemzadeh, D. Peng, M.E.M. Stamp, W. Tong, V. Rajagopal, M. Miansari, D.J. Collins, Periodic Rayleigh streaming vortices and Eckart flow arising from traveling-wave-based diffractive acoustic fields, Phys Rev E, 104 (2021) 045104.

[199] K. Knoerzer, P. Juliano, P. Roupas, C. Versteeg, Innovative food processing technologies: advances in multiphysics simulation, John Wiley and Sons and Institute of Food Technologists, 2011.

[200] I. Reyt, V. Daru, H. Bailliet, S. Moreau, J.C. Valiere, D. Baltean-Carles, C. Weisman, Fast acoustic streaming in standing waves: generation of an additional outer streaming cell, J Acoust Soc Am, 134 (2013) 1791-1801.

[201] F.J. Trujillo, K. Knoerzer, A computational modeling approach of the jet-like acoustic streaming and heat generation induced by low frequency high power ultrasonic horn reactors, Ultrason Sonochem, 18 (2011) 1263-1273.

[202] J. Lighthill, Acoustic streaming, J Sound Vib, 61 (1978) 391-418.

[203] J. Lighthill, Waves in fluids, Cambridge University Press, 1978.

[204] T. Sillanpaa, J. Makinen, A. Holmstrom, T. Pudas, J. Hyvonen, P. Lassila, A. Kuronen, T. Kotiaho, A. Salmi, E. Haeggstrom, Quantifying the Role of Transport by Acoustic Streaming in MHz Focused-Ultrasound-Based Surface Sampling, in: 2022 IEEE International Ultrasonics Symposium (IUS), Venice Convention Center, Venice, Italy, 2022, pp. 1-4.

[205] J.T. Karlsen, P. Augustsson, H. Bruus, Acoustic force density acting on inhomogenous fluids in acoustic fields, Phys Rev Lett, (2016).

[206] J.S. Bach, H. Bruus, Supression of acoustic streaming in shape-optimized channels, Phys Rev Lett, 124 (2020).

[207] L.E. Kinsler, A.R. Frey, A.B. Coppens, J.V. Sanders, Fundementals of acoustics, 4 ed., John Wiley and Sons, United States of America, 2000.

[208] M. Lim, M. Ashokkumar, Y. Son, The effects of liquid height/volume, initial concentration of reactant and acoustic power on sonochemical oxidation, Ultrason Sonochem, 21 (2014) 1988-1993.

[209] Y. Son, Y. No, J. Kim, Geometric and operational optimization of 20-kHz probe-type sonoreactor for enhancing sonochemical activity, Ultrason Sonochem, 65 (2020) 105065.

[210] B. Avvaru, A.B. Pandit, Experimental investigation of cavitational bubble dynamics under multi-frequency system, Ultrason Sonochem, 15 (2008) 578-589.

[211] J. Lighthill, The fourth annual fairey lecutre: The propagation of sound through moving fluids, J Sound Vib, 24 (1972) 471-492.

[212] T.W. Chapman, G.L. Bauer, Stagnation-point viscous flow of an incompressible fluid between porous plates with uniform blowing, Appl Sci Res, 31 (1975) 223-239.

[213] J.E. Piercy, J. Lamb, Acoustic streaming in liquids, Proc. R. Soc. Lond. Ser. A. Math. Phys., 226 (1954) 43-50.

[214] P.R. Gogate, P.A. Tatake, P.M. Kanthale, A.B. Pandit, Mapping of sonochemical reactors: Review, analysis, and experimental verification, AIChеE J, 48 (2002) 1542-1560.

[215] J. Newman, Numerical solution of coupled, ordinary differential equations, Ind Eng Chem Fund, 7 (1968).

[216] O. Dubrovski, J. Friend, O. Manor, Theory of acoustic streaming for arbitrary Reynolds number flow, J Fluid Mech, 975 (2023).

[217] M.B.a.Y. Dentry, L. Y. and Friend, J. R., Frequency effects on the scale and behavior of acoustic streaming, Phys Rev E Stat Nonlin Soft Matter Phys, 89 (2014) 013203.

[218] D.R. Miller, E.W. Comings, Static pressure distribution in the free turbulent jet, J Fluid Mech, 3 (1957).

[219] C. Feuillade, The attenuation and dispersion of sound in water containing multiply interacting air bubbles, JASA, 99 (1996) 3412–3430.

[220] H. Stommel, Trajectories of small bodies sinking slowly through convection cells, J. Mar. Res., 8 (1949) 24-29.

[221] P.F. Toobey, G.L. Wick, D. Isaacs, The motion of a amall sphere in a rotating velocity field: A possible mechanism for suspending particles in turbulence, J. Geophys. Res., 82 (1977) 2096-2100.
[222] M.J. Manton, On the motion of a small particle in the atmosphere, Bound. Lay. Meteorol 6(1974) 487-504.
[223] M.R. Maxey, The motion of small spherical particles in a cellular flow

field, Phys. Fluids, 30 (1987) 1915-1928.
[224] K. Tio, A. Linan, J.C. Lasheras, A.M. Ganan-Calvo, On the dynamics of buoyant and heavy partióles in a periodic stuart vortex flow, J. Fluid Mech., 254 (1993) 671-699.
[225] A.M. Ganan-Calvo, J.C. Lasheras, The dynamics and mixing of small spherical particles in a plane, free shear laye, Phys. Fluids A, 3 (1991) 1207-1217.
[226] Y. Kojima, Y. Asakura, G. Sugiyama, S. Koda, The effects of acoustic flow and mechanical flow on the sonochemical efficiency in a rectangular sonochemical reactor, Ultrason Sonochem, 17 (2010) 978-984.
[227] S. Hatanaka, K. Yasui, T. Kozuka, T. Tuziuti, H. Mitome, Influence of bubble clustering on multibubble sonoluminescence, Ultrasonics, 40 (2002) 655-660.
[228] G. Viciconte, V.P. Sarvothaman, P. Guida, T.T. Truscott, W.L. Roberts, High-speed imaging and Coumarin dosimetry of horn type ultrasonic reactors: Influence of probe diameter and amplitude, Ultrason Sonochem, 119 (2025) 107362.
[229] D. Fernandez Rivas, L. Stricker, A.G. Zijlstra, H.J. Gardeniers, D. Lohse, A. Prosperetti, Ultrasound artificially nucleated bubbles and their sonochemical radical production, Ultrason Sonochem, 20 (2013) 510-524.
[230] M. Ashokkumar, The characterization of acoustic cavitation bubbles - an overview, Ultrason Sonochem, 18 (2011) 864-872.
[231] B. Wang, T. Zeng, J. Shang, J. Tao, Y. Liu, T. Yang, H. Ren, G. Hu, Bubble dynamics model and its revelation of ultrasonic cavitation behavior in advanced oxidation processes: A review, Journal of Water Process Engineering, 63 (2024).
[232] M. Minnaert, XVI. On musical air-bubbles and the sounds of running water, The London, Edinburgh, and Dublin Philosophical Magazine and Journal of Science, 16 (1933) 235-248.